A NUMERICAL STUDY OF TURBULENCE-FLAME INTERACTION IN MILD COMBUSTION

VINCENZO PANEBIANCO

UNIVERSITY OF PORTSMOUTH
SCHOOL OF ENGINEERING

A DISSERTATION SUBMITTED FOR THE DEGREE OF DOCTOR OF PHILOSOPHY

December 2016

Dubium sapientiae initium.

René Descartes

Per Nunzia

Declaration

Whilst registered as a candidate for the above degree, I have not been registered for any other research award.
The results and conclusions embodied in this thesis are the work of the named candidate and have not been submitted for any other academic award.
This dissertation contains approximately 72000 words including bibliography, footnotes, tables and equations.

Vincenzo Panebianco
Thursday 3rd August, 2017

Acknowledgements

The present dissertation marks the end of my period at the University of Portsmouth. I remember as it were yesterday the induction week during which I filled up with several suggestions. Among the others, enjoy as much as I could one of the happiest period of a student's life. Soon I realised that the post-graduate period does not properly evolve along a straight line, and the happiness requires to be chased by putting lot of efforts. The help and suggestions from a number of people have been crucial during my period in Portsmouth.

Firstly, I would like to express my sincere gratitude to my advisors Dr. James Buick and Dr. Andy Aspden for their continuous support and patience. Their insightful guidance accompanied me along this four years adventure. I would also like to thank the rest of supervising team, Dr. Jason Knight and Prof. Jie Tong, for their precious comments and encouragement.

My sincere thanks goes to the university of Portsmouth, which funded my research and allowed me to be part of the post-graduate school at the engineering department.

My sincere thanks also goes to Robert Elliott from the petroleum lab. His continuous encouragements and his discreete presence in my life made him a true loyal friend.

I would like to thank Prof. Robert Crittenden from the ICG department, who has been fundamental to brighten my student path with all his precious advises, bringing me more times back on track. Equally important has been Gary Burton from the same department for his infinite patience in sorting out my numerous mistakes with the Sciama supercomputer.

All the numerous friends I met made this period an unforgettable experience: Serena, Toni, Marco, Maria, Luigi, Brad, Thiru, Katerina, Shafini, Saleh and all the others. You all made every day at the university a special day. Thank you for being part of my life.

I would like to thank my family: my parents, my brothers, my nephews, my nieces and all the relatives. They probably know very little about this experience, but their love and support has been with me always.

The last few sentences are all for Gina, my wife. She has been with me since the very beginning. She encouraged me and pushed me to overcome all the difficulties all the time. Describing in few words my gratitude for all her love and support is an impossible task. Our wedding and the life together straightened out all the issues and brought to me the happiness.

Contents

List of Tables

Summary

The transition in the energy market, from large fossil fuel consumption to the broad diffusion of renewable energies, involves an intermediate phase where more efficient techniques are developed for the existing power generation technologies. Among new combustion techniques, MILD (Moderate or Intense Low-oxygen Dilution) combustion is particularly attractive because of its potential characteristic to enhance thermal efficiency and reduce emissions like nitrogen oxides (NOx).

The successful application of MILD combustion requires a significant entrainment of hot combustion products into the fuel and/or oxidizer stream(s), yielding an increase of the reacting mixture temperature over its auto-ignition value. Such intense dilution causes a reduction in peak temperature levels, with a consequent reduction of NOx emissions, and a homogeneous temperature field followed by enhanced flame stability. Also the overall thermal efficiency is improved because of the recuperated heat.

The relative ease of obtaining reactant dilution in a full scale burner makes the MILD combustion regime interesting also from a technological point of view. Despite some interesting applications of MILD technique in industrial cases, its broad adoption is prevented by gaps in the knowledge of this combustion regime. Particularly, the development of simple and reliable numerical models is required to allow testing of full scale industrial burners with reasonable computational expense.

The present dissertation is focused on how the oxidiser temperature, oxidiser concentration and fuel concentration affect the complex interaction among molecular transport, chemical kinetics and turbulence that leads to self-ignition in MILD combustion.

The diffusion-chemistry contribution to ignition is investigated by means of a one dimensional (1D) zero velocity Direct Numerical Simulations (DNS) of two mixing layers representing a cold fuel mixture and a hot diluted oxidiser. Different oxidiser mixtures as well as different fuel blends are considered. Each case studied showed a different ignition behaviour. An in deep investigation of physical and chemical changes observed for each case along the ignition period is provided. A temporal and a spatial scaling methods are proposed to account for ignition behaviour differences and compare cases. The comparison revealed different aspects

of the self-ignition process. The differential diffusion effect plays an important role in the early stages of ignition, for cases presenting methane/hydrogen fuel mixture. If high is the level of hydrogen in the fuel blend, major stages of methane (CH_4) consumption pathway, from the CH_4 dehydrogenation to the carbon dioxide (CO_2) release, are significantly affected by hydrogen (H_2) chemistry. In the latest stages of ignition, the methane pathway is also affected by the drop in oxygen level.

The influence of turbulence on the diffusion-chemistry interaction is studied by means of three-dimensional (3D) Direct Numerical Simulations modelling a methane/hydrogen circular jet mixing with a diluted oxidiser co-flow. The effects of different fuel and oxidiser blends is also considered in the 3D study. In cases where large is the H_2 presence in the fuel jet, the presence of turbulent mixing has a minimal effects on early stages of self-ignition, where instead differential diffusion still plays a major role. As turbulence develops, more marked differences between 1D and 3D studies are observed. The role of turbulent mixing dominates over chemistry where the fuel blend includes a low amount hydrogen. For this configuration the temperature increment is strongly limited compared to corresponding 1D study.

The outcome of this study is expected to be of use to other researches in MILD combustion, particularly those adopting existing RANS and LES models to MILD combustion cases.

Chapter 1

Introduction

Anthropogenic greenhouse gas (GHG) emissions have increased since the pre-industrial era, driven by economic and population growth. This led to cumulative high atmospheric levels of carbon dioxide (CO_2), methane (CH_4) and nitrous oxide (N_2O), universally recognised as causes of the observed planet warming [1].

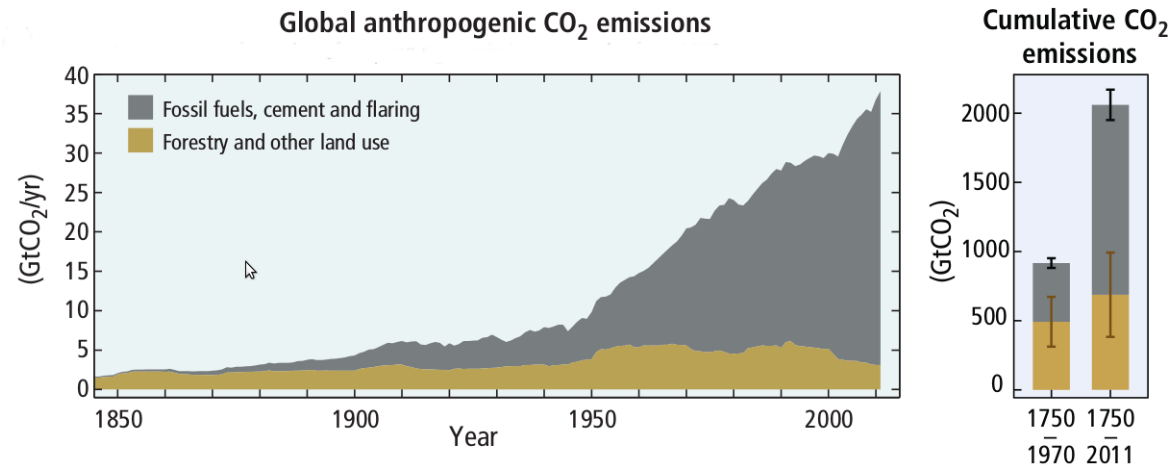

Figure 1.1: Global anthropogenic CO_2 emissions from burning of fossil fuel, cement production and flaring as well as forestry and other land use. Cumulative emissions of CO_2 from these sources and their uncertainties are shown on the right hand side [1].

In the last decades significant efforts have been made to developing cleaner and more efficient energy technologies to control GHG emissions. This commitment brought to decouple economic growth and energy-related emissions, for the first time in the last 40 years [2]. Renewable energy plants accounted for nearly half of all new power generation capacity in 2014, with strong investments and costs continuing to fall [2]. Carbon capture and storage (CCS) also achieved a major target in 2014, with the first coal fired power plant (Boundary Dam Power Station) coming in-line with post-combustion carbon dioxide (CO_2) capture. Together with the 15 large-scale CCS projects currently in operation, the current worldwide CO_2 capture capacity is set to around 28 million tonnes per year (Mtpa) [3].

The current pace of progress, however, is far from sufficient to reach the challenging target set during the 2015 United Nations Climate Change Conference (COP 21) held in Paris. In the document drafted as members agreement, the 196 attending parties agreed to reduce their carbon output in order to keep the global warming below 2 °C, relatively to the pre-industrial period. This temperature limit is generally accepted by the scientific community as a threshold beyond which climate change becomes potentially catastrophic [4].

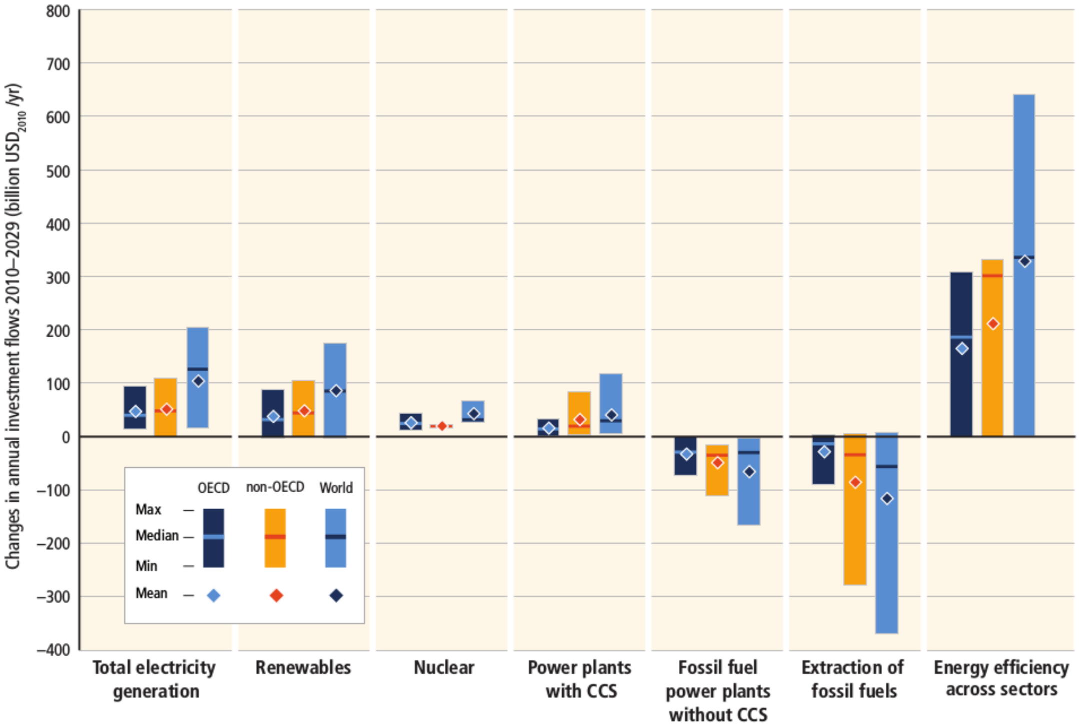

Figure 1.2: Change in annual investment flows over the next two decades (2010 to 2029) for mitigation scenarios that stabilize concentrations within the range of 430 to 530 ppm of equivalent CO_2 by 2100. The vertical bars indicate the range between the minimum and maximum estimate, while the horizontal bar indicates the median.

Despite the so called "Kyoto gases" (CH_4, N_2O, etc) represent an additional risk to exceed the warming threshold, the dominant (about 78% of total) anthropogenic climate change contribution is from CO_2 emissions due to fossil fuel combustion and industrial processes [1]. In its latest report, the Intergovernmental Panel on Climate Change (IPCC) estimates that, if the world can produces a maximum of 3000 gigatonnes (Gt) of carbon dioxide, it will have a 66-100% chance of limiting the global warming to 2 °C. Accounting for the CO_2 already emitted before 2014 (almost 2000 Gt as shown on figure 1.1), the total carbon "budget" deliverable into the atmosphere reduces to 1000 Gt. Assuming an yearly rate of CO_2 emission constant at 37 Gt, the emission budget will be exhausted in less than 30 years, significantly before all the recoverable fossil fuel resources will be consumed [5].

The proposed mitigation pathway requires a substantial emissions reduction (from 40 to 70% lower than 2010) over the next few decades and near zero emissions of cumulating GHG by the end of the century, leaving an estimated CO_2 equivalent concentration in the atmosphere in the range from 430 to 530 parts per million (ppm). This scenario strongly relies on the wide implementation of carbon capture systems and highly efficient combustion technologies, during the transition which will lead to the complete adoption of renewable energy sources [1]. In a similar way, the investments pattern will experience large changes. Over the next two decades, annual investments in conventional fossil fuel technologies associated with the electricity production are projected to decline, while annual investment in low carbon electricity supply will significantly rise (Fig. 1.2) [1].

In this challenging context, MILD combustion has caught the attention of scientific and industrial community because of its promising features of both high efficiency and lower pollutant emissions.

1.1 MILD technique overview

Among the different emission control technologies, MILD combustion has attracted the attention of the scientific and industrial communities for its combined capabilities to enhance combustion efficiency (thus reducing CO_2) and reduced NOx emissions.

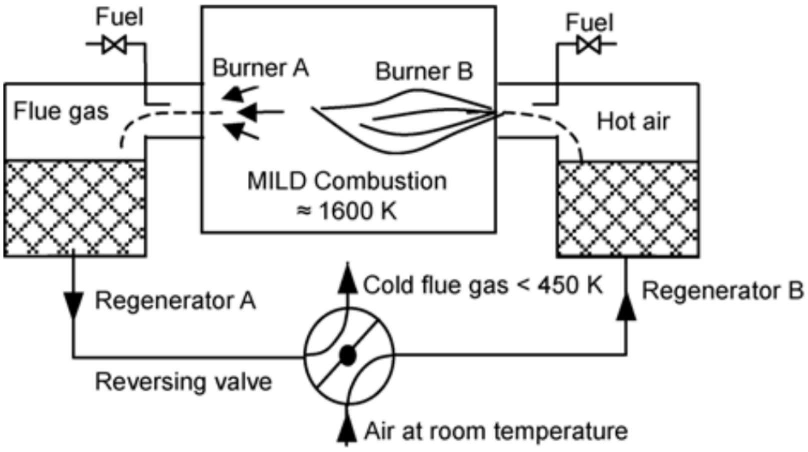

Figure 1.3: Schematic of a MILD burner coupled with a regenerative heat exchanger [6].

The heat and flue gas recirculation (either internally or externally) are the key factors determining the mild regime [6]. The recirculation of hot combustion products decreases the oxygen concentration and increases the temperature of the reactants. As a consequence, reaction rates are lowered and the volume of the reaction zone is increased. Distributing the heat release to a larger volume causes more uniform temperature field (compared to traditional combustion), with reduced peak temperatures. The benefits are important from an industrial point of view, since the net radiation flux results enhanced and lower are the emissions of temperature dependent pollutants such as NOx [6].

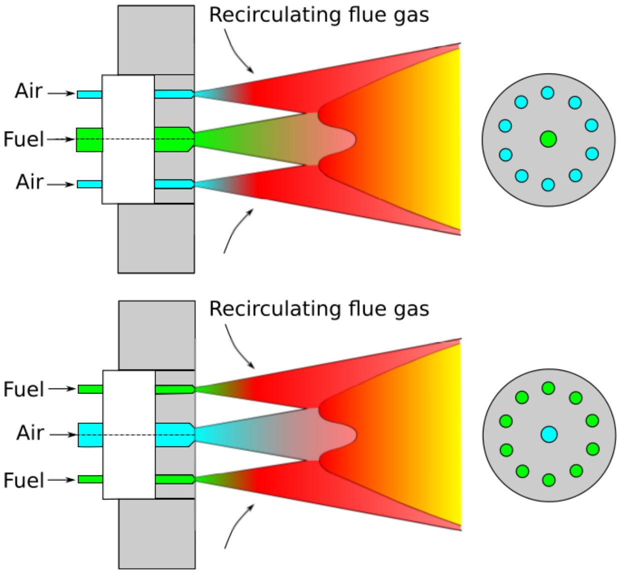

Figure 1.4: Schematic representation of two different exhaust gas entrainment methods [7].
Top: Entrainment of exhaust gas into the oxidizer stream.
Bottom: Entrainment of exhaust gas into the fuel stream.

In addition, the use of recuperated heat increases the thermal efficiency and improves considerably the flame stabilization [8]. The high flame stability under the MILD regime brings, also, the beneficial secondary effect to remove restrictions regarding the fuel which can be used. MILD regime can be successfully implemented with gaseous, liquid or solid fuels, either with high or low calorific value; once the requirements on the reactants dilution and heating are met [9]. Figure 1.5 compare, as an example, conventional and MILD firing modes achieved by using heavy oil with pre-heated and vitiated air.

The high dilution rate, well beyond the critical limits for conventional flame stabilization, is the features which distinguish the MILD technique from other conventional combustion strategies, such as staged combustion or exhaust gas recirculation (EGR), used to reduce emissions. In order to prevent flame quenching in such diluted conditions, MILD burners are usually coupled with air preheating systems which raise the temperature of reactants above their self-ignition temperature, sustaining oxidation reactions. Air preheating temperatures in the order of $800 - 1200°\mathrm{C}$ are possible by means of recuperative or regenerative heat exchangers, which recover energy from exhaust gases [9]. A schematic sample of MILD burner coupled with a regenerative heat exchanger is given in figure 1.3 [6].

Among different methods to obtain the correct reactants dilutions (the reactants dilution is also known in literature as *inertisation* [9]), two are the most widely used [10]. The first method, as described by Wunning et al. [11], considers a central jet of fuel surrounded circumferentially by a number of air jets supplying preheated combustion air. The air jets entrain large quantities of the recirculated combustion products before mixing with the fuel. In the second method, the combustion air is provided by a central high-momentum air jet, surrounded by a number of low-momentum fuel jets.

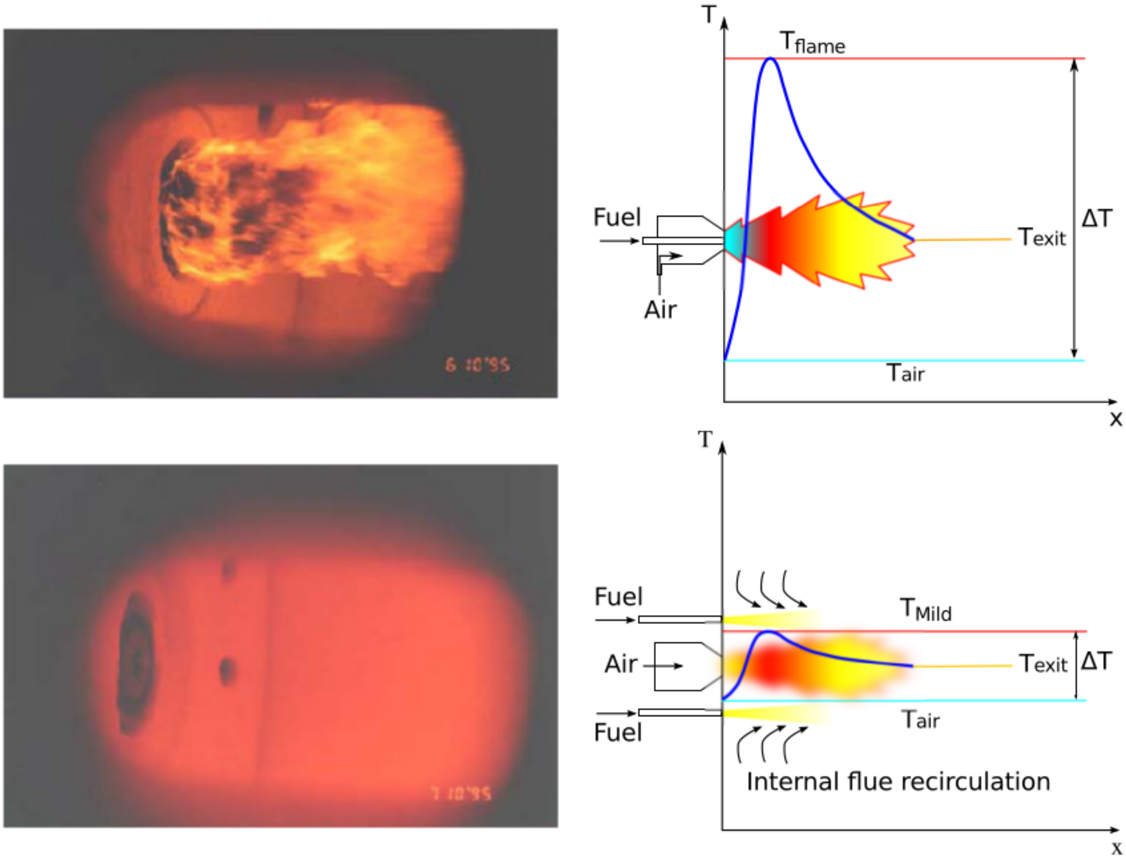

Figure 1.5: **Top**: Convention heavy oil firing. The fuel and air high velocity cold jets join a primary chamber to achieve early mixing and a stable flame.
Bottom: MILD heavy oil firing. Fuel and pre-heated high velocity air are injected separately into the flue gases within the furnace space. No concentrated flame front is visible, but reactions occur in a large volume of the furnace, where they proceed to completion [12].

The fuel jets are injected into recirculated combustion products, diluting the fuel before it mixes with the combustion air [13]. A schematic representation of both methods is shown on figure 1.4.

MIlD combustion technique is successfully utilised in many fields (metallurgy, power generation, gas turbine, engines, etc) and in different countries. Its industrial application dates back to the early 1990s [6]. Since then, different names have been used to identify this technology. Researchers who focused their interest principally on high temperature reactants, by preheating regenerative systems applied to combustion air, used the acronym HPAC (highly preheated air combustion) or HiTAC (High Temperature Air Combustion) [14, 15]. Similarly the term HiCOT (High temperature Combustion Technology) is mentioned in literature to refer, in a broader sense, to all technologies which uses high temperature reactants, not limiting the pre-heating to the air only [16].

Cavaliere *et al.* identified, under the name MILD, a precise subset of HiTAC and HiCOT domains, by defining the maximum temperature achievable. MILD regime definition is as follow:

“A combustion process is named MILD when the inlet temperature of the reactant mixture is higher than the mixture self-ignition temperature whereas the maximum allowable temperature increase with respect to inlet temperature during combustion is lower than mixture self-ignition temperature (in Kelvin)” [17]. More precisely, a firing mode operates under MILD conditions the following are verified:

$$\begin{cases} T_{\text{in}} > T_{\text{si}} & \text{Inlet Conditions,} \\ \Delta T < T_{\text{si}} & \text{Working Conditions,} \end{cases} \tag{1.1}$$

where T_{in} and T_{si} are respectively the oxidizer inlet temperature of the reactant mixture and the self-ignition temperature, while ΔT is the maximum temperature of the exhaust gases with respect to inlet temperature. The self-ignition temperature, refers to the fuel/air/diluent mixture. Different self-ignition temperatures may be obtained for different compositions. In a similar way, ΔT value varies according to different system configurations. For instance, if reactants are not premixed, the maximum temperature corresponds to the adiabatic flame temperature referred to the stoichiometric condition.

The conditions under which a MILD mode is operating, are graphically clarified by comparison with other combustion modes in figure 1.6. Here the combustion study of a $CH_4/O_2/N_2$ mixture with 0.1/0.05/0.85 molar fractions is presented. The mixture is burnt within a Well Stirred Reactor (WSR) for a residence time of 1s at atmospheric pressure. The diagram is divided in three regions by two lines intercepting the self-ignition temperature (T_{si}) on both axis. As the figure clearly shows, the main difference of MILD with respect to more traditional combustion modes like *feedback* and *high temperature combustion*, is that the heat released by reactants is not sufficient to sustain the flame, without some preheating.

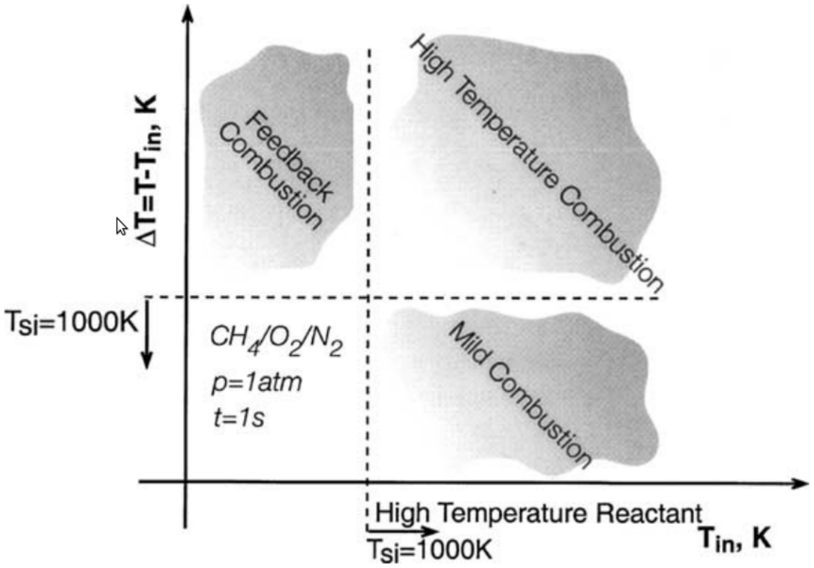

Figure 1.6: Comparison of different combustion modes achievable for a methane/oxygen/nitrogen mixture in a well stirred reactor [17].

Definitions often related to MILD combustion, despite related to different properties, are *flameless combustion* and *colorless combustion*. Flameless and colorless combustion definitions refer to properties occurring within the combustion chamber rather than to inlet conditions. As reported by IFRF institute, flameless combustion is defined as a mode in which two conditions must be satisfied wherein the reactions take place: (1) the reactants must exceed self-ignition temperature; (2) the reactants must have entrained enough inert combustion products to reduce the final reaction temperature well below adiabatic flame temperature, so much that a stable flame front is deliberately suppressed [9, 17] and no visible emissions are detectable. On this thesis work only the term MILD will be used thoroughly, referring to the conditions described by (1.1).

All the described MILD combustion benefits, should not hide potential problems linked with this regime, for instance the possibility to have partial oxidations and local instabilities due to the low-temperatures. An in-deep investigation of all potential drawbacks of MILD combustion along with the investigation of all its beneficial features, is required from the scientific community in order to promote a broader application of this technique.

This thesis work aims to contribute to this target, providing further insights into the MILD regime.

1.2 Thesis outline

This whole thesis work is structured into 8 chapters. An overview of the MILD combustion technique and its beneficial effects is presented in chapter 1. Chapter 2 describes the state of the art of the practical and numerical studies on this technique. The literature review on the numerical studies gives a particular focus to the ongoing studies on the kinetic processes involved once MILD regime is achieved, and highlights existing gaps in knowledge. Also a brief overview of the fundamental equations used to perform all the simulations in this thesis work, along with their numerical solver, are presented. Chapter 3 provides an overview of the methodology employed to analyse all diffusion cases investigated. Emphasis is given to the numerical set-up along with the numerical techniques developed to describe self-ignition. Chapter 4, chapter 5 and chapter 6 presents an extensive study of the diffusion-chemistry interplay during self-ignition under MILD firing mode. The knowledge acquired on the most reactive fuel/oxidiser configuration considered (chapter 4) is then expanded with the investigation on the MILD flexibility to different oxidiser mixtures (chapter 5) and fuels (chapter 6). In Chapter 7 the additional effect of turbulence on the diffusion-chemistry interplay during self-ignition period is explored. The numerical set-up presents 3D cylindrical fuel jets which aim to mimic an experimental set-up widely used in literature. Finally, chapter 8 summarises the insights resulting from the whole thesis work and highlights potential future works.

Chapter 2

Background

Combustion modelling requires knowledge of thermodynamic, chemical kinetics, fluid mechanics and numerical techniques. The present chapter gives a short overview of topics from each of these disciplines without any pretence to be exhaustive. A discussion on the state of the art of practical and numerical MILD combustion studies, is also presented.

2.1 Flame regimes

The vast majority of flame modes fall within two large sub-ranges, depending on the mixing of reactants: *premixed* and *non-premixed* flames.

Premixed flames constitute a specific class of combustion problems where fuel and oxidiser are mixed before they enter in the combustion chamber. Once the reactants are ignited, the flame front propagates towards the burner until a steady state is reached. Because the reactants pre-mixed, this firing mode is dominated by chemistry and presents fast reaction rates. The fast and complete combustion which typically characterises this regime, reduces the amount of pollutants produced but presents some safety issues. Some flammability limitations, due to the reactants mixing, characterise this flame mode: flames too rich or too lean cannot propagate [18].

A classical example of premixed combustion is given by the steady state *Bunsen* cone flame, where the laminar burning velocity is equal to the flow velocity component (v_n) normal to the flame front (fig.2.1). Behind the flame front unburned intermediates mix with the air leading to post flame oxidation and radiation.

The presence of eddies in the laminar flow significantly change the premixed combustion mode, with a strong increase of the mass consumption rate and the flame thickness. Similarly, the flame front affects the turbulent field with two opposing actions: it acts as a turbulence dampener, by increasing the gas viscosity, and accelerates and stretches the flow as a consequence of the gas expansion due to heat release (“flame-generated turbulence”) [18].

Premixed flame regimes are usually applied whenever intense combustion within a small volume is required (e.g. internal combustion engines).

In the second mode of combustion, reactants are stored separately and mix only within the combustion chamber. Fuel mixes with the surrounding air by convection and diffusion as combustion occurs. Combustion take places in proximity of the stoichiometric mixture surface, where composition of reactants allows for an almost complete consumption (fig.2.1). This leads to high flame temperature but also to higher pollutions level.

In most cases, chemical reactions are much faster than diffusion, so that diffusion is the rate limiting factor which controls the combustion process. The reason why this firing mode is often called “diffusion flame”rely on the controlling action of diffusive processes. Non-premixed flames are intrinsically safer than premixed counterpart and, being able to burn with any fuel/oxidiser flow rate, do not present any flammability limits [18].

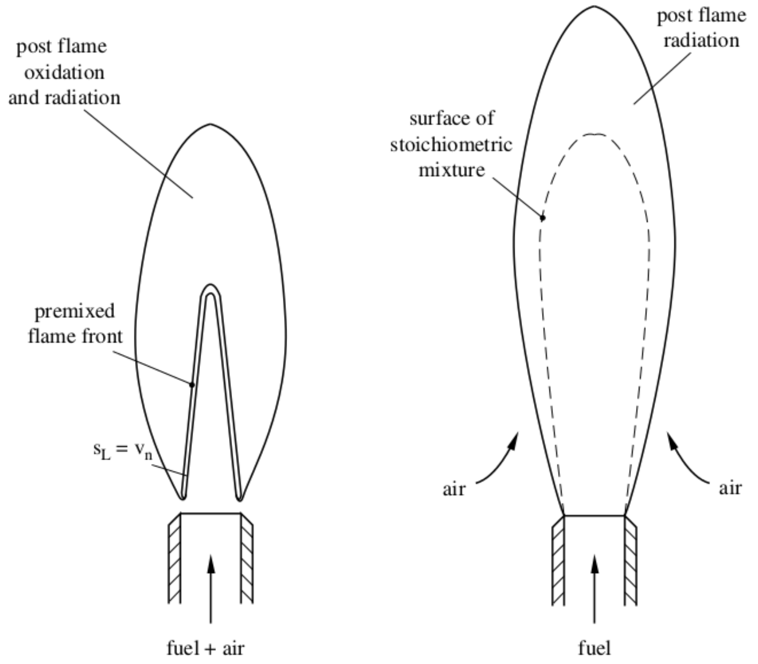

Figure 2.1: Schematic representation of laminar premixed (left) and non-premixed (right) flames [19].

Phenomena observed in turbulent premixed flames like flame-generated turbulence, viscous effects and flow stretching, are also found in the non-premixed flames. The main difference with respect to premixed flames is represented by the absence of flame propagation and the strong role of molecular diffusion. Reacting species in fact, require to reach the flame front by diffusion before reacting, even in presence of turbulence eddies. However turbulence has a strong effect on the molecular diffusion, either promoting (accelerating the convection of reactants close to the stoichiometric region) or hampering (interacting with reactants already close to the stoichiometric region) the process.

Large industrial furnaces usually operate under non-premixed conditions.

2.2 Governing equations

The Navier-Stokes (N-S) equations are the basic governing equations for a viscous, heat conducting fluid [20]. They are often referred as “momentum equation” , since they are obtained by applying, in vector form, the Newton’s law of motion to a fluid volume. The momentum equation is usually coupled with two additional scalar relations: the species conservation and the energy equation. This set of equations represent a powerful and widely used tool able to describe, in theory, every fluid-dynamic problem [1].

For a 3D problem, this set consists of five coupled scalar equations. Six dependent variables are described: the pressure p, the density ρ, the temperature T and the three components of the velocity vector $\mathbf{u}$. All the dependent variables are considered to be continuous functions of the spatial coordinates and time. In order to solve for all the six variables, an additional equation is necessary to close the system. This is usually represented by the ideal gas law.

An overview of the form used, in this thesis, for the species conservation equation, the momentum equation, the energy equation and the ideal gas law is provided below.

Species conservation equation

The species conservation equation is expressed in differential form for each species i as [21,22]:

$$\frac{\partial \rho Y_i}{\partial t} + \nabla \cdot (\rho \mathbf{u} Y_i) = \nabla \cdot (\rho D_i \nabla Y_i) + \dot{\omega}_i, \tag{2.1}$$

where the Y_i term is the mass fraction of the i-th species, $D_i(Y_i, T)$ represents the species mixture-averaged diffusion coefficient (described in more details in section 2.3) and $\dot{\omega}_i$ is the production rate. The physical meaning of relation (2.1) is clear: the rate of change of mass per unit volume ($\partial \rho Y_i / \partial t$) is due to the bulk motion of the fluid (convective term $\nabla \cdot (\mathbf{u} \rho Y_i)$), to the diffusion of chemical species (diffusive term $\nabla \cdot (\rho D_i \nabla Y_i)$) and to the production rate for ρY_i (reaction term $\dot{\omega}_i$).

Summing the species equations and noting that $\sum_i Y_i = 1$, $\sum_i D_i \nabla Y_i = 0$ and $\sum_i \dot{\omega}_i = 0$, equation (2.1) leads to the well known form:

$$\frac{\partial \rho}{\partial t} + \nabla \cdot (\rho \mathbf{u}) = 0. \tag{2.2}$$

In case of negligible pressure variation, as for the low Mach number study here presented, the flow is usually considered as incompressible and the following assumption is made:

$$\frac{D\rho}{Dt} = \frac{\partial \rho}{\partial t} + \mathbf{u} \cdot \nabla \rho = 0, \tag{2.3}$$

where the term $D\rho/Dt$ is the material derivative of the density. Equation (2.3) coupled with

---

[1] Commonly, the term Navier-Stokes is used to refer to all of these equations.

(2.2) leads to the divergence free condition:

$$\nabla \cdot \mathbf{u} = 0, \tag{2.4}$$

which represents the common expression of the *continuity* equation for non-reacting continuous flows with low Mach number. However, because of the strong density variation due to heat release, the expression (2.1) is used in this thesis work to describe the mass balance.

Momentum equation

The momentum equation is an application of Newton's second law to fluid flow. Particularly, for a volume of fluid V_0 having a surface S_0, the rate change of momentum equals the sum of all applied forces:

$$\int_{V0} \frac{\partial \rho \mathbf{u}}{\partial t} \mathrm{d}V + \int_{S0} \rho \mathbf{u}\mathbf{u} \cdot \mathbf{n} \mathrm{d}S = \mathbf{F}. \tag{2.5}$$

The forces acting on the fluid can be grouped in two fields: body forces $\mathbf{F_v}$ (acting throughout the volume of the fluid element) and surface forces $\mathbf{F_s}$ (acting only on the external surface of the fluid element). The former fields includes weight, Coriolis and centrifugal force, while pressure and viscous forces belong to the latter. More specifically, the surface and volume forces can be defined as:

$$\mathbf{F_s} = \int_{S_0} \bar{\bar{\mathbf{T}}} \cdot \mathbf{n} \mathrm{d}S, \tag{2.6}$$

$$\mathbf{F_v} = \int_{V_0} \rho \mathbf{f} \mathrm{d}V, \tag{2.7}$$

where $\bar{\bar{\mathbf{T}}}$ is the surface stress tensor, $\mathbf{n}$ is the versor normal to S_0 and $\mathbf{f}$ is the specific body force (per unit mass). The stress tensor can be decomposed into an isotropic part due to the pressure forces, which tends to change the volume of the fluid body, and a deviatoric part due to the viscous forces, which tends to deform the body. Mathematically this is presented as:

$$\bar{\bar{\mathbf{T}}} = -p\bar{\bar{\mathbf{I}}} + \bar{\bar{\tau}}, \tag{2.8}$$

where $\bar{\bar{\mathbf{I}}}$ is the identity tensor and $\bar{\bar{\tau}}$ is the deviatoric part of the stress tensor. Considering the relation (2.8) and neglecting body forces, the differential form of the momentum balance can be expressed as [23]:

$$\frac{\partial \rho \mathbf{u}}{\partial t} + \nabla \cdot (\rho \mathbf{u}\mathbf{u}) = -\nabla p + \nabla \cdot \bar{\bar{\tau}}. \tag{2.9}$$

In the case of a Newtonian and isotropic fluid, such as the gas mixture considered in this thesis, the tensor $\bar{\bar{\tau}}$ can be expressed as [23, 24]:

$$\bar{\bar{\tau}} = \mu \left[\nabla \mathbf{u} + (\nabla \mathbf{u})^{\mathrm{T}} - \frac{2}{3} \bar{\bar{\mathbf{I}}} (\nabla \cdot \mathbf{u})) \right], \tag{2.10}$$

where $\mu(Y_i, T)$ is the fluid viscosity.

In a way similar to the species conservation equation it is possible to provide a physical explanation of the equation (2.9). The $\nabla \cdot (\rho \mathbf{u}\mathbf{u})$ term on the left hand side represents the momentum transport due to the bulk motion of the fluid, often referred as inertia forces. The diffusive term is $\nabla \cdot \bar{\bar{\tau}}$, which is related to fluid viscosity. Turbulence and its dissipation are a consequence of the balance of these two terms.

Even though the momentum equation does not include explicit reaction terms, so the same expression can be used for a non-reacting mixture, the flow is modified by combustion. The dynamic viscosity μ is strongly dependent on the temperature. As a consequence, the local Reynolds number varies much more than in a non reacting mixture, strongly affecting the flow behaviour.

Energy equation

The definition of the energy equation for a multi-component reacting fluid, relies on the application of the first law of thermodynamic. For a defined fluid volume V_0 having a surface S_0, the rate of change of energy equals the work and heat exchanged per unit time, as follow:

$$\int_{V0} \frac{\partial \rho \epsilon}{\partial t} \mathrm{d}V + \int_{S0} \rho \epsilon \mathbf{u} \cdot \mathbf{n} \mathrm{d}S = \dot{L} + \dot{Q}. \tag{2.11}$$

The variable ϵ represents the total specific energy, while $\dot{L}$ and $\dot{Q}$ are respectively the time rate of change of work and heat exchanged. In a way similar to the derivation of the momentum equation, it is possible to split both the work and heat terms into surface and volume contributions:

$$\dot{L}_s = \int_{S_0} (\bar{\bar{\mathbf{T}}} \cdot \mathbf{n}) \cdot \mathbf{u} \mathrm{d}S \qquad \text{and} \qquad \dot{L}_v = \int_{V_0} \rho \mathbf{f} \cdot \mathbf{u} \mathrm{d}V, \tag{2.12}$$

$$\dot{Q}_s = -\int_{S_0} \mathbf{K} \cdot \mathbf{n} \mathrm{d}S \qquad \text{and} \qquad \dot{Q}_v = \int_{V_0} \rho \dot{q} \mathrm{d}V, \tag{2.13}$$

where $\mathbf{K}$ represents the heat flux entering in the system through the volume surface and $\dot{q}$ is the specific heat generated within the volume considered [2]. The term $\dot{q}$ does not express the heat released by combustion, but rather the heat generated, for example, by a radiative flux

---

[2] The negative expression for $\dot{Q}_s = -\int_{S_0} \mathbf{K} \cdot \mathbf{n} \mathrm{d}S$ is due to the orientation of $\mathbf{n}$, which is positive if pointing externally to the system. Having defined $\mathbf{K}$ positive if entering in the system, the product $\mathbf{K} \cdot \mathbf{n}$ would result negative for heat fluxes entering in the system

or an electric spark [18].

Considering the decomposition of the stress tensor shown in (2.8) and assuming that the volume contribution of both $\dot{L}$ and $\dot{Q}$ are negligible, the differential form of the energy equation can be given as:

$$\frac{\partial \rho \epsilon}{\partial t} + \nabla \cdot (\rho \epsilon \mathbf{u}) = -\nabla \cdot (p\mathbf{u}) + \nabla \cdot (\bar{\bar{\tau}} \cdot \mathbf{u}) - \nabla \cdot \mathbf{K}. \tag{2.14}$$

The heat flux $\mathbf{K}$ can be expressed, neglecting the *Soret* and *Dufour* effect, which will be mentioned in section 2.3, as:

$$\mathbf{K} = -\lambda \nabla T - \sum_i \rho h_i D_i \nabla Y_i, \tag{2.15}$$

where the first term on the right hand side expresses the Fourier's law, while the second represents the diffusion of species having different enthalpies $h_i(T)$. Differentiating the expression for gas mixture specific enthalpy ($h = \sum_i Y_i h_i$) and considering the temperature dependence of h_i ($\frac{\partial h_i}{\partial T} = c_{p_i}$), the heat flux can be written as [25]:

$$\mathbf{K} = -\frac{\lambda}{c_p} \nabla h + \sum_i h_i (\frac{\lambda}{c_p} - \rho D_i) \nabla Y_i, \tag{2.16}$$

where λ represents the fluid heat conductivity, c_{p_i} is the i-th species specific heat at constant pressure and c_p is the fluid specific heat at constant pressure ($c_p = \sum_i Y_i c_{p_i}$). Considering also the total specific energy as:

$$\epsilon = e + \frac{u^2}{2}, \tag{2.17}$$

where the specific internal energy e is:

$$e = h - \frac{p}{\rho}, \tag{2.18}$$

the differential expression of the energy conservation equation assumes the form:

$$\frac{\partial (\rho h)}{\partial t} + \nabla \cdot (\rho \mathbf{u} h) = \nabla \cdot \frac{\lambda}{c_p} \nabla h + \sum_i \nabla \cdot \left[h_i (\rho D_i - \frac{\lambda}{c_p}) \nabla Y_i \right], \tag{2.19}$$

Ideal gas law

The ideal gas law relates density (or volume), pressure and temperature without introducing any additional quantity, as follow [22, 24]:

$$p = \rho R T \sum_i \frac{Y_i}{W_i} \tag{2.20}$$

The equation (2.20) describes the pressure for a mixture of i gaseous species having mass fraction equal to Y_i and molecular weight equal to W_i. R is the universal gas constant.

2.3 Heat and species diffusion

Accurate modelling of transport phenomena, like heat and species diffusion, represents a critical aspect in the simulation of the structure and behaviour of flames, where a multitude of chemical species interact strongly with each other in narrow spatial domains [26]. This is particularly true in the MILD regime, where autoignition follows the mixing of reactants at different temperatures and with different diffusion speeds.

These aspects are accounted for in the governing equations by means of species diffusion and heat flux, both relying on the mathematical description of the species *diffusion flux* [25].

The heat flux, for example, is usually represented as proportional to the temperature gradient (Fourier's law) and species diffusion, neglecting the *Dufour* effect (heat flux due to species mass fraction gradients). With this assumption the heat law expression assume the form:

$$\mathbf{K} = -\lambda \nabla T + \sum_i h_i \mathbf{J}_i, \tag{2.21}$$

The most general form for the diffusion flux ($\mathbf{J}_i$) of a N-species mixture is written as:

$$\mathbf{J}_i = \sum_j -\rho Y_i D_{ij} \nabla X_j - \frac{\rho Y_i \theta_i}{T} \nabla T, \tag{2.22}$$

commonly referred in literature as *multicomponent* formulation [25]. In the aforementioned equation the X_j and θ_i terms express the mole fraction and the thermal diffusion coefficient (described in more details later in this section) of the j-th and i-th species respectively. Moreover, the term D_{ij} represents the i-th species diffusion coefficient into each j-th species.

The multicomponent diffusion model, derived from the Boltzmann equation of kinetic theory, offers the most rigorous diffusion description for combustion simulations [26]. Particularly, the *Soret* effect (final term in equation (2.22), molecular species diffusion due to temperature gradients) is considered in this model, while usually neglected in simpler expressions of species diffusion. The implementation of this model however, requires the calculation of the diffusion coefficients for each pair of species (D_{ij}) to account for different species diffusing simultaneously (species i into j). This could be achieved, at a computational cost, by resolving a further system of equations which gives species diffusion velocities, but this method is usually not adopted, preferring instead the calculation of the diffusion coefficient with simpler approaches [18].

A good accuracy is offered by the *mixture averaged* diffusion model [26]. By neglecting the Soret effect, the expression (2.22) reduces to the Fick's law form as follow:

$$\mathbf{J}_i = -\rho D_{i,\mathrm{mix}} \nabla Y_i, \tag{2.23}$$

where the $D_{i,\mathrm{mix}}$ term expresses the *diffusion coefficient* of each i-th species into a mixture made by the remaining N-1 species. The mathematical formulation of the $D_{i,\mathrm{mix}}$ [3] diffusion coefficient is [27] :

$$D_{i,\mathrm{mix}} = \frac{1 - Y_i}{\sum_{j \neq i}^{N} X_j D_{ji}}. \tag{2.24}$$

Since for each of the i species a specific $D_{i,\mathrm{mix}}$ coefficient is computed, the differential diffusion effect is caught. The mixture averaged approach significantly reduces the computational cost [26] despite remaining a reasonable simplification, especially for multicomponent mixtures where one component occurs in large amounts (e.g. combustion in air where nitrogen is abundant [28]). Nonetheless, it should be noted that the equation (2.24) does not guarantee that the $\sum_i^N D_{i,\mathrm{mix}} \nabla Y_i = 0$ (net species diffusion flux) condition is satisfied. As such, correction schemes are required when using this approach.

Another widely used approximation consists in characterising the diffusion coefficients in terms of the *Lewis* number defined as:

$$\mathrm{Le}_i = \frac{\lambda}{\rho c_p D_i} = \frac{\theta}{D_i}, \tag{2.25}$$

where λ is the thermal conductivity while $\theta = \lambda/\rho c_p$ expresses the mixture thermal diffusivity coefficient. As equation (2.25) explains, this non-dimensional variable compares the heat diffusion speed (θ) with the species diffusion (D_i).

Even though the Lewis number is a local quantity, a further simplification of the diffusion law consists of expressing diffusion coefficients in terms of constant Le_i. In order to account for differential diffusion, some codes assign to each species involved an estimated Le_i value (an example of tabulated values is shown in table 2.1) [19].

Species	CH_4	H_2	O_2	CO_2	CO	H_2O	H	O
Le_i	0.97	0.30	1.11	1.39	1.10	0.83	0.18	0.70
Species	OH	CH_3	HO_2	HCO	H_2O_2	CH_2O	CH_3O	
Le_i	0.73	1.00	1.10	1.27	1.12	1.28	1.30	

Table 2.1: Estimated values of Lewis numbers for some reacting species occurring in methane-air flames [19].

The simplest, but also least accurate approach, in modelling diffusion, neglects the preferential diffusion between heat and species by setting the Lewis number equal to unity ($\lambda/\rho c_p = D_i$). This implies a constant value of D_i for all the species and the differential diffusion is no longer accounted for.

In this thesis work, the mixture averaged model is used to account for the transport phenomena. Soret and Dufour effects are neglected.

---

[3] It should be noted that the mixture averaged diffusion coefficient $D_{i,\mathrm{mix}}$ is shown in governing equation as D_i. Nonetheless its physical meaning remains unchanged.

2.4 Mixture fraction

The vast majority of industrial furnaces operate under non-premixed conditions and MILD burners, because of safety requirements linked to the high reactant temperature, make no exception in this regard.

In diffusion as well as turbulent flames, mixing brings reactants into the reaction zone at a fast enough rate for combustion to proceed. Achieving the proper mixing, represents a major tasks in industrial furnaces in order to avoid flame quenching or incomplete combustion. From a numerical point of view, the modelling of mixing is of the utmost important for tracking reactants in the reaction zone and gaining fundamental insights on the flame structure.

A common tool used by the combustion community to investigate reactant mixing under non-premixed condition is the *mixture fraction*. This variable provides insights into the local fuel/oxidiser ratio in the mixture. The mixture fraction is formulated, according to Bilger's definition, as a function of C, H and O elements as follow [29]:

$$Z = \frac{Z^* - Z^*_{\mathrm{ox}}}{Z^*_{\mathrm{fu}} - Z^*_{\mathrm{ox}}}, \text{ with} \tag{2.26}$$

$$Z^* = 2\frac{Y_C}{W_C} + \frac{1}{2}\frac{Y_H}{W_H} - \frac{Y_O}{W_O}, \tag{2.27}$$

where the subscripts "fu" and "ox" refer to the fuel and oxidiser streams while Y_j and W_j represents respectively the mass fraction and atomic mass of the element j. The superscript "*" distinguishes the not-normalised expression of mixture fraction from the normalised one (without "*"). More precisely, the Z term is normalised with respect to values of mixture fraction computed in the fuel (Z^*_{fu}) and oxidiser (Z^*_{ox}) streams. As such, the Z value ranges from zero (pure oxidiser) to one (pure fuel).

Z is a passive (or conserved) scalar which changes because of diffusion and convection, but not reaction, since elements are conserved during combustion [4]. If $Z < Z_{\mathrm{st}}$, the stoichiometric mixture fraction, fuel is deficient and the mixture is fuel lean. On the other hand if $Z > Z_{\mathrm{st}}$, there is an excess of fuel and the mixture is considered fuel rich.

2.5 Adiabatic flame temperature

For a combustion process that takes place adiabatically with no shaft work and neglecting incomplete combustion and dissociation effects, the temperature of the products is referred as the *adiabatic flame temperature*. This value represents the maximum temperature that can be achieved theoretically under specified physical and chemical condition.

The mathematical description of the adiabatic flame temperature for domains with constant

---

[4] Reaction plays an indirect role on Z controlling temperature and, therefore, density and velocity fields, and thus diffusion and convection

pressure, a typical condition for non-premixed burners, is based on the first law of thermodynamics, which, under the aforementioned assumptions, equals the absolute enthalpy of reactants at the initial state ($T = T_{\mathrm{in}}$, $p = 1\mathrm{atm}$) with the absolute enthalpy at final state ($T = T_{\mathrm{ad}}$, $p = 1\mathrm{atm}$) as follow [30]:

$$h(T_{\mathrm{in}}) = h(T_{\mathrm{ad}}) \tag{2.28}$$

The enthalpy at the initial (unburnt) and final (burnt) state can be expressed, for a mixture of N species, as follow [18]:

$$h(T_{\mathrm{in}}) = \sum_{i=1}^{N} \nu_i^{'} \left(\Delta H_{\mathrm{f},i}^{0,\mathrm{m}} + \int_{T_0}^{T_{\mathrm{in}}} {c_{p_i}}^{\mathrm{m}} dT \right), \tag{2.29}$$

$$h(T_{\mathrm{ad}}) = \sum_{i=1}^{N} \nu_i^{''} \left(\Delta H_{\mathrm{f},i}^{0,\mathrm{m}} + \int_{T_0}^{T_{\mathrm{ad}}} {c_{p_i}}^{\mathrm{m}} dT \right), \tag{2.30}$$

where the mole fraction of species i for reactants and products are defined respectively as $\nu_k^{'}$ and $\nu_k^{''}$. As equations (2.29) and (2.30) show, the absolute enthalpy formulation is split into the *formation* ("f" subscript) and *sensible* (integral expression) terms. The former relates to the energy exchanged because of the chemical bonds cleavage at T_0 = 298.15 K, while the latter represents the energy exchanged because of the increase in temperature from the reference. Both terms are expressed in molar form as indicated by the superscript "m".

The value of the adiabatic flame temperature is estimated by solving equation (2.28) for T_{ad} using a ${c_{p_i}}^{\mathrm{m}}$ value found from an estimate of T_{ad}.

In section 3.3.2 is practically described the solution of (2.28) in order to estimate T_{ad} values for each case investigated.

2.6 Chemical kinetics and pathways

In real combustion systems, the chemical fuel/oxidiser interaction is advanced by a sequence of different *elementary* steps, which form the so-called *chain reaction*. The rate at which chemical species are created and/or destroyed via elementary reactions is limited by the chemical kinetics. Together with convection and diffusion, chemical kinetics is of the utmost importance in describing the overall characteristic of a flame.

A chain reaction is *initiated*, *propagated* and then *terminated* through the production and/or destruction of intermediates, known as chain *carriers*. In combustion processes, intermediates often present an unpaired valence electron in their structure. This feature gives to the intermediates, named *radicals* in this particular case, a characteristic of high reactivity with respect to other species.

The formation of the first radical in a chemical reaction is termed the initiation step [5]. The chain reaction continues via multiple propagating processes (the formed radical contributes to the consumption a stable species and produces another radical) until a step involving the consumption of free radicals and the formation of a stable species stops the chain (chain-terminating step). A typical feature of combustion chain reaction is the presence of a chain *branching* processes: these steps produce more radicals than they consume. The spontaneous ignition of a fuel-oxidiser mixture relies on branching processes, since it happens when a large enough level of radicals is present to sustain and accelerate oxidation. A schematic example of all the steps that a reaction chain undergoes is shown in figure 2.2.

$$\begin{array}{ll}
\mathrm{A} \longrightarrow \mathrm{B} + \mathrm{C}^{\cdot} & \qquad \text{Initiation} \\
\mathrm{A} + \mathrm{B}^{\cdot} \longrightarrow \mathrm{C}^{\cdot} + \mathrm{D}^{\cdot} & \qquad \text{Branching} \\
\mathrm{A} + \mathrm{B}^{\cdot} \longrightarrow \mathrm{C} + \mathrm{D}^{\cdot} & \qquad \text{Propagation} \\
\mathrm{A}^{\cdot} + \mathrm{B}^{\cdot} \longrightarrow \mathrm{C} & \qquad \text{Termination}
\end{array}$$

Figure 2.2: A schematic example of all the parts a chain reaction is made of. The radicals are represented by dotted symbols.

The elementary reactions occur due to collisions among specific molecules in the reaction zone. More frequent collisions correspond to more rapid reactions. The quantity which describes the evolution in time of an elementary reaction is called the *reaction rate*. Its formulation can be obtained by considering a generic elementary reaction and its rate coefficient (k_f, described later in this section), as shown on figure 2.3. Here the molecule A reacts with B to form C and D. The reactants are shown with stoichiometric coefficients ν', while the products with ν''.

$$\nu'_{\mathrm{A}}\mathrm{A} + \nu'_{\mathrm{B}}\mathrm{B} \xrightarrow{k_f} \nu''_{\mathrm{C}}\mathrm{C} + \nu''_{\mathrm{D}}\mathrm{D}$$

Figure 2.3: An example of a forward elementary reaction and its rate of progress.

The rate of consumption of species A and B is proportional to the molar concentration of A and of B (indicated as [A] and [B]) as:

$$\left(\frac{d[\mathrm{A}]}{dt}\right)_f = -\nu'_{\mathrm{A}} k_f [\mathrm{A}]^{\nu'_{\mathrm{A}}} [\mathrm{B}]^{\nu'_{\mathrm{B}}} = -\nu'_{\mathrm{A}} r_f, \tag{2.31}$$

$$\left(\frac{d[\mathrm{B}]}{dt}\right)_f = -\nu'_{\mathrm{B}} k_f [\mathrm{A}]^{\nu'_{\mathrm{A}}} [\mathrm{B}]^{\nu'_{\mathrm{B}}} = -\nu'_{\mathrm{B}} r_f. \tag{2.32}$$

---

[5] In the ignition process of an hydrocarbon, it typically consists of the abstraction of a hydrogen atom.

The exponents $\nu^{'}_{\mathrm{A}}$ and $\nu^{'}_{\mathrm{B}}$ represent the *reaction order*, which control how the reactants concentration affects the reaction rate. They depend on the reaction mechanism considered and usually differ from stoichiometric coefficient. However, for elementary reactions they equal the stoichiometric coefficients of each reactant [19]. The k_f constant of proportionality, termed *reaction rate coefficient*, is usually expressed as a function the temperature. The subscript f indicates the forward progress of the reaction. Since the molar concentration of A/B reduces in time, the time derivatives are expressed with a negative sign. The equations 2.32 and 2.32 indicates with r_f the reaction rate. More generically, for an elementary reaction containing an arbitrary number of reactants n the reaction rate can be expressed as:

$$r_f = k_f \prod_{j=1}^{n} [X_j]^{\nu^{'}_j} \tag{2.33}$$

Similarly to the forward reaction rate, it is possible to define for every elementary reaction a backward reaction rate when products collide to form reactants (fig.2.4).

$$\nu^{'}_{\mathrm{A}}\mathrm{A} + \nu^{'}_{\mathrm{B}}\mathrm{B} \xleftarrow{k_b} \nu^{''}_{\mathrm{C}}\mathrm{C} + \nu^{''}_{\mathrm{D}}\mathrm{D}$$

Figure 2.4: An example of a backward elementary reaction and its rate of progress.

The rate of molar production of A/B species is then expresses as:

$$\left(\frac{d[\mathrm{A}]}{dt}\right)_f = \nu^{'}_{\mathrm{A}} k_b [\mathrm{A}]^{\nu^{'}_{\mathrm{A}}} [\mathrm{B}]^{\nu^{'}_{\mathrm{B}}} = \nu^{'}_{\mathrm{A}} r_b, \tag{2.34}$$

$$\left(\frac{d[\mathrm{B}]}{dt}\right)_f = \nu^{'}_{\mathrm{B}} k_b [\mathrm{A}]^{\nu^{'}_{\mathrm{A}}} [\mathrm{B}]^{\nu^{'}_{\mathrm{B}}} = \nu^{'}_{\mathrm{B}} r_b, \tag{2.35}$$

while the generic expression of backward reaction rate is formulated as:

$$r_b = k_b \prod_{j=1}^{n} [X_j]^{\nu^{'}_j}. \tag{2.36}$$

It follows that the net reaction rate $(\mathrm{mol/m^3 \cdot s})$ for an elementary reaction with n reactants can be written as the sum of the forward and backward expressions:

$$r = k_f \prod_{j=1}^{n} [X_j]^{\nu^{'}_j} - k_b \prod_{j=1}^{n} [X_j]^{\nu^{'}_j}. \tag{2.37}$$

Reaction rate coefficient

As the temperature rises, molecules move faster and collide more vigorously, and the possibility of bond cleavages and molecular rearrangements increases. The strong dependence of molecular rearrangement, and so reaction, to temperature is included in the mathematical description of rate coefficients (k_f and k_b parameters in equations (2.33) and (2.36), represented by the Arrhenius law formulation:

$$k_\mathrm{f}(T) = A_\mathrm{f}\mathrm{e}^{-\left(\frac{E_\mathrm{f}}{RT}\right)}, \tag{2.38}$$

$$k_\mathrm{b}(T) = A_\mathrm{b}\mathrm{e}^{-\left(\frac{E_\mathrm{b}}{RT}\right)}. \tag{2.39}$$

The modified three-parameter Arrhenius form is considered in this dissertation to describe mathematically the reaction rate coefficients. This form, widely used in literature, is flexible enough to describe the temperature dependence of k_f and k_b over a wide range of temperatures [27]. It is defined as follow:

$$k_\mathrm{f}(T) = A_\mathrm{f}T^{\beta_\mathrm{f}}\mathrm{e}^{-\left(\frac{E_f}{RT}\right)}, \tag{2.40}$$

$$k_\mathrm{b}(T) = A_\mathrm{b}T^{\beta_\mathrm{b}}\mathrm{e}^{-\left(\frac{E_b}{RT}\right)}, \tag{2.41}$$

whereA_f is the frequency factor, T is the temperature, E_f is the activation energy and R is the universal gas constant. The subscripts f and b refers to the forward and backward directions of elementary reactions. The three parameters consist in the A, β and E terms, which will be discussed below.

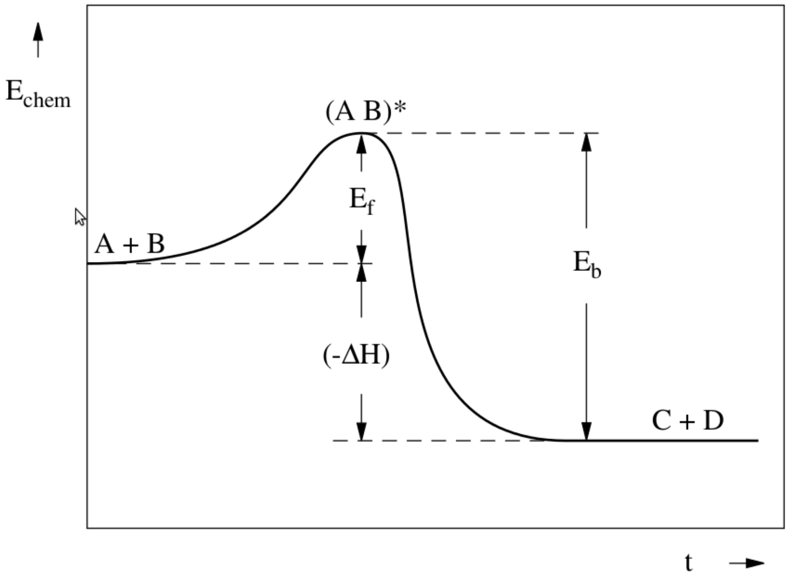

Figure 2.5: The chemical energy $\mathrm{E}_{\mathrm{chem}}$ contained in the different species is plotted schematically against time along the reaction progress. The intermediate activated complex is shown as AB^* [19]

As shown in figure 2.5, the activation energy is the threshold energy (E_f) that the reactants must acquire before reaching the transition state (or activated complex). Then, assuming the reaction is exothermic, the products reach a more stable configuration at a lower energetic level, and the energy difference between reactants and products ($-\Delta$H) is released as heat. A similar process is necessary for the backward direction, with the difference of an higher threshold energy required (E_b). The term RT represents a different form of energy, the average kinetic energy, which is a linear function of the temperature. The ratio between these two form of energies (activation and kinetic) controls the rate of reaction. The larger the ratio, the lower will be the rate. This means that high temperature and low activation energy produce larger rate constants, and thus speed up the reaction.

The frequency of collisions, due to the orientation and structure of reactants, is accounted for the frequency factor, A_f and A_b, also termed as *pre-exponential factor*. Its value may vary with different temperature values. The algebraic power dependence T^{β_f}, referred as pre-exponential temperature dependence, makes explicit the temperature dependence of the pre-exponential factor.

The appendix A provides a detailed list of A_f, β_f and E_f term for each of the elementary reaction considered.

Reaction Path analysis

While the kinetic analysis sheds light on the rates of each elementary reaction in the reaction chain, a global overview of the path followed by species is provided by reaction path analysis. The reaction path diagram shows, in a nodes/arrows fashion, the atoms transfer from one species to another, as the example provided in figure 2.6. The description is both qualitative and quantitative since the direction of arrows show the atom path, while their thickness is proportional to the atoms exchange rate between species.

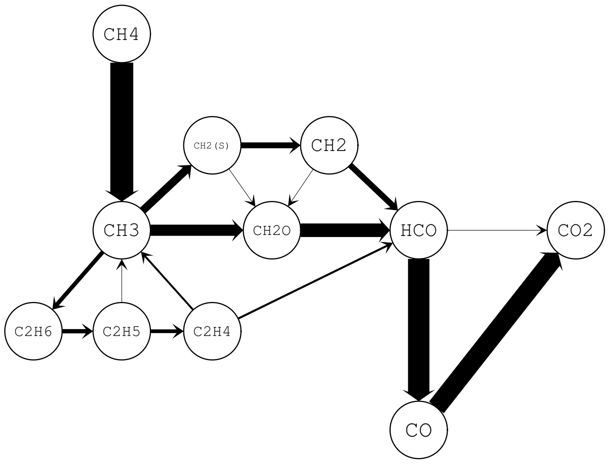

Figure 2.6: Example of the pathway followed by the carbon atom in a pure methane combustion case under MILD conditions.

More precisely, the arrows width quantifies the so called *reaction flux* (or *chemical flux*), defined as the amount of substance transformed per unit volume and time, and then integrated over space [31]. The reaction flux computes the transport of a conserved scalar, a chemical element, by species. As such, the reaction path analysis is specific to carbon, hydrogen, oxygen or nitrogen. As an example, considering the i elementary reaction which deal with the atomic hydrogen abstraction in a volume $dV(\mathrm{m}^3)$:

$$i\text{:}\ \mathrm{CH_4 + H \longrightarrow CH_3 + H_2}$$

it is possible to define the conserved scalar $n_i(\mathrm{C}, \mathrm{CH_4}, \mathrm{CH_3})$ as the number of carbon atoms that a single forward instance of reaction i moves from CH_4 to CH_3. It follows that for the aforementioned forward reaction $n_i(\mathrm{C}, \mathrm{CH_4}, \mathrm{CH_3}) = 1$. Similarly if the reaction proceeds backward $n_i(\mathrm{C}, \mathrm{CH_3}, \mathrm{CH_4}) = -1$. The contribution of reaction i in the selected region of space will then be shown on the reaction path diagram as an arrow between CH_4 and CH_3 having a weight proportional to $n_i(\mathrm{C}, \mathrm{CH_4}, \mathrm{CH_3}) r_i dV$, where r_i is the reaction rate.

If m different elementary reactions contribute to move the C atom from CH_4 to CH_3, (e.g. R20 or R51 described in appendix A), the thickness of the $\mathrm{CH_4}{-}{>}\ \mathrm{CH_3}$ edge in the volume V of interest is then proportional to:

$$R(\mathrm{C}, \mathrm{CH_4}, \mathrm{CH_3}) = \sum_{i=1}^{m} \int_V n_i(\mathrm{C}, \mathrm{CH_4}, \mathrm{CH_3}) r_i dV \quad [\mathrm{mol/s}]. \tag{2.42}$$

The sign of the R value determines the direction of the arrow: if positive then $\mathrm{CH_4} \rightarrow \mathrm{CH_3}$, if negative then $\mathrm{CH_4} \leftarrow \mathrm{CH_3}$.

In order to draw the pathway followed by the carbon atom, this method is applied to all the elementary reactions of the combustion mechanism used, the DRM19 mechanism, which is overviewed in section 3.2 and appendix A.

2.7 Turbulence and turbulence-chemistry interaction

The observation of a turbulent flow is a daily experience that is often identified with the apparently chaotic motion of a fluid. Even if this may be understood as the main effect that turbulence has on the behaviour of a flow, a deeper study can show that this is only the most visible aspect of a more complex phenomenon [23].

A turbulent flow may be described as an unsteady, irregular and completely three-dimensional motion having velocity fluctuations able to transport any quantity (scalar or vector) much more easier than a laminar one, even at a molecular level. Those fluctuations have a non-deterministic behaviour making every result, coming from experiments, unique (e.g. fig.2.7).

From a mathematical point of view, this behaviour is due to the non-linear terms of the N-S equations, the same terms that are also responsible for the production of local fluctuations able to create much smaller fluid-dynamic structures.

From a physical point of view, velocity fluctuations come from the instability of the biggest eddies that fragment themselves producing smaller structures. This is better clarified by the sketch in figure 2.8. A vortex with dimension L, during its rotation, is subject to instabilities that modify its structure into smaller eddies having dimension that are a fraction α (with $\alpha < 1$) of the original one. The kinetic energy of the larger eddies is transferred to smaller according to the phenomenon known as *energy cascade*. This phenomenon does not stop until viscosity dissipates the kinetic energy at the smallest scale.

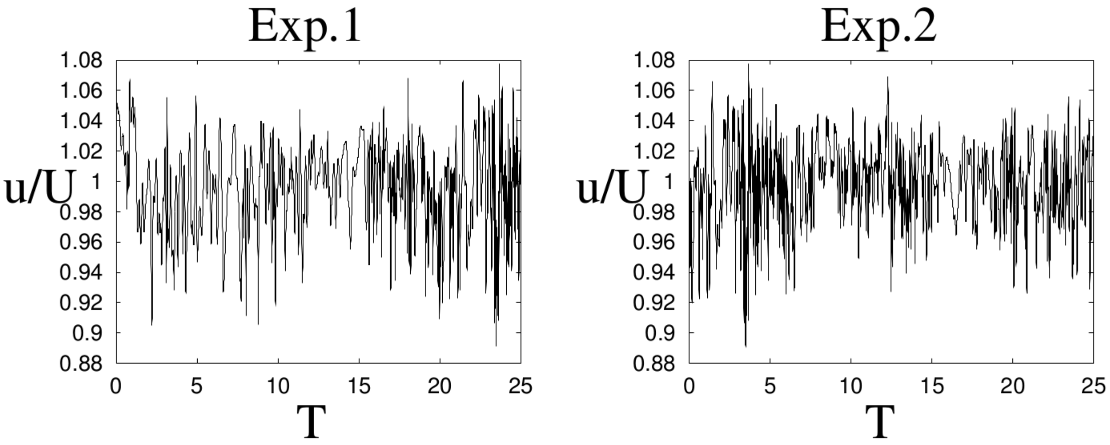

Figure 2.7: Velocity fluctuations recorded in the same time interval for two consecutive realisation of the same experiment. The figure shows the ratio between the fluctuating (u) and the mean (U) part of the local flow velocity [32].

The antagonist roles between the energy cascade (non-linear terms of the N-S equations) and the viscous dissipation (viscous terms of the N-S equations) have been made more rigorous by the work of Kolmogorov [33,34] concerning homogeneous and isotropic turbulence [6]. The importance of this work lies in the estimation of smallest scales (the *Kolmogorov* scales) properties (the length η_k, the velocity u_k, and time t_k) given as:

$$\eta_k = \left(\frac{\nu^3}{\epsilon}\right)^{1/4}, \quad u_k = (\nu\epsilon)^{1/4}, \quad t_k = \left(\frac{\nu}{\epsilon}\right)^{1/2}, \tag{2.43}$$

and the relationship between these properties and the properties of the largest scales (the *integral* scales), namely:

$$\frac{L}{\eta_k} = Re^{3/4}, \quad \frac{U}{u_k} = Re^{1/4}, \quad \frac{T}{t_k} = Re^{1/2}. \tag{2.44}$$

The term ν represents the kinematic viscosity and ϵ is turbulent kinetic energy dissipation rate (the power per unit mass that is dissipated).

---

[6] Turbulence can be defined homogeneous and isotropic when its characteristics are, respectively, statistically independent from space and equal in all directions [32]. It is worth noting that homogeneous and isotropic turbulence is a conceptual abstraction which cannot be reproduced entirely in any physical system. Nonetheless, real systems satisfy locally the conditions of homogeneous and isotropic turbulence. As a consequence this assumption is commonly adopted to simplify the mathematical description of turbulence.

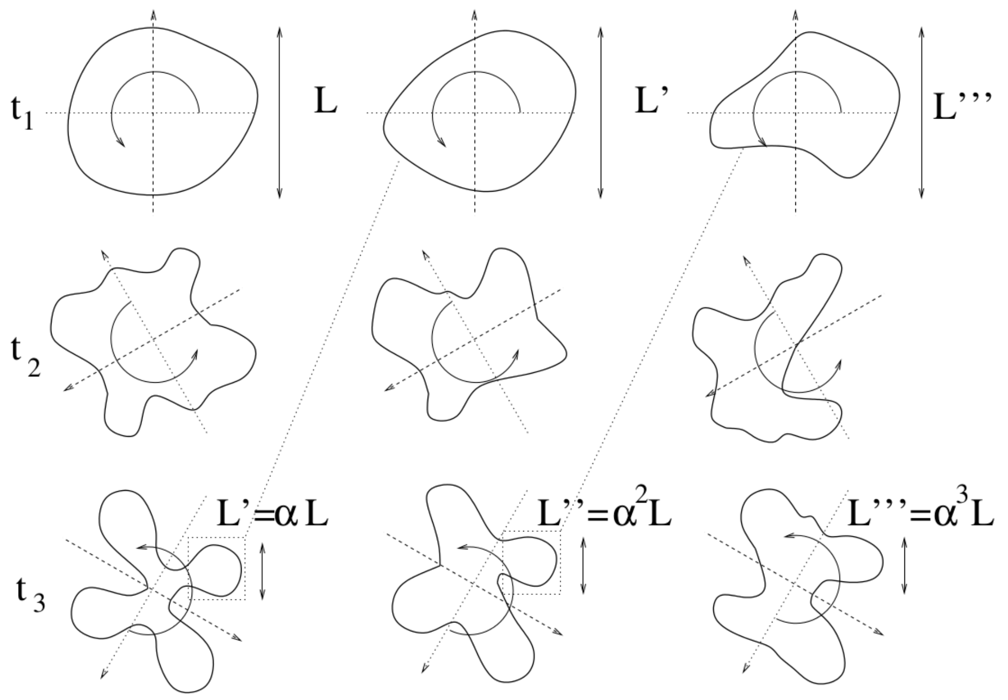

Figure 2.8: Sketch of the vortex instability. Cascade Mechanism [32].

The non-dimensional quantity Re, known as *Reynolds number*, is used to characterize a flow regime. For high Re, the flow is observed as turbulent and, according to equation (2.44), the difference between integral and Kolmogorov scales increases as $Re^{3/4}$. The Reynolds number is often expressed as:

$$Re = \frac{\rho u_r(r) r}{\mu}, \tag{2.45}$$

where $u_r(r)$ is the characteristic velocity of the motion of size r. With the assumption of homogeneous and isotropic turbulence, the velocity u_r and the size r of any eddy participating in the energy cascade are linked by:

$$\epsilon = \frac{u_r^3}{r}. \tag{2.46}$$

The relations (2.43) and (2.44) are based on the first and second Kolmogorov hypothesis. The first Kolmogorov hypothesis states that "At sufficiently high Re, the small scale turbulent motions ($r \ll L$) are statistically isotropic". The second Kolmogorov hypothesis specifies that "In every turbulent flow at sufficiently high Re, the statistics of the small scale turbulent motions ($r \ll L$) have a universal form that is uniquely determined by the viscosity ν and the energy dissipation rate ϵ ".

The third Kolmogorov hypothesis focuses instead on the intermediate range of scales known as *inertial* (sub)range. Particularly it states that, "In every turbulent flow at sufficiently high Re, the statistics of the motion of scale r in the range $\eta \ll r \ll L$ have an universal form that is uniquely determined by the energy dissipation rate ϵ, independent on the viscosity ν ". It follows from the aforementioned hypothesis the estimation of the velocity and time scales of size r structures as follow:

$$u_r = \frac{U}{L^{1/3}} r^{1/3}, \quad t_r = \frac{L^{1/3}}{U} r^{2/3}. \tag{2.47}$$

The expressions shown in (2.47) provides useful insights into the dynamic of the r scales. Particularly, they show as intermediate scales have a characteristic velocity that grows with $r^{1/3}$, while their characteristic time grows with $r^{2/3}$. As a consequence, larger eddies have higher velocity but a slower dynamic (a longer time is required before they reduce to smaller structures). Conversely, higher velocity gradients ($\nabla u \sim u_r/r \approx r^{-2/3}$) correspond to smaller structures, explaining the stronger role of turbulent dissipation for these scales [7]

From the third Kolmogorov hypothesis it is also possible to derive the well know power law ($k^{-5/3}$) for the energy spectrum in the inertial (sub)range. The energy spectrum ($E(k)$) provides a powerful description on how the turbulent kinetic energy distributes among eddies of different wavenumber k [8]. The integral of $E(k)$ over all the wavenumbers is expresses as follow:

$$K = \int_0^{\infty} E(k) dk, \tag{2.48}$$

where K is the kinetic energy of the flow per unit of mass. According to third Kolmogorov hypothesis, the $E(k)$ value will not depend on ν, but solely on ϵ and the wavenumber k. As such, by dimensional considerations, $E(k)$ can be expressed in the inertial (sub)range as:

$$E(k) = C\epsilon^{2/3} k^{-5/3}, \tag{2.49}$$

where C corresponds to the universal Kolmogorov constant. The full spectrum is instead expressed as:

$$E(k) = C\epsilon^{2/3} k^{-5/3} f_L f_\eta, \tag{2.50}$$

where factors f_L and f_η controls respectively the *energy containing* range (largest structures) and the *dissipation* range (smallest structures).

The graphical description of the energy spectrum evolution is provided by the log-log graph in figure 2.9.

An important issue of turbulent combustion modelling is to describe how eddies interact with the flame front. To this end two parameters are often used as a preliminary tool to gain insights into the flame/vortex interaction: the *Damköhler* and *Karlovitz* number.

The Damköhler number compares a typical chemical time scale (τ_c) to the integral turbulent scale (T), while the Karlovitz number corresponds to the ratio of chemical time scale τ_c and

---

[7] Along with the expression (2.46), the turbulent dissipation rate can be also expressed as a function of viscosity and velocity gradients.

[8] To higher wavenumber correspond a smaller eddy size.

the smallest turbulent time scale τ_k as follow:

$$Da = \frac{T}{\tau_c}, \quad Ka = \frac{\tau_c}{\tau_k}. \tag{2.51}$$

The Damköhler number measures the importance of the interaction between chemistry and turbulence. For sufficiently fast chemistry (low τ_c), $Da > 1$ and turbulence does not affect the reaction zone structure. As a consequence, the reaction zone assumes the characteristic of a laminar flame, although wrinkled by turbulent oscillations ("flamelet" regime [9]). On the contrary if $Da < 1$, turbulence is dominant over chemistry, therefore the overall reaction rate is controlled by chemistry whereas reactants are mixed by turbulent motion ("perfectly stirred reactor" regime).

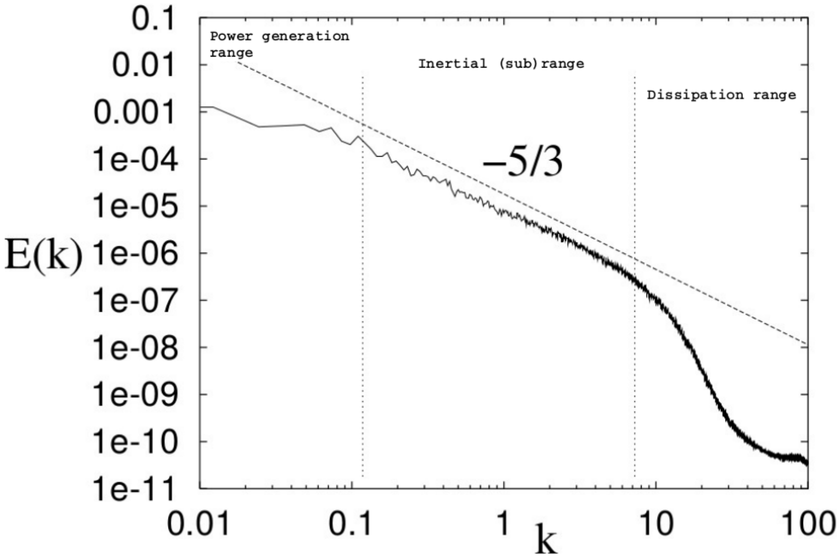

Figure 2.9: Energy spectrum for the homogeneous and isotropic turbulence. The dashed line represents the $k^{-5/3}$ power law shown as comparison [32].

In a similar way the Karlovitz number compares chemical and turbulent scales, even though it focuses on the smallest turbulent scales. If $Ka < 1$ the chemical reactions occur faster than all turbulent scales. Turbulence does not alter the flame structure and the chemical region is in laminar conditions.

2.8 DNS, LES and RANS approach

The investigation of turbulent combustion processes by means of Computational Fluid Dynamic (CFD) can be achieved by three different strategies. The difference between them consists in the number of the scales (spatial and temporal) modelled rather than computed or, in

---

[9] The basic idea behind flamelet modelling is to assume that a small instantaneous flame element embedded in a turbulent flow has the structure of a laminar flame [18].

other words, in the position where the energy cascade is cut and a turbulent model used to account for the smaller scales which are not simulated.
The strategies are represented by the Reynolds Averaged Navier Stokes equations (RANS), the Large Eddy Simulation (LES) and Direct Numerical Simulation (DNS).

RANS

From a historical point of view the Reynolds Averaged Navier Stokes simulations have been the first CFD approach adopted because of the relatively low computational resources required [18]. Reynolds averaging technique is based on splitting all the quantities transported by a turbulent flow, f, into a mean part $\bar{f}$ and a fluctuating part f' (fig.2.10), and solve the governing equation for only $\bar{f}$.

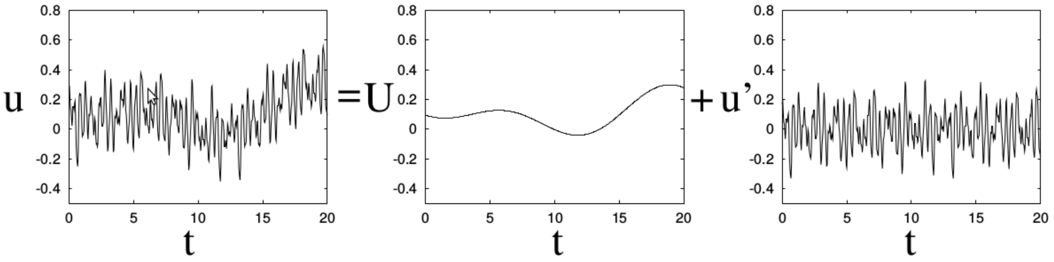

Figure 2.10: Decomposition of an oscillating velocity signal (u) into a mean (U) and an oscillating part ($u^{'}$) [32].

This approach introduces new unknown quantities and the averaged equations require closure models (involving empirical constants) to represent the unresolved physics. Even though the accuracy of the RANS approach is limited in combustion models, its implementation presents almost no limitations in terms of domain size, geometry and operating conditions.
At the moment this approach is widely used in the industrial field for its reduced computational cost [35].

LES

In LES, the turbulent fields are separated into two contributions: large-scale, which are resolved, and small-scale, which are unresolved. A spatial filtering operation applied to the instantaneous turbulent fields removes turbulent motion at length scales smaller than the filter size Δ. The governing equations for the remaining large-scale velocity field are discretised using a mesh with grid spacing of order Δ or smaller. This substantially reduces computational cost by a factor $Re_{\Delta}^{9/4}$ [36], where Re_{Δ} is the *subfilter* Reynolds number expressed as:

$$Re_{\Delta} = \frac{\rho u \Delta}{\mu}.$$

Although LES is a more computationally expensive technique than RANS, it offers two significant advantages. First, the large scale motion of the turbulence, that contains most of the turbulent kinetic energy and controls the dynamics of the turbulence, is resolved (computed directly). Second, knowledge of the large-scale dynamics and the assumption that an applied model should be valid independently on the filter size leads to the formulation of the so-called dynamic models [37], where model coefficients are determined as part of the solution.

Chemical reactions in turbulent flows essentially occur on the smallest turbulent scales. For example in non-premixed systems combustion can only take place when fuel, oxidizer and heat are mixed at molecular level, so that self-sustained chemical reactions can take place. Similarly, in premixed combustion fuel, oxidizer and heat are mixed, but, when the combustion process is started, only molecular mixing increases the temperature of the unburned mixture with hot combustion products above ignition temperature [38]. This implies that for LES, as well as for RANS, the filtered chemical source term requires modelling. In spite of this, non-reactive and reactive system studies show that LES predicts the scalar mixing process and dissipation rates with considerably improved accuracy compared to RANS [39].

LES studies are starting being applied to industrial cases, particularly where RANS cannot guarantee a good level of accuracy (unsteady flows, ignition, combustion instabilities).

DNS

DNS for turbulent combustion corresponds to the full solution of the instantaneous Navier-Stokes equations without any model for the turbulent motion.

Since every fluid-dynamics problem, under the assumption of continuum, can be theoretically described by the direct solution of N-S equations, all turbulent scales and their effects on chemistry can potentially be captured by the DNS approach. Because of the typically small dimension of turbulent scales in highly turbulent flow, the full solution of N-S equation provides a high degree of accuracy with the upfront cost of highly demanding computational resources. For this reason some level of simplifications are often introduced to reduce the numerical expenses.

As an example, simulation of hydrocarbon/air combustion are often performed with simplified chemistry (e.g. the DRM19 mechanism describes the methane/air combustion with a set of 84 elementary reaction instead of the more complex Gri-Mech which uses 325 different steps). For the same reason periodic boundary conditions are often used to limit the domain size of the phenomenon being investigated. DNS-like techniques have also been used in some simulations based on Adaptive Mesh Refinement (AMR) in order to reduce the computation requirements in areas of the computational domain where a highly refined grid is not necessary [40].

Currently DNS study are limited to academic studies with simple geometries, even though recent progress in High Performance Computing (HPC) allows for an increased level of complexity of the domains studied [41, 42].

2.9 LMC code

The numerical tool used on this thesis to solve the governing equations, is the Low Mach Combustion (LMC) code developed at the Centre for Computational Sciences and Engineering (CCSE) of Lawrence Berkley National Laboratory, California. Other than coding the initial conditions for the studies presented here, no development of the algorithm has been necessary for this work. For this reason, it is here provided only a brief overview of LMC. The reader is referred to Day *et al.* [22] for more details about the code.

LMC code is a variable density solver which uses a second-order projection method to solve the Navier-Stokes equations. The code is capable of Adaptive Mesh Refinement (AMR) and parallel computing. The algorithm used by LMC code treats the fluid as a mixture of perfect gases. A mixture-averaged model is used to account for differential diffusion effect, neglecting Soret and Dufour effects. Equally neglected are body forces and radiative heat transfer, while the assumption of Newtonian and isotropic fluid is considered to define the stress tensor [22,43]. The low-Mach number formulation of pressure models p as the sum of the ambient pressure p_0 and a perturbation pressure field π as follow:

$$p(x,t) = p_0 + \pi(x,t). \tag{2.52}$$

The model assumes that the perturbation term π satisfies the $\pi/p_0 \sim \mathcal{O}(M^2)$ constraint, where M is the Mach number. By neglecting the sound waves effects, the time step is restricted only by the fluid speed, and so larger time steps can be taken [10].

With the aforementioned set of assumptions, the set of relations describing momentum, mass species and enthalpy balance are given by (see section 2.2 for an overview of the derivation of these relations):

$$\frac{\partial \rho \mathbf{u}}{\partial t} + \nabla \cdot (\rho \mathbf{u}\mathbf{u}) = -\nabla \pi + \nabla \cdot \bar{\bar{\tau}}, \tag{2.53}$$

$$\frac{\partial \rho Y_i}{\partial t} + \nabla \cdot (\rho \mathbf{u} Y_i) = \nabla \cdot (\rho D_i \nabla Y_i) + \dot{\omega}_i, \tag{2.54}$$

$$\frac{\partial (\rho h)}{\partial t} + \nabla \cdot (\rho \mathbf{u} h) = \nabla \cdot \frac{\lambda}{c_p} \nabla h + \sum_i \nabla \cdot \left[h_i (\rho D_i - \frac{\lambda}{c_p}) \nabla Y_i \right], \tag{2.55}$$

where ρ is the density, $\mathbf{u}$ is the velocity, $\bar{\bar{\tau}}$ is the stress tensor, Y_i represents the mass fraction of species i, $D_i(Y_i, T)$ is the species mixture averaged diffusion coefficient and $\dot{\omega}_i$ is the produc-

---

[10] For a compressible code the time step is defined as $dt = dx/(u + a)$, where dx is the cell size, u the fluid velocity and a refers to the speed of sound. For a low Mach number code the time step is defined as $dt = dx/u$. As a consequence, if u is small compared to a, the low Mach number time step is significantly larger.

tion rate for ρY_i due to chemical reactions. Also, h is the specific enthalpy of the gas mixture, $\lambda(Y_i, T)$ is the thermal conductivity, c_p is the specific heat of the mixture and $h_i(T)$ represents the specific enthalpy for species i. For this thesis, the production rate value for ρY_i is specified via a collection of elementary reactions using DRM19 database (DRM19 mechanism is overviewed in section 3.2 and appendix A).

The equations (2.53), (2.54) and (2.55) are supplemented by the perfect gas law and a relationship between enthalpy, species and temperature as follow:

$$p_0 = \rho RT \sum_i \frac{Y_i}{W_i} \tag{2.56}$$

$$h = \sum_i Y_i h_i(T), \tag{2.57}$$

where R is the universal gas constant, T is the temperature and W_i is molecular weight of species i. Overall, the momentum equations (x3) combined with the energy (x1) and species equations (x21) [11] were solved to describe the evolution of the proposed cases. This evolution is also constrained by relations (2.56) and (2.57) [44].

The LMC algorithm solves for species mass densities and enthalpy as primary unknowns. The discretisation of mass and energy relations (Eq. 2.54 and 2.55), in conserved form, allow the approximate solution to drift off the constraint imposed by the equation of state at fixed ambient pressure. An appropriate correction term is used to prevent the algorithm from drifting too far off the ideal gas law [22].

The spatial discretization uses finite volume differencing with ρ, $\mathbf{u}$, h, $\nabla\pi$ and Y_i defined on cell centers. The perturbational pressure (π) is staggered in both space and time. Advection is discretized using a second-order Godunov-type procedure while diffusion is approximated with standard finite different methods. The temporal discretization strategy is a fractional step approach based on a projection approximation [22].

The projection method is an effective tool to solve time-dependent fluid problems presenting the advantage of decoupling the velocity and pressure fields [45]. The algorithm of the projection method is based on the decomposition (known as Helmholtz decomposition) of any vector field into a divergence-free (solenoidal) and an irrotational part as:

$$\mathbf{u} = \mathbf{u}_{\text{sol}} + \mathbf{u}_{\text{irrot}} = \mathbf{u}_{\text{sol}} + \nabla\phi. \tag{2.58}$$

The divergence of equation (2.58) leads to $\nabla \cdot \mathbf{u} = \nabla^2\phi$ which can be solved for the scalar ϕ if $\mathbf{u}$ is known. This allows the solenoidal part of the velocity field to be found as:

$$\mathbf{u}_{\text{sol}} = \mathbf{u} - \nabla\phi. \tag{2.59}$$

---

[11] The DRM19 mechanism used for this work is a 21 species set.

This decomposition is applied within a two stages algorithm. In the first stage, known as *predictor* step, the transport equations are advance in time to a mid-timestep. All the variables are computed included an intermediate velocity field $\mathbf{u}^*$. In the second stage, known as *corrector* step, the time-centred estimated values are used to evaluate the transported variables at the next $(n+1)$ timestep. In particular, by imposing the $\nabla \cdot \mathbf{u^{n+1}} = 0$ condition, π^{n+1} and $\mathbf{u}^*$ values decouple in the momentum equation (eq.2.53) and it is possible to solve for π^{n+1}. Once π^{n+1} is known, the divergence-free part of $\mathbf{u^{n+1}}$ is obtained from equation (2.59).
The overall LMC numerical code is known to converge with second-order accuracy in space and time [22, 43]. Evidence of this is provided in section 3.2.1.

2.10 Mild combustion - State of the art

The first exhaustive review of the potentialities of a combustion technique combining air preheating, with exhaust gas recirculation, dates back to 1997 [11]. In his paper Wünning reviews the first attempts made by German researcher in early 1990s, to achieve low NOx emissions with strong exhaust gas recirculation. Wünning provides a detailed description on how to practically reduce the temperature peaks in a combustion chamber by the entrainment of combustion products with reactants, either externally (exhaust gases mixed to air upstream of the combustion chamber by a blower) or internally (exhaust gases mixed within the combustion chamber aerodynamically). A variable measuring the degree of dilution of reactants by the flue gas, called *recirculation rate* ($\mathrm{K_v}$), was defined in this paper. The recirculation rate was defined as ratio between mass flow rates as follow:

$$K_v = \frac{\dot{M}_{\mathrm{E}}}{\dot{M}_{\mathrm{F}} + \dot{M}_{\mathrm{A}}}, \tag{2.60}$$

where the subscript E expresses the recirculated exhaust gas, while F and A represent respectively the fuel and combustion air. The flammability limit for conventional hydrocarbons and air combustion, was set up for $\mathrm{K_v} \leq 0.5$. Wünning stated that, for very high exhaust gas recirculation rate, well beyond the flammability limits ($\mathrm{K_v} > 0.5$), it was possible to stably sustain reactions, with the help of integrated air-preheating systems, either recuperative or regenerative. The guiding design principles to obtain low NOx burners with high exhaust gas recirculation and air-preheating, were also enriched with a schematic ignition procedure explaining how to switch, from a conventional high velocity firing mode to a low NOx flameless mode.
An in-deep review of air-preheating systems used to rise reactants temperature above autoignition, is present in the 1998 work of Katsuki and Hasegawa [14]. In this paper attention is particularly focused on regenerative heat exchangers, which, as stated by the authors, give the possibility to achieve simultaneously large energy savings (up to 50% of fuel saving) and high air temperature (typically above 1300K), by recovering waste heat. With strong air pre-

heating (air pre-heated to 1200K), it was observed that a stable combustion of an air/propane mixture was possible even with oxygen content as low as 3% (mass basis).

The applicability of MILD technique to a broad set of different industrial contexts, was outlined in 2001 by Milani and Saponaro [12]. This review provided industrial examples of existing furnaces, for the steel and power generation industries, adapted for working under MILD conditions. It was pointed out that the MILD firing mode, because of the high turbulence required to entrain burnt gases and the low reaction rate caused by the oxygen dilution, is controlled both by chemical kinetics and by mixing, unlike the conventional burner firing where mixing is the rate limiting step. Consequently, the combustion region was found no longer concentrated close to the flame front, but extended over the whole combustion chamber, resulting in a volumetric rather than superficial combustion. The authors also highlighted the important peculiarity of MILD combustion to be flexible to use with different type of fuels, particularly hydrocarbons considered "difficult" due to their low calorific value.

The flexibility of the MILD combustion to different typology of fuels was the focus of Weber *et al.* research [46]. The possibility to achieve MILD regime using natural gas, heavy and light oil and coal in an industrial burner, was extensively reviewed by the author. For each fuel, low NO production and zero CO emissions were observed at the furnace exit.

The formation mechanisms of NOx for coal combustion under the MILD mode was further investigated in the work of Stadler *et al.* [47]. He performed experiments with lignite and bituminous coals in a university test burner reporting an NOx reduction of 20-50% depending on the fuel used.

Along with industrial application of MILD, a number of different experimental and numerical studies were reported in the literature, aimed at obtain fundamental insights into this firing mode and broaden its implementation.

The review of Wünning was followed by the experimental study of Plessing *et al.* [48] who studied the methane/air flame structure obtained in an experimental burner with highly preheated air and strong exhaust gas recirculation. Fuel and air were pumped separately into the combustion chamber, where a strong re-circulation of exhaust gases was present (fig.2.11). Because of the peculiarity of very low flame luminosity under these conditions, the reaction zone was visualised by detecting the fluorescence of OH radical by means of a Laser Induced Pre-dissociative Fluorescence (LIPF) technique. The flame structure was compared with measurements in a conventional turbulent premixed methane/air bunsen flame. The investigation revealed only disconnected reaction zones, due to strong flame stretch, within the flame obtained with burnt gases recirculation, with a temperature rise between the un-burnt and burnt side of the reaction zones varying between 200 and 400 K, depending on the dilution.

Cavigiolo *et al.* [49] carried out a detailed experimental study on the influence of $\mathrm{K_v}$ on the reaction temperature and formations of NOx and CO in the natural gas combustion process. The author performed the study in a laboratory-scale burner, using two different gases: methane and ethane. The burner was characterised by a single high-velocity nozzle into which the fuel stream was injected perpendicularly via a capillary pipe (Fig. 2.12). The air was vitiated with inert gases and preheated along a preheating section. Then combustion air and fuel were partially premix in the nozzle before entering the combustion chamber. The resulting jet entrains a large amount of exhaust gases in the combustion chamber. A secondary air inlet was used to preheat the combustion chamber with a conventional flame before switching to MILD.

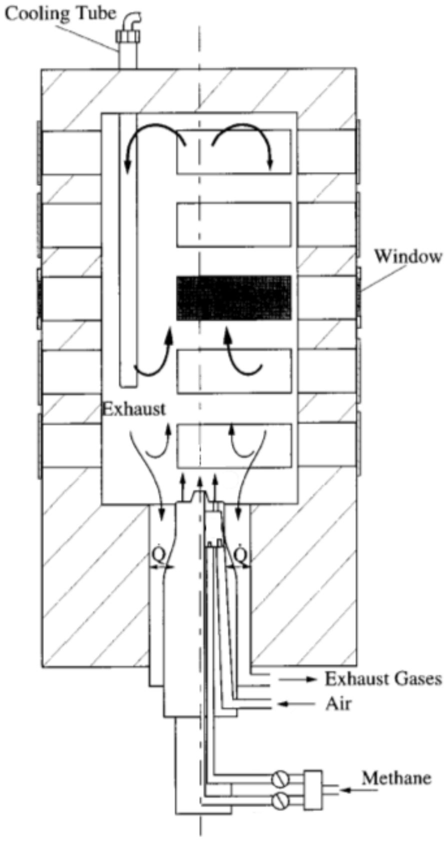

Figure 2.11: Layout of the experimentally burner used by Plessing *et al.* [48]. Two separated fuel ducts are visible. The upper duct feeds six circular stabilised flames used to heat up the furnace. Once the chamber has reached a temperature above 800°C, a control valve switches the fuel flow to a single center nozzle fed by the lower duct. Image from [48]

The MILD regime was achieved with recirculation rate values (K_v) larger than 4 for methane and 3.5 for ethane (O_2 content lower than 5% on mass basis), and combustion chamber temperatures higher than 800-850 °C for methane and 600-650 °C for ethane. The experiment showed a strong reduction in NOx emissions due to the thermal homogenization. A similar strong reduction was obtained, once MILD conditions were achieved, for different furnace temperatures and types of fuel, outlining the flexibility of MILD to a broad range of industrial applications.

Likely Cavigiolo *et al.* [49], with the same laboratory scale burner, Derudi *et al.* [50] and Effugi *et al.* [51] tested the adaptability of MILD combustion to non-conventional methane/hydrogen and biogas mixtures. The methane/hydrogen mixture consisted in an 40%/60% CH_4/H_2 molar blend, the so called coke oven gas (COG), which showed, with respect to MILD combustion of methane, to require increased jet velocity to achieve MILD regime. The authors also outlined the ability of hydrogen to enhance, leading to completion, the hydrocarbon oxidation in very diluted conditions ($K_v > 5$). The biogas, an equimolar CH_4/N_2 mixture, demonstrated the possibility of implementing the MILD regime using low calorific value fuels. The knowledge about MILD flexibility to different gaseous fuels was further expanded by Derudi *et al.* [52] with the successful implementation of MILD regime with different liquid hydrocarbons.

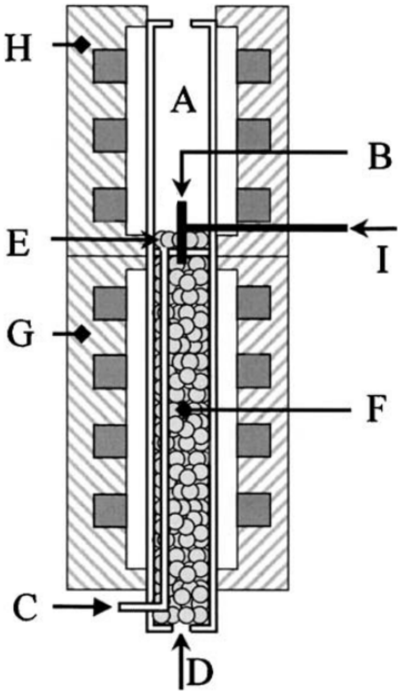

Figure 2.12: Layout of the experimentally burner used by Cavigiolo *et al.* [49]. A: reaction chamber; B: nozzle; C: secondary air inlet; D: primary air and inert gas inlet; E: quartz pellets sparger; F: preheating zone; G: preheating oven; H: upper oven for heat maintenance; I: fuel inlet. Image from [49].

The use of hydrogen as "fuel enhancer" was similarly the focus of research made by Sabia *et al.* [53]. With the aim of widening the range of operating conditions of the methane Mild combustion process, they reported the study of a quartz jet stirred flow reactor operating with a $CH_4/H_2/O_2/N_2$ mixture. The study showed that hydrogen addition results in an enhancement of the system reactivity caused by the significant production of OH radicals which accelerate the dehydrogenation of methane (CH_4) to methyl (CH_3).

The experimental device used by Dally *et al.* [54] to study the MILD regime has received a lot of attention from the scientific community, being able to mimic the common set-up of an industrial scale MILD burner. The device, called Jet in Hot Coflow (JHC), consists of a central fuel jet (internal diameter = 4.25 mm) and an annulus (internal diameter = 82 mm) with a secondary burner mounted upstream (Fig. 2.13). The aim of the secondary burner is to produce hot combustion products (CO_2 and H_2O) which mix with the air (O_2 and N_2) through two side oxidant inlets upstream of the annulus exit. The resulting oxidiser is a hot

$O_2/N_2/CO_2/H_2O$ blend. While the the amount of combustion products is kept constant, three different values of the O_2/N_2 ratio are used to investigate different oxygen dilutions. The fuel jet, a high speed equimolar mixture of CH_4/H_2, is kept, within the burner, insulated and separated from the oxidiser. The oxidiser, almost steady, is issued by the fuel only downstream the burner. The results revealed substantial changes in the reaction zone structure with the decrease in oxygen level. These changes include a peak temperature drop of up to 400K and a drop in OH and CO levels.

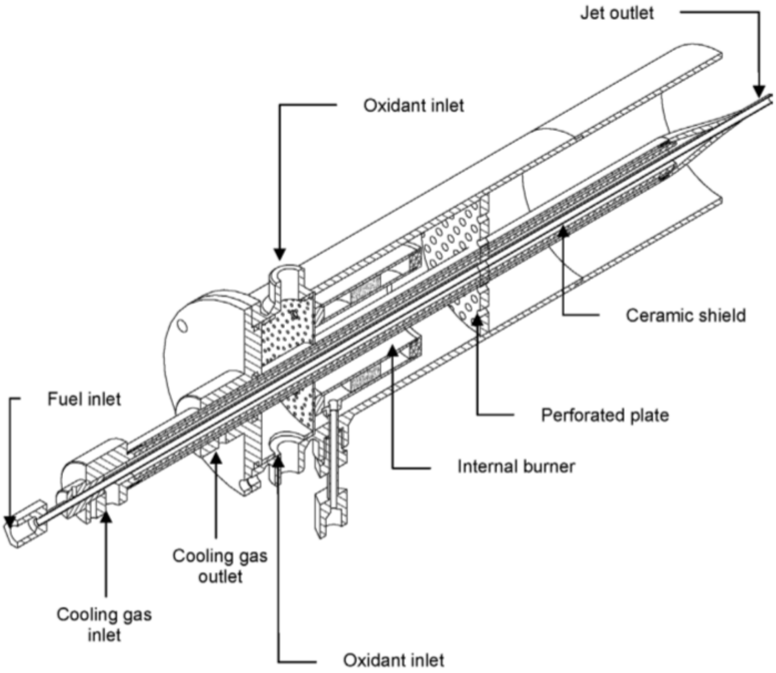

Figure 2.13: Layout of the experimental burner used by Dally *et al.*. In figure is visible the central fuel duct and the secondary burner mounted upstream of the annulus. A mixture of O_2/N_2 is fed trough the two side inlets mounted upstream the annulus exit. Image from [54].

The peculiar characteristic of the MILD mode to slow the reaction rates and, as a consequence, enhance the influence of molecular diffusion on flame characteristics, challenged the applicability of numerical combustion models that assumes fast chemistry and neglect the differential diffusion effects. The fully characterised temperature and species fields for different oxygen levels (3%, 6% and 9% by mass) resulting from Dally work, resulted in a number of publications aiming at testing different numerical approaches.

Christo *et al.* [55] proposed a comparison among different turbulence models (three variants of the $\mathrm{k}-\epsilon$ model) and combustion models (conserved scalar and volumetric reaction models) based on the turbulent non-premixed methane/hydrogen jet issuing the hot coflow under MILD conditions. In particular they showed that mixture fraction/probability density function (ξ/PDF) and flamelet approaches perform poorly for the MILD combustion regime. The eddy dissipation model (EDM) also gave unsatisfactory results. Better predictions were achieved through combustion models considering both detailed chemistry (GRI-3.0) and differential diffusion effects, such as the eddy dissipation concept (EDC) model. In addition the authors reported the numerical solution to be sensitive to the turbulent kinetic energy at the fuel inlet. As a consequence the mean turbulent kinetic energy needed to be adjusted to a value 4 times larger than experimentally estimated mean turbulent kinetic energy, to yield the best agreement between the model and experimental data.

A similar RANS study was performed by Kim *et al.* [56] to predict the flame structures and NO formation in the MILD combustion mode. The authors applied the Conditional Moment Closure (CMC) model, coupled with a reduced chemical mechanism (GRI-2.11) to compare numerical data with the Dally JHC laboratory burner. The differential diffusion effect was not accounted for in the used model. The CMC model was seen to be a good choice to predict the flame structures and NO formation in the MILD mode, even though the reaction zone thickness and NO level were underpredicted for the low oxygen case.

Frassoldati *et al.* [57] expanded the study of Christo *et al.* [55] by applying a more detailed chemical kinetic mechanism, able to track NOx emissions, to the EDC model. The authors also tested different turbulence models (standard $k-\epsilon$, modified $k-\epsilon$ and the Reynold Stress Model (RSM)) as well as different intensities of the turbulent kinetic energy into the boundary conditions. The modelling results showed some discrepancies observed between the measured and the predicted OH, CO and NO profiles, outlining the non-negligibility of differential diffusion effects.

The EDC model, coupled with the GRI-2.11 mechanism, was also used by Mardani *et al.* [58] with the aim of clarifying the importance of differential diffusion effect. To this end they used three different methods for computing the molecular diffusion in the species transport equations: Fick's law with equal diffusion coefficients for all species; Fick's law with different diffusion coefficients; and the multi-component diffusion equations. The comparison with the experimental data showed the importance of considering the differential diffusion effect in a simulation of the MILD regime.

The LES approach was used by Ihme *et al.* [59] to account for the the external cold air stream in the experiments of Dally *et al.* [54]. To account for the mixing between the three reactant streams (fuel, vitiated air and cold air) a three-stream flamelet/progress variable (FPV) formulation was utilised. All the oxygen dilution (9%, 6% and 3% by mass) studied by Dally were investigated. The paper showed that the addition of the third stream produced satisfactory agreement between experimental and numerical species profiles.

The LES approach was also employed by Afarin *et al.* [60] to investigate the effect of the initial fuel stream turbulence intensity on the flame structure. They superimposed three different values of initial turbulence intensity (4%, 7% and 10%) in the CH_4/H_2 fuel mixture to trigger fuel/oxidiser instabilities. The effects of turbulence intensity on the flame structure were studied for two oxygen concentrations (3% and 9% by mass) and three oxidiser temperatures (1300K, 1500K and 1750 K). The turbulence-chemistry interaction of the under-resolved scales was modelled by means of the Partially Stirred Reactor (PaSR) method, where the GRI-2.11

mechanism accounted for the chemical kinetics. The comparison of temperature, CO and OH profiles with Dally experiment showed a very good accuracy between numerical and experimental data when 4% initial turbulent intensity was used. Furthermore, the research showed that fuel inlet turbulence intensity had a significant effect on the flame structure, particularly in the low oxygen case.

The mentioned numerical studies described above provided the combustion community with valuable informations regarding MILD combustion and its modelling. Some of them showed a good agreement between experimental and numerical results, some others presented less satisfactory predictions. Particularly, the models used were found to be sensitive to the initial conditions and to the chemical kinetic mechanism they were coupled with. Furthermore, all models described were validated against experimental data recorded, for practical reason, only at discrete points in the burner domain. This gives only a partial evaluation of the models behaviour since they are not validated against all points in the domain.

Because of their ability to describe all the fluid-dynamic structures of a flame and the complex interaction between turbulence, chemistry, and diffusion, DNS simulations can provide the same high quality data as the experimental results, with the advantage of providing an accurate set of data at each point in the computational domain. Because of their high computational expenses, only a limited number of high quality DNS data sets are present in the literature for the MILD regime. This holds particularly true for non-premixed turbulent flames, which represent the most common condition to achieve MILD regime in a real burner.

Van Oijen [8] presented a detailed 2D DNS study of autoignition phenomenon under MILD conditions. The author simulated numerically, by means of two-dimensional mixing layers domain, the JHC burner of Dally *et al.* [54]. The reduced DRM19 mechanism accounted for the kinetic of ignition. The 2D simulation was compared with a 1D diffusive study where the unsteady motion of the layers was absent. The comparison showed similar ignition times between 1D and 2D cases outlining a strong dependence of self-ignition on differential diffusion effects. Moreover, the author performed homogeneous reactor simulations to investigate the role of chemistry on the ignition process, outlining the dominant role of hydrogen chemistry in the CH_4/H_2 reaction zone. Despite the insights provided into the MILD ignition process, the vortex stretching and the energy cascade phenomena could not be considered in Van Oijen 2D study, leaving unexplained the effect of real turbulence on the ignition process. Furthermore, insights on chemical kinetics evolution with mixing layers were not provided, since the chemistry role was explained by means of the Well Stirred Reactor (WSR) approach.

Minamoto *et al.* [61,62] presented two 3D studies of a turbulent premixed MILD flame, focusing on the morphology of MILD reaction zones. In these studies the turbulence field was generated by a previous DNS simulation and the reactants mixture was obtained via a 1D laminar flame simulation. The outcome of the study was compared to a conventional premixed flame, suggesting that the MILD flame presents regions, mostly having a “pancake-like” structure, with strong chemical activities distributed over a large portion of the computational domain, unlike the premixed flame case. Although the Minamoto *et al.* studies presented a detailed explanation of MILD premixed reaction zones, the authors did not provide insights of spontaneous mixing and reaction among reactants, which is a common scenario in MILD burners including the JHC system.

To the author's knowledge, the only 3D study in literature which analyses the mixing and self-ignition of reactants under MILD conditions is Göktolga *et al.* [63] paper. In this work, the authors present a scaled version of Dally's work, where the CH_4/H_2 jet is simulated as a 2mm thick layer in order to limit the computational expense. In order to account for the heat loss effects observed in the Dally's experiment, temperature and species initial profiles recorded in the JHC burner were adopted. The 3D simulation of the most diluted (3% of O_2 by mass) Dally case was compared to a 2D case and 1D laminar case to identify differences in the self-ignition behaviour. Turbulence was observed to have an important impact in reducing the self-ignition delay through the enhanced entrainment of the fuel within the hot oxidizer. In addition, it was observed that the flame formation is initiated by different self-ignition spots close to the mixture fraction region, rather than by a single auto-ignition spot followed by a flame propagation. The work of Göktolga focuses on the turbulence-flame interaction in MILD combustion, providing valuable informations on the flame structure and self-ignition behaviour of MILD regime. Nonetheless, because of the scaling of the actual geometrical domain, the real conditions of the Dally's experiment could not be simulated, hence a proper comparison with the experimental data is not possible. Furthermore, this study, does not analyse the physical and chemistry change of the MILD flame with different values of oxygen dilution, as done on Dally's experiment, but focuses on a single dilution case.

2.11 Importance and Contribution of Proposed Research

A broad range of different experimental and numerical studies is present in the literature investigating the complex interaction among turbulence, diffusion and chemistry in a MILD flame. Nonetheless the broad diffusion of this combustion regime in the industrial field is hampered by the lack of MILD specific numerical models able to test full-scale burners, operating with different geometries and reactants, and capable of produce reliable sets of predictions. Development of reliable numerical models requires high quality sets of data against which the models can be validated. Only few studies in the literature present such data [8, 61–63].

The present thesis work expands the present knowledge of MILD combustion by investigating the complex interplay between turbulence, diffusion and chemistry, by means of high quality DNS simulations. Different fuel and oxidiser mixtures are considered with the aim to broaden the sets of cases available in the literature. Furthermore, the chemistry of reactants is investigated along the mixing of fuel and oxidiser in order to shed light on changes in chemical paths caused by molecular diffusion.

The set of simulations here presented are based on the JHC burner experiment of Dally *et al.*

[54] which provided valuable info to achieve a MILD regime. Advanced numerical techniques and parallel supercomputing facilities have been used.

Chapter 3

1D Study - Introduction and set-up

Although the MILD combustion regime is achieved under turbulent conditions, the similarity of turbulent and chemical timescales, a consequence of the slow reaction rates due to the oxidiser dilution, suggest that molecular diffusion and chemical kinetics play an important role in the flame characteristics (Sect. 2.10). For this reason, an extensive laminar diffusion flame analysis has been performed to obtain a deep understanding of the diffusion and chemical mechanisms involved in the MILD regime, decoupling these processes from turbulent fluctuations.

Counterflow MILD diffusion flames have been extensively reported in literature from both the numerical and experimental point of view. As an example, in 2013 Van Oijen [8] presented a detailed analysis about the role of molecular diffusion and chemistry in controlling the ignition event in a 1D laminar mixing layer MILD combustion study. This work, reviewed in section 2.10, presented a description of the diffusion-chemistry interaction of an equimolar methane/hydrogen fuel mixture with a highly diluted oxidiser. Despite the non-premixed nature of the domain described, the chemistry aspect of the research was investigated by means of homogeneous reactor simulation. A similar approach is shown in other work recently presented in the literature [63–65].

Since a major milestone in the complete understanding of the MILD combustion regime is knowledge of the fuel/oxidiser mixing process that leads to self-ignition, the temporal evolution of the chemical interplay of non-premixed reactants requires a deep understanding. To the authors knowledge, although substantial research has been performed on MILD combustion regime, little attention has been paid to the diffusion-chemistry interaction in non-premixed cases during the mixing processes.

For this reason, emphasis is given, in 1D diffusion cases, to the temporal evolution of the kinetic scenarios describing the fuel/oxidiser interaction.

3.1 Problem description

The DNS 1D study consists of on investigation of the temporal evolution of two reacting layers. Being the turbulence effects neglected, the interplay of diffusion and chemical kinetics can be investigated.

The oxidiser layer occupies the top-half ($y > 0$) of the domain while in the bottom-half ($y < 0$) only fuel is present. The fuel mixture is composed by a blend of CH_4 and H_2 at an initial temperature of 305K. The oxidiser on the other hand, is modelled as a mixture of O_2, N_2, H_2O and CO_2 at an initial temperature of 1300K.

The first case study presented (Chap. 4) analyses an equimolar CH_4/H_2 mixture which matches the fuel composition of the experiment performed by Dally *et al.* [54]. The investigation of fuel blends with reduced presence of hydrogen (10% and 0% by volume) are then presented in chapter 6. Similarly to the fuel blend, different oxidiser compositions are considered. In the most reactive case (Chap. 4) the oxidiser contains the 9% by mass of oxygen. The effects of a stronger O_2 dilution (6% and 3% oxygen by mass) are presented on chapter 5. Following the Dally *et al.* paper, the oxidiser blends containing the 9%, 6% and 3% by mass of oxygen are respectively referred to as HM3, HM2 and HM1.

Since 1D version of the LMC code is not present in the literature, the governing equations are solved on a two-dimensional domain with a width of 1.25mm (x-direction) and a length of 40mm (y-direction). The initial velocity of both streams is zero, hence the the problem becomes dependent only to the cross-stream direction (y), where it is studied.

The whole set of cases investigated along with the chemical composition of fuel and oxidiser are described in table 3.1.

Case	Fuel			Oxidizer				
	T(K)	Y_{CH_4}	Y_{H_2}	T(K)	Y_{O_2}	Y_{N_2}	Y_{H_2O}	Y_{CO_2}
HM1-1300K-50%	305	0.889	0.111	1300	0.03	0.85	0.065	0.055
HM2-1300K-50%	305	0.889	0.111	1300	0.06	0.82	0.065	0.055
HM3-1300K-50%	305	0.889	0.111	1300	0.09	0.79	0.065	0.055
HM3-1300K-10%	305	0.986	0.014	1300	0.09	0.79	0.065	0.055
HM3-1300K-0%	305	1.000	0.000	1300	0.09	0.79	0.065	0.055

Table 3.1: Set of cases considered for the investigation of the diffusion-chemistry interaction under MILD conditions. The chemical composition of the fuel and oxidiser are shown as mass fractions.

3.2 Numerical set-up

The two-dimensional domain is discretised by 32 points uniformly distributed in the stream-wise (x) direction and 1024 points equally distributed on the cross-stream direction (y). The resulting mesh has a size of 39μm, consistent with the resolution used for the 3D studies (Chap. 7).

In the stream-wise direction periodic boundary condition are applied. In the cross-stream direction the top and bottom boundaries are respectively set up as outflow and symmetric.

In order to reduce the computational expenses, the DRM19 is the kinetic mechanism used to follow, in time, the rates of each elementary reaction involved in the reaction. It is a reduced reaction set (describing 84 reversible reactions and 19 species) derived from the more detailed GRI-Mech mechanism (325 reactions involving 53 species) [66]. Despite the reduced list of species, the DRM19 mechanism accounts for almost all major pathways describing methane and hydrogen combustion. Particularly, it includes the C_2 chemistry (recombination of the methyl molecules to form ethane) observed to play an important role when the oxidiser is diluted [67, 68]. A full description of the DRM19 reaction set is provided in the appendix A.

Because of the separation of the fuel and oxidiser layers, the initial chemical composition presents a step profile which is smoothed by applying a 1-2-1 filter 10 times, following [8]. As a consequence of the smoothing, density and temperature present also a smoothed profile at the interface.

3.2.1 Error analysis

The accuracy of the LMC code has been tested trough a convergence test using five different resolution of the domain grid. The two-dimensional domain, having dimension 2.5×40mm, has been discretised respectively by 4×64, 8×128, 16×256, 32×512 and 64×1024 points. As a consequence the studied mesh sizes are 625, 313, 156, 78 and 39μm.

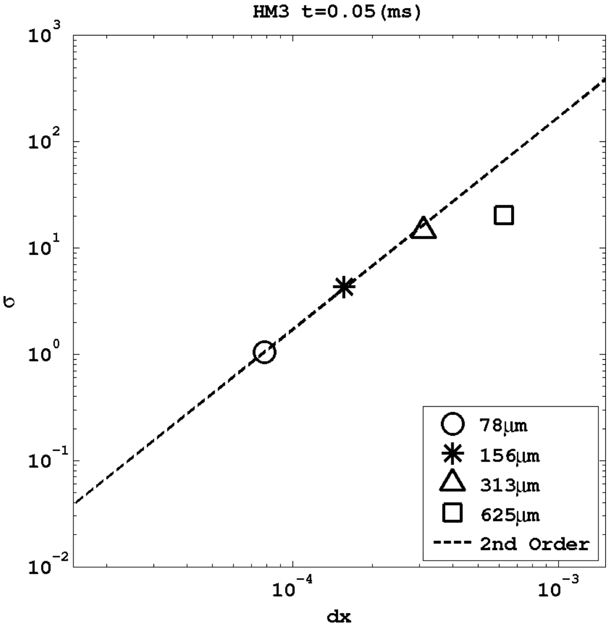

Figure 3.1: Temperature standard deviation plotted against grid resolution at t=0.05(ms). Both axis are presented in form of logarithmic scale.

For each grid, the temperature standard deviation (σ) at t=0.05ms along the cross-stream direction was found, using the most refined grid (39μm) as a reference. As an example, the temperature standard deviation for the 32x512 grid (78μm) is computed as follow:

$$\sigma = \sqrt{\frac{1}{N}\sum_{i=1}^{N}\left(T_{i,78} - \bar{T}_{i,39}\right)^2}, \tag{3.1}$$

where N is the number of points along the cross-stream direction and $\bar{T}_{i,39}$ is average temperature value at the point i for the most refined case.
The σ values as a function of the grid resolution are shown on the log-log graph in figure 3.1. The figures shows that the LMC code converges to a 2nd order accuracy as the grid resolution refines.

3.2.2 Time stepping analysis

The initial conditions were set up exploiting an anomaly found in the HM3-1000K-50% case. The only difference between HM3-1000K-50% and HM3-1300K-50% case is the reduced oxidiser temperature of the former. The lower oxidiser temperature was observed to be particularly challenging for the correct prediction of the time interval (dt) used to advance the governing equation. For this reason, the HM3-1000K-50% case has been used as a tool for setting up the initial conditions, although not included in the case list to be investigated (Tab. 3.1).
The set of governing equations, advance in time with a time interval specified as follow:

$$dt^{(i)} = \text{IS} \cdot dt^{(0)} \quad \text{for } i = 1, \tag{3.2}$$

$$dt^{(i+1)} = \min\left[\text{CFL} \cdot \frac{\Delta x}{|u|},\ \text{CM} \cdot dt^{(i)}\right] \quad \text{for } i > 1, \tag{3.3}$$

where Δx is the cell width and $|u|$ is the absolute value of the fluid velocity. The CFL (Courant, Friedrichs and Lewy) number is a constant value kept lower than one in order to guarantee the numerical scheme stability. Together with the CFL number, two other parameters are used by the LMC code to advance the solution of the governing equations. The *Initial Shrink* (IS) parameter is set up in order to scale back the initial dt. The *Change Max* (CM) value is used to prevent large increases in the the dt value. The LMC code uses CFL=0.5, IS=0.1 and CM=1.1 as standard values.
The HM3-1000K-50% case was found to exhibit oscillations in the temperature profile when run with the standard inputs, as shown on figure 3.2a at t=2.1ms. The reduction of the CFL was found effective in smoothing the oscillation. Figure 3.2b clearly shows the difference found by reducing the CFL number by an order of magnitude. Equally effective were CFL values in the range [0.2,0.01]. In order to guarantee a correct prediction of all variables and to avoid an

excessive increase in the simulation time, a CFL value of 0.1 was set up as new standard input for all cases studied.

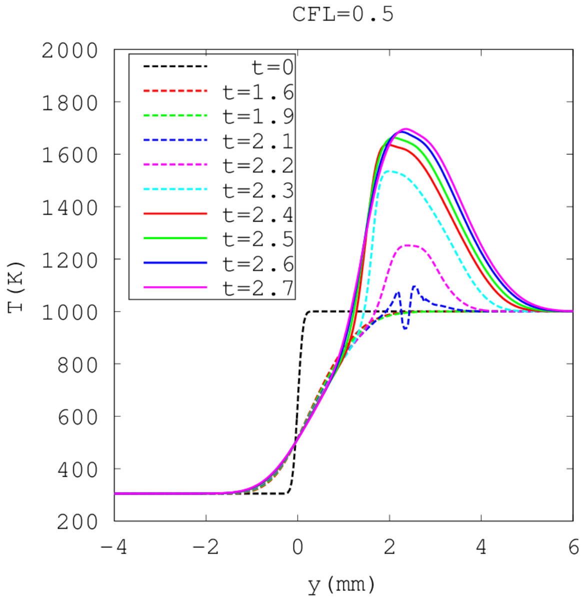

(a) CFL=0.5 **(b)** CFL=0.05

Figure 3.2: Evolution of the temperature profiles for the HM3-1000K-50% case. Values obtained from test case run with CFL=0.5 (left) are compared with values from case run with CFL=0.05 (right).

Another issue was observed by investigating the ignition time (t_{ig}) and the evolution of the temperature difference (ΔT) [1]. Both parameters were in fact found to be sensitive to the CFL value, as shown on figure 3.3a, while they were expected to be independent.

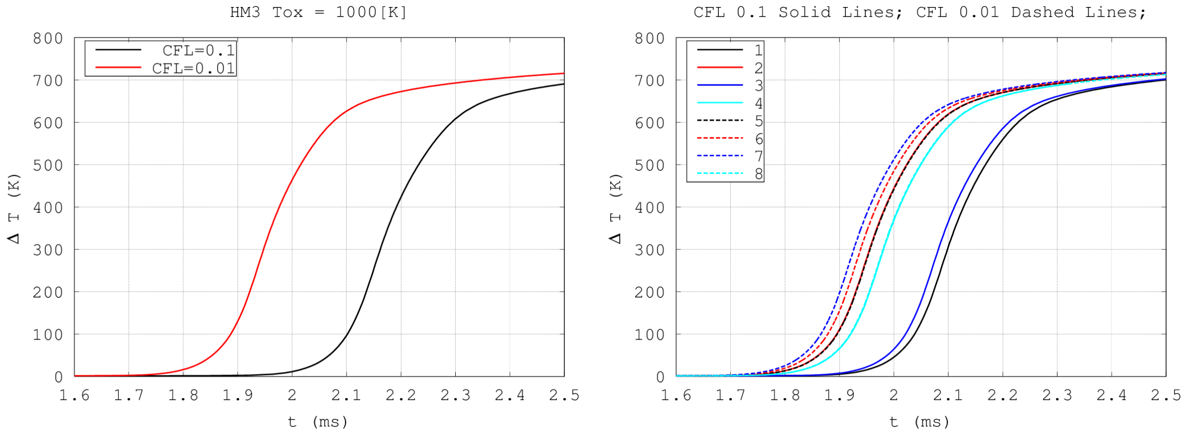

(a) **(b)**

Figure 3.3: **Left (a)**: Evolution of the ΔT profiles computed for case HM3-1000K-50% using CFL=0.1 (black curve) and CFL=0.01 (red curve) values.
Right (b): Evolution of the ΔT profiles computed for case HM3-1000K-50% using the values given in table 3.2.

---

[1] The ignition time was evaluated at the maximum gradient of the ΔT profile. The techniques used to compute ignition time and plot the temperature difference are reported in section 3.3

The values of dt before ignition time were examined in more detail for different CFL, and a large difference was found. Capping dt values before t_{ig} to a constant values was the first attempt made to fix the issue. Despite the fixed dt, the ignition time was still found sensitive to the CFL number. It was therefore argued that the sensitivity of the ignition time to the CFL was due to the earliest timesteps rather than timesteps close to t_{ig}. IS and CM parameters, which control the earliest dt, where thus thought to be responsible for sensitivity of t_{ig} to the CFL change.

In order to investigate the influence of IS and CM parameters, the HM3-1000K-50% case was run by using 8 different sets of initial conditions, as described on table 3.2. The ignition time and ΔT profiles of cases with matching IS/CM values were compared. The best agreements were found in cases 4/8, which showed an excellent agreement in terms of both ignition time and ΔT profiles (on figure 3.3b the cyan solid and dashed lines overlap entirely), independently to the value of CFL used and keeping constant IS and CM numbers to 0.01 and 1.01.

For this reason, IS=0.01 and CM=1.01 were set up as the new standard input values for all the 1D simulations considered here.

	CFL	Init. Shrink	Change Max.	t_{ig}(ms)
Test 1	0.1	0.1	1.1	2.085
Test 2	0.1	0.1	1.01	1.953
Test 3	0.1	0.01	1.1	2.068
Test 4	0.1	0.01	1.01	1.966
Test 5	0.01	0.1	1.1	1.953
Test 6	0.01	0.1	1.01	1.935
Test 7	0.01	0.01	1.1	1.923
Test 8	0.01	0.01	1.01	1.964

Table 3.2: Sets of initial conditions used to simulate the the HM3-1000K-50% case. The ignition values obtained by varying CFL, IS and CM parameter are shown in the rightmost column.

3.3 Ignition time and normalisation

The different fuel and oxidiser blends were found to affect significantly the physical and chemical scenario of each case investigated, making a direct comparison between cases particularly difficult. An example of how oxygen reduction affects the temperature profile and the ignition time is shown in figure 3.4.

For this reason a normalisation technique able to facilitate the comparison among cases was developed. This technique required the calculation, for each case case study, of the followings:

- Evolution of the temperature difference (ΔT),
- Calculation of the ignition time (t_{ig}),

- Calculation of the adiabatic flame temperature (T_{ad}).

The evaluation of these variables is described in the following subsections.

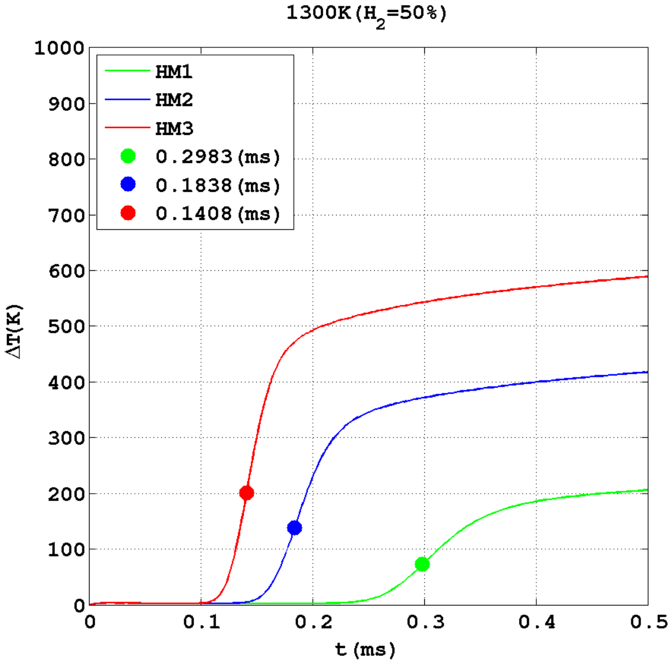

Figure 3.4: Evolution of the temperature difference (ΔT) plotted against time for three different oxidiser blends. The coloured dots represents the ignition time (t_{ig}).

3.3.1 Temperature rise and ignition time evaluation

The temperature rise (ΔT) is defined as the maximum temperature increase, in mixture fraction space, with respect to the initial temperature profile as shown in Eq. (3.4):

$$\Delta T(t) = \max_{Z}\{T(Z,t) - T(Z,0)\}. \tag{3.4}$$

The mixture fraction (Z) is a widely used parameter to measure the fuel/oxidiser ratio in non-premixed combustion modelling. Its mathematical definition has been given in section 2.4. To the best of our knowledge only one technique has been reported in literature for computing MILD combustion ignition [8]. This technique, here referred as *MaxGrad*, evaluates the ignition time at the maximum gradient of the ΔT function. Differently, the method used in all cases studied hereafter and referred as *Ratio-0.25*, defines t_{ig} as the time at which the following relation is satisfied:

$$\frac{\Delta T}{\Delta T_{\mathrm{ad}}} = 0.25, \tag{3.5}$$

where ΔT_{ad} refers to the difference between the adiabatic flame temperature (T_{ad}) and the initial oxidiser temperature (T_{ox}).

The Ratio-0.25 ignition time predictions have been compared with the MaxGrad method. Figures 3.5a and 3.5b compares the ignition time predictions of both methods for cases with different level of oxygen and hydrogen. The symbols describing the ignition time are overlaid on the ΔT evolution curve specific to each case. The figure 3.5a compares the ΔT evolution relative to the cases described by Dally *et al.* [54]. These cases present a high hydrogen content in the fuel blend and steep temperature gradients. As the figure shows, both methods show good agreement in ignition time predictions. Figure 3.5b shows cases with lower hydrogen content and reduced temperature gradient steepness.

The Ratio-0.25 method was found particularly effective in these cases. As the figure shows, the MaxGrad method predicted the HM2 ignition earlier than HM3, which is not consistent with the reduced oxygen level, and the ΔT profile. The Ratio-0.25 method shows more consistent ignition times predictions.

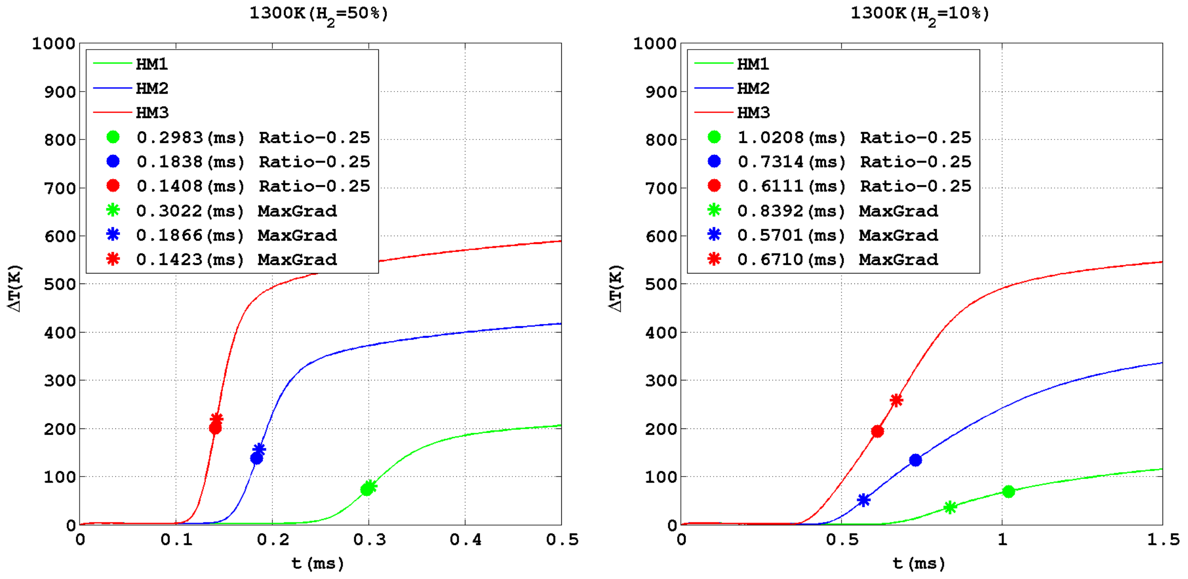

(a) 50% H_2 **(b)** 10% H_2

Figure 3.5: Comparison between MaxGrad (star) and Ratio-0.25 (circle) methods accuracy for computing ignition time. Figure analyse the cases with the 50% (left) and 10% (right) of hydrogen blended into the fuel.

3.3.2 Adiabatic flame temperature calculation

The adiabatic flame temperature calculation is based on the following hypothesis:

- The enthalpy of reactants ($h(T_{\text{in}})$) is considered equal to the enthalpy of products ($h(T_{\text{ad}})$),
- The pressure is considered constant,
- Dissociation effects are neglected,
- The intermediate species formation effects are neglected,
- The *equivalence ratio* (ϕ) is considered equal to one,

- Fuels and oxidiser are stoichiometrically balanced according to the reaction:

  $$(1-x)\mathrm{CH}_4 + x\mathrm{H}_2 + (2-\frac{3}{2}x)\mathrm{O}_2 = (2-x)\mathrm{H}_2\mathrm{O} + (1-x)\mathrm{CO}_2,$$

  where x is the hydrogen mole fraction.

- An equal amount of N_2, H_2O, and CO_2 is added to the left and the right of the reaction. The amount is calculated in order to keep the O_2/N_2, O_2/H_2O and O_2/CO_2 molar ratios consistent with the initial oxidiser chemical composition of each dilution case.

The enthalpies of reactants and products are respectively expressed as follow:

$$\begin{aligned} h(T_{\mathrm{in}}) &= \sum_{i=1}^{N} \nu_i^{'} \left(\Delta h_{\mathrm{f},i}^{0,\mathrm{m}} + \int_{T_0}^{T_{\mathrm{in}}} c_{p_i}^{\mathrm{m}} dT \right), & (3.6) \\ h(T_{\mathrm{ad}}) &= \sum_{i=1}^{N} \nu_i^{''} \left(\Delta h_{\mathrm{f},i}^{0,\mathrm{m}} + \int_{T_0}^{T_{\mathrm{ad}}} c_{p_i}^{\mathrm{m}} dT \right), & (3.7) \end{aligned}$$

where T_0, T_{in} and T_{ad} are the temperature at standard conditions, the pre-heating temperature and the adiabatic temperature respectively. The mole fraction of reactants and products are defined as $\nu_i^{'}$ and $\nu_i^{''}$, where the subscript i indicates the chemical specie of interest. $\Delta h_{\mathrm{f},i}^{0,\mathrm{m}}$ represents the enthalpy of formation, while $\int_{T_0}^{T_{\mathrm{in}}} c_{p_i}^{\mathrm{m}} dT$ and $\int_{T_0}^{T_{\mathrm{ad}}} c_{p_i}^{\mathrm{m}} dT$ express the sensible enthalpy of reactants and products. The subscript f and the superscript m stand respectively for *formation* and *molar*. Equation (3.7) can be rearranged as follow:

$$h(T_{\mathrm{ad}}) = \sum_{1}^{N} \nu_i^{''} \Delta h_{\mathrm{f},i}^{0,\mathrm{m}} + \nu_i^{''} \int_{T_0}^{T_H} c_{p_i}^{\mathrm{m}} dT + \nu_i^{''} \int_{T_H}^{T_{\mathrm{ad}}} c_{p_i}^{\mathrm{m}} dT. \quad (3.8)$$

The value T_H is taken equal to 1300K because all the cases were observed to reach or exceed this temperature. In this way it was possible to compute the exact value of $\int_{T_0}^{T_H} c_{p_i}^{\mathrm{m}} dT$. Furthermore the c_p value in the term $\int_{T_H}^{T_{\mathrm{ad}}} c_{p_i}^{\mathrm{m}} dT$ could be linearly approximated with a reasonable error considering the narrowed gap between T_H and T_{ad}. In order to calculate an approximate value of c_p, T_{ad} was guessed. Table 3.3 shows the computed values of the adiabatic temperature. The guessed temperature values are also shown.

Case	T_{guess}	T_{ad}
HM3 (50% mole H_2)	2100K	2105K
HM2 (50% mole H_2)	1900K	1855K
HM1 (50% mole H_2)	1600K	1589K
HM3 (10% mole H_2)	2100K	2078K
HM3 (0% mole H_2)	2100K	2074K

Table 3.3: Computed values of the adiabatic temperature together with the guessed temperature values for all the 1D cases investigated.

3.3.3 Normalisation technique

The first step of the technique consists in defining the rate of temperature increase by the following gradient:

$$G(t) = \frac{d(\Delta T)}{dt} \; [\mathrm{K/s}], \tag{3.9}$$

where ΔT represents the temperature difference expressed in equation (3.4).
The temperature increase rate G_{ig} at the ignition time is then found:

$$G_{\mathrm{ig}} = \left.\frac{d(\Delta T)}{dt}\right|_{t=t_{\mathrm{ig}}} \; [\mathrm{K/s}], \tag{3.10}$$

where t_{ig} corresponds to the value found from equation (3.5), the Ratio-0.25 method. The time period Δt_{ig} required to reach the adiabatic flame temperature at the rate G_{ig} is found as:

$$\Delta t_{\mathrm{ig}} = \frac{T_{\mathrm{ad}} - T_{\mathrm{ox}}}{G_{\mathrm{ig}}} \; [\mathrm{s}], \tag{3.11}$$

This time period is used to normalise the time as follow :

$$\tau = \frac{t - t_{\mathrm{ig}}}{\Delta t_{\mathrm{ig}}}. \tag{3.12}$$

By plotting the ratio $\Delta T/\Delta T_{\mathrm{ad}}$ against the normalised time τ for each case of interest a graph normalised and non-dimensional on both the x and y axis (Fig. 3.6b) is obtained.

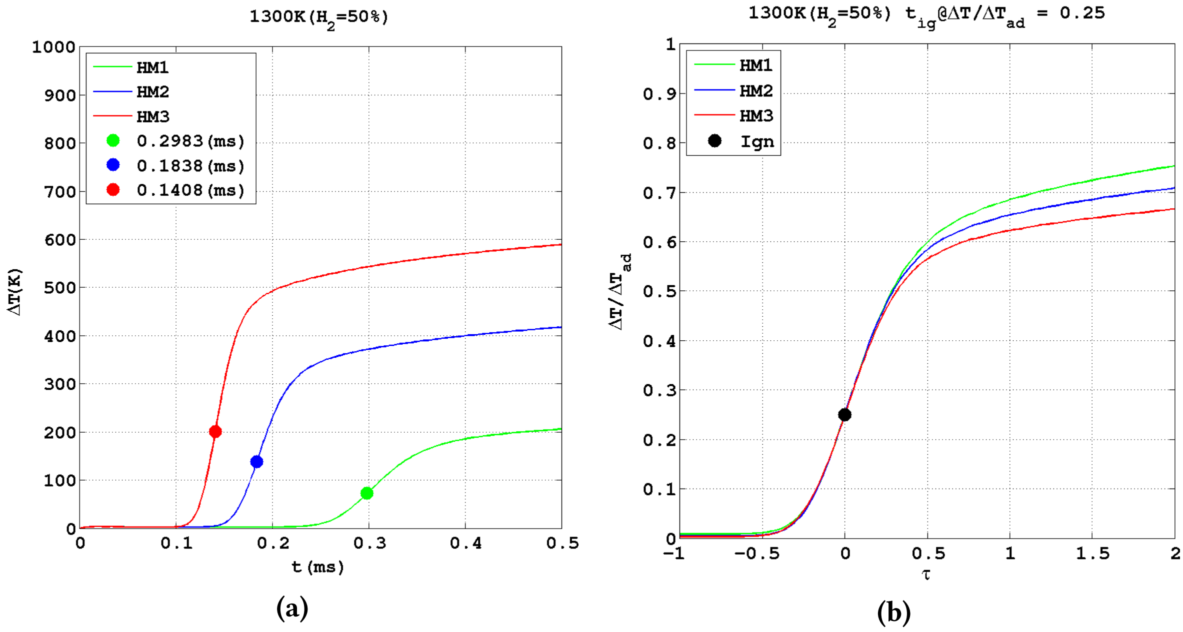

Figure 3.6: Comparison of temperature evolution curve for HM1, HM2 and HM3 cases, with (right) and without (left) being normalised.

As the example in figure 3.6b shows, the normalisation allows the ΔT curves in figure 3.6a to collapse through the main ignition process. It is worth noting that for $\tau > 0.3$ (Fig. 3.6b) curves tend to diverge and the normalisation is less effective. A potential explanation is that the stronger dissociation effects and the larger intermediates formation at higher temperature weaken some of the assumptions made in section 3.3.2. Nonetheless, since the normalisation techniques collapses the ΔT curves for a large part of the ignition process, it is used as a valuable tool to study the physical and chemical properties of cases showing different time scales. More precisely, the normalisation technique is used on this dissertation to compare cases with different oxygen level (HM1, HM2 and HM3) and different hydrogen addition (0%, 10% and 50%).

3.4 Space-time contour plots

Many of the results from the 1D study are presented in a space time contour plot. It shows in time (x-axis) and space (y-axis) the evolution of each variable of interest. The time is presented in the normalised form as explained on section 3.3.3.

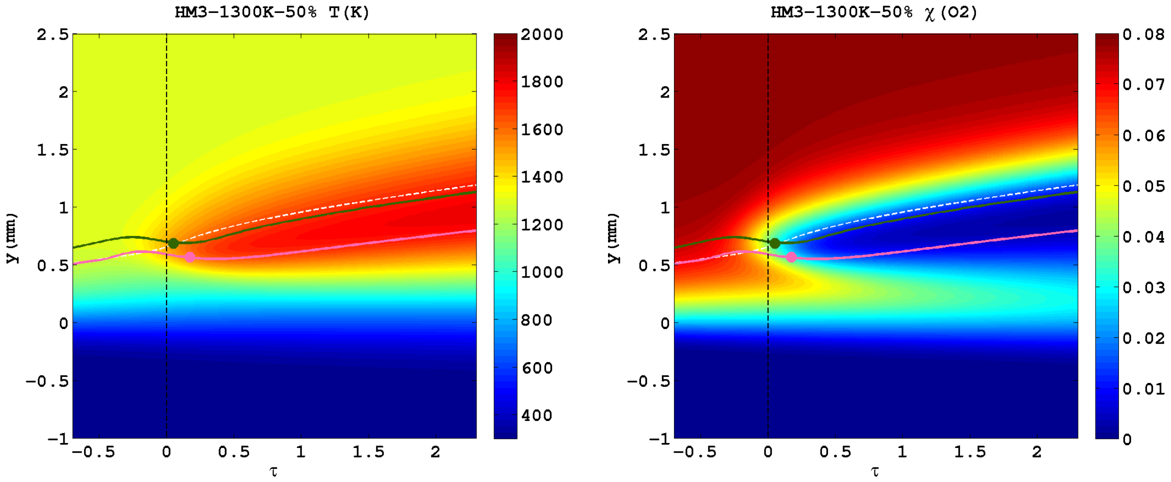

(a)

(b)

Figure 3.7: Examples of space-time contour plots showing the temperature (left) and the O_2 mole fraction evolution for the HM3-1300K-50% case.

Almost all the space-time contour plots presented on this thesis also contain four different lines: two dashed and two solid. The vertical black dashed line indicates the ignition time, calculated by equation (3.5), representing $\tau = 0$. The *pre-ignition* is the period of time for $\tau < 0$, while the *post-ignition* is the period of time for $\tau > 0$. The presence of the ignition time line helps to easily locate the pre-ignition (left of the black line) and the post-ignition (right of the black line) periods.

The white dashed line shows the location of the stoichiometric mixture fraction region, often referred as $Z = Z_{\mathrm{st}}$. The stoichiometric mixture line, computed according to equation (2.27), indicates the region of space where reactants are mixed in such a way that complete combustion is possible. The area above the line, closer to the oxidiser layer, indicates a region where Z is lower than Z_{st} and the fuel/oxidiser mixture is *lean*. On the contrary, the area below the white line represents the *rich* region, where the fuel/oxidiser mixture is more abundant in fuel.

Finally, the two solid lines locates, in space and time, the region of the domain where the highest consumption rate of methane (pink line) and hydrogen (green line) are reached. They are referred hereafter as *consumption paths*. The circles on the consumption paths highlight the points where the peak in the consumption rate is reached. They are referred as *consumption peaks*. These lines represents a valuable tool to describe the flame front geometry and identify regions of particular interest.

3.5 Kinetic bar chart

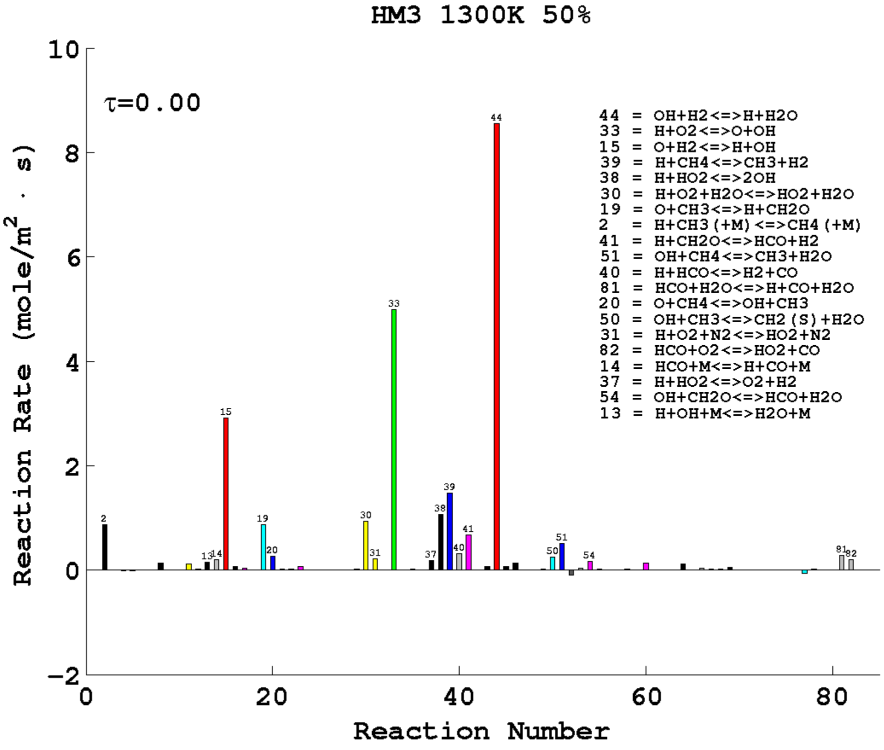

Figure 3.8: Rates of reaction of the DRM19 mechanism at ignition time for the HM3-1300K-50% case. The reaction rate of each elementary step is integrated along the cross-stream (y) direction.

Figure 3.8 shows another plot widely used in this thesis. It presents in the form of a bar chart, the rates of reaction of all the elementary steps listed in the DRM19 mechanism. The 20 reactions with the highest rate are numbered and described, in descending order of rate, in the legend.

To account for the spatial distribution of each reaction, each bar considers the integrated rate value, over the cross-stream direction, of the step represented. A color coding is used to identify major processes responsible for specific chemical roles as follow:

- Blue: Colour used to identify reactions which describe, in the forward direction, the abstraction of an atomic hydrogen from the methane molecule (CH_4). This color is used for tagging R20, R39, R51, R63 and R71 steps.
- Red: Colour used to identify reactions which describe, in the forward direction, the abstraction of an atomic hydrogen from molecular hydrogen (H_2). This color is used for tagging R15, R44, R61 and R68 steps.
- Green: Colour used to identify reactions which describe, in the forward direction, the abstraction of an atomic oxygen from molecular oxygen (O_2). This color is used for tagging R33 and R75 steps.
- Cyan: Colour used to identify reactions which describe, in the forward direction, the abstraction of one atomic hydrogen from methyl molecule (CH_3). This color is used for tagging R19, R49, R50, R76, and R77 steps.
- Yellow: Colour used to identify reactions which describe, in the forward direction, the production of hydroperoxyl molecule (HO_2). This color is used for tagging R11, R29, R30, R31, R32, R83 and R84 steps.
- Magenta: Colour used to identify reactions which describe, in the forward direction, the production of aldehyde molecule (HCO). This color is used for tagging R17, R18, R23, R24, R28, R41, R54, R60 and R79 steps.
- Light grey: Colour used to identify reactions which describe, in the forward direction, the production of carbon monoxide molecule (CO). This color is used for tagging R14, R21, R40, R53, R66, R67, R74, R78, R81 and R82 steps.
- Grey: Colour used to identify reactions which describe, in the forward direction, the production of carbon dioxide molecule (CO_2). This color is used for tagging R10, R22, R27, R52 and R59 steps.
- Black: Colour used to identify all the other processes.

It should be noted that some reactions could be identified, according to the aforementioned criteria, with more than one colour. Only few reactions are present these ambiguities (R27, R28, R60, R66, R67, R76 and R82) and they are observed to have a minor role in results presented in this thesis.

The kinetic bar chart is used, often in conjunction with the chemical pathway diagram, to show the evolution in time of the kinetic scenario for each case. The sensitivity of each elementary step to the evolving physical/chemical conditions are in this way easily spotted.

3.6 Carbon atom pathways

Because of its complex structure, a particular attention is devoted in this thesis to the analysis of the methane consumption pathway. The analysis is performed at different times with the help of the reaction path overviewed mathematically in section 2.6, which describes the carbon atom (C) transfer from one species to another, as shown on figure 3.9. The C atom exchange rate is integrated along the cross-stream direction and graphically shown by the thickness of the arrows.

For each case analysed and each time considered, thickness of arrows are normalised with respect to the $CH_4 -> CH_3$ path. To avoid ambiguities in comparing space-time contour plots together with chemical pathways it is important to note that, because of the normalisation, to a reduced or increased conversion of CH_3 into another intermediate, does not necessarily correspond to a reduced or increased level of that intermediate into the domain.

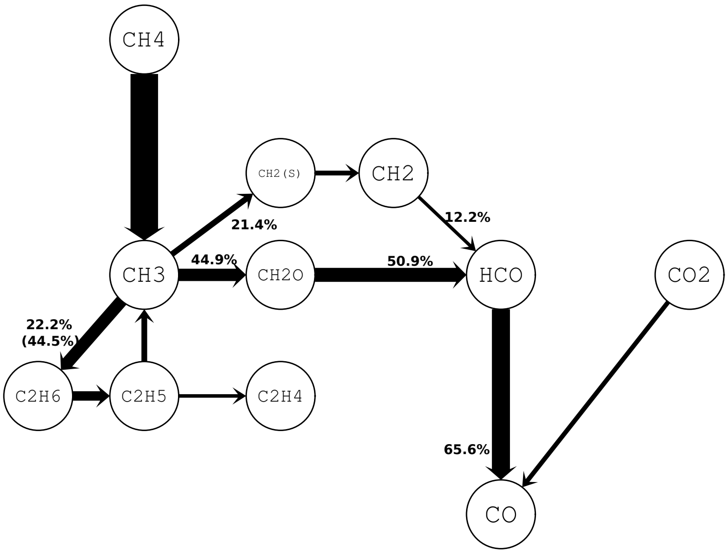

Figure 3.9: Example of the pathway followed by the carbon atom in the HM3-1300K-50% case. Arrows are proportional to the integrated transfer rate of C atoms between species, and normalized with respect to the $CH_4 \rightarrow CH_3$ step. Only arrows at least 5% of the thickest are shown. Percentages indicate the fraction of CH_4 destroyed along the various paths. Percentages are rounded to the upper decimal digit (+0.1%).

In order to outline the most important paths, only arrows at least the 5% of the thickest are shown. This implies that some some paths are not shown. For example, the transfer rate of $CH_3 -> CH_2O$ is less than the transfer rate of $CH_2O -> HCO$. This maybe due to the production of CH_2O through minor processes like $CH_2(s) -> CH_2O$ or $CH_2 -> CH_2O$ which are not shown, or to an excess of CH_2O build-up at an earlier time.

For particular paths of interest the information given by the thickness of the arrow is also augmented by percentage values, which quantifies the fraction of CH_4 destroyed along the path. The values are rounded to the upper decimal digit (+0.1%). Reactions such as $2\,CH_3 -> C_2H_6$ give the path $CH_3 -> C_2H_6$ twice the weight since two carbons are transferred. When this occurs, the percentage is divided by two to represent the reaction rate, and the original value (representing the number of C atoms transferred) is given in parenthesis.

3.7 Methane consumption spatial evolution

Along with the analysis of the methane pathway, attention is also devoted to the location and spatial extension of the CH_4 chemical mechanism. This is done by plotting representative reactions (11) of CH_4 consumption against the spatial coordinate. The rate of reaction shown and the colours used are selected taking into account the major branches of the methane consumption pathways (Fig. 3.9), as follows:

- $CH_4 \rightarrow CH_3$: methyl production process represented by R20, R39 and R51 steps shown in blue,
- $CH_3 \rightarrow CH_2(s)$: methyl destruction process (top branch of the methane pathway) represented by R50 step shown in black,
- $CH_3 \rightarrow CH_2O$: methyl destruction process (middle branch of the methane pathway) represented by R19 step shown in black,
- $2\,CH_3 \rightarrow C_2H_6$: methyl destruction process (bottom branch of the methane pathway) represented by R8 step shown in black,
- $CH_2 \rightarrow HCO$: aldehyde production process (top branch of the methane pathway) represented by R60 step shown in cyan,
- $CH_2O \rightarrow HCO$: aldehyde production process (middle branch of the methane pathway) represented by R41 step shown in cyan,
- $C_2H_4 \rightarrow HCO$: aldehyde production process (bottom branch of the methane pathway) represented by R24 step shown in cyan,
- $HCO \rightarrow CO$: carbon monoxide production process represented by R81 step shown in red,
- $CO \leftrightarrow CO_2$: carbon dioxide production/destruction process represented by R52 step shown in green.

As figure 3.10 shows, a constant scaling factor is applied to each rate of reaction. The scaling factor value often differs from unity when comparing different cases to each other. It is computed by comparing the peak rate for the $CH_4 \rightarrow CH_3$ steps of the case under investigation, with the one from the case assumed as reference. It is used the $CH_4 \rightarrow CH_3$ process to evaluate the scaling factor since the methyl production showed, in all the cases studied, the highest rates among methane consuming steps. The knowledge of the scaling factor allows to have a rough estimate of differences in reactivity among methane consumption chemistry from different cases.

The position of the stoichiometric mixture fraction region (black dashed line) is also shown on figure 3.10. This is done to better identify in which area of the domain (lean or rich) CH_4 is being consumed.

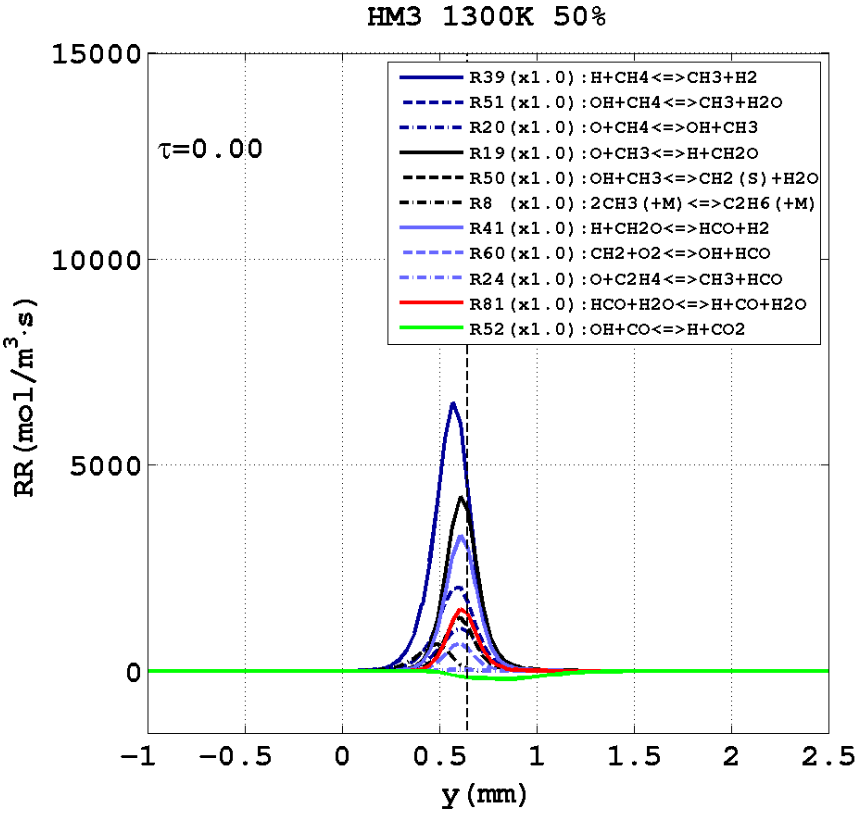

Figure 3.10: Most important rates of reaction of the methane mechanism plotted at $\tau = 0.00$ for the base case. The vertical dashed line represents the position of the stoichiometric mixture fraction region.

3.8 Reaction zone spatial evolution

Methane and hydrogen consumption were observed to occur at different rate and with different spatial extensions. In order to catch physical and kinetic differences between CH_4 and H_2 chemistry, representative rates of reaction of hydrogen and methane chemistry are shown together on a double-axis graph (Fig. 3.11).

Here, the rates of reaction representing the hydrogen chemistry (R15 and R44) are shown in red while the ones describing the methane chemistry (R20, R39 and R51) are shown in blue. It was possible to use only three rates of reactions to represent the location of the methane chemistry since it was observed that the majority of steps describing the CH_4 consumption occurred within the area of methyl producing processes (R20, R39 and R51). The consumption of hydrogen was observed being dominated by R15 and R44 processes, hence the choice to use these two steps to represent the location of H_2 chemistry. The spatial extent of oxygen consumption process is tracked by plotting the R33 rate of reaction, observed as the major step describing the O_2 depletion.

The region spanned by methane, hydrogen and oxygen consuming processes is often referred in this thesis as the *reaction zone*.

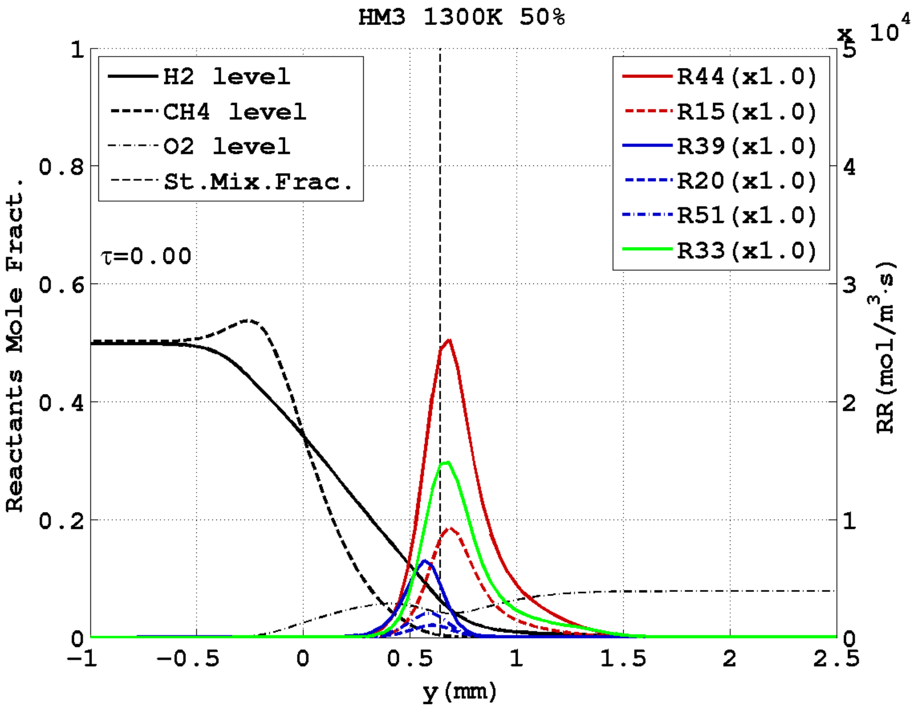

Figure 3.11: Rates of reaction representative of hydrogen (red), methane (blue) and oxygen (green) consumption processes plotted with the fuels and oxidiser mole fraction in geometrical space. The vertical dashed line represents the position of the stoichiometric mixture fraction region.

The scaling factor applied to each reaction is computed by comparing the rate of the R33 process of the investigated case with the one from the case assumed as reference. Having observed the importance of the R33 process in controlling the rate of fuels consumption, knowledge of the scaling factor gives a rough estimate of the reactivity of each case.

The molar fraction of the reactants and the location of the stoichiometric mixture fraction region is also shown. The level of reactants gives additional insight into the variables controlling the rate of reactants chemistry, while the Z_{st} position outlines the areas of the domain (lean or rich) where CH_4 and H_2 are being consumed.

Chapter 4

1D Study - The base case

The HM3-1300K-50% will be considered hereafter as the *base case*. It represents the most reactive configuration within the range of cases studied, since it considers the highest level of hydrogen (50% by mole) and oxygen (9% by mass) within the reactants. As describe in chapter 3 the oxidiser is at 1300K. The temperature value is high enough to allow self-ignition, which is the first aspect analysed.

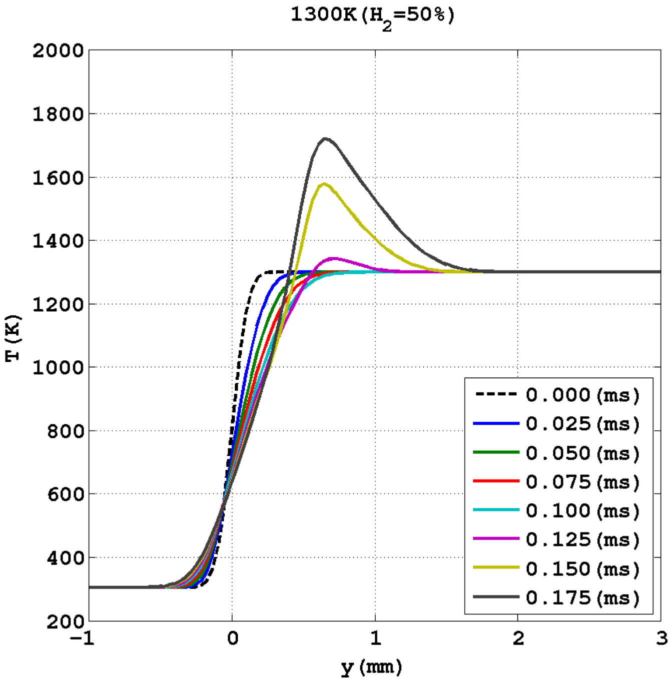

Figure 4.1: Temperature profiles as a function of y, plotted at different times. The graph represents the temperature evolution of the base case.

The evolution of the temperature profile for the base case is shown in figure 4.1. The profiles are plotted at different time as a function of y (cross-stream direction). The black dashed line plotted at t=0 ms represents the initial temperature gradient, following the 1-2-1 filter application on the top hat temperature profile (Sect.3.2). In the time range [0,0.1] ms the temperature gradient is reduced by diffusion (blue, green, red and cyan lines). For time t >0.1

ms the temperature rises (magenta, yellow and black lines) at the oxidiser side (y >0) as a consequence of fuel self-ignition.

The self-ignition event is more clearly visible in figure 4.2. Here the temperature difference (ΔT), computed using equation (3.4), is plotted against time: the bottom x-axis presents the actual time (t) while the top x-axis shows the normalised time (τ). The temperature difference is also shown scaled by $\Delta T_{\text{ad}} = T_{\text{ad}} - T_{\text{ox}}$ on the right y-axis. The process used to compute the temperature increase and its normalisation are described in detail in section 3.3.3.

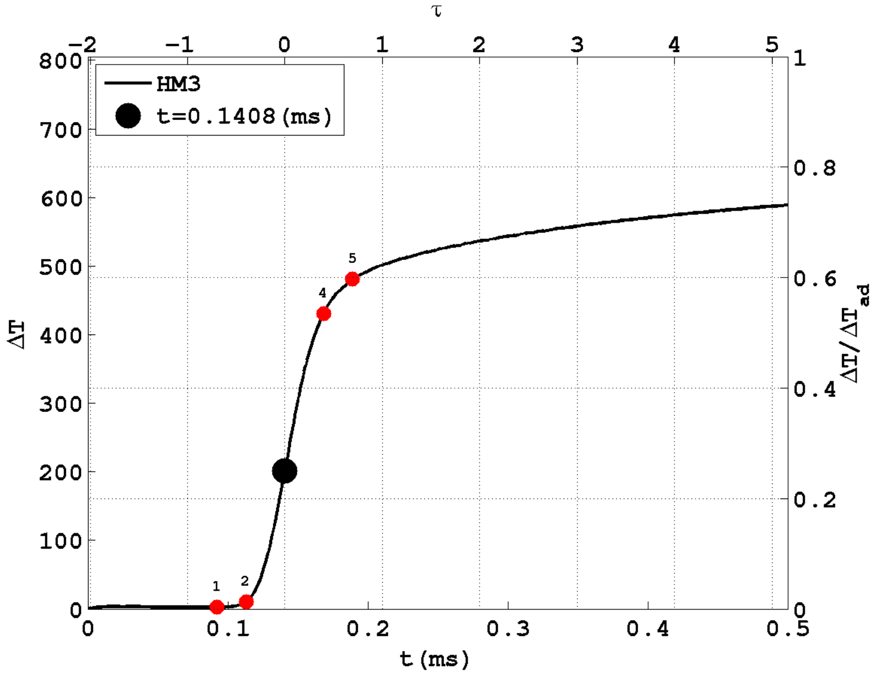

Figure 4.2: Temperature difference (ΔT) plotted as a function of time (t). The ΔT value is computed according to equation (3.4). The top axis represent the time normalised according to equation (3.12). The right axis scales the temperature difference with respect to $\Delta T_{\text{ad}} = T_{\text{ad}} - T_{\text{ox}}$. The circles overlaid on the graphs represent the five time points at which the physical/chemical scenario of the base case is investigated. The ignition time is shown in black.

The temperature starts rising for $\tau > -0.7$ ($t > 0.1$ ms) showing its steepest gradient in the range $\tau \in$ [-0.5,0.5]. Within this time period ignition occurs ($t \sim 0.14$ ms) as the 25% of the adiabatic temperature is reached (see Sect. 3.3.1). For $\tau > 0.7$ the rate of temperature increase is greatly reduced, reaching around 70% of the adiabatic temperature for $\tau = 5$. Therefore, as shown on figure 4.2, the time period $\tau \in$ [-0.7,0.7] encloses the most significant rate of temperature change.

As a consequence, this τ range has been used as the temporal range reference for in-deep investigate the major aspects of the base-case self-ignition process. More precisely five different points have been selected within this time period in order to follow the evolution of the diffusion-chemistry interaction process. The choice of the points is as follows:

- Point 1 ($\tau = -0.7$): Time investigation point representing the lower end of the ignition period. It is located on the flat initial part of the ΔT profile where a rise in temperature cannot be appreciated. It is used to analyse diffusion phenomena as a consequence of the minor role of chemistry,

- Point 2 ($\tau = -0.4$): Time investigation point placed at the beginning of the steepest part of the curve, before ignition. It is used to investigate major physical aspects and kinetic mechanisms which precede the ignition event,
- Point 3 ($\tau = 0.0$): Ignition time. Point at which the 25% of the adiabatic temperature is reached. It represents the most important point of the ignition period analysis. It is used to provide a comprehensive description of the physical/chemical scenario of the reaction zone,
- Point 4 ($\tau = 0.4$): Time investigation point placed at the end of the steepest part of the curve. Used to focus on phenomena that limits rates of reactions causing the reduction in the temperature rise rate,
- Point 5 ($\tau = 0.7$): Time investigation point representing the upper end of the ignition period. It locates the flatter part of the curve after ignition. Used to focus on diffusion-chemistry phenomena once combustion has started.

The investigation of the physical and chemical properties at each selected point is supported by the space-time contour plots of several variables of interest.

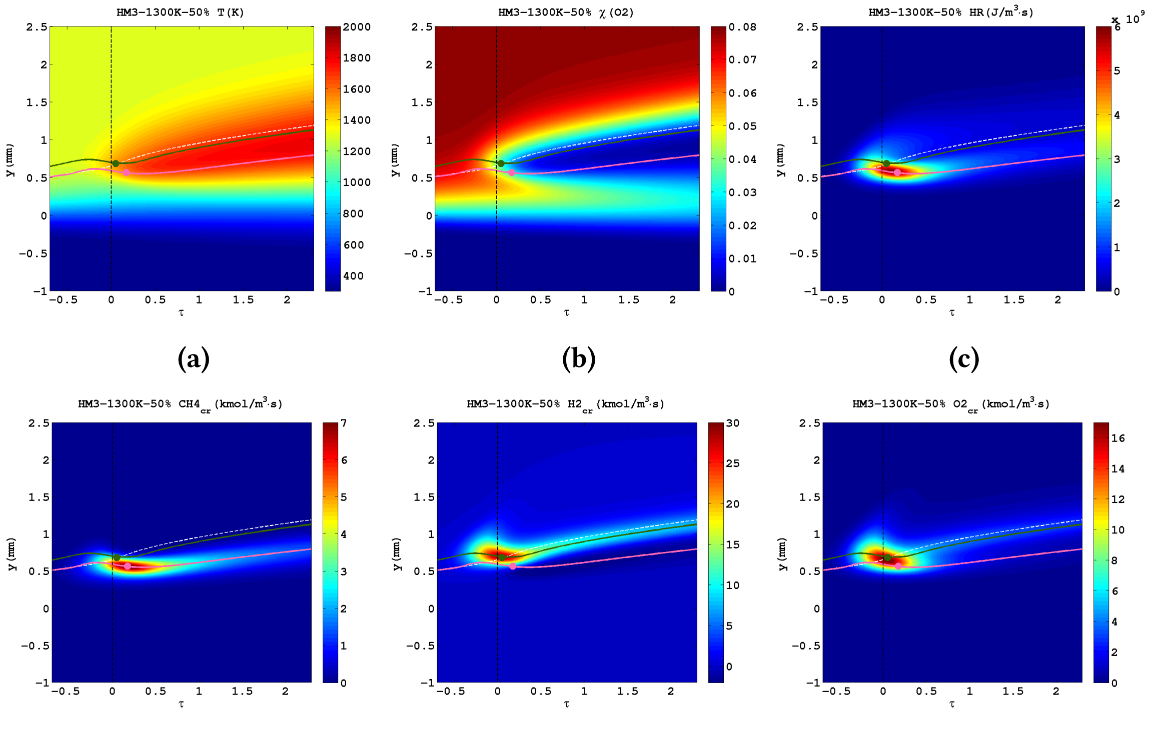

(a) (b) (c)

(d) (e) (f)

Figure 4.3: First row: Temperature (a), oxygen mole fraction (b) and heat release (c).
Second row: Consumption rate of methane (d), hydrogen (e) and oxygen (f).

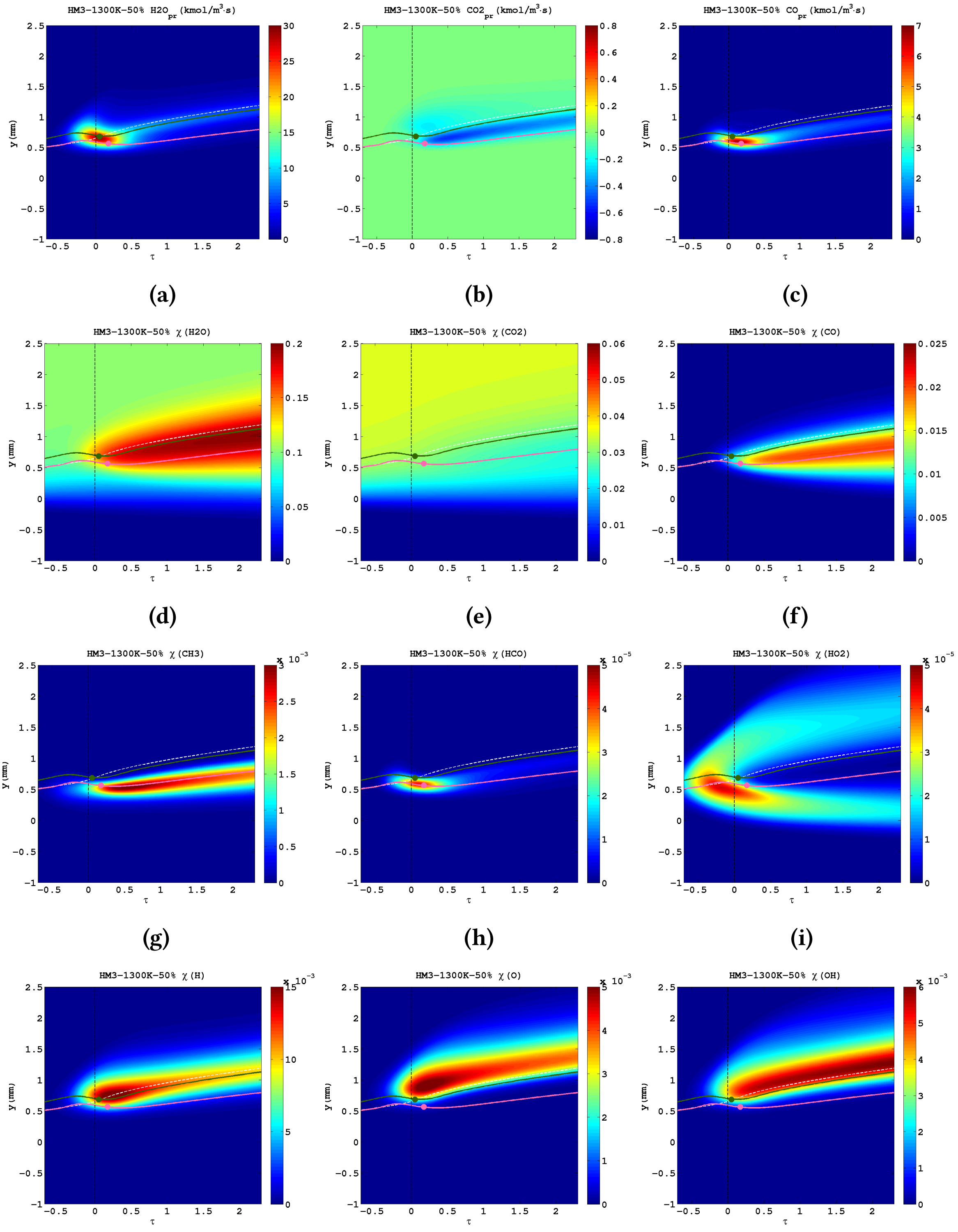

(a) (b) (c)

(d) (e) (f)

(g) (h) (i)

(j) (k) (l)

Figure 4.4: First row: Production rate of water (a), carbon dioxide (b) and carbon monoxide (c). **Second row**: Mole fraction of water (d), carbon dioxide (e) and carbon monoxide (f). **Third row**: Mole fraction of methyl (g), aldehyde (h) and hydroperoxyl (i). **Fourth row**: Mole fraction of atomic hydrogen (j), atomic oxygen (k) and hydroxyl (l).

These contours (temperature, species consumption/production rate, species mole fraction and intermediates mole fraction) are shown normalised in time, as described in section 3.4. The ignition period is completely included within the τ range described by contours.

4.1 Base case - Point 1

The first of the chosen set of investigation points is used to focus only on the diffusion processes which precede the ignition. At this time ($\tau = -0.7$) in fact, the role of the chemistry can be considered negligible, as suggested by the low value of the temperature rise (Fig. 4.2) and low CH_4 and H_2 rates of consumption (Fig. 4.3d and 4.3e). Conversely, steep species gradients can be observed at the fuel/oxidiser interface in the pre-ignition period (e.g. Fig. 4.5a and 4.5b), outlining a stronger importance of the diffusion processes.

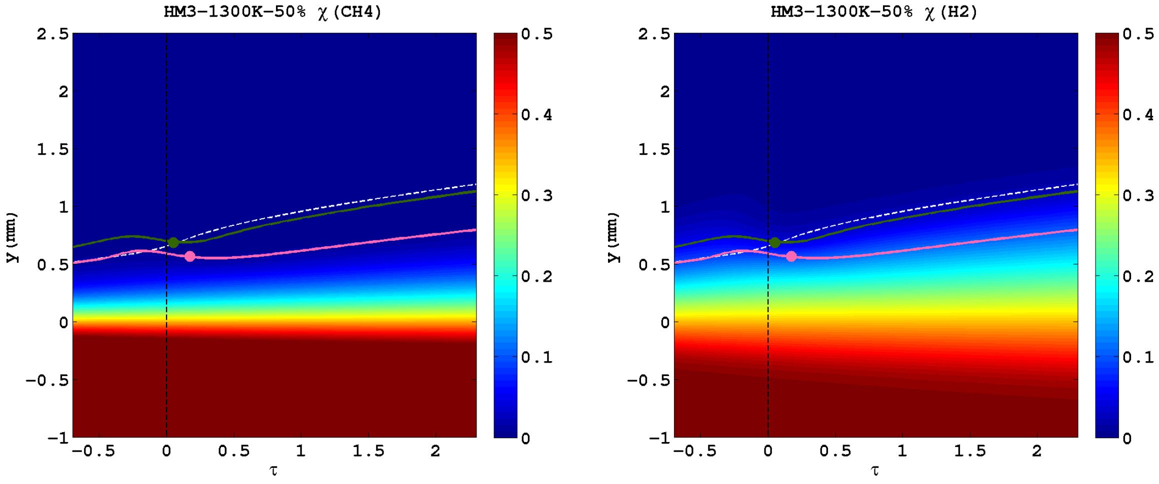

(a) (b)

Figure 4.5: Comparison of methane (left) and hydrogen (right) mole fraction evolution.

The mole fraction contours on figure 4.5a and 4.5b outline the diffusion of methane and hydrogen in the oxidiser area ($y > 0$). Moreover, they highlight differences in the diffusion behaviour of each fuel. A better picture of diffusivity differences between fuels is obtained by analysing the presence, on a mass basis, of methane and hydrogen in the mixture fraction space (Z). In particular, only the region of the mixture fraction space where ignition is most likely to occur is consider. This region is clearly visible on figure 4.6. Here the heat release contour is overlaid three dashed lines. The black line represents the stoichiometric mixture fraction region (Z_{st}). The two white dashed lines above and below the black line correspond to 0.1 and 7 times the stoichiometric mixture fraction value respectively. The area where exothermic reactions occur is almost completely enclosed between the white lines. For this reason the fuels diffusivity analysis will focus on the $Z/Z_{\mathrm{st}} \in$[0,7] range only.
In figure 4.7a and 4.7b the mass fraction of H_2 and CH_4 are plotted against scaled mixture fraction space (Z/Z_{st}) at two different times.

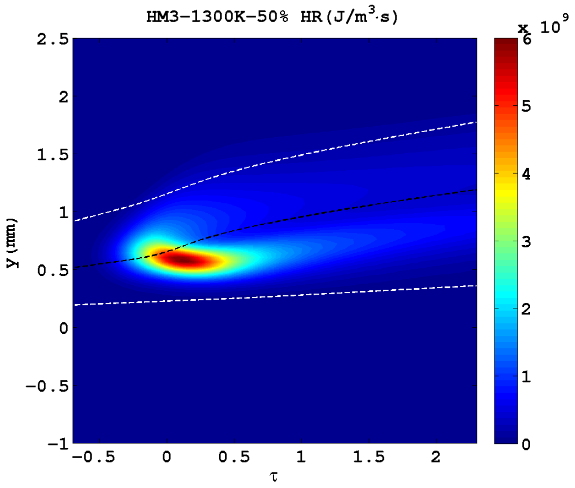

Figure 4.6: Contour of heat release for the base case. The black dashed line indicates the stoichiometric mixture fraction region. The two white dashed lines above and below the black line correspond to 0.1 and 7 times the stoichiometric mixture fraction value respectively.

At $t = 0$ (dashed lines) CH_4 and H_2 profiles follow the initial fuel set-up (Tab. 3.1), showing in both cases a linear trend. Nonetheless, at $\tau = -0.7$ (solid lines) the differential fuels diffusion results in an increased hydrogen mass fraction and a decreased methane mass fraction, highlighting the faster H_2 diffusivity and the larger H_2 content, on molar basis, in the Z/Z_{st} ∈[0,7] range [1].

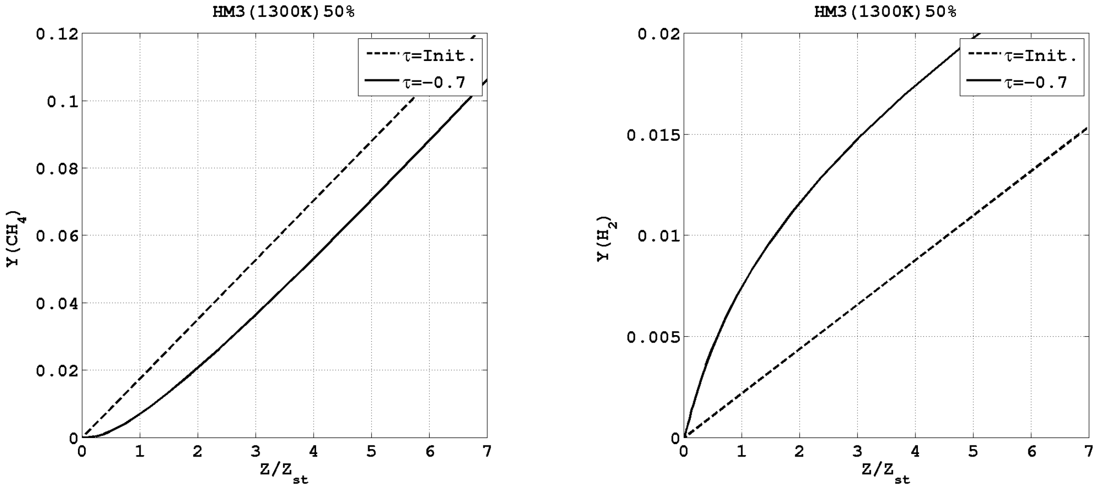

(a) CH4 **(b)** H2

Figure 4.7: Mass fraction of CH_4 (left) and H_2 (right) as a function of the scaled mixture fraction (Z/Z_{st}) at $t = 0$ (dashed line) and $\tau = -0.7$ (solid line).

---

[1] At $t = 0$ the fuel is made by an equimolar H_2 and CH_4 blend which corresponds to different hydrogen and methane mass fraction. Following the differential diffusion effect, in the same mixture fraction area at $\tau = -0.7$ the methane mass fraction decreases and the hydrogen mass fraction increases. This implicates the larger mole fraction of hydrogen in the observed mixture fraction area.

4.2 Base case - Point 2

The second point of analysis, focuses on the major physical and chemical aspects which precede the ignition event. Emphasis is given to the kinetic steps which describe both methane and hydrogen consumption.

At $\tau = -0.4$ the heat released around the stoichiometric mixture fraction region (Fig. 4.6) outlines the start of exothermic reactions. Both fuels and oxygen start reacting at approximately the same time as shown on figures 4.3d and 4.3e. Because of the low value of Z_{st} (~0.02), the chemistry of reactants lies close to the edge of the fuel/oxidiser interface ($y \sim 0.7$) as shown on figure 4.8.

Some representative rates of reaction which locates hydrogen and methane mechanism (Sect. 3.8) are shown in figure 4.8. It is outlined a unique region where the chain reaction is initiated. The methane consumption (blue lines) occurs around Z_{st} where a low availability of CH_4 is observed (black dashed line). The availability of H_2 (black solid line) is higher around Z_{st} because of the faster hydrogen diffusion. The H_2 consumption (red lines) occurs mainly ahead the Z_{st} line, spanning over a larger region which includes the CH_4 and O_2 (green line) consumption area. The difference in the regions of CH_4 and H_2 consumption is illustrated by the early separation of the fuel consumption paths in figure 4.3d and 4.3e, with the H_2 path locating above the CH_4 one.

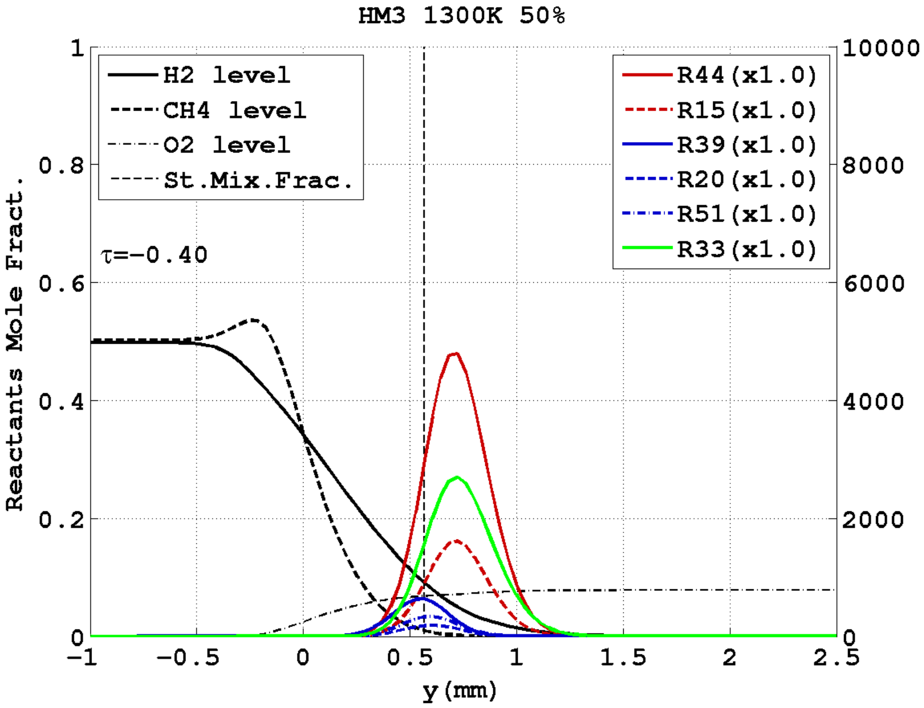

Figure 4.8: Rates of reaction representative of hydrogen (red) and methane (blue) mechanisms plotted against the fuels and oxidiser mole fraction along the cross-stream direction. The right axis expresses the value of rate of reaction in $\mathrm{mol/m^3 \cdot s}$.

Along with differences in position, the figure outlines differences in reactants rate of consumption. The rates of reaction representing H_2 and O_2 chemistry are significantly larger than the ones representing CH_4 chemistry. The same trend is observed in figures 4.9a, 4.9b and 4.9c, which show the overall reactants consumption rate at τ =-0.5, -0.4 and -0.3. Here, the hydrogen consumption outlines a rate roughly 5 times larger than methane one, confirming an important role for the hydrogen chemistry.

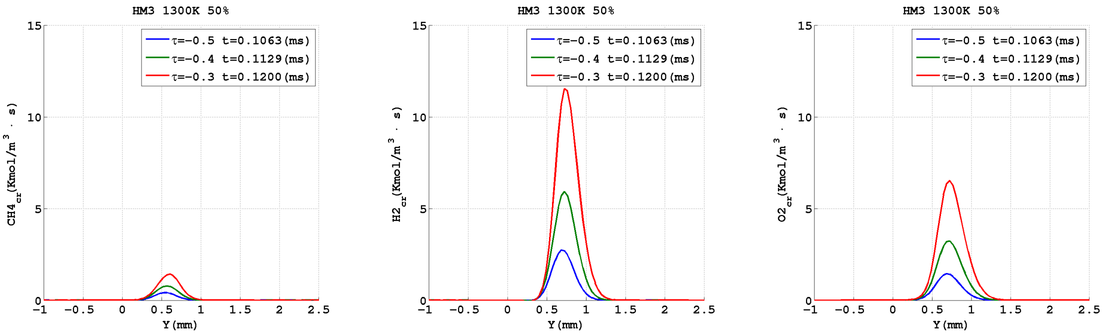

(a) CH_{4CR} **(b)** H_{2CR} **(c)** O_{2CR}

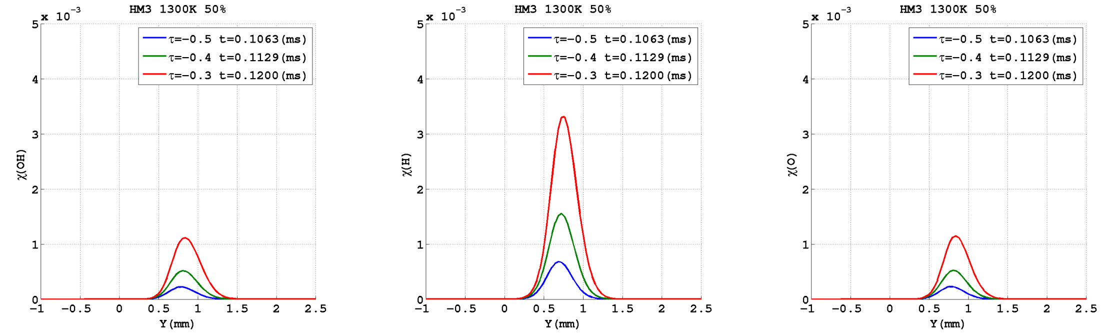

(d) OH **(e)** H **(f)** O

Figure 4.9: **Firts row**: Methane (left), hydrogen (middle) and oxygen (right) consumption rate profiles in the pre-ignition period.
Second row: Formation of OH (left), H (middle) and OH (right) radical pool in the pre-ignition period.

With the start of the reactants destruction the formation of a radical pool is observed. On figures 4.9d, 4.9e and 4.9f attention is given to H, O and OH species only (also shown in figures 4.4j, 4.4k and 4.4l). Here the stronger presence of atomic hydrogen, compared to O and OH, appears to be linked to the larger H_2 rate of consumption.

More insights into processes responsible for the formation of the radical pool and into the role of both fuels in the chemistry of the pre-ignition period, are obtained from the detailed analysis of the active kinetic steps at $\tau = -0.4$.

Figure 4.10 shows a bar chart of the base case at $\tau = -0.4$, which shows all the rates of reactions in the DRM19 mechanism. A comprehensive description of this graph is provided in section 3.5.

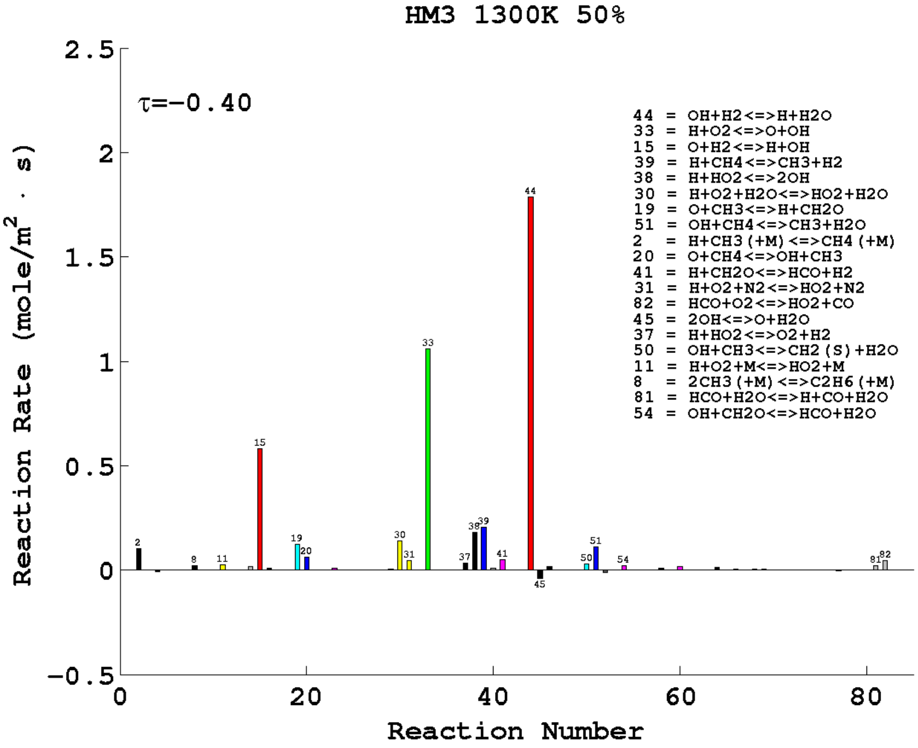

Figure 4.10: Rates of reaction of the DRM19 mechanism integrated along the cross-stream (y) direction. The reaction rates of the base case are shown.

As figure 4.10 shows, the radical production during pre-ignition can be mainly ascribed to the chain branching and propagating reactions in the H_2-O_2 mechanism (R15, R33 and R44), since they show significantly higher rates and are responsible for the H, O, OH build-up as follow:

$$\mathrm{O + H_2 \longleftrightarrow H + OH} \qquad \text{(R15)}$$
$$\mathrm{OH + H_2 \longleftrightarrow H + H_2O} \qquad \text{(R44)}$$
$$\mathrm{H + O_2 \longleftrightarrow O + OH} \qquad \text{(R33)}\,\cdot$$

Among all elementary reactions described in figure 4.10, R15 and R44 steps are the only describing the hydrogen consumption and they are both responsible for the H radical built up, confirming the link between H_2 and H dominant presence around the Z_{st} region.
Because of the large presence of H radicals, the oxygen consumption is controlled by the R33 branching step, although other processes compete for O_2:

$$\mathrm{H + O_2 + M \longleftrightarrow HO_2 + M} \qquad \text{(R11)}$$
$$\mathrm{H + O_2 + H_2O \longleftrightarrow HO_2 + H_2O} \qquad \text{(R30)}$$
$$\mathrm{H + O_2 + N_2 \longleftrightarrow HO_2 + N_2} \qquad \text{(R31)}\,\cdot$$

As the yellow color suggest, these steps represent the early production of the hydroperoxyl

(HO_2) molecule (Fig. 4.4i). Although presenting strong similarities with R33 step (all describe the reaction between H and O_2), they show a significantly lower reactivity with respect to R33, outlining the higher sensitivity of the R33 process to the oxygen presence. The production of HO_2 is common in the early stages of hydrocarbons ignition [27, 42, 69]. Those chain-termination reactions act as sinks for H radical in the fist part of ignition and the resulting HO_2 molecule remains stable and is build-up at relatively low temperature (Fig. 4.4i). Where temperature starts rising significantly, the HO_2 molecule is no longer stable and its consumption is observed. As a result, monitoring of HO_2 consumption represents a valuable tools for spotting high temperature high temperature regions.

Differently from the hydrogen chemistry, the methane consumption process involve a more complex pathway associated with lower rates of reaction. The pathway followed by the CH_4 consumption is described by the carbon atom pathway diagram in figure 4.11b.

As shown in the figure, the first step of methane consumption consists in the build-up of the methyl (CH_3) molecule. The early presence of CH_3 in the domain (Fig. 4.4g) is due to the action of three different steps, as evidence by the blue bars in figure 4.10:

$$\mathrm{O} + \mathrm{CH_4} \longleftrightarrow \mathrm{CH_3} + \mathrm{OH} \qquad \text{(R20)}$$

$$\mathrm{H} + \mathrm{CH_4} \longleftrightarrow \mathrm{CH_3} + \mathrm{H_2} \qquad \text{(R39)}$$

$$\mathrm{OH} + \mathrm{CH_4} \longleftrightarrow \mathrm{CH_3} + \mathrm{H_2O} \qquad \text{(R51)} \cdot$$

All those steps describe the abstraction of an atomic hydrogen from the CH_4 molecule by means of H/O/OH radicals. The dehydrogenation step caused by H (R39) in particular, presents the highest rate and the largest extension among reactions controlling CH_4 consumption. All the other reactions, occur within the area described by R39 (Fig. 4.11a).

Along with CH_3, a low presence of HCO is observed in the pre-ignition period (Fig. 4.4h). The destruction of CH_3 to give HCO proceeds mainly through two different branches of the carbon pathway (Fig. 4.11b). The major methyl destruction goes through the middle branch, which describes the CH_3 oxidation into CH_2O followed by HCO formation. As for the H_2/O_2 consumption (R15, R33 and R44) and the methyl build-up (R20, R39 and R51), the methyl destruction advances because of the H/O/OH presence. In particular (Fig. 4.10), the $\mathrm{CH_3}{-}{>}\ \mathrm{CH_2O}$ step (cyan bars) is described by R19, while the $\mathrm{CH_2O}{-}{>}\ \mathrm{HCO}$ one (magenta bars) is described by R41 and R54 as follow:

$$\mathrm{CH_3} + \mathrm{O} \longleftrightarrow \mathrm{CH_2O} + \mathrm{H} \qquad \text{(R19)}$$

$$\mathrm{CH_2O} + \mathrm{H} \longleftrightarrow \mathrm{HCO} + \mathrm{H_2} \qquad \text{(R41)}$$

$$\mathrm{CH_2O} + \mathrm{OH} \longleftrightarrow \mathrm{HCO} + \mathrm{H_2O} \qquad \text{(R54)} \cdot$$

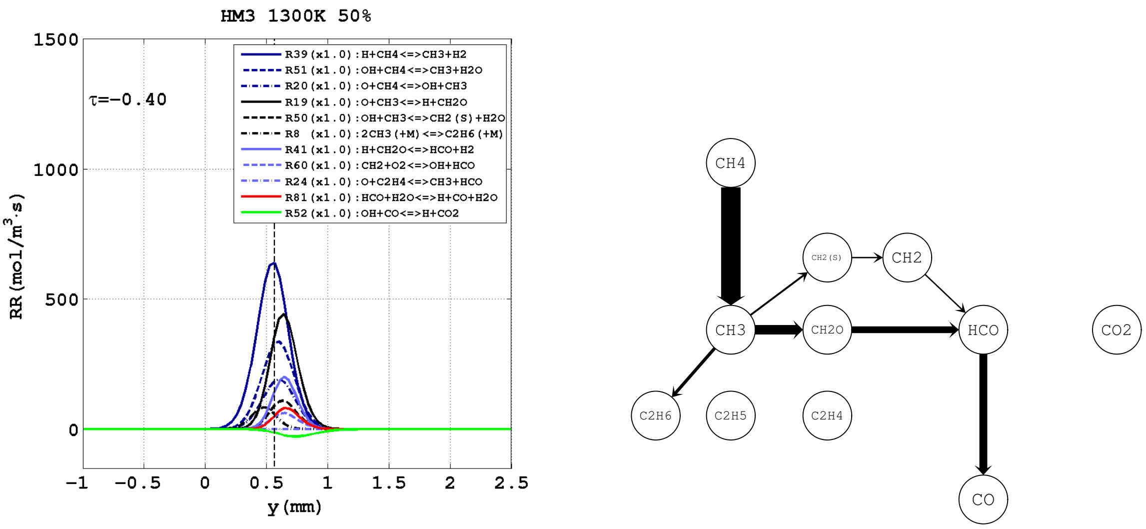

(a) **(b)**

Figure 4.11: Left: Most important rates of reaction of the methane mechanism plotted at $\tau = -0.4$ for the base case. The vertical dashed line represents the position of the stoichiometric mixture fraction region.
Right: Carbon atom pathway diagrams for the base case. Arrows are proportional to the integrated transfer rate of C atoms between species, and normalized with respect to the $CH_4 \rightarrow CH_3$ step. Only arrows at least 5% of the thickest are shown.

Three different processes characterize the upper branch. The methyl molecule is firstly converted in CH_2(S), where CH_2(S) represents the singlet state of methylene. The CH_2(S) molecule is then converted into CH_2 which is then transformed into HCO. Apart from R50 elementary reaction, describing the $CH_3 -> CH_2(S)$ process, the rates of reactions governing the upper branch are particularly low, so that they cannot be caught on figure 4.10. For this reason the equations of reactions describing the upper branch of $CH_3 -> HCO$ process are not presented at this stage.

Similarly, the description of the lower branch of the $CH_3 -> HCO$ process is not provided at this stage since it results incomplete (Only the $CH_3 -> C_2H_6$ step is visible on figure 4.11b). According to figure 4.11b, the methane chemistry is terminated by the production of carbon monoxide (CO) as a consequence of the $HCO -> CO$ process. The two reactions following described are observed controlling the $HCO -> CO$ process at this stage (Fig. 4.10) are:

$$\mathrm{HCO} + \mathrm{H_2O} \longleftrightarrow \mathrm{H} + \mathrm{CO} + \mathrm{H_2O} \qquad \text{(R81)}$$

$$\mathrm{HCO} + \mathrm{O_2} \longleftrightarrow \mathrm{HO_2} + \mathrm{CO} \qquad \text{(R82)} \cdot$$

While an initial presence of CO is observed at $\tau = -0.4$ (Fig. 4.4f), the formation of carbon dioxide is not caught (Fig. 4.4e). This is consistent with the pathway shown on figure 4.11b, where the $CO -> CO_2$ process is missing.

More insights into reactions controlling the pollutants formation can be obtained at ignition time when elementary reactions show an increase in their rates.

4.3 Base case - Point 3

As for the definition given in section 3.3, the ignition event is characterised by a significant temperature rise (25% of the adiabatic temperature). As a consequence, the physical and chemical scenarios present important changes with respect to the pre-ignition period. This investigation point represents a crucial part of the analysis of the selected time range ($\tau \in$[-0.7,0.7]). For this reason, a comprehensive description of the physical chemical phenomena observed at this time is provided.

The initiation of the chemical interaction between fuel and oxidiser observed in the pre-ignition period, is followed by different kinetic processes which are responsible for the release of heat in the domain. As the reactions evolve, the heat release and the temperature (measured through ΔT) both increase. At the ignition time, ΔT is approximately 200K (Fig. 4.2).

The temperature rise cause the gases to expand, as caught by figures 4.3d 4.3e and 4.3f. Here, in the time range around $\tau = 0$, the regions where reactant consumption occurs show an enlargement in both upward and downward direction. In the same time range, figures show an increased rate of both fuels and oxygen consumption, due to the temperature dependence of the kinetic steps describing reactant interaction (Sect. 2.6).

The rate of H_2 consumption remains stronger with respect to CH_4, suggesting a dominant role for the hydrogen chemistry at ignition, as observed in the pre-igntion period.

An interesting aspect outlined by these contour plots is the flame propagation which follow the start of methane and hydrogen reaction mechanisms. As highlighted by fuel consumption paths in figures 4.3d and 4.3e, the regions where both CH_4 and H_2 react evolves spatially in the upward direction in a monotone way till approximately $\tau = 0$. The CH_4 consumption path follows the Z_{st} line, while the H_2 consumption path remains above it. At ignition time both paths present a negative slope and change their position with respect to Z_{st}. The CH_4 path moves below the Z_{st} line (fuel rich area) while the H_2 one is located in the proximity Z_{st}. The presence of the consumption rate peak of both fuels (the H_2 consumption rate peak is observed at ignition while the CH_4 one at a slightly later time) where the paths have negative slopes, highlights a link between the downward propagation of the reacting area and the achievement of the optimal mixing conditions.

Despite the higher rate of consumption, the downward movement and the different position with respect to the Z_{st} line, the physical characterisation of the reaction zone (Fig. 4.12) remains similar to the one observed in the pre-ignition period. The larger availability of H_2 explains the more extended area where hydrogen chemistry occur. On the other hand, because of the lower CH_4 presence, due to differential diffusion, the methane chemistry remains confined in a smaller area within the one spanned by hydrogen chemistry. The blue (R20, R39 and R51) and red (R15 and R44) profiles reinforces the consumption paths in figures 4.3d and 4.3e. The reaction zone moves slightly downward, changing its position with respect to Z_{st}. The consumption of H_2 now occurs in proximity of the stoichiometric mixture fraction region, while the reaction of CH_4 takes place in the fuel rich area ($Z < Z_{st}$).

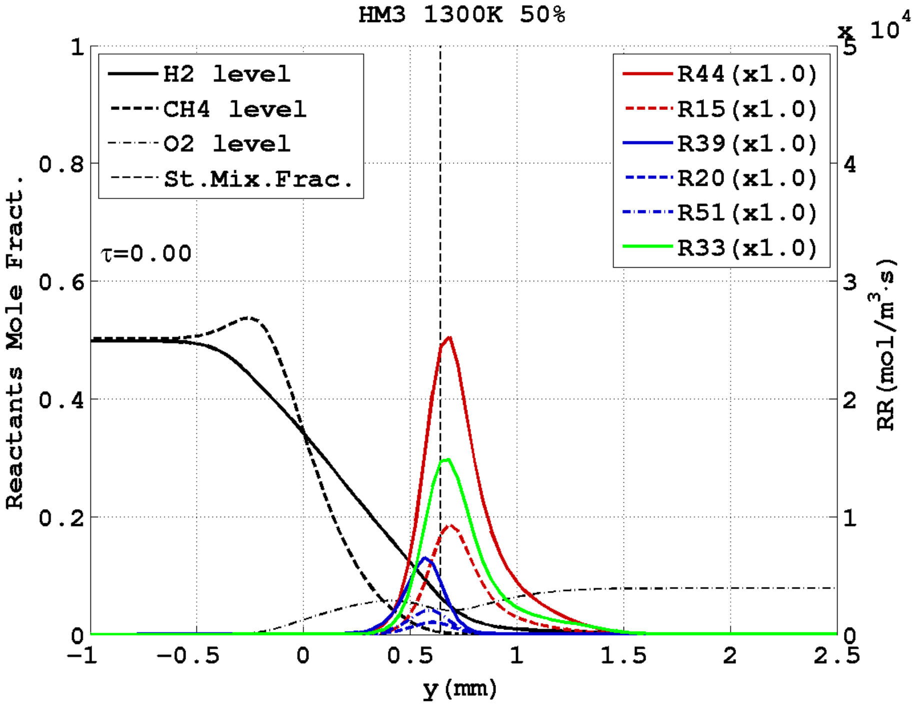

Figure 4.12: Rates of reaction representative of hydrogen (red) and methane (blue) mechanisms plotted against the fuels and oxidiser mole fraction along the cross-stream direction. The graph shows values taken at $\tau = 0$.

It is not only the reactions shown in figure 4.12 which present increased rates with respect to the previous investigation point (Fig. 4.8). An overall enhancement of elementary reaction rates describing the $H_2/CH_4/O_2$ chemical interaction is observed at ignition time. Furthermore, some reactions not previously observed, now show more important roles.

As figure 4.13a shows, the fuel oxidiser interaction remains dominated by H_2-O_2 chemistry with steps R15, R33 and R44 showing the highest rate. These reactions control the build-up of the H/O/OH pool, with the atomic hydrogen still showing the largest presence (Fig. 4.13b, 4.13c and 4.13d).

In the pre-ignition period more reactions were observed describing the consumption of O_2 by means of H radical: R11, R30, R31 and R33, with R33 having the highest rate. In particular it was outlined the role or R11, R30 and R31 steps acting as a H sink to produce the metastable HO_2 molecule. At ignition time it is possible to appreciate the temperature dependence of the hydroperoxyl molecule bonds, which tend to cleavage at higher temperature. As figures 4.14a, 4.14b and 4.14c show, a local minimum in the profiles can be observed evolving in time in the y∈[0.5,1] range. This spatial range corresponds to the area where a temperature higher than the initial 1300K is present (Fig. 4.3a), confirming the unstable behaviour of HO_2 when the temperature rises. Furthermore, since this spatial range corresponds to the part of the reaction region where mainly hydrogen combustion is observed (Fig. 4.12), the first major exothermic event can be mainly associated with the H_2-O_2 interaction.

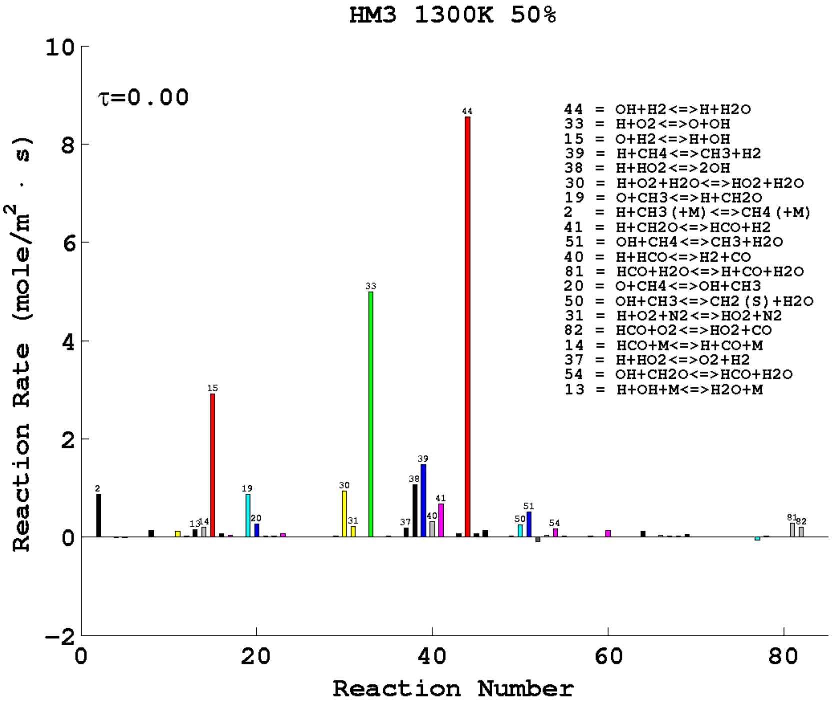

(a)

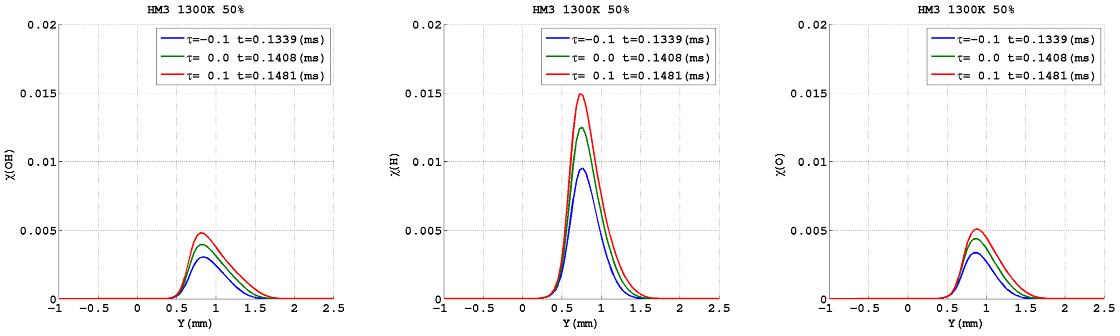

(b) OH **(c)** H **(d)** O

Figure 4.13: Top: Rates of reaction of the DRM19 mechanism integrated along the cross-stream (y) direction. The reaction rates of the base case at $\tau = 0$ are shown.
Bottom: Formation of OH (left), H (middle) and O (right) radical pool at τ=-1, 0 and 0.1

Along with a general enhancement of reaction rates describing its consumption process (Fig. 4.15a), the methane mechanism presents some similarities and some differences with respect to the previous point of analysis.

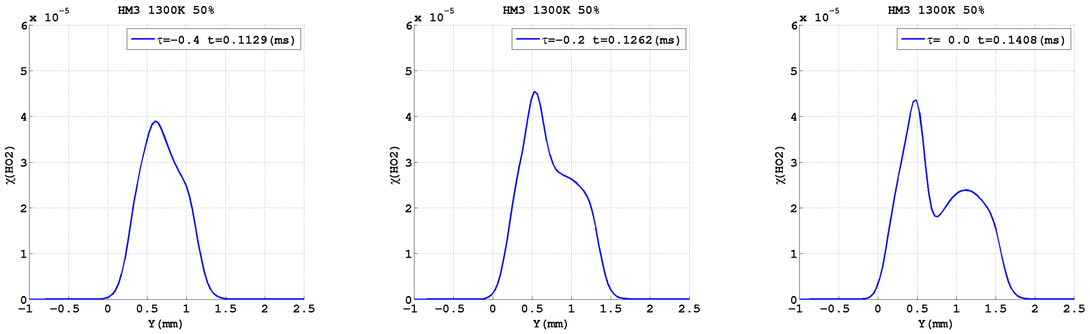

(a) $\tau = -0.4$ **(b)** $\tau = -0.2$ **(c)** $\tau = 0.0$

Figure 4.14: Mole fraction of the hydroperoxyl molecule plotted as a function of the spatial coordinates. Figures from left to right show the evolution in the pre-ignition period of the HO_2 presence, outlining a local minimum in the profile developing in the range y∈[0.5,1] range.

The methyl build-up evolves along the methane consumption path below Z_{st} (Fig. 4.4g). It remains controlled by R39, R51 and R20 where the H activated step (R39) presents the highest rate. Within the area spanned by methyl production processes, all the major steps controlling the CH_4 consumption process occur (Fig. 4.15a). The different paths followed by methyl destruction are shown on figure 4.15b, where the additional information regarding the number of carbon atoms transferred along the various paths is present. Similarly to the pre-ignition period, the methyl destruction proceeds mainly through the $\mathrm{CH_3}{-}{>}\ \mathrm{CH_2O}{-}{>}\ \mathrm{HCO}$ path via R19, R41 and R54, with the R41 step, H activated, showing a significant rate increase (Fig. 4.15a) with respect to point 2 (Fig. 4.11a). The CH_3 conversion along the top branch of the methane pathway remains limited, as well as limited is the CH_3 recombination into the C_2 form described by the bottom branch (Fig. 4.15b).

Almost 80% of the methane destroyed is converted into CO [2]. Together with R81 and R82, two more processes contribute to the $\mathrm{HCO}{-}{>}\ \mathrm{CO}$ process (Fig. 4.13a):

$$\mathrm{HCO} + \mathrm{M} \longleftrightarrow \mathrm{H} + \mathrm{CO} + \mathrm{M} \tag{R14}$$

$$\mathrm{H} + \mathrm{HCO} \longleftrightarrow \mathrm{H_2} + \mathrm{CO} \tag{R40} \cdot$$

While the common final step of the methane oxidation process ($\mathrm{CO}{-}{>}\ \mathrm{CO_2}$) is not described by the carbon atom pathway, confirming the absence of steps with significant rate describing the CO oxidation, figure 4.15b shows instead the consumption of the CO_2 molecule ($\mathrm{CO_2}{-}{>}\ \mathrm{CO}$). This unusual aspect will be analysed in more details along with the investigation of the fourth time point.

---

[2] The fraction of CH_4 destroyed is referred to the part of methane that takes part in chemical reactions.

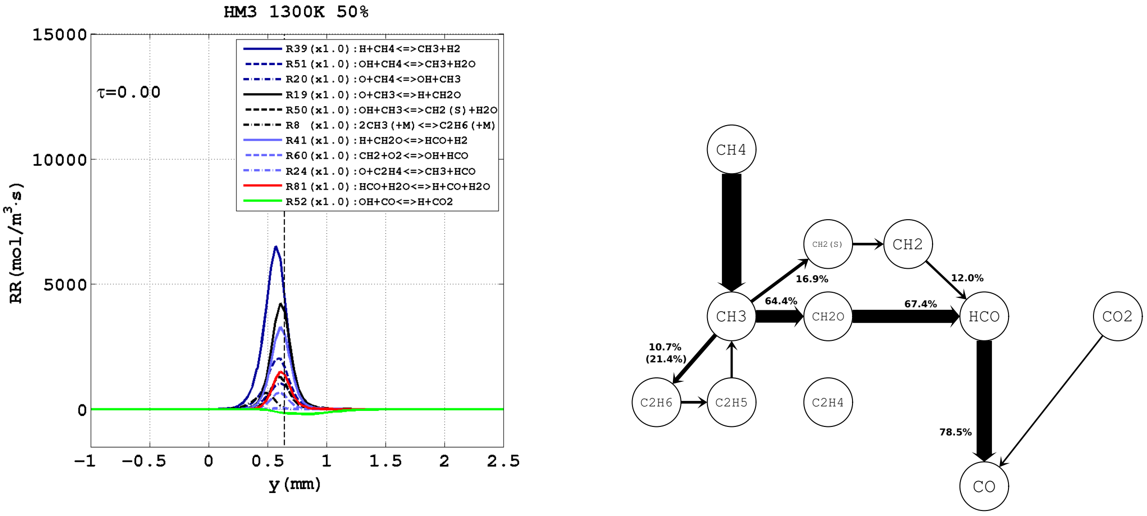

(a) **(b)**

Figure 4.15: Left: Most important rates of reaction of the methane mechanism plotted at $\tau = 0.0$ for the base case. The vertical dashed line represents the position of the stoichiometric mixture fraction region.
Right: Carbon atom pathway diagrams for the base case. Arrows are proportional to the integrated transfer rate of C atoms between species, and normalized with respect to the $CH_4 \rightarrow CH_3$ step. Percentages indicate the number of carbon atoms transferred along the various paths, relative to the number of CH_4 atoms destroyed. Percentages are rounded to the upper decimal digit (+0.1%). Only arrows at least 5% of the thickest are shown.

4.4 Base case - Point 4

After ignition, a series of important events modify the physical and chemical scenario of the reaction zone. As the chemical reactions evolve, the oxygen level in the reaction zone drops significantly (Fig. 4.16a, 4.16b and 4.16c). At $\tau = 0$ the O_2 level is down by 40%, down by 85% at $\tau = 0.4$ and down by 95% at $\tau = 0.7$, when the oxygen depletion stops in the area considered and the reaction region moves upward towards higher y. Together with the reduction of the oxygen level, is observed a general reduction in reaction rates (described in more details later in this section), a reduction of the temperature gradient (the rise of ΔT over time) and a repositioning of the consumption paths with respect to the mixture fraction space. This set of changes tend to stabilise once an equilibrium between diffusion and reaction is reached.

The point 4 is used to investigate the influence of the O_2 depletion on the kinetics of fuel consumption and to analyse changes in the physical development of the reaction zone which can affect the access to O_2.

The analysis of the reaction zone (Fig. 4.17) provides evidence of some characteristics of the flame in the post-ignition period.

The first interesting aspect regards the position of the reaction zone with respect to the Z_{st} line. At ignition time the propagation of the reaction zone towards the fuel rich region was observed, highlighted by the negative slope of both consumption paths. The hydrogen chemistry was observed evolving along the Z_{st} line, while the methane chemistry was observed staying below it (Fig. 4.12). After ignition, both paths move below Z_{st} (Fig. 4.3d and 4.3e) regaining for $\tau > 0.2$ an ascending trend [3]. Furthermore, for $\tau > 1.5$ onward, both areas where H_2 and CH_4 are being consumed, keep a constant distance to Z_{st} and show almost constant consumption rates (Fig. 4.3d and 4.3e). This indicates a diffusion-reaction equilibrium for both fuels [4].

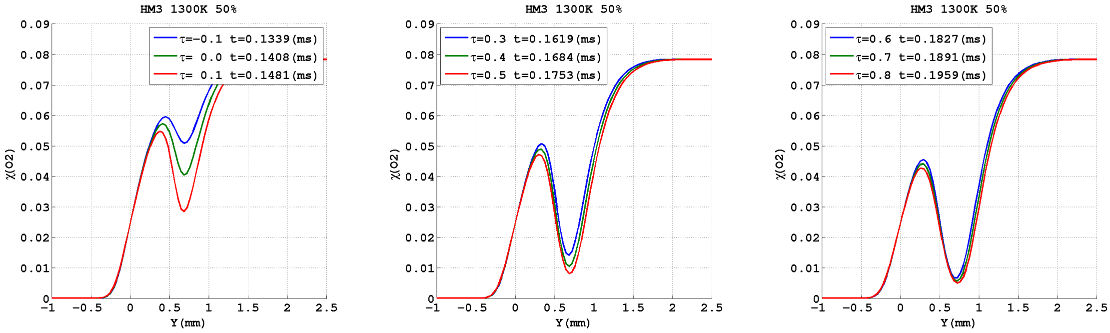

(a) $\tau = 0.0$ **(b)** $\tau = 0.4$ **(c)** $\tau = 0.7$

Figure 4.16: Evolution of the oxygen level in the reaction zone for the post-ignition period. Figures show the O_2 mole fraction plotted against space at $\tau = 0.0$ (left), $\tau = 0.4$ (middle) and $\tau = 0.7$ (right).

A second interesting aspect noted is the separation of the fuel paths, which appears more pronounced in the post-ignition period. As in fact figures 4.3d and 4.3e show, while the H_2 consumption reaches its peak rate immediately after ignition, the CH_4 consumption shows the peak rate at later time. This corresponds to the later time at which the CH_4 consumption path regains an upward motion. As a result, a larger displacement among fuel consumption paths is observed after the ignition. This displacement will give the final shape to the flame front. The explanation of the late CH_4 consumption peak will provided later in this section.

The relative displacement among fuel paths highlights another point of interest: methane and hydrogen chemistry is occurring in areas with different O_2 concentrations. As figures 4.3d and 4.3e clearly shows, the H_2 consumption occur mostly above CH_4 destruction region for the whole ignition period considered ($\tau \in$[-0.7,2.5]). Once the O_2 depletion become significant (dark blue region on figure 4.3f), the larger H_2 presence close to the oxidiser (Fig. 4.17) allows hydrogen chemistry to have privileged access to O_2. The methane chemistry on the other hand, located in the fuel rich region below H_2 consumption path, starves in a low oxygen area.

---

[3] It should be noted that the observed ascending motion of the reaction zone is due to the gas expansion as a consequence of the high temperature. The gases flow thorough the outflow boundary set up in the top of the numerical domain.

[4] More precisely, for $\tau > 1.5$ a constant rate of consumption is observed only for H_2 fuel, while the methane consumption rate tends to decrease with time. This is due to the starvation of the methane chemistry in a low oxygen area which is described later on this section.

The kinetic analysis coupled with insights from the observation of the reaction zone provides a better picture of the set of changes observed in the post-ignition period.

A general reduction of the rates of reaction is shown by the bar chart on figure 4.18a. Since the rates reduction is observed when the reaction zone locates below Z_{st} (the fuel/oxidiser mixture is oxygen deficient), it is possible to state that the O_2 depletion is the rate limiting factor. Furthermore, since the O_2 consumption is controlled by R33, this step can be considered as the rate limiting step.

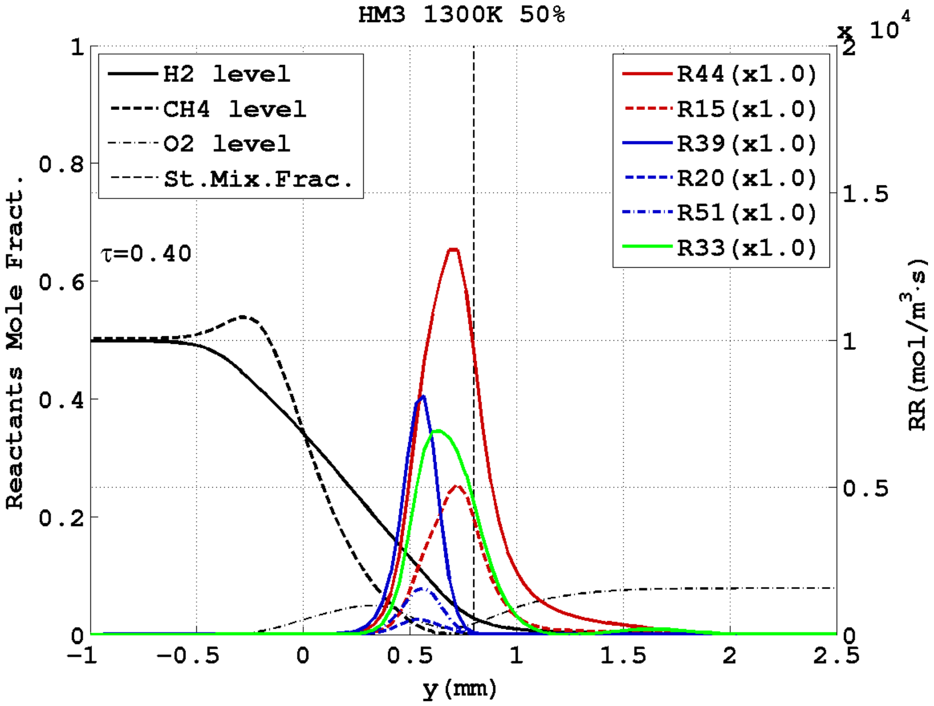

Figure 4.17: Rates of reaction representative of hydrogen (red) and methane (blue) mechanisms plotted against the fuels and oxidiser mole fraction along the cross-stream direction. The graph shows values taken at $\tau = 0.4$.

The chemical scenario presents a substantially unchanged role of the hydrogen chemistry, while the methane consumption process showing important variations. The larger H_2 presence close to the oxidiser (Fig. 4.17) explains the major role of H_2-O_2 chemistry. The steps R15, R33 and R44 present the highest rates and control the H/O/OH pool formation. As figures 4.18b, 4.18c and 4.18d show, the growth of H, O and OH level is arrested in the post-ignition. Nonetheless, the presence of atomic hydrogen remains dominant in terms of level and spatial extension.

Because of O_2 depletion, the R33 step, which showed to be highly sensitive to the H presence, presents a strong reduction of its rate (approximately half the rate observed at ignition time). Since the excess of H (Fig. 4.18c) is similar in quantity to ignition time, other H activated steps like R2, R39, R30 and R52 are enhanced (Fig. 4.18a).

The reaction R39 in particular, keeps a rate as high as at ignition time (Fig. 4.13a). This makes

R39 the controlling reaction in CH_4 dehydrogenation process. Therefore, the late methane consumption peak, aforementioned, which determine the displacement among fuel paths (Fig. 4.3d), could be then explained by the excess of atomic hydrogen which enhance the R39 rate. Moreover, the intense action of R39 also explains the significant H_2 production shown by the dark blue area along CH_4 consumption path on figure 4.3e.

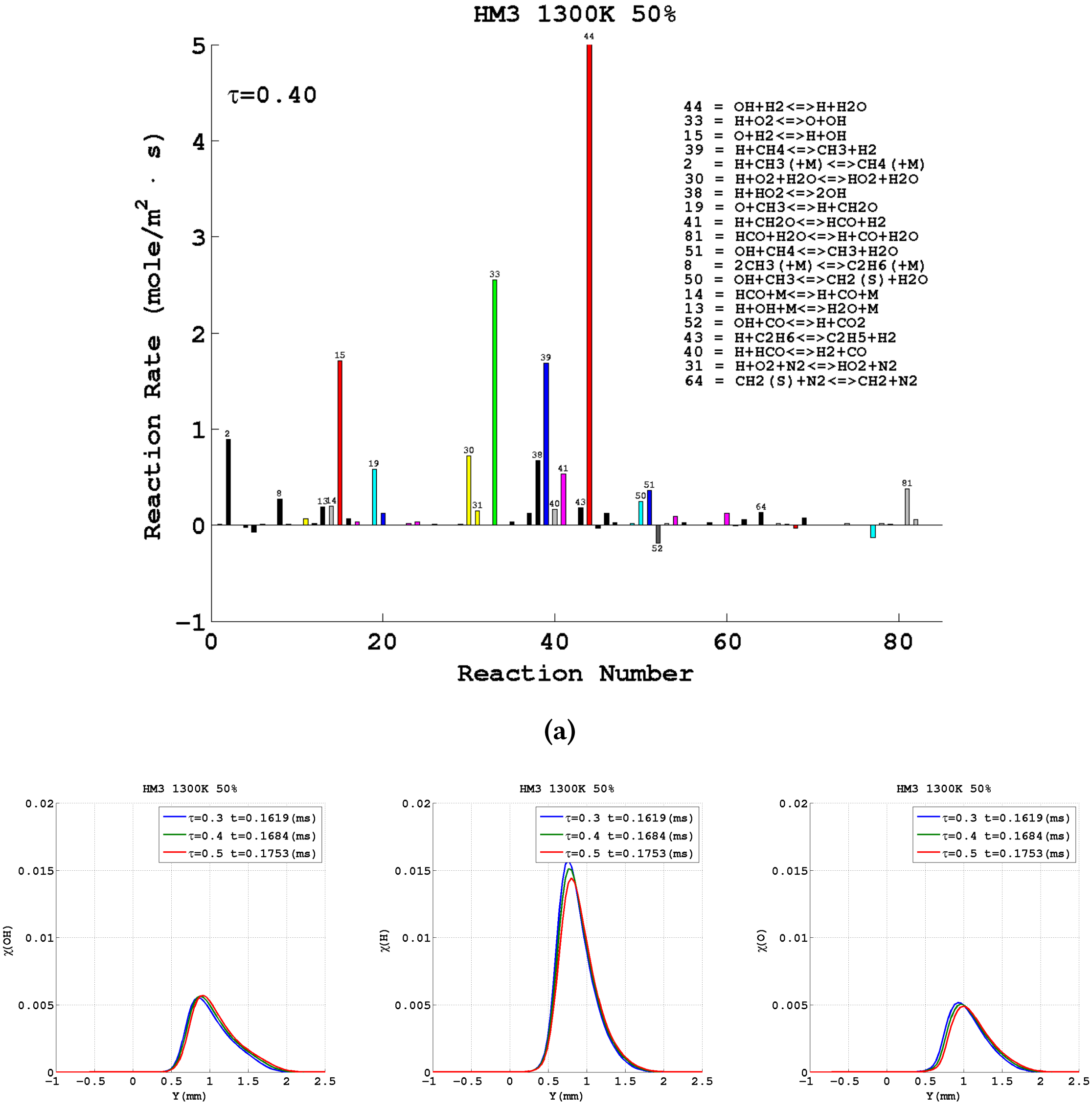

(a)

(b) OH **(c)** H **(d)** O

Figure 4.18: Top: Rates of reaction of the DRM19 mechanism integrated along the cross-stream (y) direction. The reaction rates of the base case at $\tau = 0.4$ are shown.
Bottom: Formation of OH (left), H (middle) and OH (right) radical pool in the post-ignition period.

The build-up of CH_3, evolves along the methane consumption pathway (Fig. 4.4g) and is consumed according to the three branch pathway shown of figure 4.19b.

While the upper branch presents a methyl conversion rate similar to the one observed at ignition time, it is interesting to note that, as the chemistry of methane evolves under fuel-rich conditions, the reaction of CH_3 with with O is less competitive and the central path is no longer dominant. As a consequence, a significant part of methyl produced is recombined and feed into the more stable C_2H_6 (ethane). This particular behaviour is know in literature and has been explained by Kee *et al.* [27]. Differently from what is described in literature, the C_2 hydrocarbons proceed through a series of hydrogen abstractions, C_2H_5 (ethyl group) and C_2H_4 (ethene), but there is no significant oxidation of C_2H_4. The observed lack of oxygen in the region where CH_4 is consumed, may represents a potential explanation. As a result of the reduced importance of the central path, there is a reduced conversion of CH_3 into HCO and, consequently, a relatively lower rate of CO production.

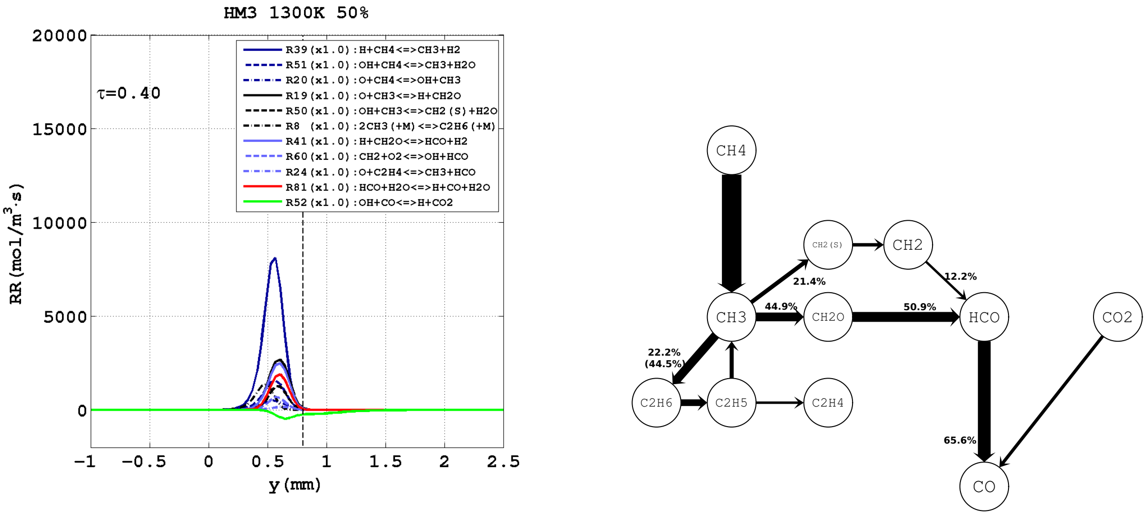

(a) **(b)**

Figure 4.19: Left: Most important rates of reaction of the methane mechanism plotted at $\tau = 0.4$ for the base case. The vertical dashed line represents the position of the stoichiometric mixture fraction region.
Right: Carbon atom pathway diagrams for the base case. Arrows are proportional to the integrated transfer rate of C atoms between species, and normalized with respect to the $CH_4 \rightarrow CH_3$ step. Percentages indicate the number of carbon atoms transferred along the various paths, relative to the number of CH_4 atoms destroyed. Percentages are rounded to the upper decimal digit (+0.1%). Only arrows at least 5% of the thickest are shown.

The CO production is not only due to the HCO conversion. The carbon atom pathway in fact, catches the same unusual $CO_2 -> CO$ process observed at ignition time. Consistently with the pathway, the bar chart on figure 4.18a do not show any CO_2 production step having a significant rate. Conversely, the R52 step, proceeding backward, presents a low but significant rate. A complete picture of all reactions responsible for CO_2 production/destruction included in the DRM19 mechanism is provided on figure 4.20a. Here it is clearly shown that R52 step controls the CO_2 destruction, and that all reactions describing CO_2 production have negligible rates [5]. The strong resemblance between the contours of CO_2 production rate (Fig. 4.20b) and the contour of R52 rate (Fig. 4.20c) represents an additional confirmation. Because of the

---

[5] In addition it is possible to note a modest rate of R74 step, which also describes CO_2 destruction

low rate of CO_2 production, it is likely that the carbon dioxide consumed originates from the oxidiser blend.

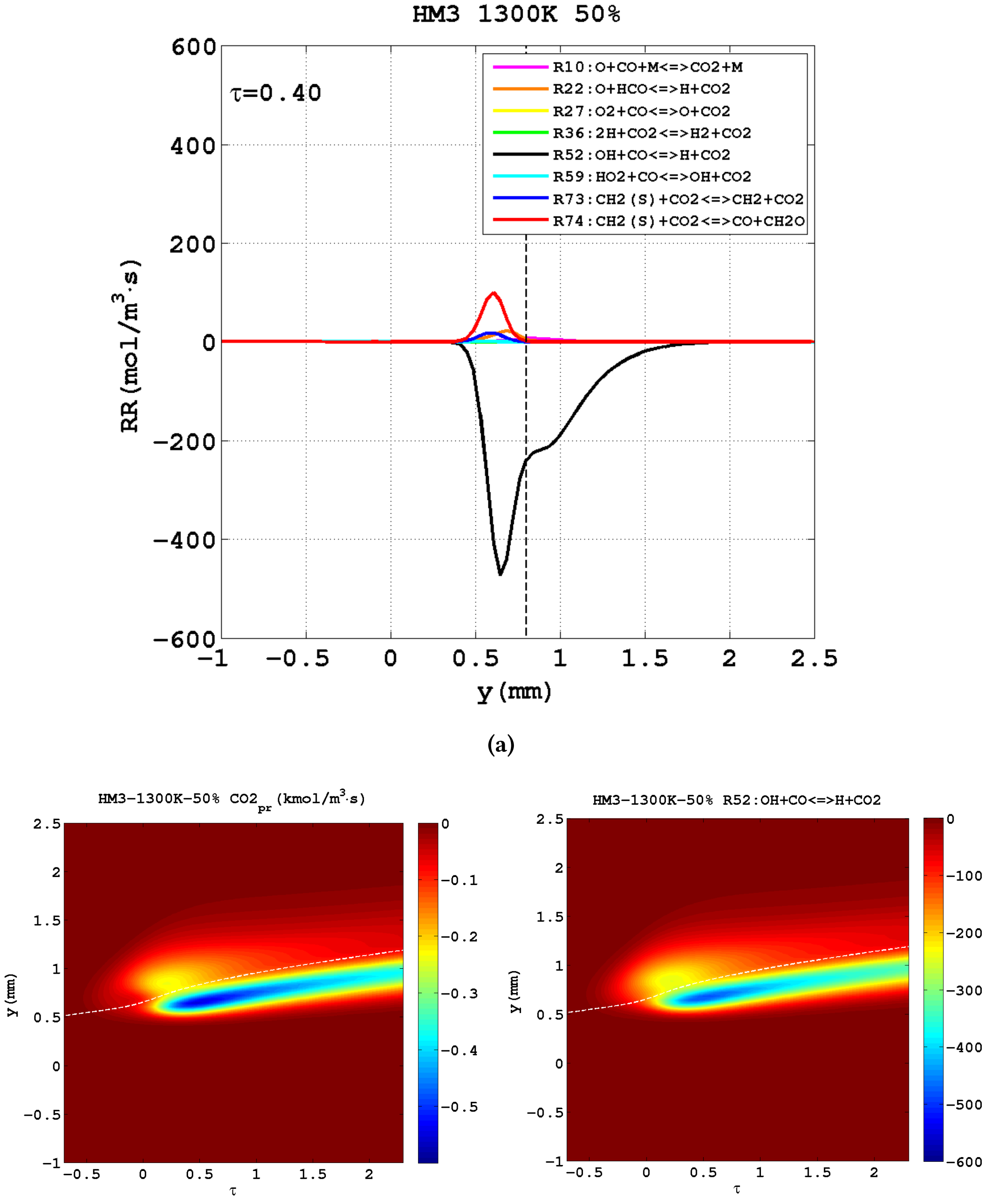

(a)

(b) (c)

Figure 4.20: Top: Rates of reaction form the DRM19 mechanism describing the CO_2 productio/destruction. The reaction rates of the base case at $\tau = 0.4$ are shown.
Bottom: Contour of the CO_2 production rate (left) and R52 step rate (right). The scale on the right contour express the rate of reaction in $\mathrm{mole/m^3 \cdot s}$.

It is interesting to note that the R52 elementary reaction occurs in a wide region spanning over the whole reaction zone (Fig. 4.20a). The highest rate of R52 is observed below Z_{st} (Fig. 4.20c) enclosed by the methane and hydrogen consumption paths (Fig. 4.4b), where the highest temperatures are reached 4.3a). The lowest rate of R52, identified by a bulge in the contours on figures 4.20b and 4.20c, are observed above Z_{st}, where lower temperatures occur. This identifies the temperature as a potential cause that limits or enhance the rate of CO_2 consumption but does not explain what causes the carbon dioxide destruction. The explanation can be found in the analysis of R52 kinetic equation described as follow:

$$\mathrm{OH} + \mathrm{CO} \longleftarrow \mathrm{H} + \mathrm{CO_2} \qquad \text{(R52)} \cdot$$

The equation clearly highlight the important role of atomic hydrogen in pushing the R52 step in the backward direction. The larger level H into a broader area, with respect to OH radical which would move the reaction in the forward direction, support this hypothesis.
As observed for the R39 step, this shed lights on the important role of atomic hydrogen once the oxygen is significantly depleted.

4.5 Base case - Point 5

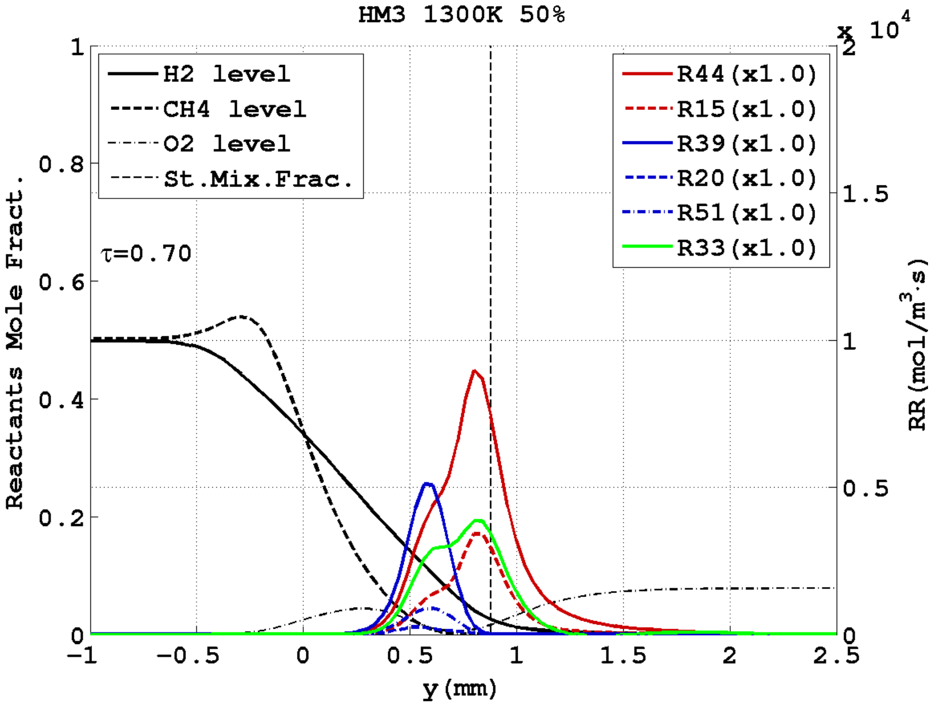

Figure 4.21: Rates of reaction representative of hydrogen (red) and methane (blue) mechanisms plotted against the fuels and oxidiser mole fraction along the cross-stream direction. The graph shows values taken at $\tau = 0.7$.

The last time point analysed is on the upper right end of temperature rise curve, where ΔT profile has significantly flattened (Fig. 4.1). It is used to investigated the main features of the reaction zone once combustion has started. At this time, the oxygen is almost completely consumed in the reaction zone and the flame front moves upward in the domain, where more O_2 is available (Fig. 4.16c). Differences with respect to the previous time point are thoroughly described while similarities are briefly mentioned.

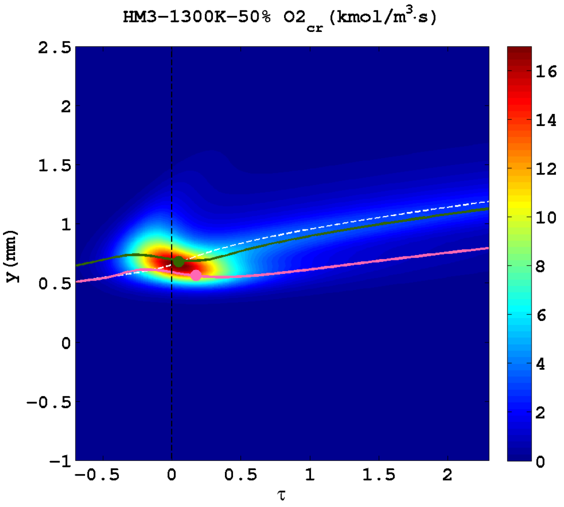

(a) O_2 rate of consumption

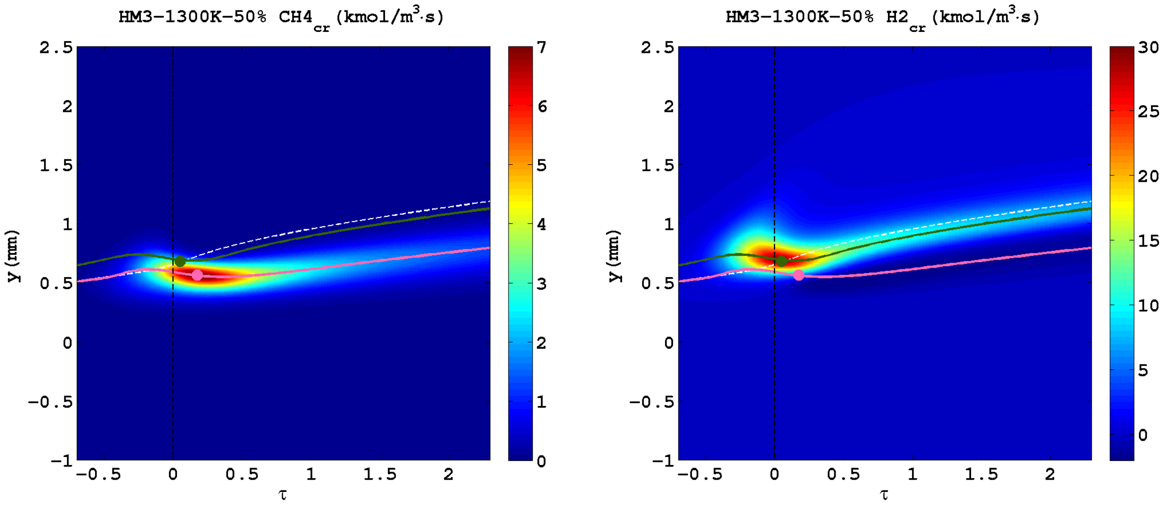

(b) CH_4 rate of consumption

(c) H_2 rate of consumption

Figure 4.22: Evolution of the O_2 (top), CH_4 (bottom-left) and H_2 (bottom-right) rates of consumption in along the considered period of time.

As with the previous points, the analysis start with an investigation of the reaction zone, shown in figure 4.21. The reaction zone remains positioned mainly below the stoichiometric mixture fraction line, where it will remain for the whole post-ignition period.

The larger presence of H_2 in the reaction zone explains the high rate of R15 and R44 steps and the larger area over which they occur. On the other hand, because of the lower CH_4 diffusion rate, the methane chemistry presents a reduced extension, closer to fuel layer and more distant from Z_{st}.

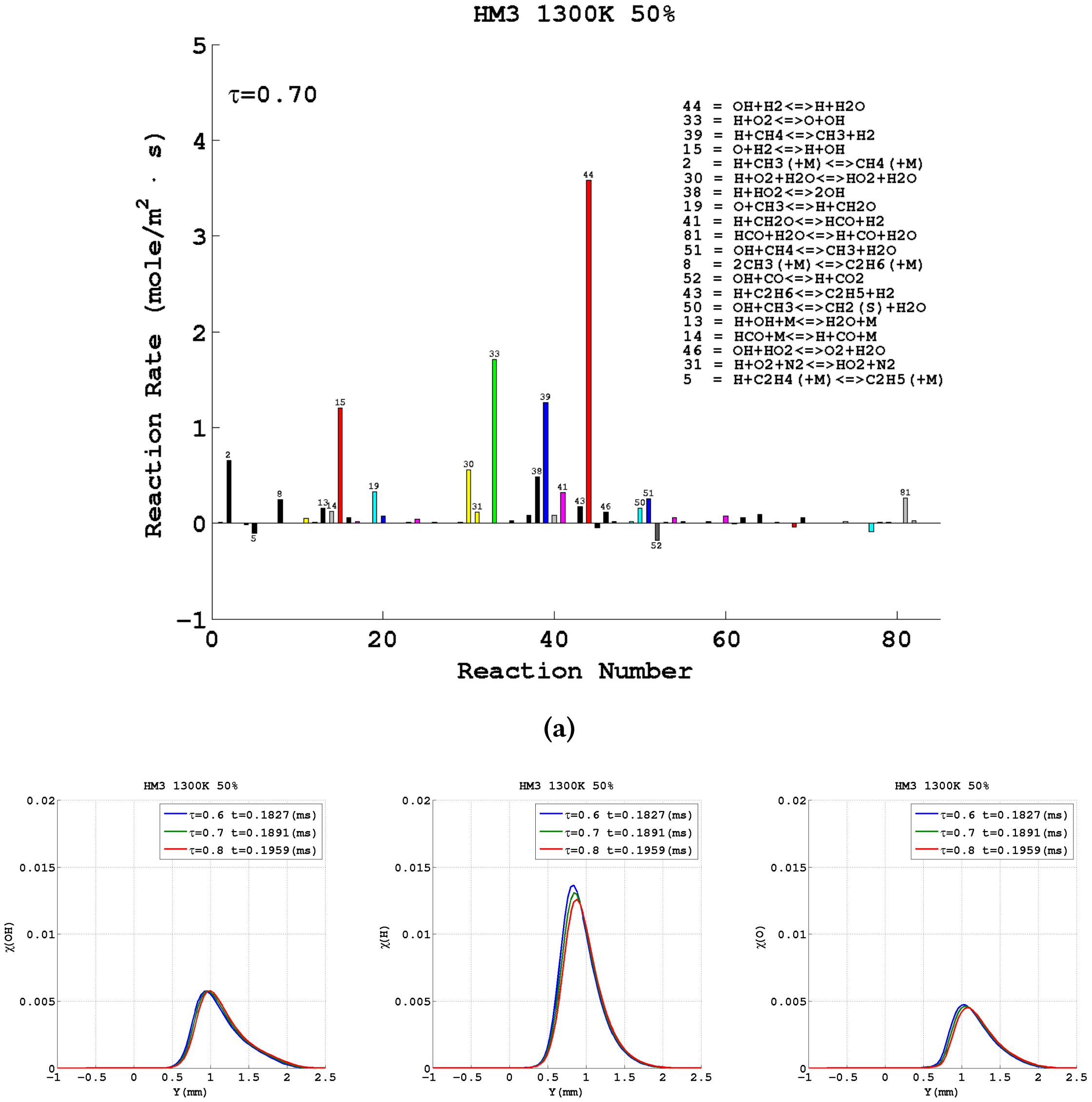

(a)

(b) OH **(c)** H **(d)** O

Figure 4.23: Top: Rates of reaction of the DRM19 mechanism integrated along the cross-stream (y) direction. The reaction rates of the base case at $\tau = 0.7$ are shown.
Bottom: Formation of OH (left), H (middle) and OH (right) radical pool in the post-ignition period.

The low concentration of O_2 is outlined by the black dash dotted profile in the reaction zone. The oxygen depletion area follows the reaction zone, which moves upwards where there is a larger O_2 availability (Fig. 4.16c).

The disadvantaged location of CH_4 chemistry, briefly mentioned during the point 4 analysis, is outlined by R15, R33 and R44 profiles, representing the H_2-O_2 chemical interaction. As figure shows, the green and red profiles present a double peak trend. The higher peaks locate close to Z_{st} region, where there is a higher O_2 availability and a reduced H_2 presence. Conversely, the lower peaks are observed at a larger distance from Z_{st}, closer to the fuel layer. Here, more H_2 is present, while the O_2 level is reduced. This highlight a lack of O_2 because, despite the large H_2 availability, the hydrogen consumption results limited. In the same area where H_2 consumption is limited, the CH_4 consumption occurs.

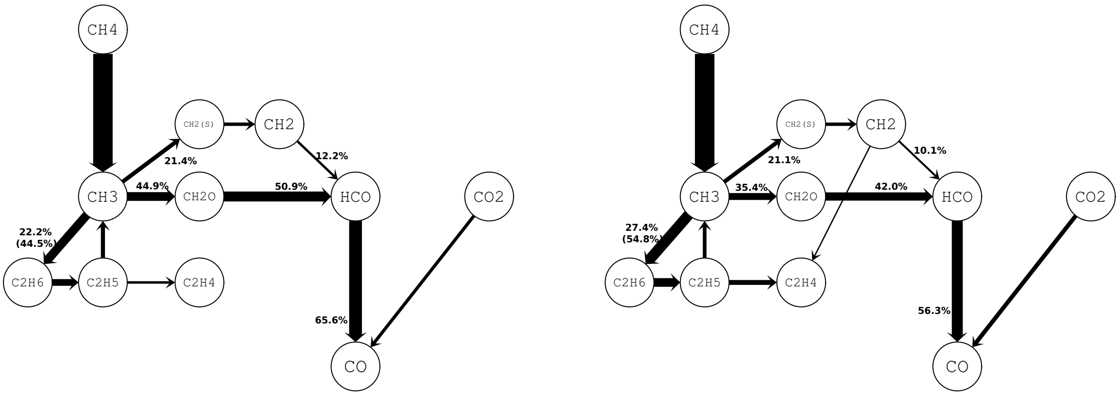

(a) $\tau = 0.4$ **(b)** $\tau = 0.7$

Figure 4.24: Comparison of the carbon atom pathway diagrams for the base case at $\tau = 0.4$ (left) and $\tau = 0.7$ (right). Arrows are proportional to the integrated transfer rate of C atoms between species, and normalized with respect to the $CH_4 \rightarrow CH_3$ step. Percentages indicate the number of carbon atoms transferred along the various paths, relative to the number of CH_4 atoms destroyed. Percentages are rounded to the upper decimal digit (+0.1%). Only arrows at least 5% of the thickest are shown.

The starvation process experienced by the CH_4 chemistry after ignition is also caught by the reactants consumption rate contours (Fig. 4.22a, 4.22b and 4.22c). In the pre-ignition period ($\tau \in$[-0.7;0]), the resemblance between O_2 and H_2 consumption rate contours, outline the dominant role of the H_2 chemistry in consuming oxygen. In the post-ignition period ($\tau \in$[0;0.7]), the O_2 consumption rate contour evolves in a double branch fashion. The upper branch follows the hydrogen consumption path, while the bottom branch follows the methane one. It is possible to observe that, while the upper branch shows for $\tau > 0.7$ a constant rate of O_2 consumption, a more and more reduce O_2 consumption is revealed along the CH_4 path. In a way similar, the CH_4 consumption rate contour presents a constantly reduced rate of methane consumption in the post-ignition period, while the H_2 consumption rate shows an almost constant trend from $\tau = 0.7$ onwards.

The analysis of processes involved in the methane consumption allows parts of CH_4 consumption pathway affected by the lack of oxygen to be identified. This is done by comparing the carbon atom pathways taken at $\tau = 0.4$ and $\tau = 0.7$ (Fig. 4.24a and 4.24b). The comparison sheds light on the reduced CH_3 oxidation along the middle branch of the methane pathway and, as a consequence, on the reduced conversion of CH_3 into HCO. Conversely the CH_3 recombination assumes an even higher importance at $\tau = 0.7$, even though a significant oxidation of the C_2 species is not observed. Because the $\mathrm{CH_3}{->}$ HCO conversion through the upper branch of the methane pathway is mainly unchanged, the final HCO production is reduced with respect to the previous time point. As a result, only the 56% of the consumed CH_4, results converted into CO. As for $\tau = 0.4$, a partial contribution to the CO production comes from the carbon dioxide consumption via R52.

4.6 Base case - Conclusions

The base case investigates the diffusion-chemistry interaction, under MILD conditions, of two layers of fuel and oxidiser initially separated. The oxidiser, which initially occupies the top half of the domain, is a blend of O_2 , N_2, H_2O and CO_2 at 1300K. The fuel, locating in the bottom half of the domain, is defined as an equimolar mixture of methane and hydrogen at 305K.

The layers self-ignition process is investigated by analysing the physical and chemical scenarios observed at selected time points, spanning over the computed ignition period. Two points are selected before ignition and two points after ignition. The computed ignition time ($\sim$0.14ms) represents an additional point of analysis.

The analysis showed differential diffusion playing a major role in the pre-ignition period. As a consequence of its higher diffusion rate, a larger H_2 presence is observed close to the stoichiometric region. Here, earliest reactions are observed and the flame front starts developing. The flame front outlines two different paths along which methane and hydrogen are being predominantly consumed: the hydrogen path is closer to the oxidiser layer while methane is located below it. Differences are also observed in the chemistry of both fuels: the H_2 chemistry is dominant, since the earliest part of ignition period. It represents the major cause of oxygen consumption and controls the formation of the H/O/OH radical pool.

As the flame front propagates towards the fuel rich part of the domain, a general increase of reaction rates is observed. After ignition, the equilibrium among diffusion and reaction of reactants is observed and the flame front occupies its final position mostly below Z_{st}. The strong oxygen depletion observed after ignition causes an overall reduction of reaction rates. Because of their different spatial displacement, the CH_4 and H_2 mechanisms are affected differently by the lack of O_2. While the upper position in the flame front of the hydrogen chemistry corresponds to a higher O_2 concentration, the lower position of the methane chemistry cause its starvation in a low oxygen area. The investigation of the CH_4 consumption pathway outlines that the $\mathrm{CH_3} -> \mathrm{CO}$ process is particularly affected. The CH_3 oxidation is partially inhibited while the methyl recombination into the C_2 form is more important.

The dominant presence of atomic hydrogen in the radical pool is a common aspect observed over the whole ignition period. It explains the strong methyl production via R39 and the unusual CO_2 destruction when combustion is started.

Chapter 5

1D Study - Effect of oxygen reduction

The study presented in chapter 4 explored the self-ignition process of the base case, the most reactive configuration within the range of cases studied. The self-ignition followed the interaction between a fuel layer, an equimolar mixture of methane and hydrogen, and an oxidiser layer, a $O_2/N_2/H_2O/CO_2$ blend containing 9% by mass of oxygen.

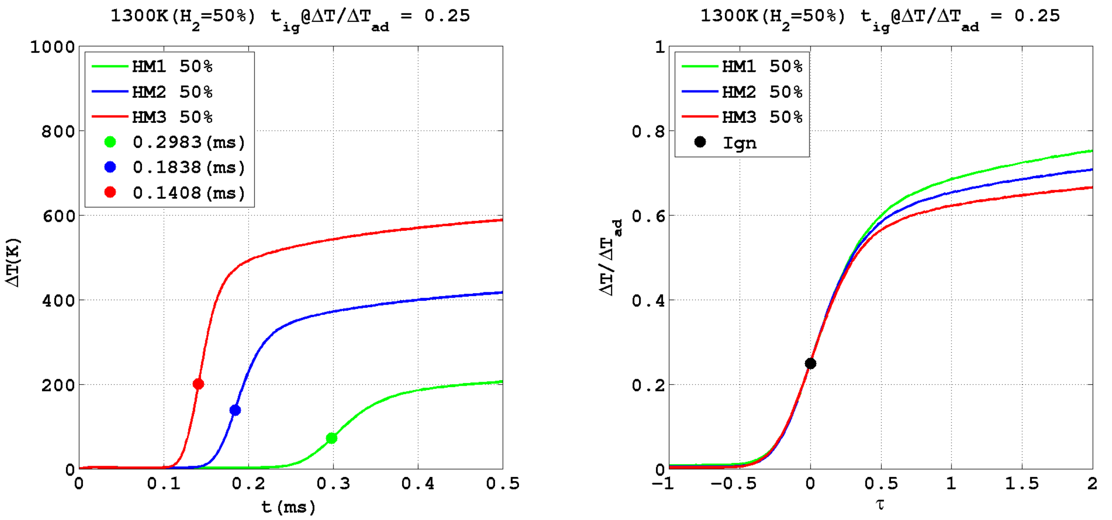

(a) **(b)**

Figure 5.1: Left: Evolution in time of the temperature rise for cases with different oxygen dilution levels. The circles represent the ignition, calculated as the time at which the 25% of the adiabatic temperature is reached.
Right: Comparison of the temperature rise curves for different level of oxygen dilutions. The profiles are presented normalised on both axis according to technique described in section 3.3.3.

The investigation is now expanded to cases where the hydrogen addition in the fuel is kept constant, while the oxygen level in the oxidiser is reduced. More precisely, the present study compares the base case with HM2-50% and HM1-50% configurations having respectively 1.5 and 3 times less oxygen in the oxidiser blend. The reduction in oxygen is balanced by increasing the N_2 presence in the oxidiser, as described in table 3.1. In this section, since the hydrogen concentration is fixed at 50%, the three cases analysed will be often referred as HM1, HM2 and HM3 or, more simply, *dilution cases*.

One of the key points that arose from the previous chapter was the major impact of the O_2 level in controlling and limiting rates of reaction that describe the fuel/oxidiser interaction. In more detail, an overall reduction of reaction rates and the flattening of the of the temperature increase (ΔT) over time were observed, as a consequence of the significant O_2 depletion in the reaction zone.

A first look at temperature rise profiles obtained for different oxygen dilution confirms the insights from the base case. The oxygen level and flame temperature appear strongly linked. In the HM2 case, with 1.5 times less oxygen than the HM3 case, the ΔT is approximately 1.5 times lower. Similarly in the HM1 case, with 3 times less O_2, ΔT is reduced by approximately three times (Fig. 5.1a). Also the ignition time is affected by the oxygen dilution. With respect to HM3 case, the self-ignition takes approximately 1.3 times longer in the HM2 case and approximately 2 times in the HM1.

In order to help in investigating and comparing the role of the oxygen dilution in HM1, HM2 and HM3 cases, the temporal normalization (Sect. 3.3.3) is used as a tool to appropriately select five time points for further study. As figures 5.1b shows, the ignition period of the three cases, once normalised, remains enclosed within the [-0.7,0.7] τ range. The temperature rise curves collapse nicely in the τ $\in$[-0.7,0.5] range, while a small displacement is observed for τ >0.5. This allow for a choice of investigation points consistent with the base case (τ=-0.7, -0.4, 0.0, 0.4 and 0.7). As shown on figures 5.2a, 5.2b and 5.2c, the selected points cover appropriately, in each dilution case, the ignition period, respecting the set of qualitative rules given in the base case chapter.

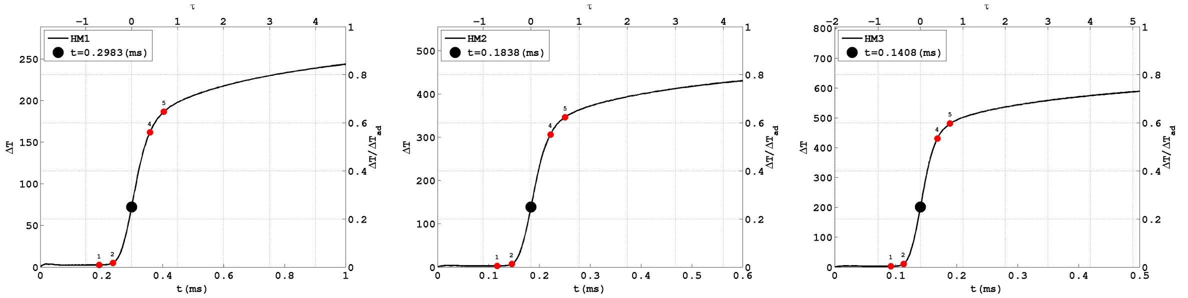

(a) HM1 **(b)** HM2 **(c)** HM3

Figure 5.2: Temperature rise (ΔT) plotted against time for the HM1 (left), HM2 (middle) and HM3 (right) case. Each graph is presented on a double axis to account for the temperature ($\Delta T/\Delta T_{\mathrm{ad}}$) and time ($\tau$) normalisation. The five circles overlaying each curve represent the points at which the physical and chemical properties of each configuration are investigated.

As shown in the base case, the characterisation of the MILD regime across the different time points is often supported by the analysis of the space-time contour plots. A similar approach will be used in this section, with the difference that the contour plots will be compared to observe differences between the dilution cases. As a consequence of the delayed ignition, reactants in HM1 and HM2 take longer, with respect to HM3 case, to diffuse along cross-stream direction (y) before being consumed, making comparison among contour plots more difficult. This is clearly shown of figures 5.3a and 5.3b, which outline the higher location of the oxygen consumption area in the case of increased O_2 dilution.

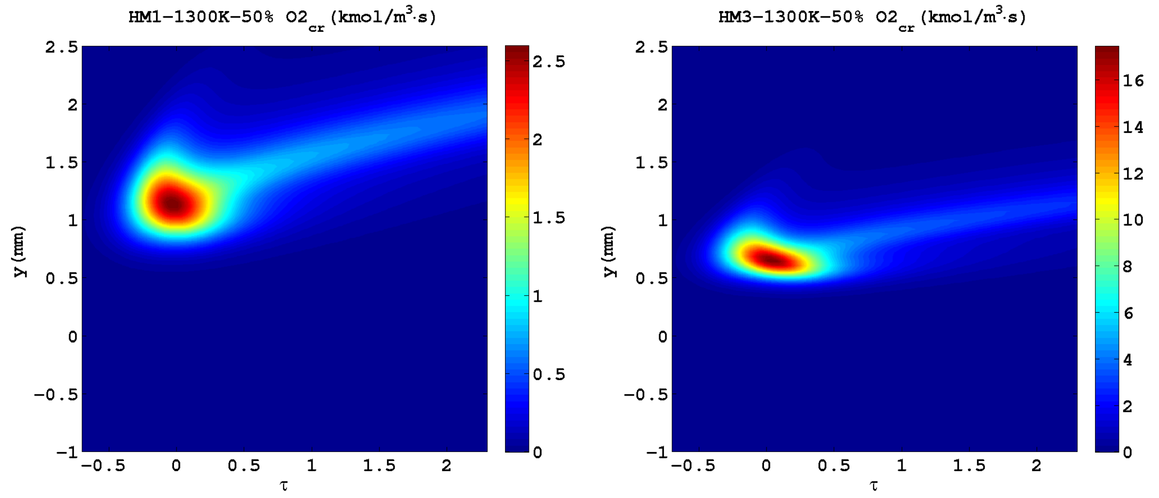

(a) HM1

(b) HM3

Figure 5.3: Evolution of the oxygen consumption rate for the HM1 (left) and HM3 (right) case. Because of the longer upward diffusion of reactants, HM1 field locates at a higher position of the computational domain.

In order to account for this diffusion, the cross-stream direction (y) was normalised as follow:

$$\eta = \frac{y - y_0}{y_0}. \tag{5.1}$$

The parameter y_0 locates the peak of the oxygen consumption rate. It is used in the numerator to center each field in the area where oxygen consumption reaches its maximum rate, and, in the denominator, as a scaling factor which squashes or stretches the field. Higher the y_0 value, wider is assumed the reactants diffusion into the oxidiser.

The space normalisation, along with the time normalisation are applied on each contour. The time period of interest ($\tau \in$[-0.7,0.7]) is entirely included within the τ range described by the contours. With the purpose of simplifying the thesis structure, the whole set of fields used (temperature, species consumption/production rate, species mole fraction and intermediates mole fraction) is following shown (Fig. 5.4 - 5.8). During the analysis, these figures will be referred to as required.

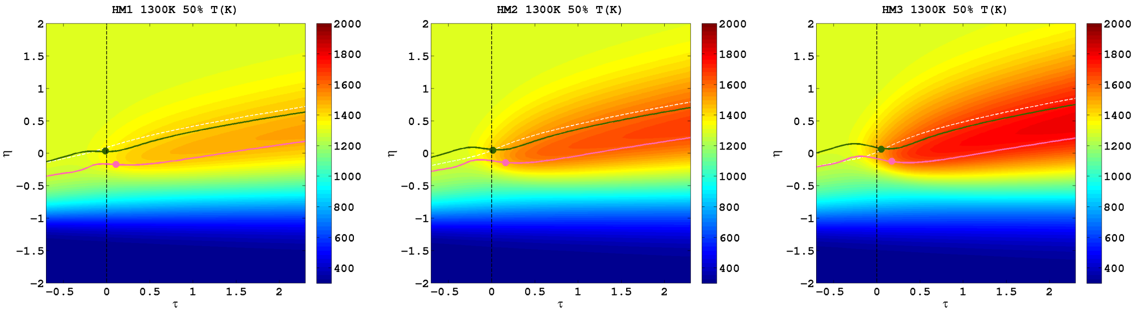

(a) HM1 **(b)** HM2 **(c)** HM3

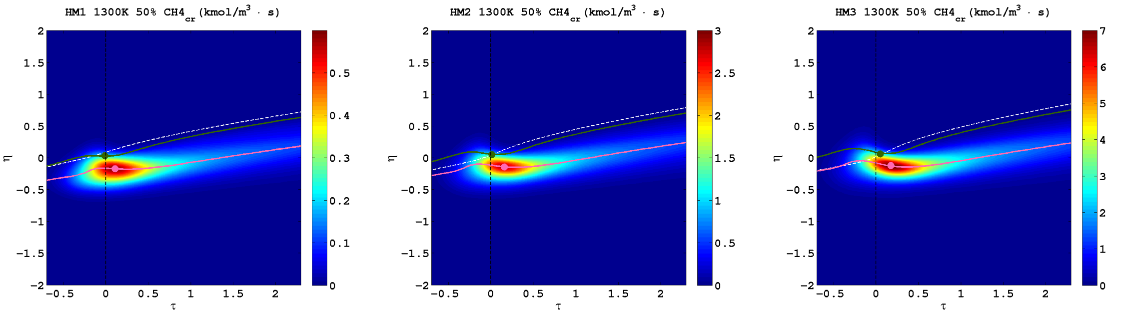

(d) HM1 **(e)** HM2 **(f)** HM3

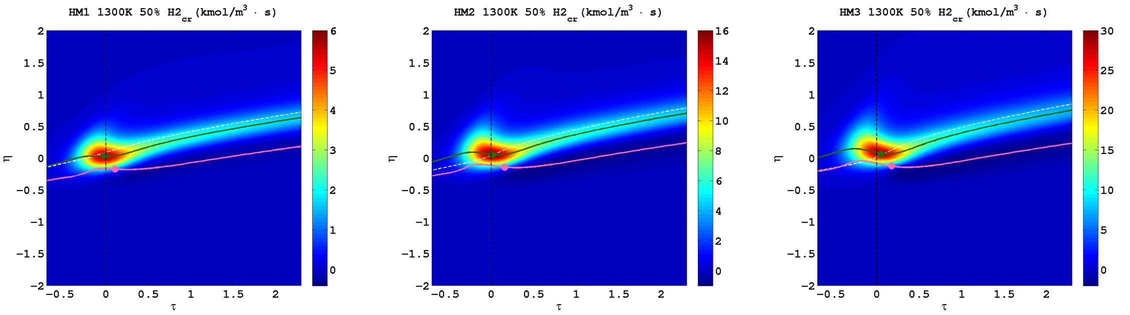

(g) HM1 **(h)** HM2 **(i)** HM3

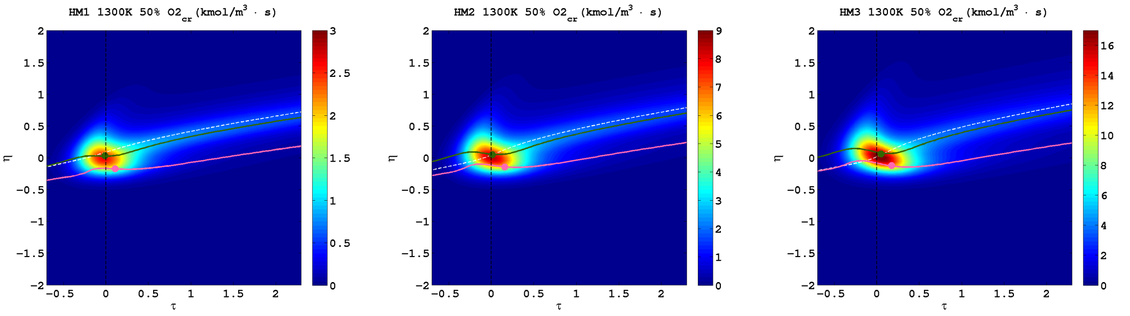

(j) HM1 **(k)** HM2 **(l)** HM3

Figure 5.4: Comparison of the temperature (first row), methane consumption rate (second row), hydrogen consumption rate (third row) and oxygen consumption rate (fourth row) fields for the HM1 (left), HM2 (middle) and HM3 (right) cases. Fields are presented normalised on both axis.

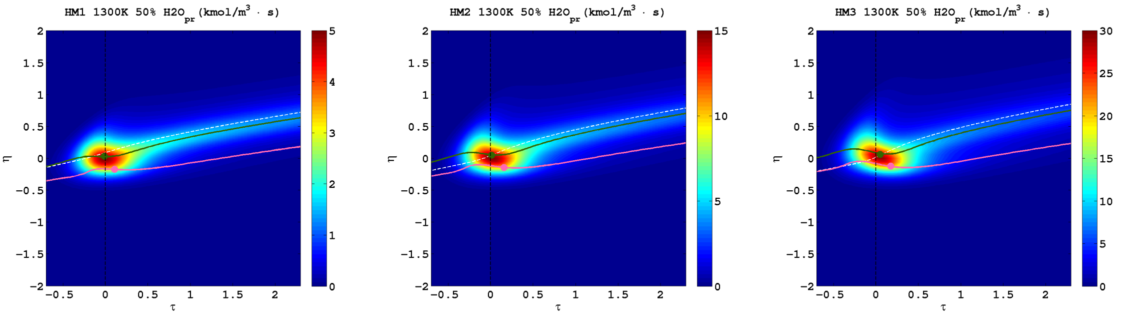

(a) HM1 **(b)** HM2 **(c)** HM3

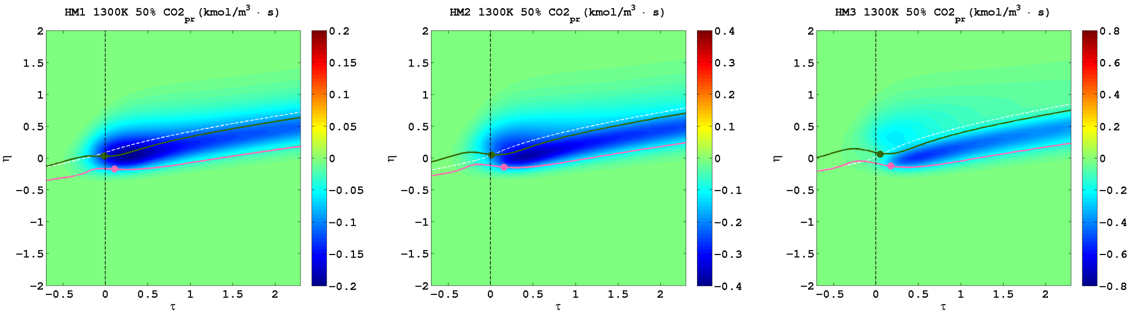

(d) HM1 **(e)** HM2 **(f)** HM3

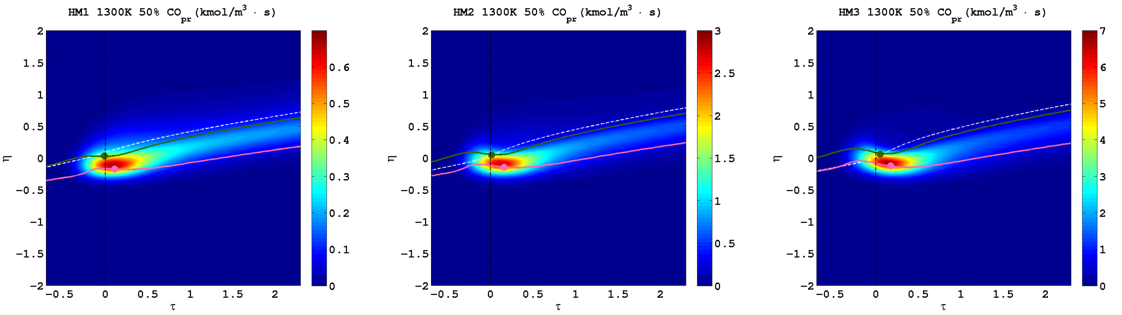

(g) HM1 **(h)** HM2 **(i)** HM3

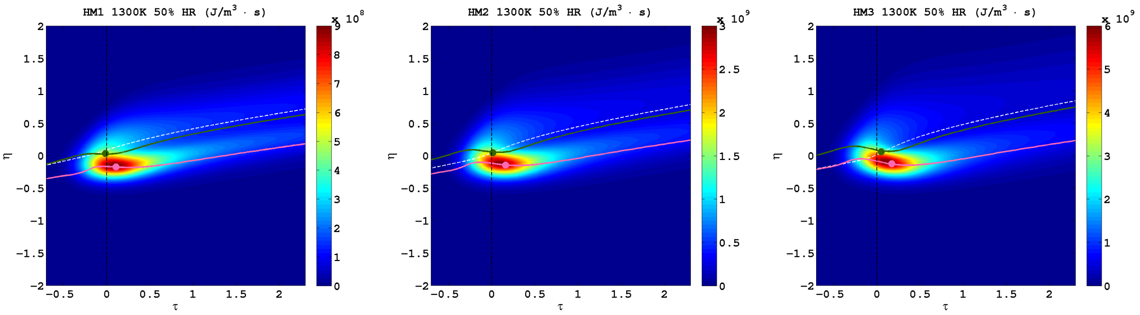

(j) HM1 **(k)** HM2 **(l)** HM3

Figure 5.5: Comparison of the water production rate (first row), carbon dioxide production rate (second row), carbon monoxide production rate (third row) and heat release (fourth row) fields for the HM1 (left), HM2 (middle) and HM3 (right) case. Fields are presented normalised on both axis.

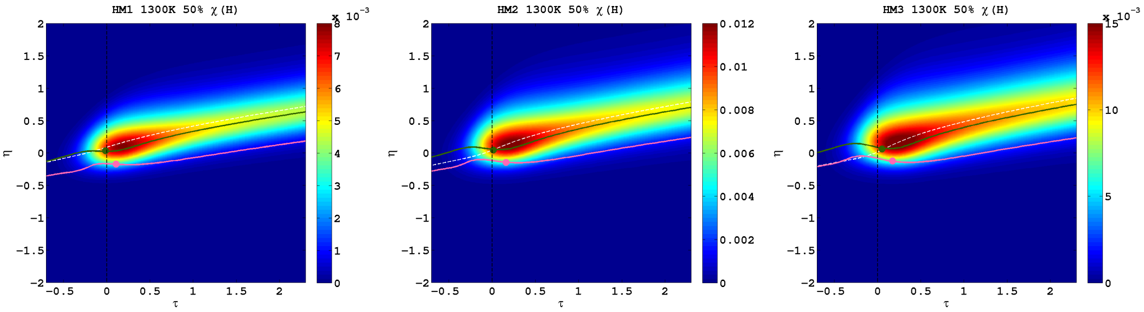

(a) HM1 **(b)** HM2 **(c)** HM3

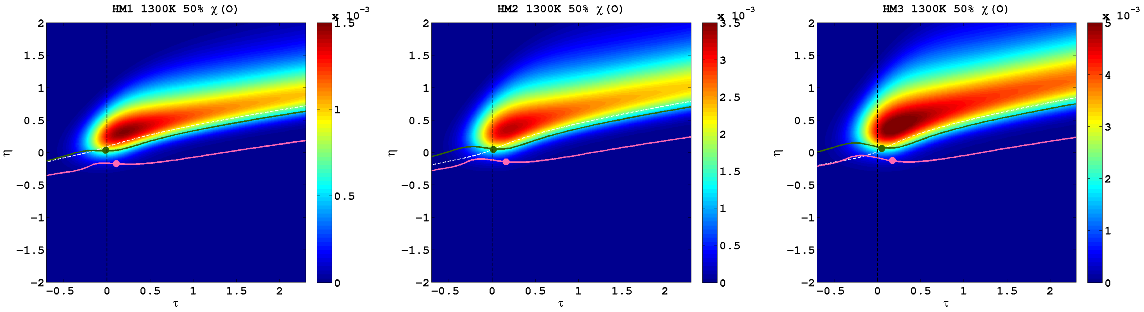

(d) HM1 **(e)** HM2 **(f)** HM3

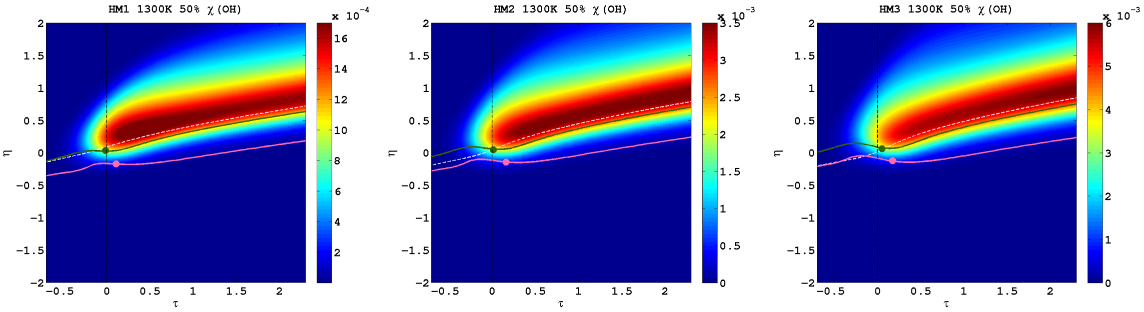

(g) HM1 **(h)** HM2 **(i)** HM3

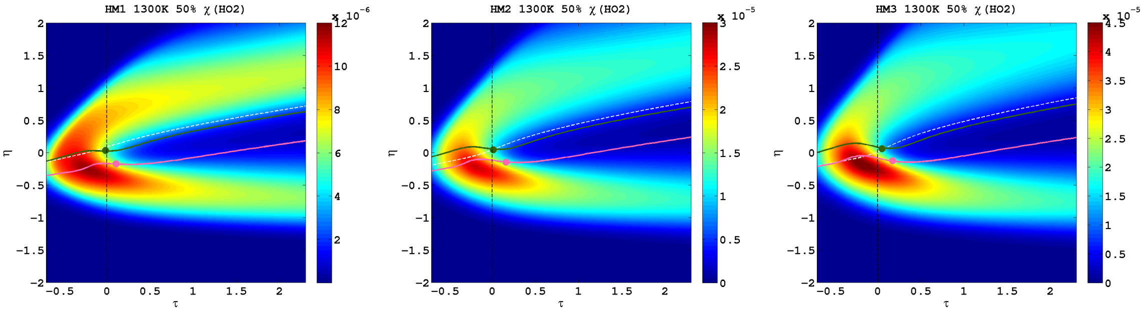

(j) HM1 **(k)** HM2 **(l)** HM3

Figure 5.6: Comparison of the atomic oxygen (first row), atomic hydrogen (second row), hydroxyl radical (third row) and hydroperoxyl radical (fourth row) mole fraction fields for the HM1 (left), HM2 (middle) and HM3 (right) case. Fields are presented normalised on both axis.

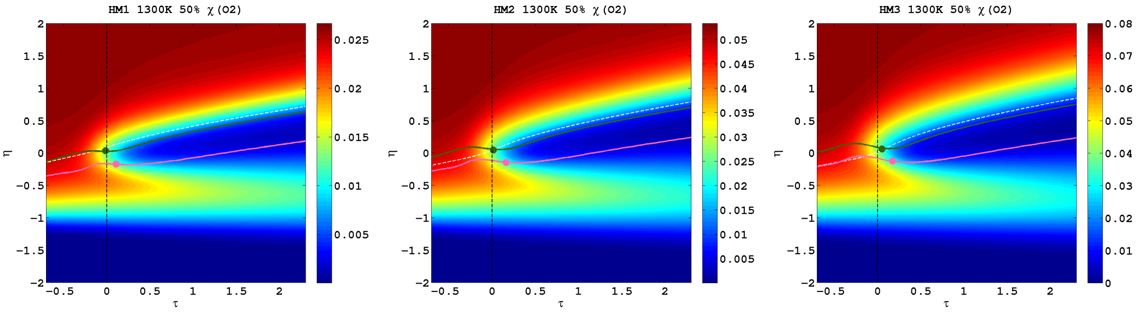

(a) HM1 **(b)** HM2 **(c)** HM3

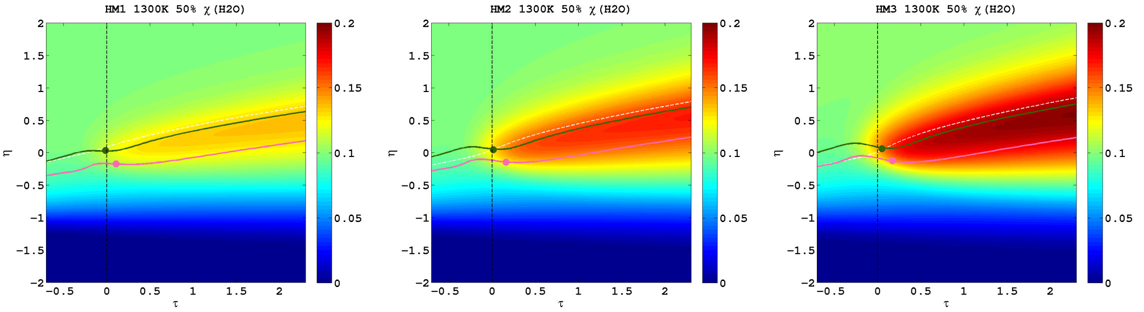

(d) HM1 **(e)** HM2 **(f)** HM3

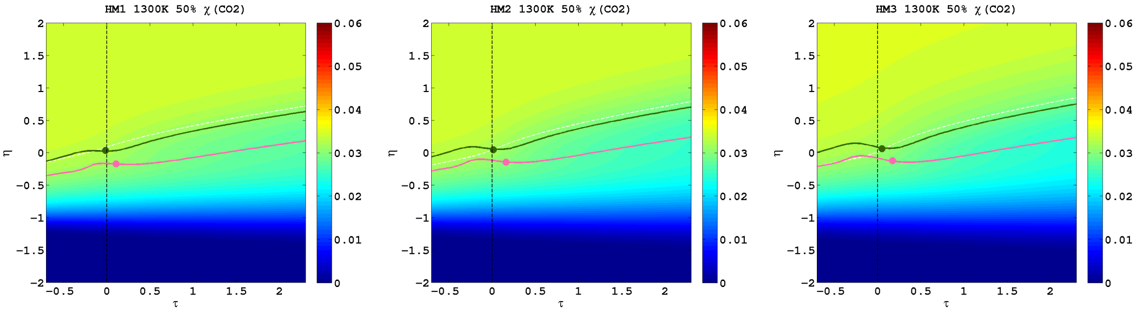

(g) HM1 **(h)** HM2 **(i)** HM3

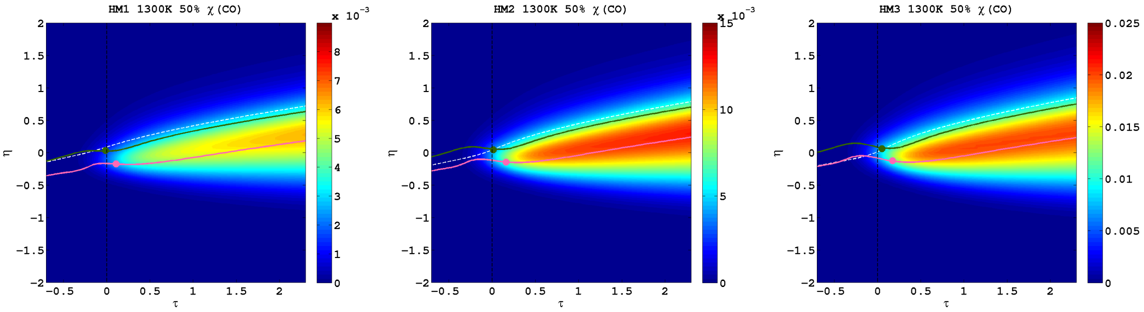

(j) HM1 **(k)** HM2 **(l)** HM3

Figure 5.7: Comparison of the oxygen (first row), water (second row), carbon dioxide (third row) and carbon monoxide (fourth row) mole fraction fields for the HM1 (left), HM2 (middle) and HM3 (right) case. Fields are presented normalised on both axis.

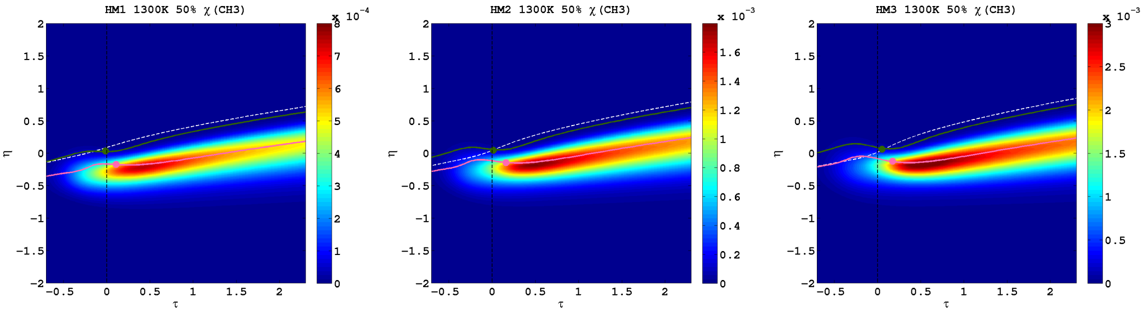

(a) HM1 **(b)** HM2 **(c)** HM3

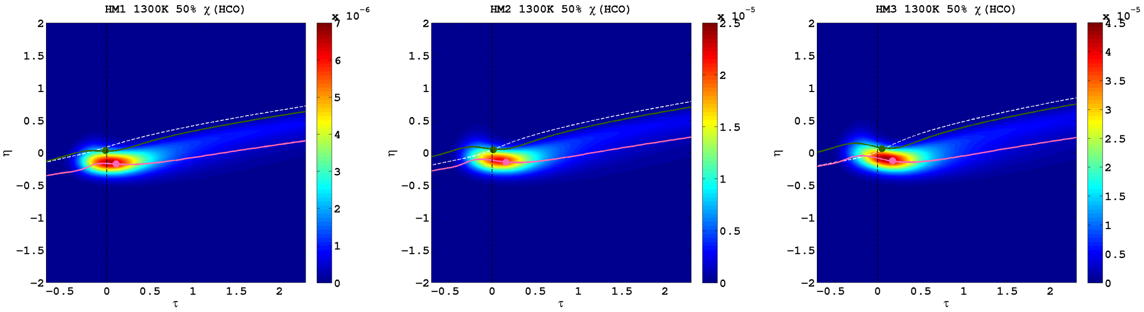

(d) HM1 **(e)** HM2 **(f)** HM3

Figure 5.8: Comparison of the methyl (first row) and aldehyde (second row) mole fraction fields for the HM1 (left), HM2 (middle) and HM3 (right) case. Fields are presented normalised on both axis.

5.1 Effect of oxygen reduction - Point 1

In the base case description, the first point of analysis was used to focus the analysis on the diffusion processes preceding the ignition. This was because of the low temperature rise at τ=-0.7 (Fig. 5.2c), which indicated a negligible chemistry role, and the steep species gradient at the fuel/oxidiser interface, which highlighted the important role of diffusion. The HM2 and HM1 cases have the same geometrical set-up [1] and show a similar low temperature rise at τ=-0.7 (Fig. 5.2a and 5.2b), suggesting that similar processes are occurring.

The important role of differential diffusion was observed in the base case with the H_2 diffusing more than CH_4 in the oxidiser. The HM1 and HM2 case present different oxidiser blends which could potentially affect the diffusion scenario presented in the HM3 case. As such, the presence of the methane and hydrogen in the mixture fraction space is investigated also for the low oxygen configurations. The analysis (Fig. 5.9), remains focused in the $Z \in [0.1 \cdot Z_{\mathrm{st}}, 7 \cdot Z_{\mathrm{st}}]$ range , where ignition is most likely to occur. This is demonstrated in figures 5.10a and 5.10b which clearly show that the heat released along the ignition process remain enclosed by $Z = 0.1 \cdot Z_{\mathrm{st}}$ and $Z = 7 \cdot Z_{\mathrm{st}}$ iso-lines.

---

[1] The fuel and oxidiser layers are initially separated with steep species gradient at the interface.

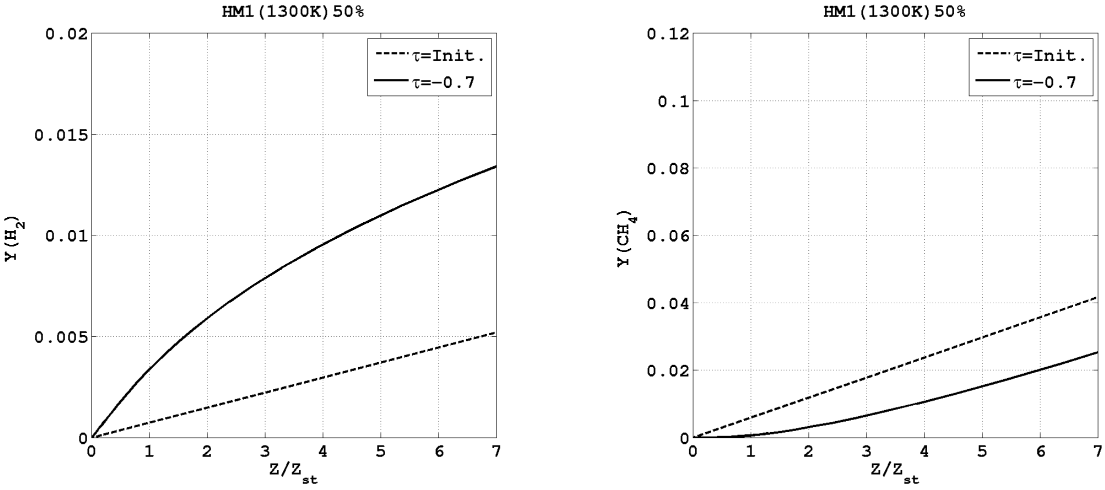

(a) HM1 **(b)** HM1

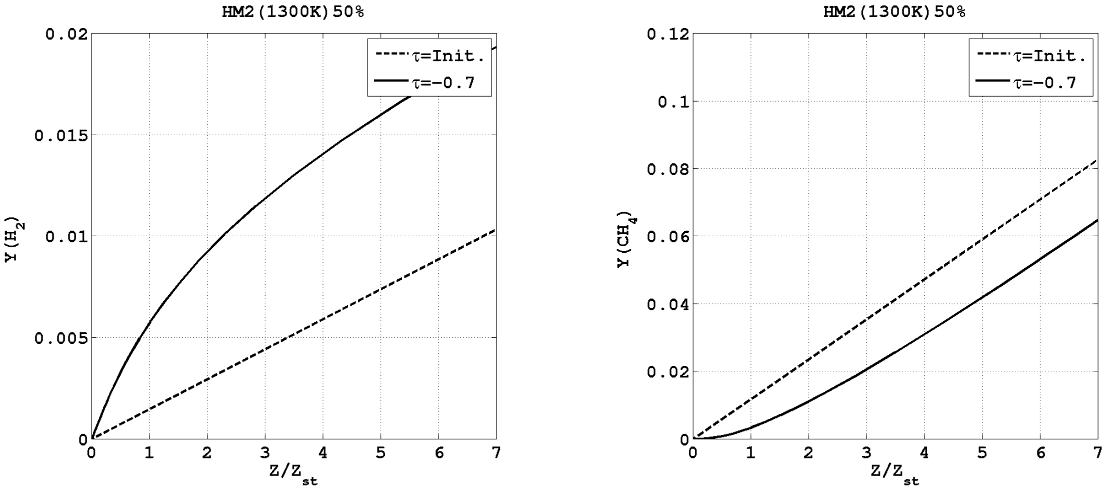

(c) HM2 **(d)** HM2

Figure 5.9: Mass fraction of H_2 and CH_4 as a function of the scaled mixture fraction (Z/Z_{st}) at $\tau = -0.7$ for HM1 (top row) and HM2 (bottom row) oxygen dilutions respectively.

The mass fraction of H_2 (Fig. 5.9a and 5.9c) and CH_4 (Fig. 5.9b and 5.9d) is plotted against scaled mixture fraction space (Z/Z_{st}) at two different times. The initial separation of the fuel/oxidiser layers is shown for both HM1 and HM2 cases by the linear trend of the dashed lines at t=0. As the species gradient starts being smoothed by diffusion, the linear trend is no longer observed. At $\tau = -0.7$ (solid lines) methane and hydrogen diffusion confirm the scenario observed in the base case: the differential diffusion of H_2 and CH_4 results in an increased hydrogen mass fraction and a decreased methane mass fraction for each level of oxygen dilution. This highlights a peculiar aspect of the fuel mixture since the earliest time of layers mixing: H_2 diffuses out more quickly into the region where ignition occurs. Here, as a result, the initial CH_4/H_2 equimolar balance is no longer respected, while a larger hydrogen presence is observed.

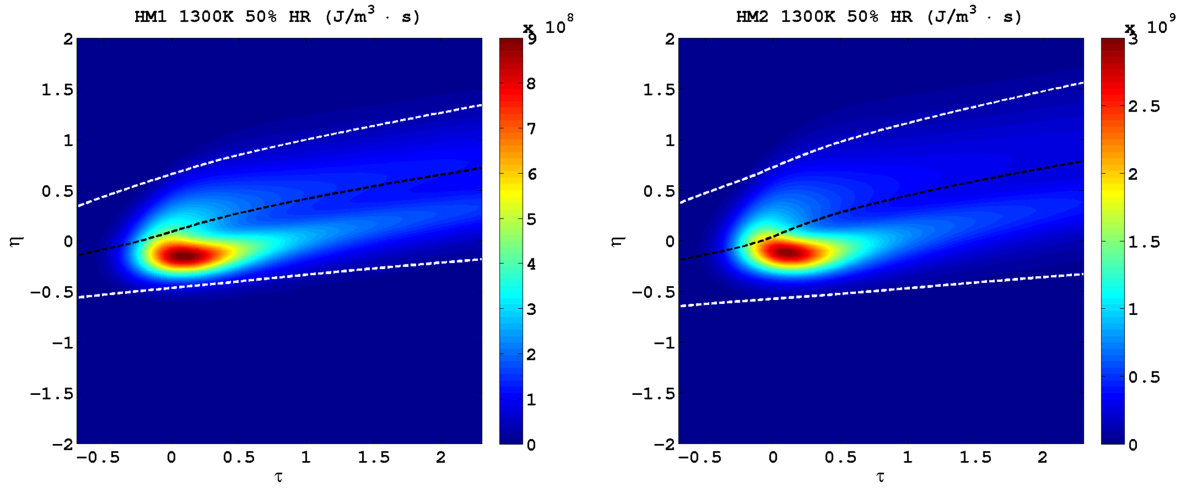

(a) HM1 **(b)** HM2

Figure 5.10: Contours of heat release for the HM1 (left) and HM2 (left) cases. The black dashed line indicates the stoichiometric mixture fraction region. The two white dashed lines above and below the black line correspond to 0.1 and 7 times the stoichiometric mixture fraction value respectively.

5.2 Effect of oxygen reduction - Point 2

The second point of analysis (τ=-0.4), focuses on the major physical and chemical aspects which precede the ignition event. The chemical aspects in particular, start being relevant in each of the dilution cases, as outlined by the initial rise of temperature (Fig. 5.2a, 5.2b and 5.2c). Particular emphasis is given here to chemical differences observed with the different oxygen dilution levels (HM3, HM2 and HM1).

The investigation of the early chemical reactions started, in the base case study, by focusing on the Z_{st} region, where the release of heat was first observed (Fig. 5.5l). The observation of reactants rate of consumption (Fig. 5.4l, 5.4f and 5.4i) revealed, in this area, the interaction of both fuels with oxygen. A better picture of the reaction zone was provided by showing some rates of reaction representative of hydrogen and methane mechanisms, plotted against the concentration of fuels and oxygen (Fig. 5.11a). The figure outlined a region, lying close to the edge of the fuel/oxidiser interface, where H_2 and CH_4 were consumed. Within this area, H_2 and CH_4 are present with different concentrations. The larger availability of H_2, due to differential diffusion effects, explained the broader extension and the higher rate of hydrogen consuming reactions. Conversely, the reduced availability of CH_4 explained the reduced rate and reduced extension of methane consuming reactions, confined in the lower end of the reaction zone.

In a way similar to the base case, the high O_2 dilution configurations (HM2 and HM1) show early reaction at τ=-0.4 around the Z_{st} region. The start of chemical reactions is identified by the release of heat (Fig. 5.5j and 5.5k) and the low but significant rate of reactants consumption

(Fig. 5.4d, 5.4e, 5.4g, 5.4h, 5.4j and 5.4k).

Reaction zone characteristics of the HM1 and HM2 cases (Fig. 5.11c and 5.11b) show similarities and some differences with respect of the base case. Each of the rates shown on figures, are multiplied by a scaling factor which accounts for the differences in the peak rate of O_2 consumption (R33) among dilution cases (Sect. 3.8).

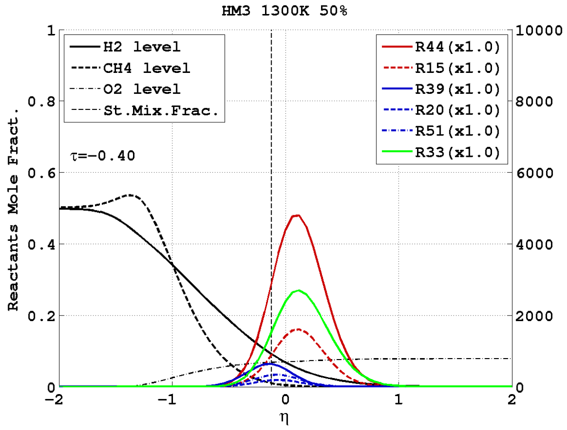

(a) HM3

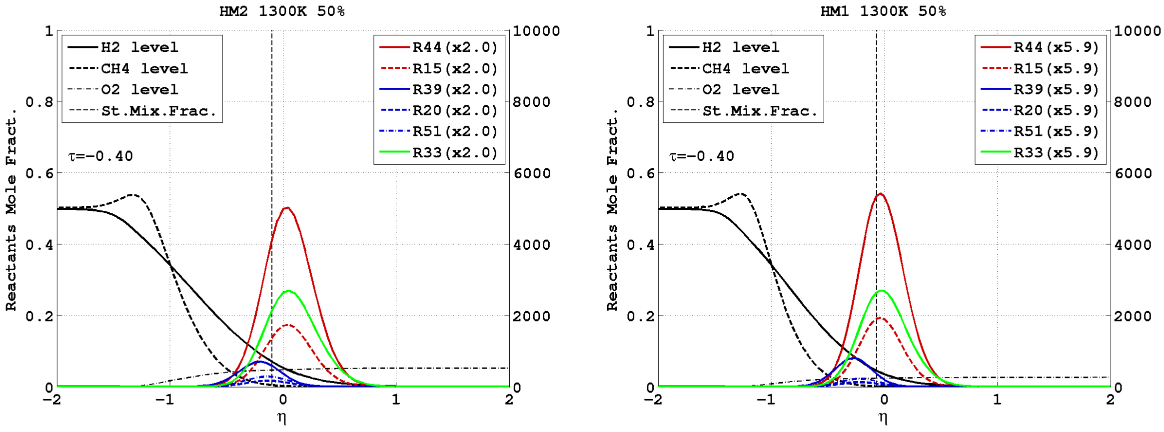

(b) HM2 **(c)** HM1

Figure 5.11: Rates of reaction representative of hydrogen (red) and methane (blue) mechanisms plotted with the fuels and oxidiser mole fraction along the cross-stream direction. The figure shows data from the HM3 (top), HM2 (bottom-leff) and HM1 (bottom-right) cases. The right axis expresses the rate of reaction in $\mathrm{mol}/\mathrm{m}^3 \cdot \mathrm{s}$. The scale factor compares the peak rate of the R33 step with the base case.

The presence of the scaling factor provides an estimation of the important rates reduction (approximately down to 6 and 2 time respectively in HM1 and HM2 case) which follows the oxygen dilution. Nonetheless, the rates reduction does not affect the overall physical features of HM1 and HM2 reaction zones, which appear substantially unchanged with respect to the HM3 one. The hydrogen chemistry is dominant in all cases in terms of rates of reaction and spatial extension, defining the reaction zone borders On the other hand, as a consequence of the CH_4 reduced diffusion, the methane chemistry zone remains confined within a lower extent of the reaction zone, and shows reduced consumption rates.

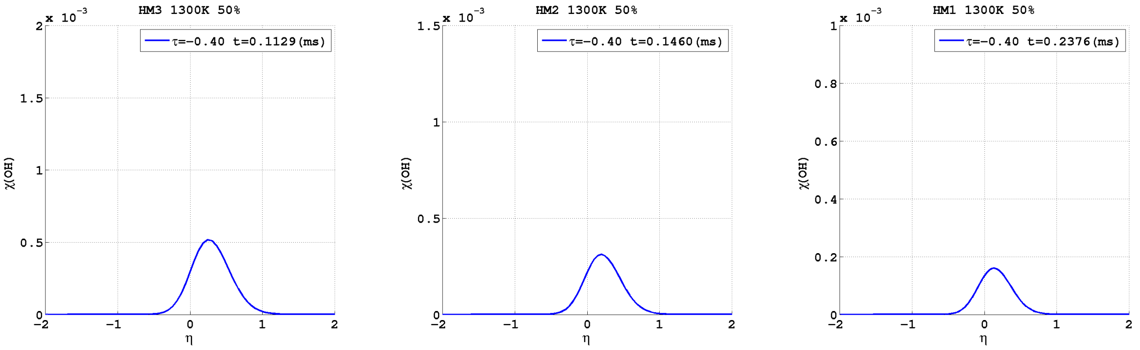

(a) $\chi(OH)$ HM3 **(b)** $\chi(OH)$ HM2 **(c)** $\chi(OH)$ HM1

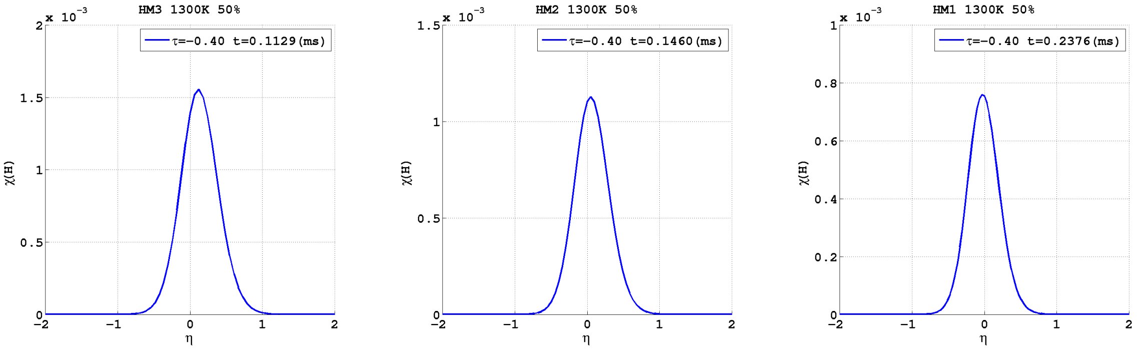

(d) $\chi(H)$ HM3 **(e)** $\chi(H)$ HM2 **(f)** $\chi(H)$ HM1

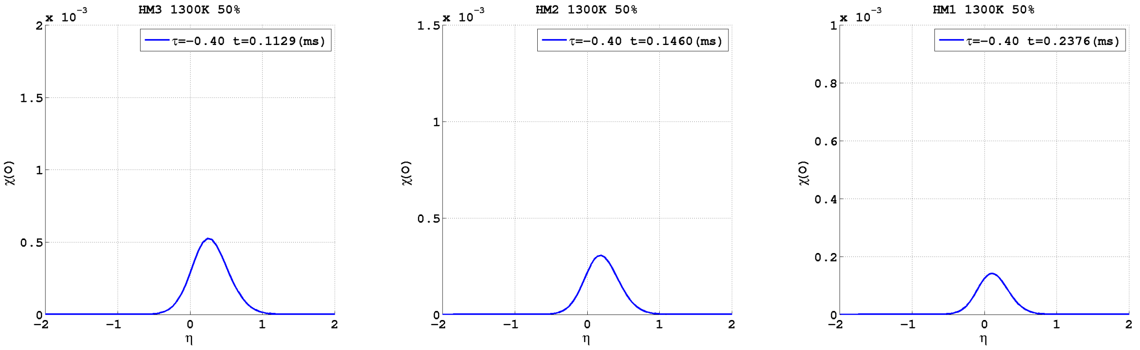

(g) $\chi(O)$ HM3 **(h)** $\chi(O)$ HM2 **(i)** $\chi(O)$ HM1

Figure 5.12: Level of OH (top row), H (middle row) and O (bottom row) radicals in the pre-ignition period for the HM3 (left), HM2 (middle) and HM1 (right) cases.

As a consequence of their different spatial extension, elementary reactions representing CH_4 and H_2 chemistry show their peak rate at different locations. The peak rate of steps describing methane consumption (R20, R39 and R51), occur in the lower end of reaction zone, misaligned with respect to R15 and R44 steps (H_2 chemistry). This explain the early displacement of fuel consumption paths observed in each of the dilution case (Fig. 5.4j and 5.4k), with the H_2 path locating above the CH_4 one.

The initiation of chemical interactions among the reactants causes the formation and build-up of the radical pool. Because of the dependence of reaction rates to the concentration of reactants (Sect. 2.6), elementary reactions describing the O_2 consumption in the HM2 and HM1 cases (R33 is the step controlling the O_2 consumption in all cases studied), present a rate reduction as the O_2 level is reduced. The R33 step is one of the major branching steps which produces highly reactive radicals (O and OH) able to advance the fuel chemistry [2]. As such, with higher oxygen dilutions, a reduced radicals build-up is expected.

Figure 5.12 considers the H/O/OH radical pool for each of the case analysed here. With increasing level of oxygen dilution a reduction of radicals build-up is observed. As the figure clearly shows, the HM1 case presents approximately half the level of H, O and OH radicals compared to the base case. The lower level of highly reactive radicals like H, O and OH reduces the reactivity of HM1 and HM2 configurations and delays self-ignition.

Despite overall radicals reduction observed, the H/O/OH pool in HM1 and HM2 case keep the same characteristics of the base case, with a dominant presence of H compared to OH and O. The analysis of active kinetic steps at τ=-0.4 for each dilution case, provides more insights into the processes responsible for the formation of the radical pool, as well as into the role of methane and hydrogen chemistry in controlling early ignition.

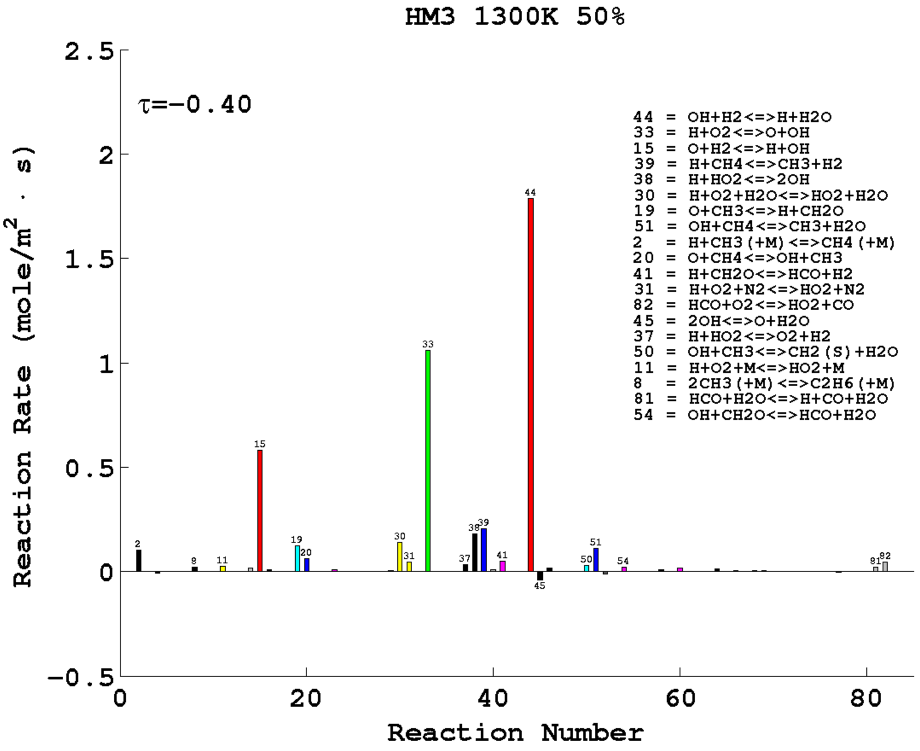

Figure 5.13: Rates of reaction of the DRM19 mechanism integrated along the cross-stream (y) direction. The reaction rates of the base case are shown.

---

[2] In the base case it was observed that O and OH radicals mainly contribute to the consumption of H_2 (R15 and R44) and to the consequent release of H in the domain. As such, a reduced O_2 consumption rate is expected to lower also the rate release of atomic hydrogen.

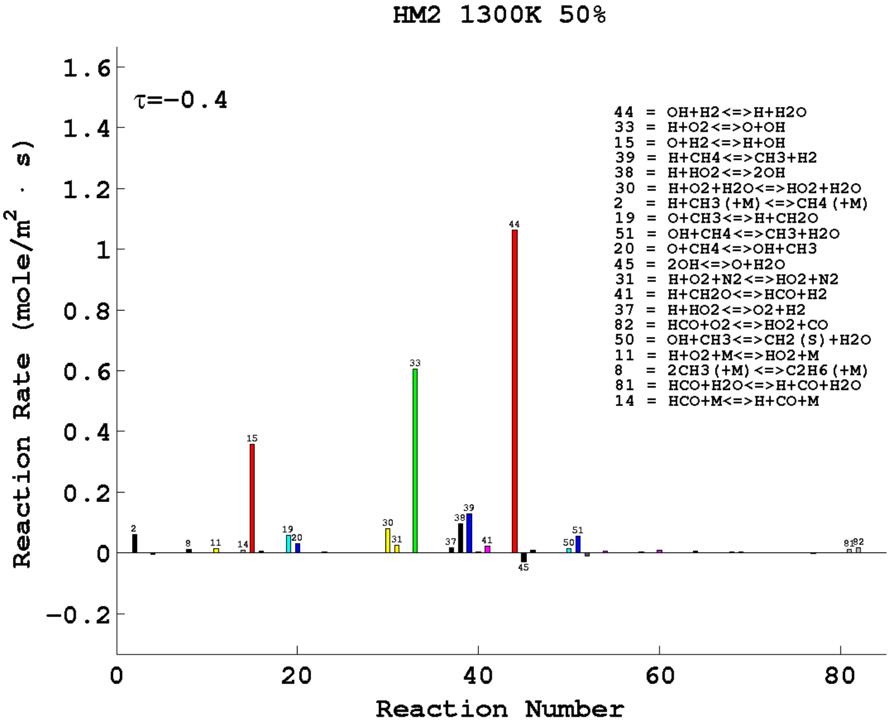

(a) HM2

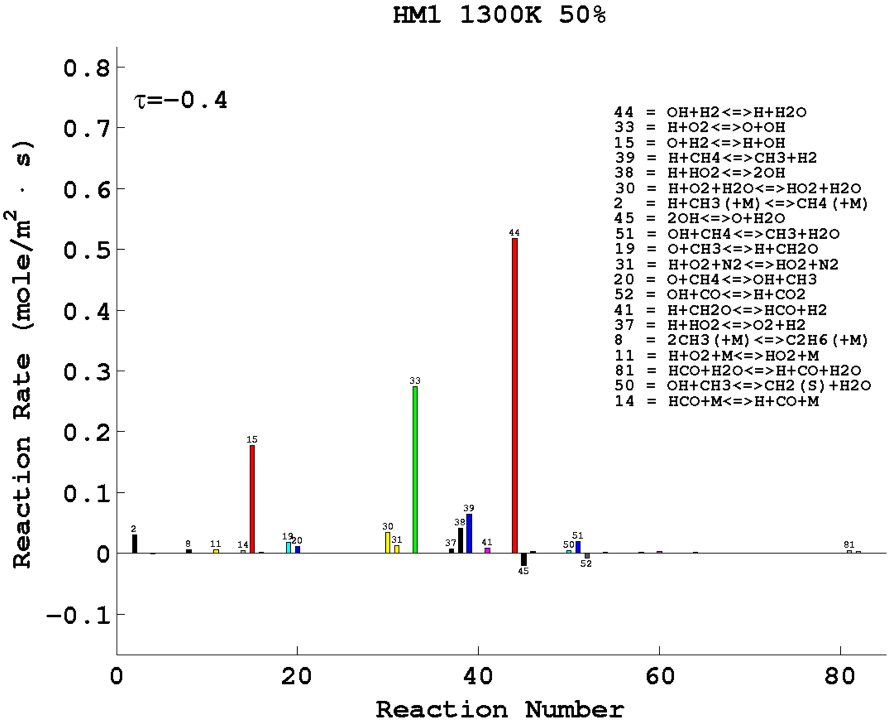

(b) HM1

Figure 5.14: Rates of reaction of the DRM19 mechanism integrated along the cross-stream (y) direction. The reaction rates of the HM2 and HM1 cases are shown. The ordinates are scaled by 1/3 (HM1) and 2/3 (HM2) with respect to the base case, to account for differences due to the oxidiser dilutions.

The bar charts in figures 5.13 5.14a and 5.14b outline an overall reduction of reaction rates with increasing level of dilution [3]. Nonetheless the kinetic scenario does not differ much with dilution levels. The chain branching reactions R33 and R15, together with the chain propagating R44, dominates the pre-ignition process of each dilution case. The major O_2 consumption step (R33) is highly responsive to the H presence, where the atomic hydrogen production can be mainly ascribed to the H_2 consuming steps (R15 and R44). As such, the radical production during pre-ignition relies on the H_2-O_2 interaction, and the large excess of H can be directly linked to the hydrogen consumption, for each oxygen level.

Another similarity between the base case and the low oxygen configurations, is the presence of the hydroperoxyl (HO_2) molecule where fuel/oxidiser interaction is observed (Fig. 5.6l, 5.6k and 5.6j). As in the base case, the early HO_2 production is controlled by R11, R30 and R31 steps which act as a sink for the H excess radicals and compete for O_2.

Analysis of the methane consumption process reveals more significant differences between dilution cases. In the base case study, the CH_4 consumption showed a complex pathway (Fig. 5.15b) associated with rates of reaction lower than those observed for the H_2-O2 interaction (Fig. 5.15a). The R39 step, H activated, was shown to play a major role in the abstraction of atomic hydrogen from the CH_4 molecule and the build-up of methyl in the reaction zone.

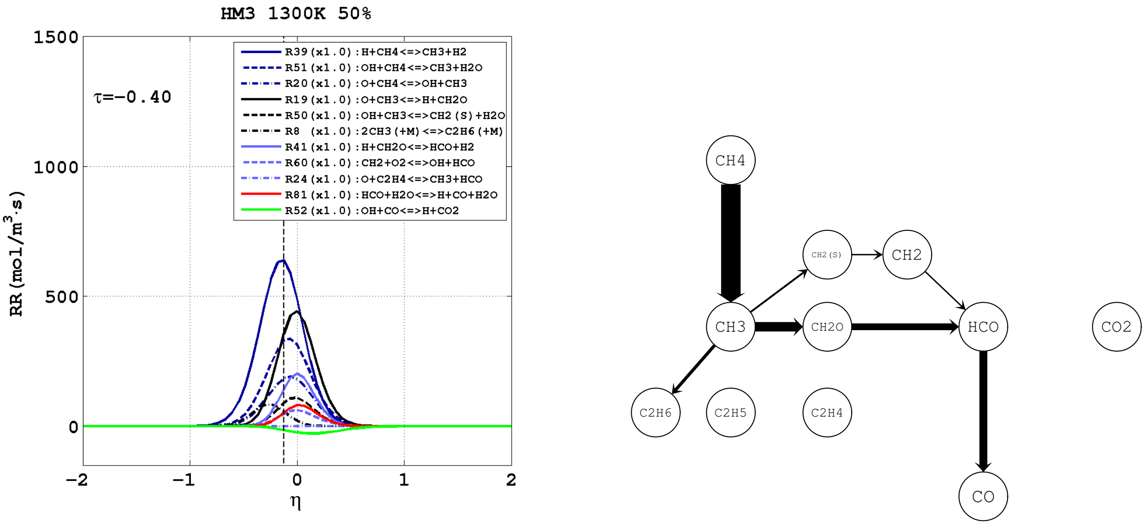

(a) HM3 **(b)** HM3

Figure 5.15: Left: Most important rates of reaction for the methane mechanism plotted at $\tau = -0.4$ for the base case. The vertical dashed line represents the position of the stoichiometric mixture fraction.
Right: Carbon atom pathway diagram for the base case. Arrows are proportional to the integrated transfer rate of C atoms between species, and normalized with respect to the $CH_4 \rightarrow CH_3$ step. Only arrows at least 5% of the thickest are shown.

---

[3] It should be noted that the ordinates on bar charts describing the HM2 and HM1 cases are scaled by 2/3 and 1/3 respectively with respect to the base case. This in order to account for differences due to the oxidiser dilutions.

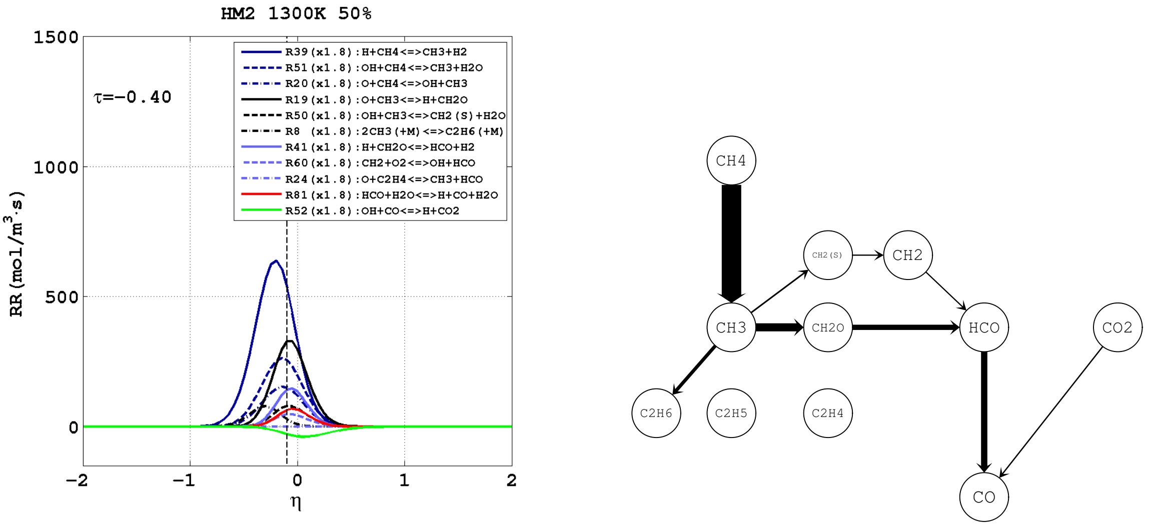

(a) HM2 **(b)** HM2

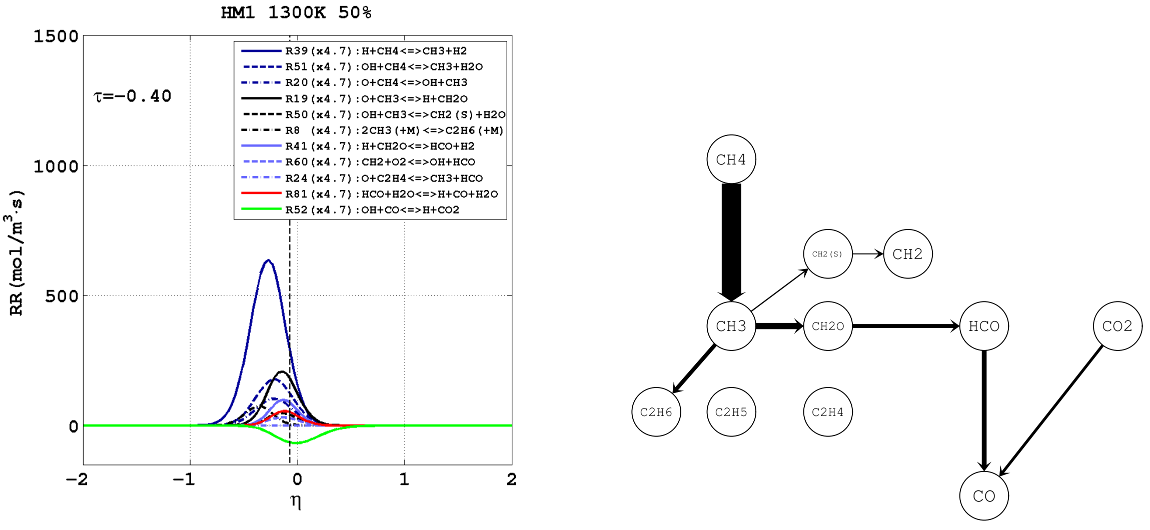

(c) HM1 **(d)** HM1

Figure 5.16: Left row: Most important rates of reaction for the methane mechanism plotted at $\tau = -0.4$ for the HM2 (top) and HM1 (bottom) case. The vertical dashed line represents the position of the stoichiometric mixture fraction.
Right row: Carbon atom pathway diagrams for the HM2 (top) and HM1 (bottom) case. Arrows are proportional to the integrated transfer rate of C atoms between species, and normalized with respect to the $CH_4 \rightarrow CH_3$ step. Only arrows at least 5% of the thickest are shown.

The CH_3 conversion into HCO was observed to proceed along two different pathways. The major conversion was due to the CH_3 oxidation into CH_2O via R19 and then following the $CH_2O-> HCO$ process through R41 and R54 steps. The less important conversion was caused by $CH_3-> CH_2(s)$ (R50), $CH_2(s)-> CH_2$ and $CH_2-> HCO$ sequential processes. Two steps controls the HCO conversion into CO in the pre-ignition period (R81 and R82)), while the final $CO-> CO_2$ process was not observed.

With a reduced presence of O_2 in the oxidiser blend, the processes of CH_4 consumption, shows reduced rates of reaction (Fig. 5.14a and 5.14b). This is reflected by smaller build-up of CH_3, HCO and CO in the domain (Fig. 5.8a, 5.8b, 5.8d, 5.8e, 5.7j and 5.7k), with respect to the base case (Fig. 5.8c, 5.8f and 5.7l,). In figures 5.16a and 5.16c, the major rates of reaction representative of the CH_4 consumption pathway are multiplied by a scaling factor which account for differences in the peak rate of methane dehydrogenation (R39) (Fig. 5.15a). The scaling factor values provide an order of magnitude of rate reduction of CH_3 production process (2 times lower in the HM2 case and 5 times lower in the HM1) (Fig. 5.11b and 5.11c).

Compared to $\mathrm{CH_4}{-}{>}\ \mathrm{CH_3}$, the reduction in the rate of steps describing the $\mathrm{CH_3}{-}{>}\ \mathrm{HCO}$ process (e.g. R19 and R41), is more strongly reduced with higher O_2 dilutions. The bigger impact of oxygen dilution on the methyl consumption is caught by the carbon atom pathways in figures 5.16b and 5.16d, which show the weakening of the middle branch of the $\mathrm{CH_3}{-}{>}\ \mathrm{HCO}$ processes and, as a consequence, the reduced importance of the HCO conversion into CO.

Another interesting aspect caught by the pathways, which differentiate the base case from high dilution cases, is the role of the CO_2 consuming process (R52), which becomes more important with higher oxygen dilutions (Fig. 5.14a and 5.14b).

A better picture of reactions controlling pollutants formation and, in general, controlling the fuel/oxidiser chemical interaction will be provided in the next points of analysis.

5.3 Effect of oxygen reduction - Point 3

The base case showed at ignition time (τ=0) a significant rise in temperature (ΔT $\sim$200K) (Fig. 5.2c) accompanied by an overall increase in the major rates of reaction. In the same period of time, steep temperature rises over time are observed for the HM2 and HM1 case (Fig. 5.2b and 5.2a). As a consequence of the higher oxygen dilutions, lower ΔT was recorded: approximately 140K in the HM2 case and 70K in the HM1.

As the chemical reactions evolve in time, higher levels of heat release (Fig. 5.5j, 5.5k and 5.5l) and higher levels of temperature (Fig. 5.4a, 5.4b and 5.4c) are observed where reactions occur. Different aspects, directly linked to the rise in temperature, characterise all dilution cases at ignition: the gas expansion, the peak rate of reactants consumption and the peak rate of products release. The gas expansion is identifiable by the broadening of the regions were reactants are consumed (e.g. Fig. 5.4j, 5.4k and 5.4l). The broadening is significant in the time range τ $\in$[-0.2,0.2]. In the same time range, reactants show, because the reaction rates are temperature dependent, a large increase in their consumption (Fig. 5.4d, 5.4e, 5.4f, 5.4g, 5.4h and 5.4i). Similarly, the rate of products generation at this time (Fig. 5.5a, 5.5b, 5.5c, 5.5g, 5.5h and 5.5i) is also significant.

As figure 5.4j, 5.4k and 5.4l show, the flame front presents an upward evolution in the pre-ignition period, identified by the monotone ascending trend of the fuel consumption paths. This trend stops at around the ignition time and a downward movement is seen for a short period of time. The change in direction is outlined by the negative slope of both fuel paths at τ=0. As observed in the base case analysis, the downward flame propagation is linked to the achievement of the optimal mixing conditions, as outlined by the peak rate of fuels consumption where the negative slopes are observed. The achievement of the optimal mixing conditions is characterised by the repositioning of the flame front in the $Z < Z_{\text{st}}$ region: both consumption paths relocate, for τ >0, below the Z_{st} line, with the CH_4 path at a larger distance from it. It is interesting to note that, while the flame propagation is particularly emphasised in the base case, where both CH_4 and H_2 path lines move from above Z_{st} line (τ <0) to below it (τ >0), it is less evident in the HM1 case, where both lines remain below Z_{st} in the entire ignition period. The explanation for this difference can be found in the lower value of Z_{st} for the HM1 case (Z_{st}=0.0067) with respect to HM3 one (Z_{st}=0.0198). This moves the stoichiometric mixture fraction region deeper into the oxidiser, limiting the fuel diffusion nearby Z_{st}. Figures 5.11a, 5.11b and 5.11c show that, at earliest stages of ignition, the fuel level reduces in the $Z > Z_{\text{st}}$ region moving from HM3 to HM1 cases.

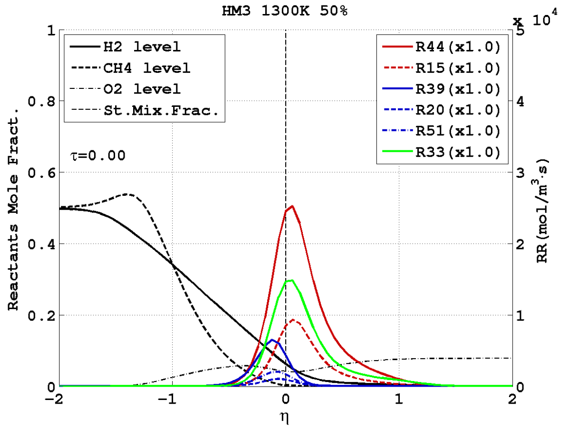

(a) HM3

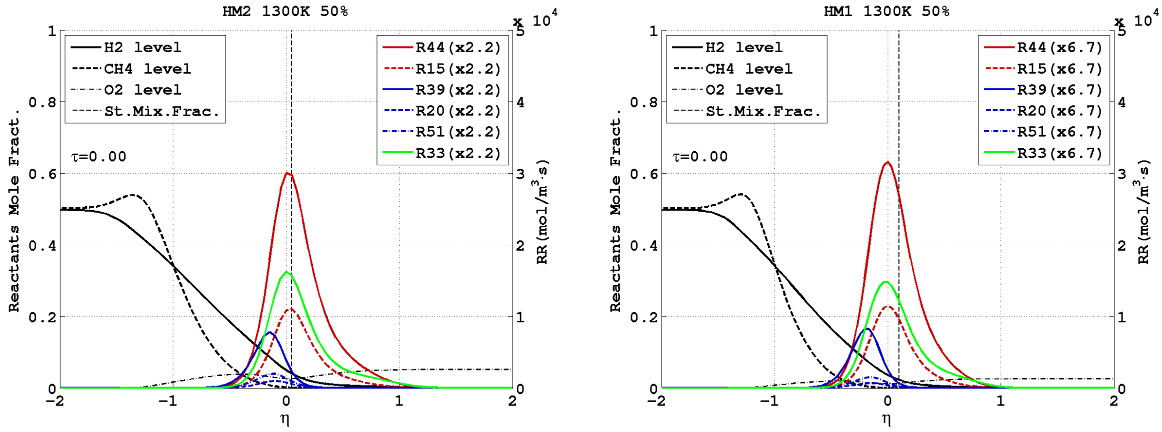

(b) HM2 **(c)** HM1

Figure 5.17: Rates of reaction representative of hydrogen (red) and methane (blue) mechanisms plotted with the fuels and oxidiser mole fraction along the cross-stream direction. The figure shows data from the HM3 (top), HM2 (bottom-left) and HM1 (bottom-right) cases. The right axis expresses the rate of reaction in $\mathrm{mol}/\mathrm{m}^3 \cdot \mathrm{s}$. The scale factor compares the peak rate of the R33 step with the base case.

A comparison of the reaction zones for the different dilution cases is shown in figures 5.17a, 5.17b and 5.17c. The physical appearance of each reaction zone remains substantially unchanged with respect to the previous time point (Fig. 5.11a, 5.11b and 5.11c). As a consequence of the higher hydrogen diffusivity, concentration level of H_2 is higher in the reaction zone as well as broader is its spatial extension. As such, the major H_2 consuming processes (R15 and R44) show a dominant role of the hydrogen chemistry in terms of rates and spatial extension. Conversely, the steps describing the CH_4 consumption (R20, R39 and R51) present lower rates of reaction and a narrower extension, because of the reduced methane diffusivity. The CH_4 chemistry, remains enclosed within the H_2 chemistry borders but a larger distance from Z_{st}, as shown by the blue and red profiles in figures 5.17a, 5.17b and 5.17c. The H_2 and O_2 consumption are aligned, indicating the major role of hydrogen chemistry in consuming oxygen [4].

All cases show, at ignition, an increase of reactants consumption rate. In the base case (Fig. 5.17a), the rate increase of the steps shown is approximately five times larger than at τ=-0.4 (Fig. 5.11a). The scaling factors values for the low oxygen configurations (Fig. 5.17b and 5.17c), being in the order of values at τ=-0.4 (Fig. 5.11b and 5.11c), indicate a similar rate increase for the HM2 and HM1 cases.

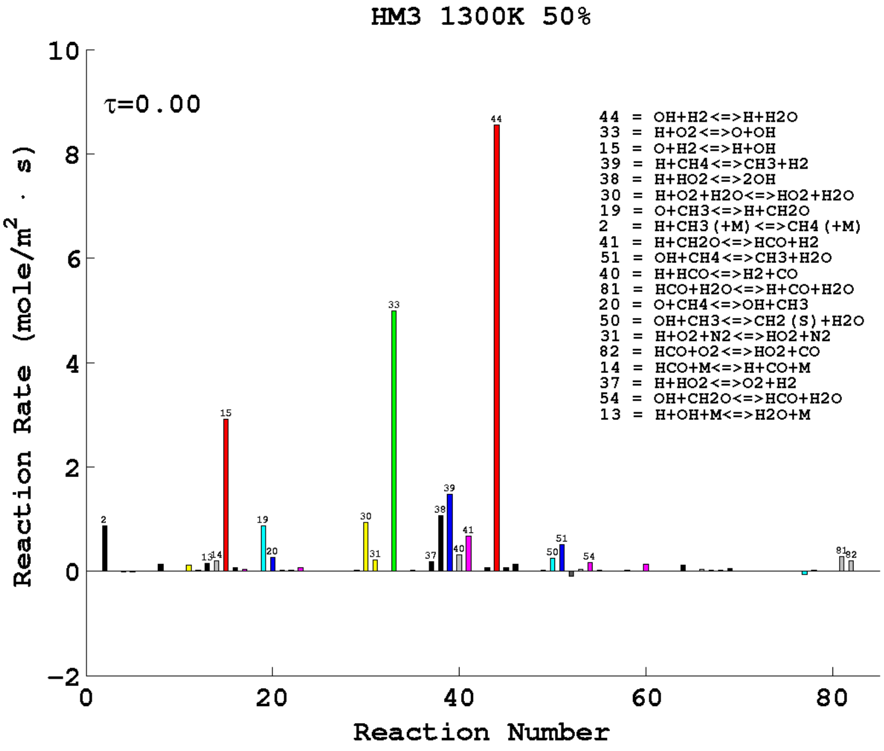

Figure 5.18: Rates of reaction of the DRM19 mechanism integrated along the cross-stream (y) direction. The reaction rates of the base case are shown.

---

[4] The major role of hydrogen chemistry in consuming oxygen can be also deduced by the similarity of O_2 (Fig. 5.4j, 5.4k and 5.4l) and H_2 (Fig. 5.4g, 5.4h and 5.4h) consumption rate contours in the first half part of the ignition period.

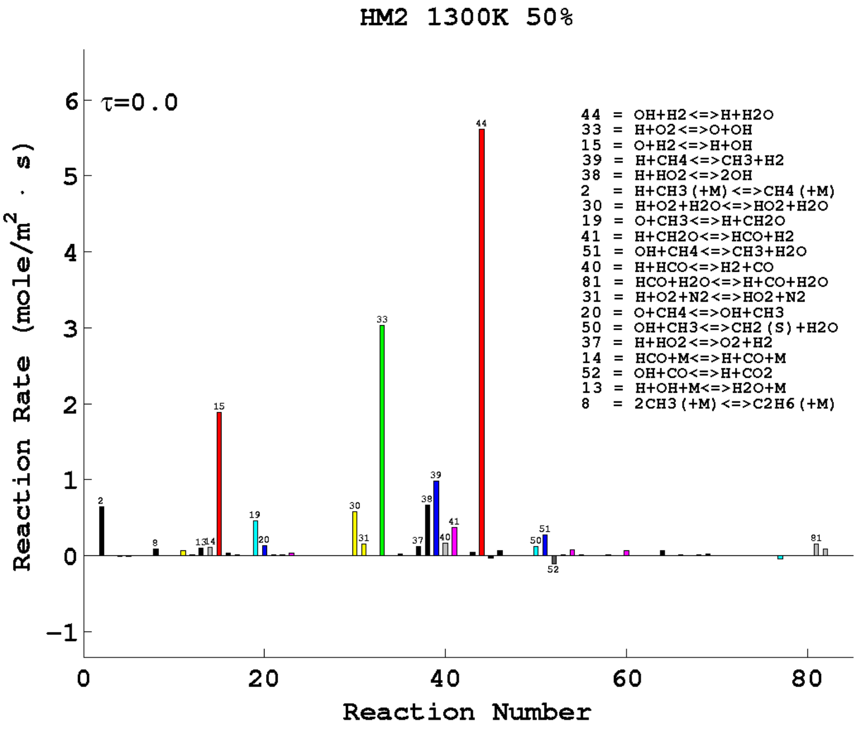

(a) HM2

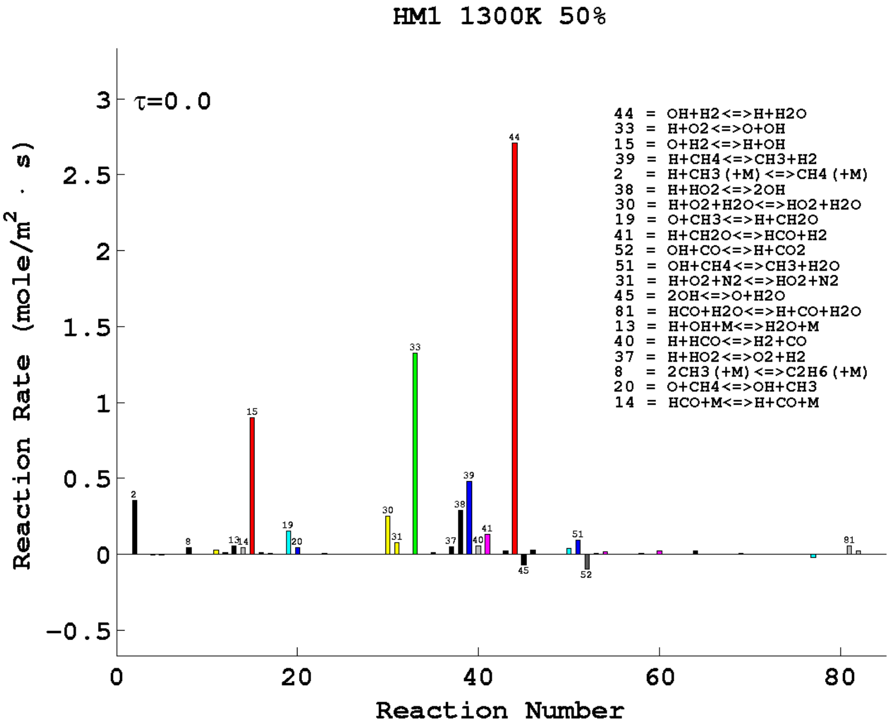

(b) HM1

Figure 5.19: Rates of reaction of the DRM19 mechanism integrated along the cross-stream (y) direction. The reaction rates of the HM2 and HM1 cases are shown. The ordinates are scaled by 1/3 (HM1) and 2/3 (HM2) with respect to the base case, to account for differences due to the oxidiser dilutions.

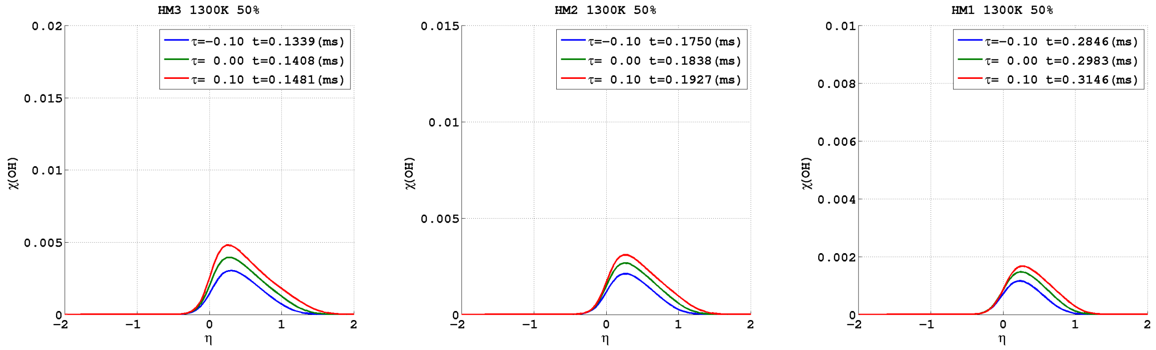

(a) $\chi(OH)$ HM3 **(b)** $\chi(OH)$ HM2 **(c)** $\chi(OH)$ HM1

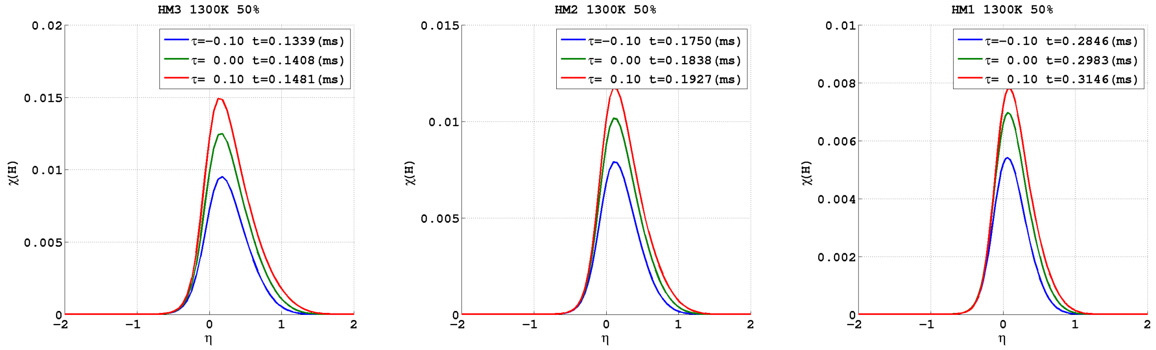

(d) $\chi(H)$ HM3 **(e)** $\chi(H)$ HM2 **(f)** $\chi(H)$ HM1

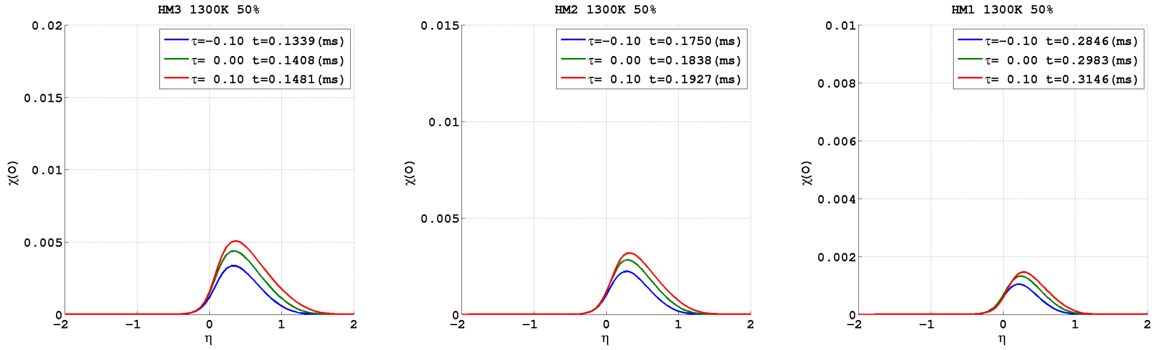

(g) $\chi(O)$ HM3 **(h)** $\chi(O)$ HM2 **(i)** $\chi(O)$ HM1

Figure 5.20: Level of OH (top row), H (middle row) and O (bottom row) radicals at ignition for the HM3 (left), HM2 (middle) and HM1 (right) cases.

The increase of reaction rates at τ=0 is not limited to only steps representing CH_4, H_2 and O_2 consumption. The bar charts in figures 5.18, 5.19a and 5.19b, show an overall increase of rates describing fuel/oxidiser kinetic. As the figures show, the fuel/oxidiser interaction remains dominated by H_2-O_2 chemistry. Steps R15, R33 and R44 present, for each dilution, integrated rate values significantly higher than the rest of the DRM19 steps. As pointed out in the previous section, this outlines the controlling action of H_2-O_2 chemistry over the H/O/OH pool build-up.

All dilution cases present, with respect to the pre-ignition period, higher levels of H, O and OH radicals. The major presence of H atom, is a common feature of each case (Fig. 5.20).

Nonetheless, because of the lower O_2 presence, the H/O/OH excess remains less important in the HM1 and HM2 cases.

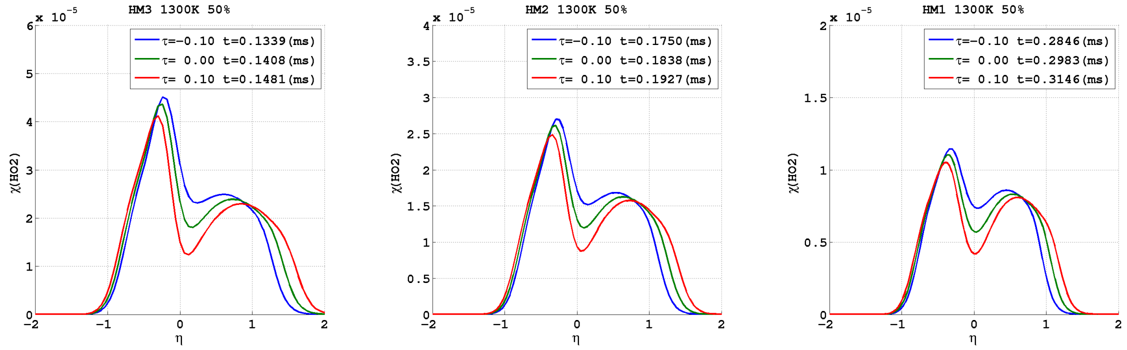

(a) HM3 **(b)** HM2 **(c)** HM1

Figure 5.21: Mole fraction of the hydroperoxyl molecule plotted as a function of the spatial coordinate. Figures, from left to right, show the evolution in the ignition period of the HO_2 presence for HM3, HM2 and HM1 cases. A local minimum in the profiles is shown in proximity of η=0.

Along with H, O and OH formation, the HO_2 build-up is another characteristic which can be found in each dilution case. As shown in figures 5.19b, 5.19a and 5.18, the R30 and R31 steps control the hydroperoxyl production, since they present significant rates in each case. It is interesting to note that, despite the lower temperature which characterise the flame front in the HM2 and HM1 cases (Fig. 5.4a and 5.4a) with respect to HM3, the HO2 breaking due to its molecular instability at high temperature, is observed also in low oxygen configuration. This is clearly shown on figures 5.21c, 5.21b and 5.21a. Here, the local minimum in the HO_2 mole fraction profiles identifies the part of the reaction zone where a significant exothermic event occurs. In each figure $\eta \in$ [-0.5,0.5] is the spatial range where the temperature rise is observed. Within this area, the H_2 chemistry shows a dominant role independently of the O_2 dilution (Fig. 5.17a, 5.17b and 5.17c). This outlines that the self-ignition process, in the cases analysed here, is strongly linked to hydrogen chemistry.

As pointed out in the base case analysis, the CH_4 chemistry differs from the H_2 one because of its greater complexity. The methane consumption is in fact advanced by a set of different processes which control the CH_4 molecule destruction, from the initial CH_4 dehydrogenation to the final CO/CO_2 release. The analysis of the previous time point shed lights on the different way the various stages of the methane chemistry respond to different oxygen level. At τ=0 a similar scenario is observed.

The H abstraction from CH_4, remains the process which present the highest conversion rate as well the broadest spatial extent within the methane chemistry. More precisely, the R39 step shows, in each dilution case, a dominant role within the CH_4 chain reaction. This is clearly shown on figures 5.23c, 5.23a and 5.22a, where the R39 profiles mostly enclose the rest of the reaction rate curves shown. Here the scaling factors, are comparable with those shown at

τ=-0.4 (Fig. 5.15a, 5.16a and 5.16c). As such, the rate reduction of R39 in the low oxygen cases, mainly follows the trend observed in the pre-ignition period.

In contrast, the CH_3 conversion into HCO shows a reduced importance moving from HM3 to HM1. This is clearly shown by R19 (CH_3 oxidation into CH_2O) and R41 (CH_2O conversion into HCO) step profiles, which outline reduced importance with respect to R39 when moving from higher (Fig. 5.22a) to lower (Fig. 5.23a and 5.23c) O_2 level.

Carbon atom pathways in figure 5.22b, 5.23b and 5.23d confirm this trend. Here, the presence of percentage values helps to better appreciate how the CH_4 consumption pathway modifies in the various cases. A trend can be observed in the upper and middle branch of the $CH_3 -> HCO$ process. As the O_2 dilution increases, the conversion of methyl into HCO is reduced along these two branches. Particularly evident is the reduction of the methyl conversion along the middle branch, which relies on the oxygen presence to oxidise CH_3 into CH_2O. It is interesting to note that, with the reduced $CH_3 -> HCO$ conversion, the CH_3 recombination into C_2 form results more important in high dilution cases. Despite the significant ethane production, especially in the HM1 configuration, the $C_2H_6 -> HCO$ is minor. Conversely, the C_2H_6 build-up results partially converted, through an hydrogen abstraction (C_2H_5), back into CH_3.

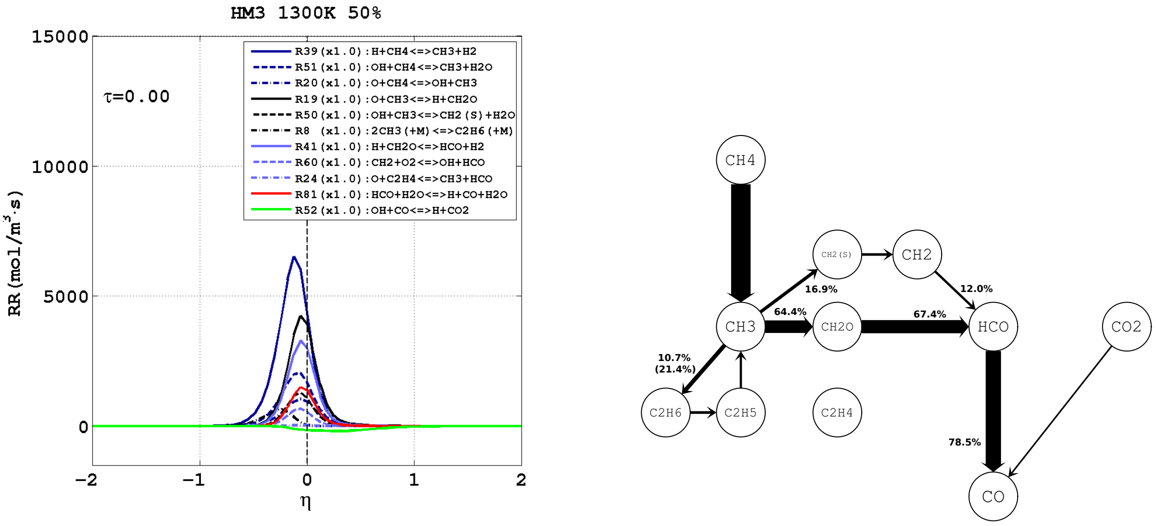

(a) HM3 **(b)** HM3

Figure 5.22: Left: Most important rates of reaction of the methane mechanism plotted at τ=0 for the base case. The vertical dashed line represents the position of the stoichiometric mixture fraction region.
Right: Carbon atom pathway diagrams for the base case at τ=0. Arrows are proportional to the integrated transfer rate of C atoms between species, and normalized with respect to the $CH_4 \rightarrow CH_3$ step. Percentages indicate the number of carbon atoms transferred along the various paths, relative to the number of CH_4 atoms destroyed. Percentages are rounded to the upper decimal digit (+0.1%). Only arrows at least 5% of the thickest are shown.

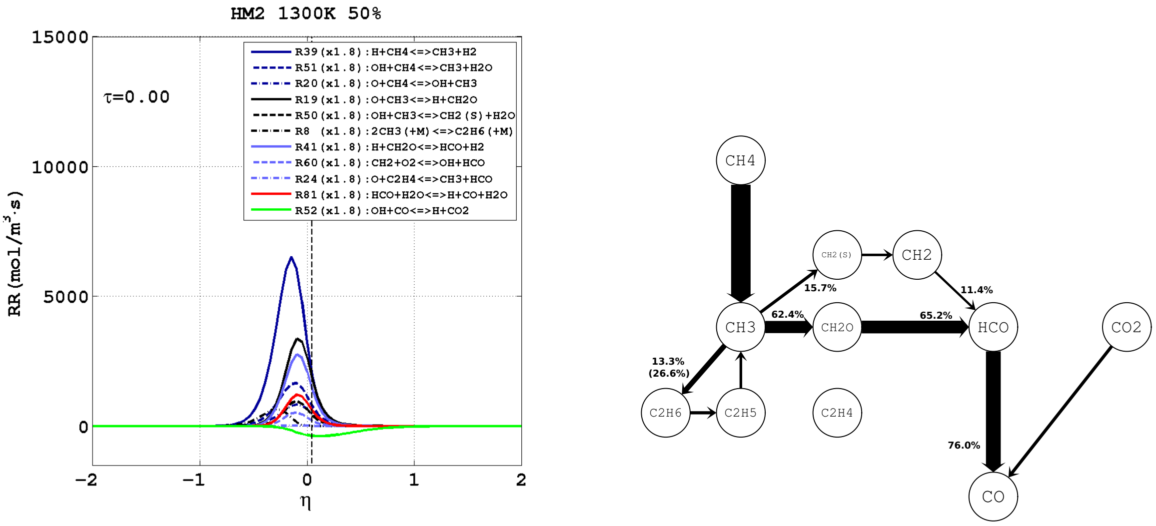

(a) HM2 **(b)** HM2

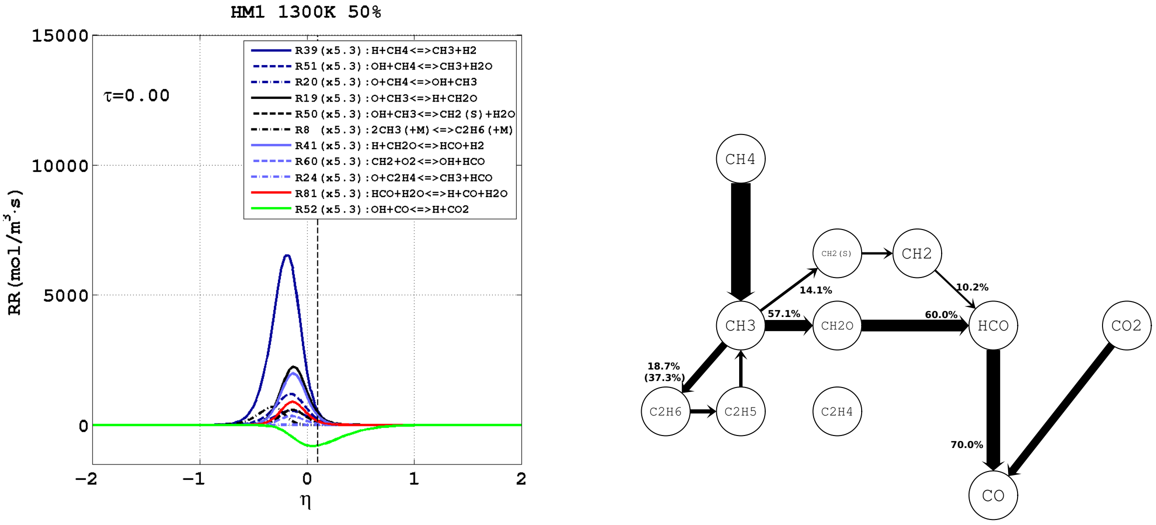

(c) HM1 **(d)** HM1

Figure 5.23: Left column: Most important rates of reaction of the methane mechanism plotted at τ=0 for HM2 (top) and HM1 (bottom) case. The vertical dashed line represents the position of the stoichiometric mixture fraction region.

Right column: Carbon atom pathway diagrams for the HM2 (top) and HM1 (bottom) case at τ=0. Arrows are proportional to the integrated transfer rate of C atoms between species, and normalized with respect to the $CH_4 \rightarrow CH_3$ step. Percentages indicate the number of carbon atoms transferred along the various paths, relative to the number of CH_4 atoms destroyed. Percentages are rounded to the upper decimal digit (+0.1%). Only arrows at least 5% of the thickest are shown.

Along with CH_3 recombination, the CO_2 consumption into CO presents greater importance in HM2 and HM1 cases. This is confirmed by the stronger role of the R52 step, which controls the $CO_2 -> CO$ process, in cases where O_2 level in the oxidiser is reduced (Fig. 5.19a, 5.19b, 5.23a and 5.23c).

In the post-ignition period, when the O_2 consumption become significant, differences in the CH_4 chemistry for different dilution cases are even more evident.

5.4 Effect of oxygen reduction - Point 4

The fourth time point is used to investigate and compare the different dilution cases after the ignition event. At this time, τ=0.4, the oxygen level in the reaction zone drops significantly causing a general reduction of reaction rates. The physical development of the flame front also show important changes with respect to the previous time point.

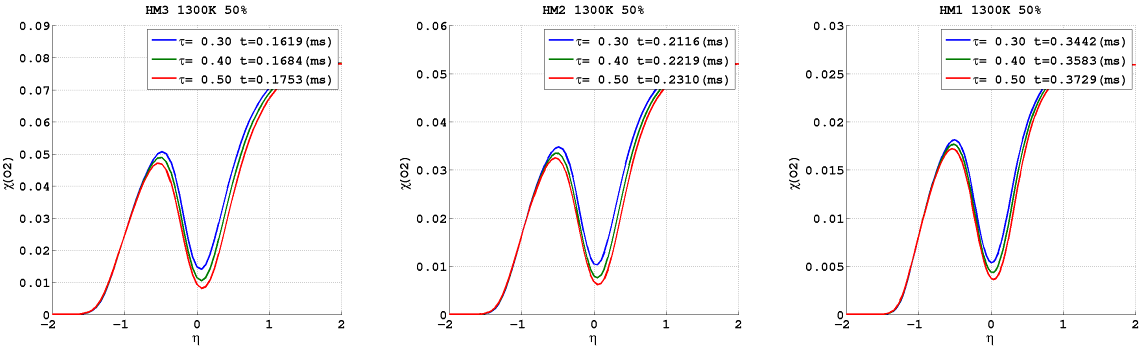

(a) HM3 **(b)** HM2 **(c)** HM1

Figure 5.24: Evolution of the oxygen level in the reaction zone along the post-ignition period. Figures show the O_2 mole fraction plotted η for the HM3 (left), HM2 (middle) and HM1 (right) case.

In the post-ignition period, after the fuels consumption rate reaches its maximum, a strong drop in the oxygen level characterise the flame front of each dilution case (dark blue regions within $\eta \in$[-1,1] on figure 5.7c, 5.7b and 5.7a). According to figures 5.24a, 5.24b and 5.24c, the oxygen level drops by approximately 85% in each dilution case. The O_2 depletion is followed by a general reduction of reaction rate (discussed in more details later in this section), a reduced rate of heat release (Fig. 5.5l, 5.5l and 5.5l), and the slowdown of the ΔT rise over time (Fig. 5.2c, 5.2b and 5.2a).

The post-ignition period is also characterised, independently for the O_2 dilution, by the end of the downward propagation of flame front. As in fact figures 5.4l, 5.4k and 5.4j show, after ignition, the fuel consumption paths move below Z_{st}, keeping this position for the rest of time period investigated.

It is interesting to note, at this time, a more pronounced displacement between the paths. As already outlined for the base case study, this is the consequence of the different times required by CH_4 and H_2 to reach the peak rate in consumption. While the H_2 consumption reaches the peak rate immediately after ignition, and then the H_2 consumption path regain the upward motion, the CH_4 consumption reaches its peak rate at later time. As a consequence, for a short time period methane and hydrogen paths move in opposite directions increasing their relative displacement and modifying the flame front shape.

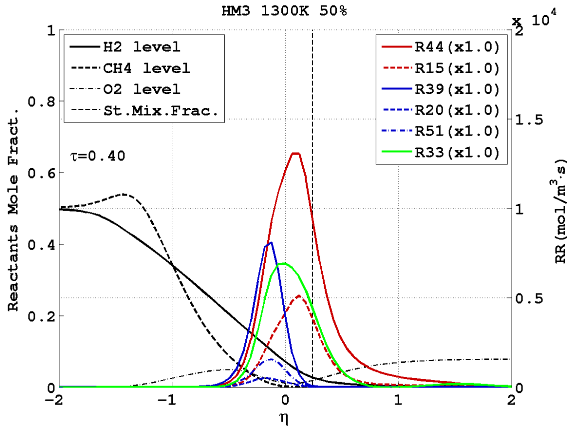

(a) HM3

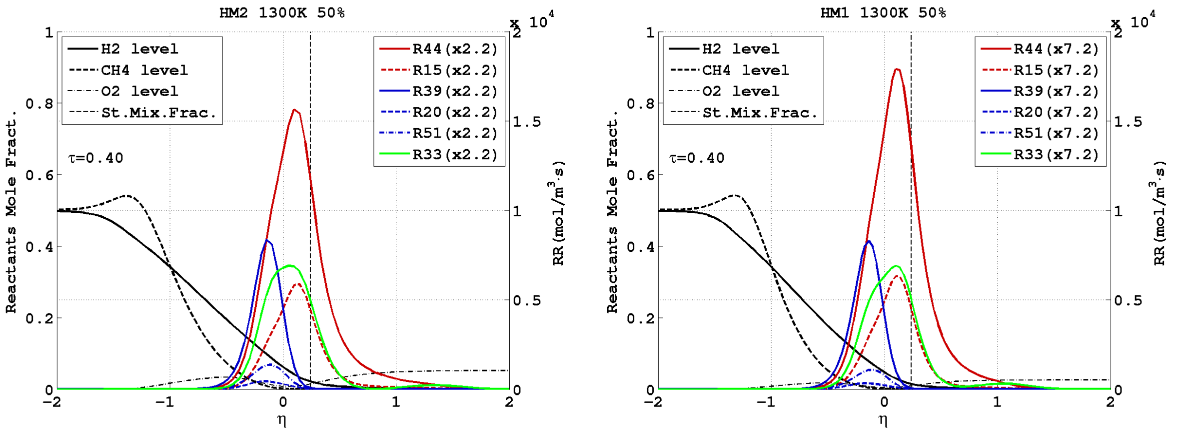

(b) HM2 **(c)** HM1

Figure 5.25: Rates of reaction representative of hydrogen (red) and methane (blue) mechanisms plotted with the fuels and oxidiser mole fraction along the cross-stream direction. The figure shows data from the HM3 (top), HM2 (bottom-leff) and HM1 (bottom-right) cases. The right axis expresses the rate of reaction in $\mathrm{mol}/\mathrm{m}^3 \cdot \mathrm{s}$. The scale factor compares the peak rate of the R33 step with the base case.

Figures 5.25a, 5.25b and 5.25c provide a clear picture of the development of reaction zones after ignition. In each case, the peaks of the rate profiles (R15, R20, R33, R39, R44 and R51), move to the left of Z_{st}, confirming the flame front motion in the fuel rich part ($Z < Z_{\mathrm{st}}$) of the domain. The repositioning of reaction zones, does not affect particularly the relative importance between hydrogen and methane chemistry. At τ=0.4, HM1, HM2 and HM3 cases reveal, in a similar way to that observed in the previous time point, a larger H_2 presence where major reactions occur, causing hydrogen chemistry to have higher rates and a broader spatial extension.

Comparable with the previous time point are also the scaling factor values. R33 peak rate results, with respect to the base case, halved in the HM2 case and 7 times lower in the HM1. By comparing reaction zones at τ=0.4 with those at τ=0 (Fig. 5.17a, 5.17b and 5.17c) it is also possible to appreciate the significant rate reduction associated with O_2 depletion. Steps

describing the H_2/O_2 interaction (R15, R33 and R44) show, in the base case, peak rates approximately halved with respect to ignition time. A similar trend can be observed for HM2 and HM1 cases, as a consequence of the comparable scaling factor values at τ=0.4 and τ=0.
Trend followed by methane dehydrogenation process is different. The peak rates of the R39 profiles are, at τ=0.4, higher than the R33 ones. Differently, at τ=0, the peak rates of R39 profiles present lower values with respect to the R33 curves (Fig. 5.17a, 5.17b and 5.17c).
An explanation can be found by analysing both the kinetic scenario and the radical pool of each dilution case. In each case (Fig. 5.26, 5.27a and 5.27b), steps R15, R33 and R44 have the highest rate over the domain. As such, these steps are responsible for the formation of most reactive radicals (H, O and OH), the H/O/OH pool remains controlled by H_2-O_2 chemistry. The mole fraction profiles in figure 5.28 reveal that, at τ=0.4, the growth of H, O and OH radical result arrested in each case.
The presence of atomic hydrogen remains dominant in the reaction zone, in terms of level and spatial extension. In particular, the H level remains as high as at ignition time (Fig. 5.20d, 5.20e and 5.20f). Because the R33 step rate, which has been shown to be sensitive to atomic hydrogen presence, is limited by the O_2 depletion, the large excess of H enhances other H activated steps, like R2, R39, R30 and R52. This is outlined in figures 5.26, 5.27a and 5.27b, where those elementary steps show rates comparable to the previous time point (Fig. 5.18, 5.19a and 5.19b).

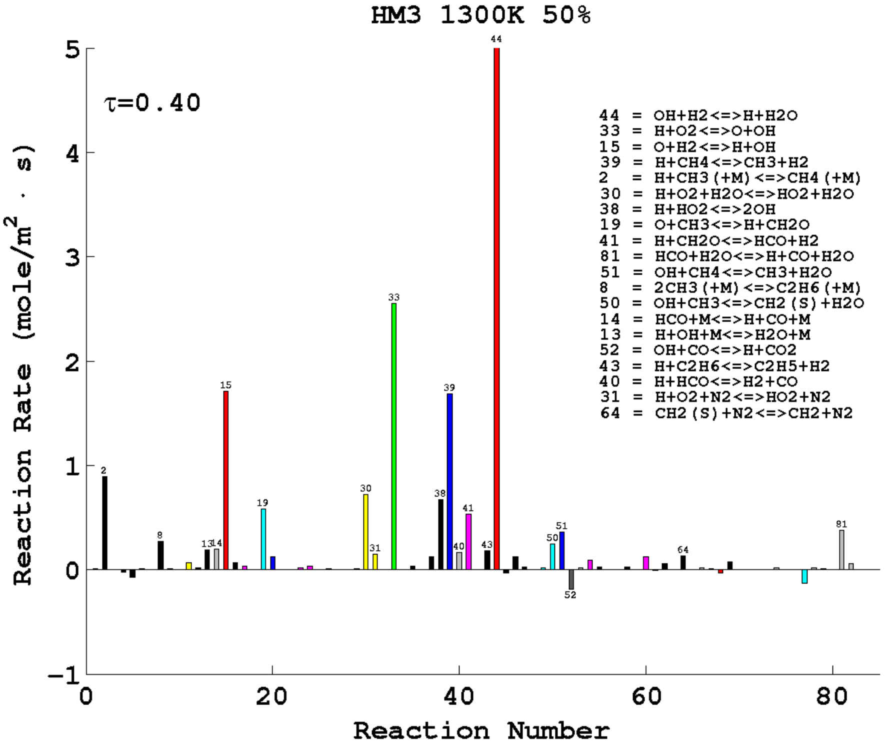

Figure 5.26: Rates of reaction of the DRM19 mechanism integrated along the cross-stream (y) direction. The reaction rates of the base case are shown.

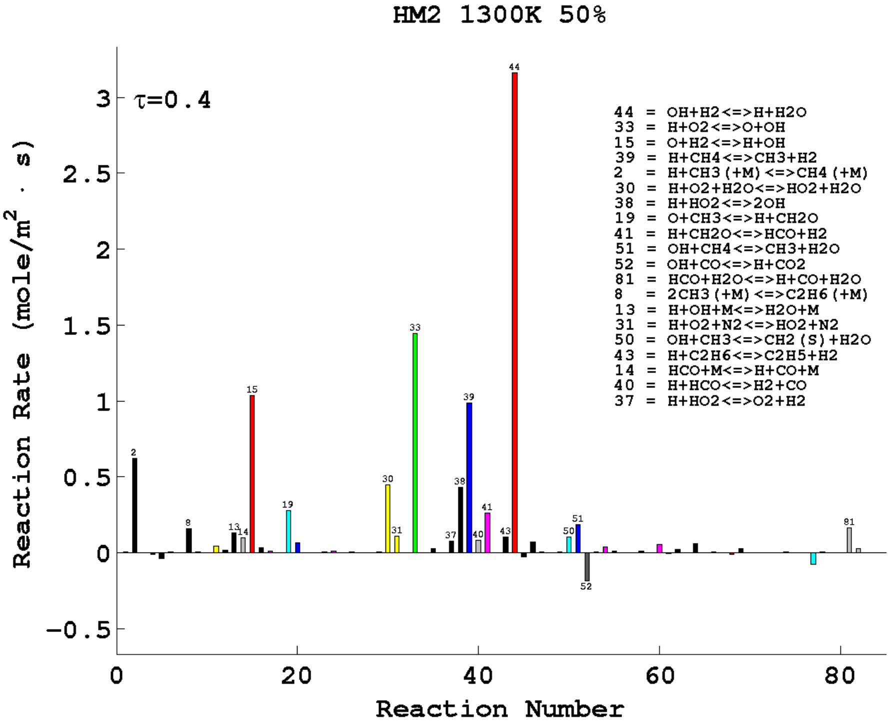

(a) HM2

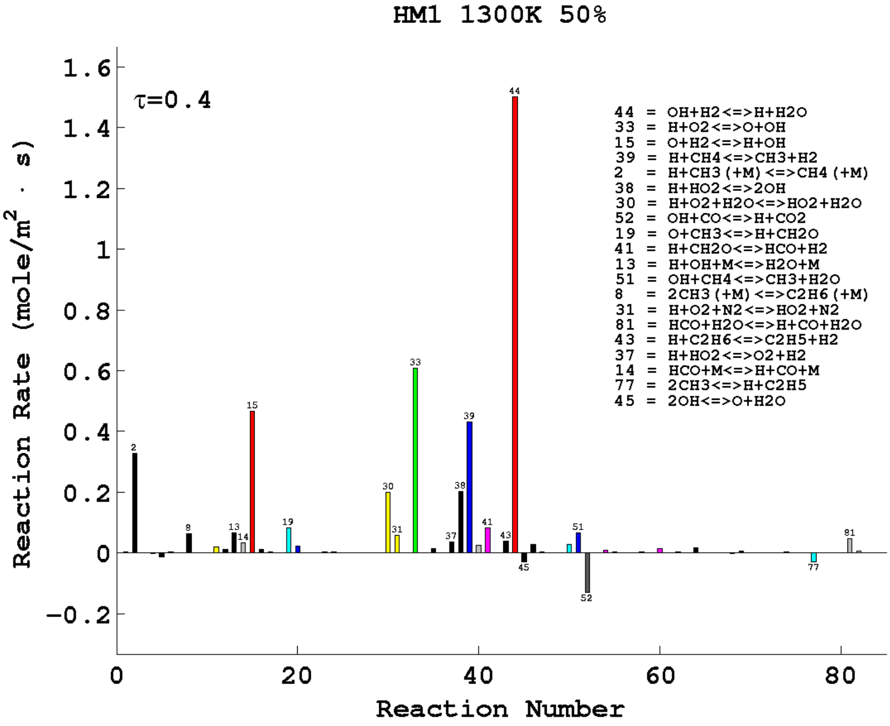

(b) HM1

Figure 5.27: Rates of reaction of the DRM19 mechanism integrated along the cross-stream (y) direction. The reaction rates of the HM2 and HM1 cases are shown. The ordinates are scaled by 1/3 (HM1) and 2/3 (HM2) with respect to the base case, to account for differences due to the oxidiser dilutions.

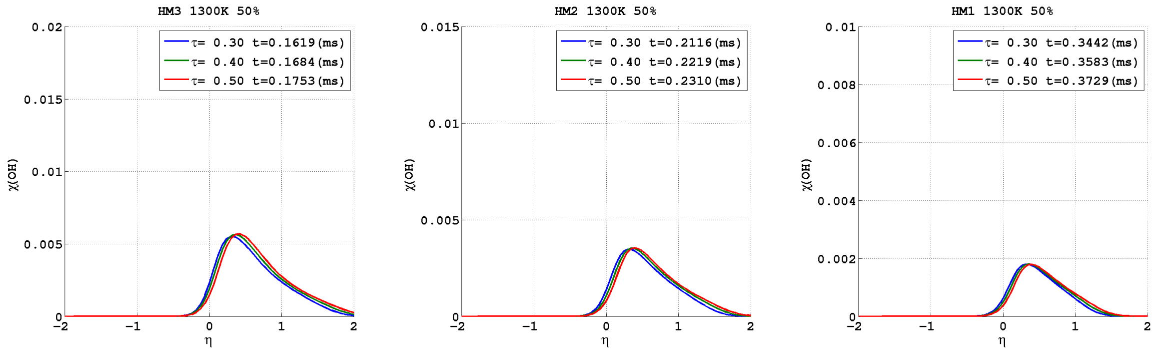

(a) $\chi(OH)$ HM3 **(b)** $\chi(OH)$ HM2 **(c)** $\chi(OH)$ HM1

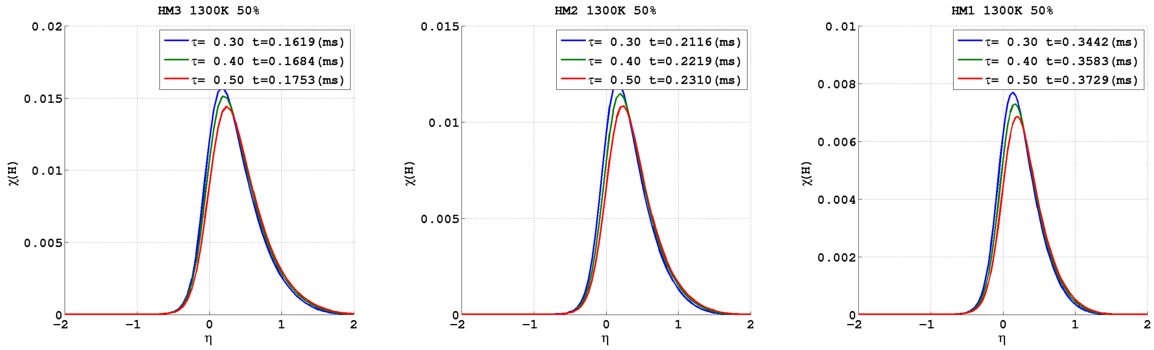

(d) $\chi(H)$ HM3 **(e)** $\chi(H)$ HM2 **(f)** $\chi(H)$ HM1

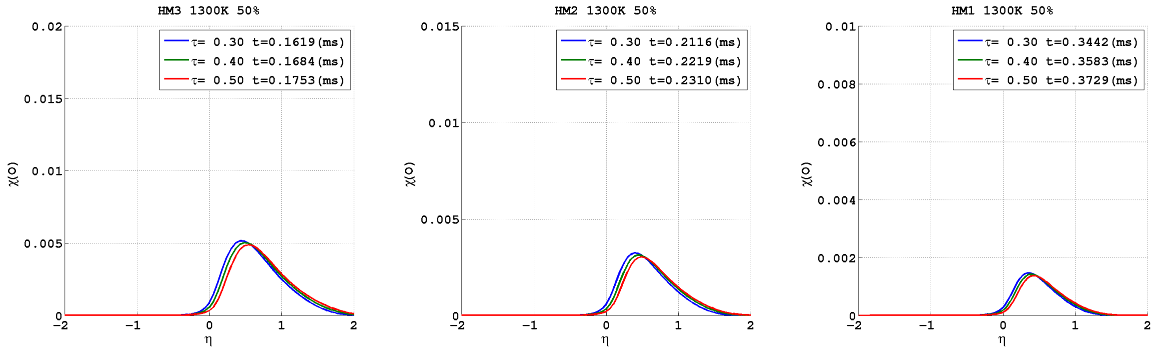

(g) $\chi(O)$ HM3 **(h)** $\chi(O)$ HM2 **(i)** $\chi(O)$ HM1

Figure 5.28: Level of OH (top row), H (middle row) and O (bottom row) radicals in the post-ignition period for the HM3 (left), HM2 (middle) and HM1 (right) cases.

The enhancement of the R39 step after ignition, justifies the late peak in methane consumption rate, which has been observed causing the displacement of the fuel paths in HM1, HM2 and HM3 case (Fig. 5.4l, 5.4k and 5.4j). Moreover, it also explains the significant H_2 production outlined on figures 5.4i, 5.4h and 5.4g by the dark blue area along the CH_4 consumption path for $\tau > 0$.

The oxygen depletion, the repositioning of the flame front and the more pronounced displacement between paths, sheds light on another interesting aspect of the post-ignition period of each dilution case: the hydrogen has privileged access to the oxidiser, while methane consumption remains confined in a low O_2 area. Methane and hydrogen consumption paths in figures 5.7c, 5.7b and 5.7a provide a better picture of this aspect. Here, the lack of oxygen within the reaction zone is identified by the dark blue regions within η $\in$[-1,1] range for τ >0. The hydrogen path lies constantly at the fuel/oxidiser interface. Conversely the methane consumption path, displaced from the hydrogen one, lies in a low oxygen area once the O_2 depletion become significant.

The low O_2 availability to CH_4 chemistry results, in the limited CH_3 oxidation, with respect to earlier times, through the middle branch of the CH_3−> HCO process and in the reduced CO conversion (Fig. 5.29b). As pathways in figure 5.30b and 5.30d outline, this phenomenon is more pronounced with higher dilution level. The CH_3 recombination into C_2 form is proportionally stronger in the HM2 and HM1 cases. Nonetheless, the lack of O_2 in the area where CH_4 chemistry occurs, inhibits the further C_2H_6 oxidation, which results in each dilution case only partially converted back to CH_3.

The carbon pathways also catch another interesting trend. With lower level of oxygen in the oxidiser blend, the CO_2 conversion into CO becomes more important. The consumption of carbon dioxide in the HM2 and HM1 cases, presents strong similarities with the process analysed in the base case.

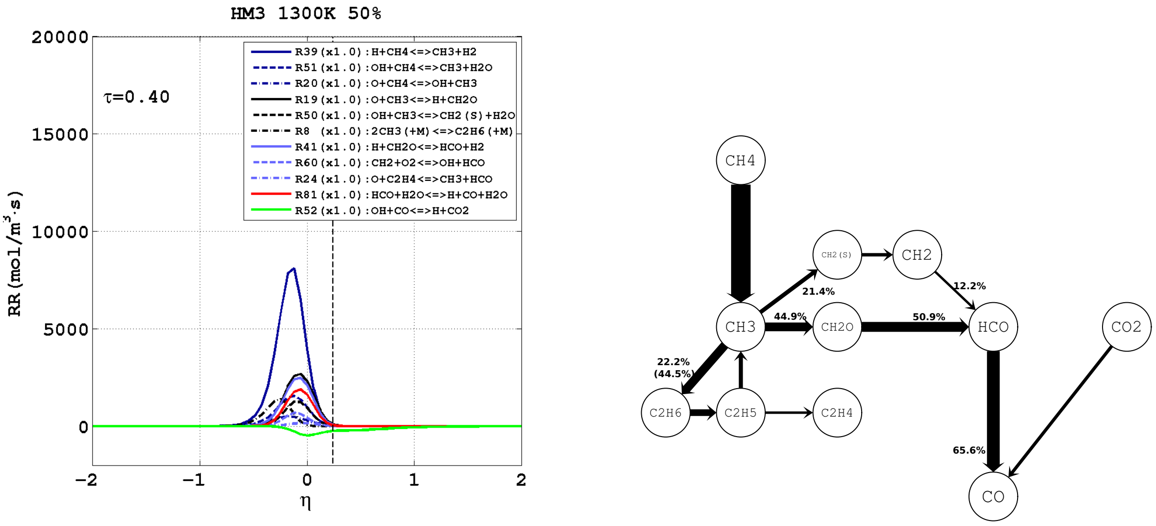

(a) HM3 **(b)** HM3

Figure 5.29: Left: Most important rates of reaction of the methane mechanism plotted at τ=0.4 for the base case. The vertical dashed line represents the position of the stoichiometric mixture fraction region.
Right: Carbon atom pathway diagrams for the base case at τ=0.4. Arrows are proportional to the integrated transfer rate of C atoms between species, and normalized with respect to the $CH_4 \rightarrow CH_3$ step. Percentages indicate the number of carbon atoms transferred along the various paths, relative to the number of CH_4 atoms destroyed. Percentages are rounded to the upper decimal digit (+0.1%). Only arrows at least 5% of the thickest are shown.

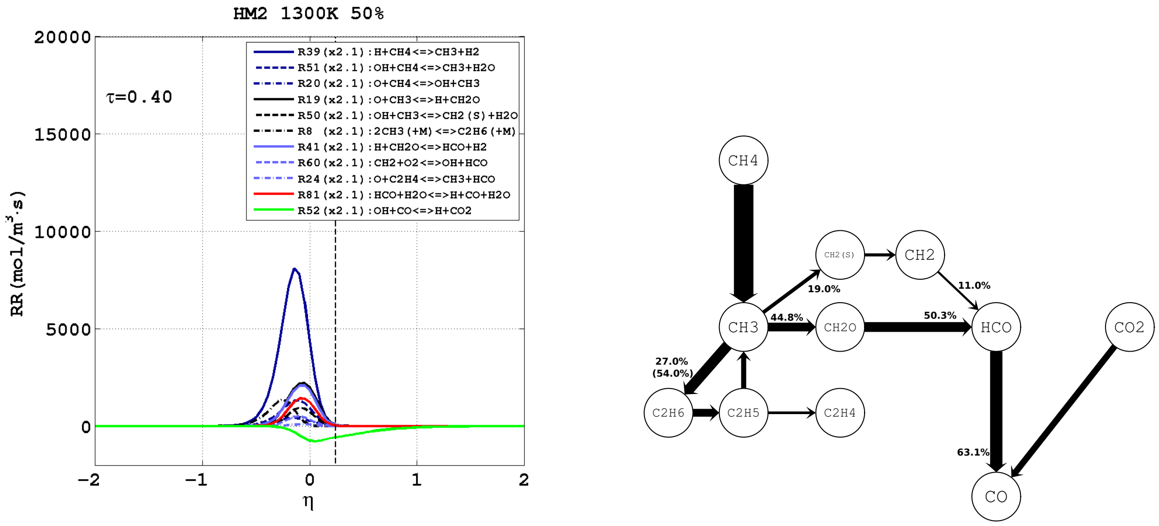

(a) HM2 **(b)** HM2

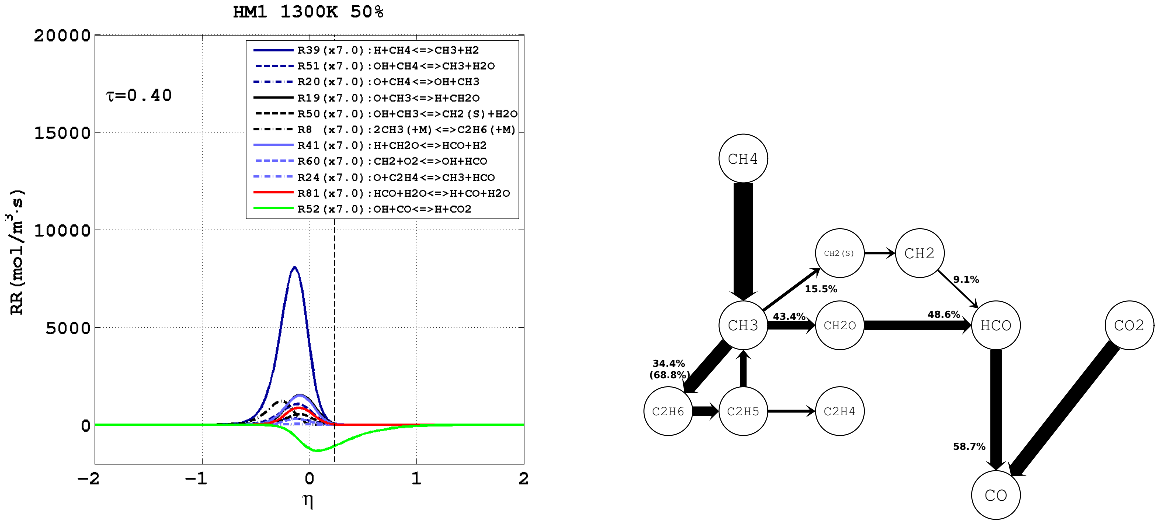

(c) HM1 **(d)** HM1

Figure 5.30: Left column: Most important rates of reaction of the methane mechanism plotted at τ=0.4 for HM2 (top) and HM1 (bottom) case. The vertical dashed line represents the position of the stoichiometric mixture fraction region.

Right column: Carbon atom pathway diagrams for the HM2 (top) and HM1 (bottom) case at τ=0.4. Arrows are proportional to the integrated transfer rate of C atoms between species, and normalized with respect to the $CH_4 \rightarrow CH_3$ step. Percentages indicate the number of carbon atoms transferred along the various paths, relative to the number of CH_4 atoms destroyed. Percentages are rounded to the upper decimal digit (+0.1%). Only arrows at least 5% of the thickest are shown.

As shown by bar charts (Fig. 5.26, 5.27a and 5.27b), the CO_2 conversion into CO is controlled, in each case, by the backward R52 step. The R52 step takes place mainly below the Z_{st} line ($\eta \in$[-0.5,0.5]), misaligned with respect to the rest of the CH_4 chemistry steps (Fig. 5.29a, 5.30a and 5.30c). No steps showing significant rate are observed describing the CO_2 production (Fig. 5.26, 5.27a and 5.27b). As such, the CO_2 consumed is most likely to originate, for each dilution case, from the carbon dioxide diluted in the oxidiser blend. The areas where CO_2 is consumed

(Fig. 5.5f, 5.5e and 5.5d) result mainly enclosed within by H_2 and CH_4 paths. The path lines also mark the areas where the highest temperatures (Fig. 5.4c, 5.4b and 5.4a) and a strong H (Fig. 5.6c, 5.6b and 5.6a) presence are observed . The combined effect of a large H presence and high temperatures, induces the R52 steps to move along the backward direction. As a results, the carbon dioxide is consumed rather than produced.

5.5 Effect of oxygen reduction - Point 5

The fifth investigation point focuses on the final part of the selected ignition period. At τ=0.7, the oxygen level is almost zero in the reaction zone, and flame front is observed moving upwards, where more oxygen is available. For each dilution case, at τ=0.7, the region of H_2 and CH_4 consumption are more distinct.

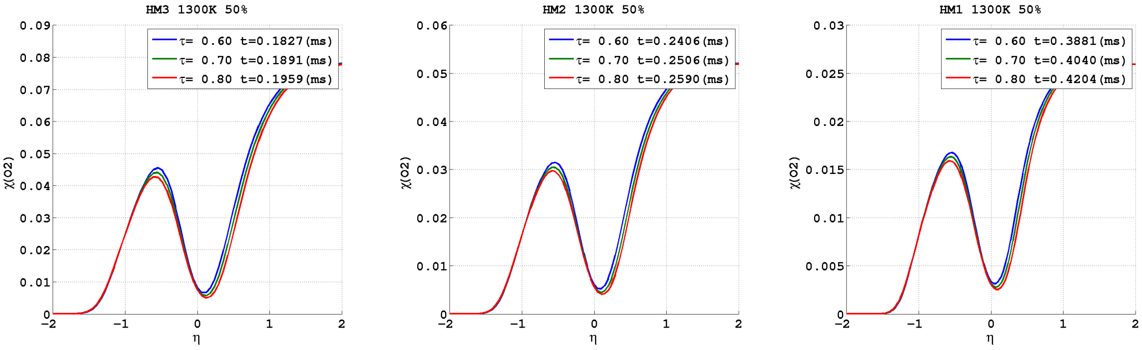

(a) HM3 **(b)** HM2 **(c)** HM1

Figure 5.31: Evolution of the oxygen level in the reaction zone along the post-ignition period. Figures show the O_2 mole fraction plotted η for the HM3 (left), HM2 (middle) and HM1 (right) case.

Figures 5.31a, 5.31b and 5.31c shown the evolution of the oxygen level in the final part of the ignition period. A significant drop in the oxygen level can be observed in the $\eta \in$[-1,1] range. Approximately the 90% of the available oxygen has been here consumed. The profiles have moved to the right compared to figure 5.24, representing the upward motion of the reaction zones towards the oxidiser layer.

This upward motion of the flame front is seen in the fuel paths overlaid on contour plots (e.g. Fig. 5.4l, 5.4k and 5.4j). For τ >0.7, both paths moves upward, keeping a constant distance from each other. The H_2 path runs along Z_{st}, the CH_4 path below it, where a lower presence of oxygen is observed (Fig. 5.7c, 5.7b and 5.7a). As outlined in the previous section, the fuel paths were observed to diverge before regaining the upward motion. In particular, the distance between paths at τ=0.7 is larger than at $\tau = 0.4$. This has been explained by the excess of H radical, which controls the CH_4 consumption after ignition.

Thus CH_4 chemistry is taking place in region of low oxygen, in contrast to the position of H_2 chemistry (Fig. 5.7c, 5.7b and 5.7a). In particular, it sheds lights on the even more disadvantaged location of CH_4 chemistry at τ=0.7. As shown on figures 5.32a, 5.32b and 5.32c, the reaction zones, which were observed evolving in the first part of the ignition period as a unique region, now present a double peak. More precisely, the profiles of R15, R33 and R44 rate (H_2-O_2 chemistry) show at τ=0.7 a double peak. The higher peaks locates close to the Z_{st} region, where the O_2 availability is higher and the H_2 presence is lower. On the other hand, the lower peaks lies within the $Z < Z_{\text{st}}$ region, richer in fuel. The low rate of R33 process, despite the large availability of H_2, demonstrates the lack of oxygen in the $Z < Z_{\text{st}}$ region. Here, aligned with the low rate part of R33 profile, the CH_4 dehydrogenation (R20, R39, R51) occurs.

Figures 5.32a, 5.32b and 5.32c outlines a further rates reduction with respect to the previous time point (Fig. 5.25a, 5.25b and 5.25c). Moreover, the scaling factor values, confirm the important rates reduction (down to 5.5 and 2 times respectively in HM1 and HM2 case) caused by the oxygen dilution.

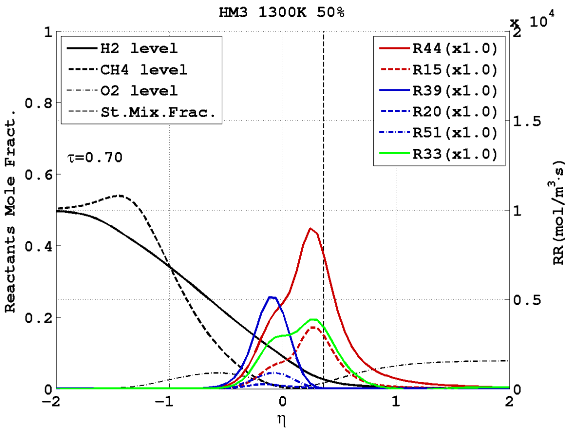

(a) HM3

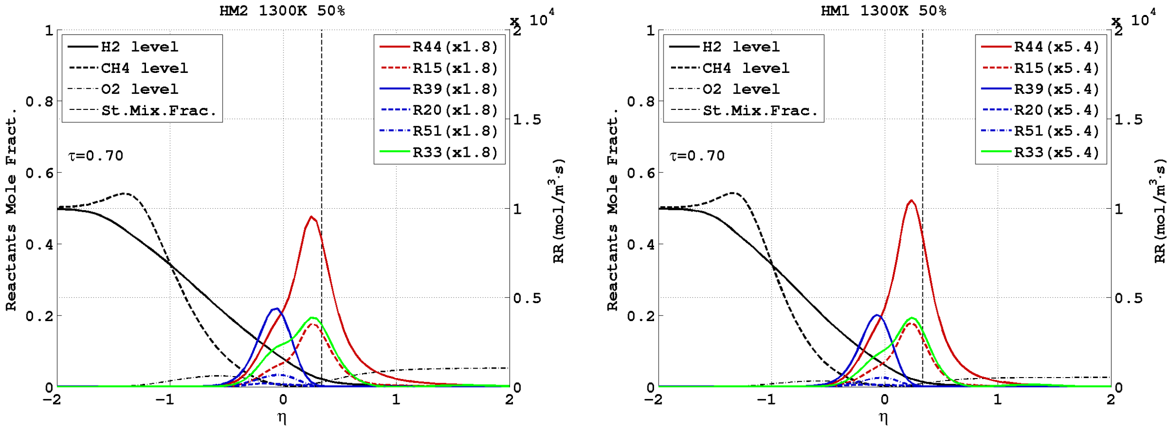

(b) HM2 **(c)** HM1

Figure 5.32: Rates of reaction representative of hydrogen (red) and methane (blue) mechanisms plotted with the fuels and oxidiser mole fraction along the cross-stream direction. The figure shows data from the HM3 (top), HM2 (bottom-leff) and HM1 (bottom-right) cases. The right axis expresses the rate of reaction in $\text{mol}/\text{m}^3 \cdot \text{s}$. The scale factor compares the peak rate of the R33 step with the base case.

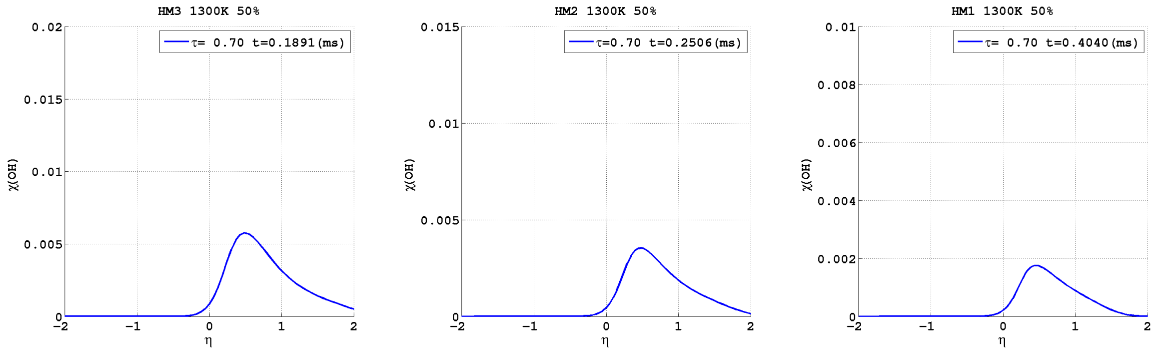

(a) $\chi(OH)$ HM3 **(b)** $\chi(OH)$ HM2 **(c)** $\chi(OH)$ HM1

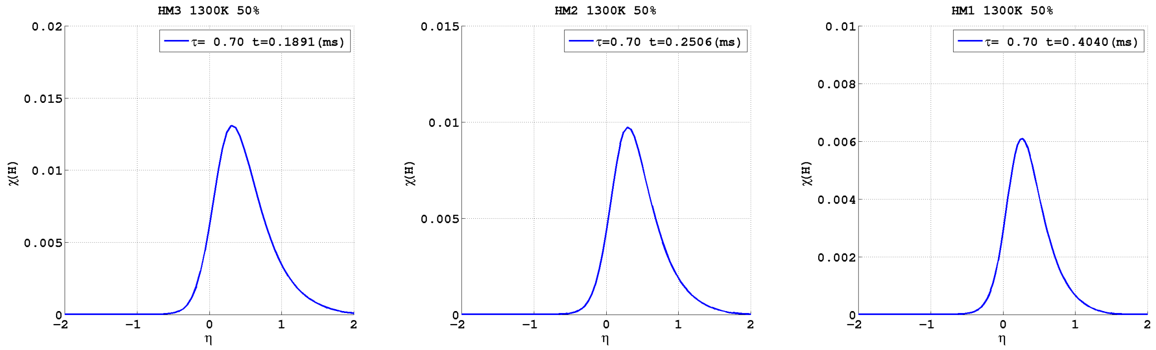

(d) $\chi(H)$ HM3 **(e)** $\chi(H)$ HM2 **(f)** $\chi(H)$ HM1

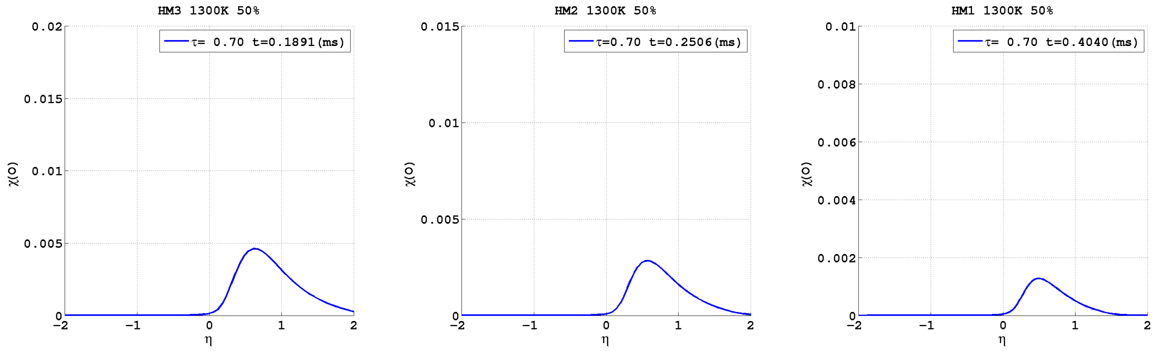

(g) $\chi(O)$ HM3 **(h)** $\chi(O)$ HM2 **(i)** $\chi(O)$ HM1

Figure 5.33: Level of OH (top row), H (middle row) and O (bottom row) radicals in the post-ignition period for the HM3 (left), HM2 (middle) and HM1 (right) cases.

Figure 5.33 provides an overview of the H/O/OH radical pool at τ=0.7. As the figure shows, the radical concentration remain substantially unchanged with respect to previous time points (Fig. 5.28). In each dilution case, the H radical show a dominant presence, while a reduced build-up of OH and O is observed. It is interesting to note that, with respect to the early part of ignition (Fig. 5.12), the excess of O and OH radicals locates now only in the η >0 area, where the CH_4 presence is limited. On the other hand, in the area where more CH_4 is present (η <0), only the excess of H atom is observed. Because the oxygen consumption process (R33) is observed to have a major role in the O/OH production, these findings confirm the low oxygen presence where CH_4 chemistry occurs.

More insights into the fuel/oxidiser chemical interaction are provided by bar charts in figures 5.34, 5.35a and 5.35b. The build-up of H/O/OH pool is still controlled by the R15, R33 and R44 steps, which show the highest rate together with R39. R44 remains, in each case, the step with the highest integrated rate value and, as such, it gives the major contribution to H formation. R15 and R33, both branching steps, contribute respectively to the formation of H/OH and O/OH pairs. R33 in particular, is the only step which releases atomic oxygen at a significant rate. With increasing level of dilution, rates of reactions are reduced. As a consequence, the excess of radical in the HM2 and HM1 cases (Fig. 5.33) is also reduced.

Because of the large H presence, the R39 step remains, in the final part of ignition period, as the most important among reactions describing methane consumption. This is clearly shown on figures 5.36a, 5.36b and 5.36c. Here, the figures describes the CH_4 consumption occurring within borders marked by the R39 step, where a poor oxygen presence is observed.

To obtain more insights into the effects caused by poor oxygen level in the methane area, the evolution of CH_4 chemistry for τ >0.4 is investigated. As such, on figure 5.37 are compared, for each dilution case, the carbon atom pathways taken at τ=0.4 with those at τ=0.7.

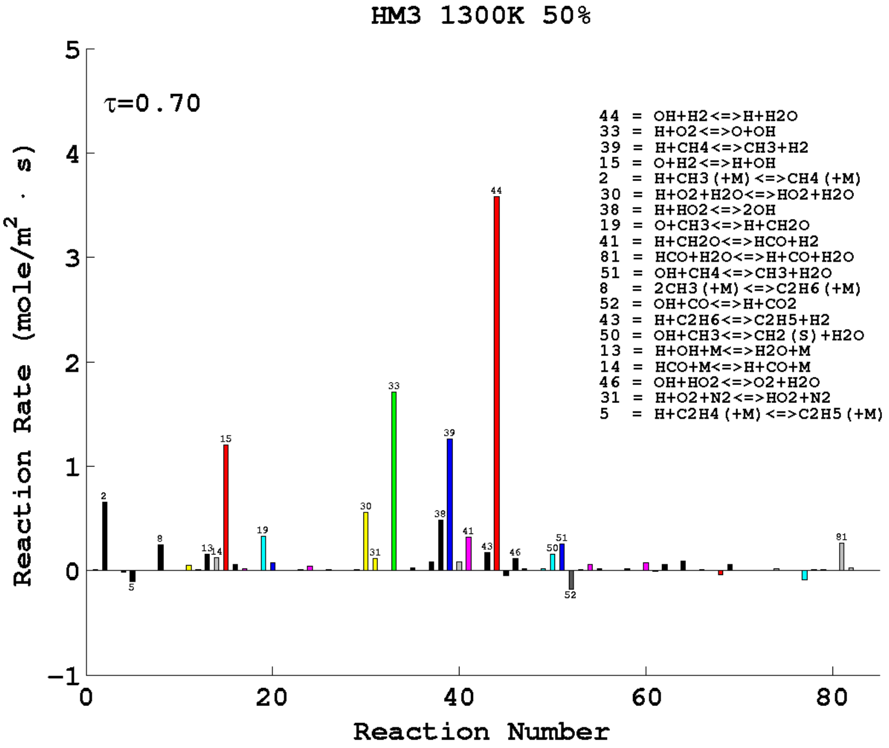

Figure 5.34: Rates of reaction of the DRM19 mechanism integrated along the cross-stream (y) direction. The reaction rates of the base case are shown.

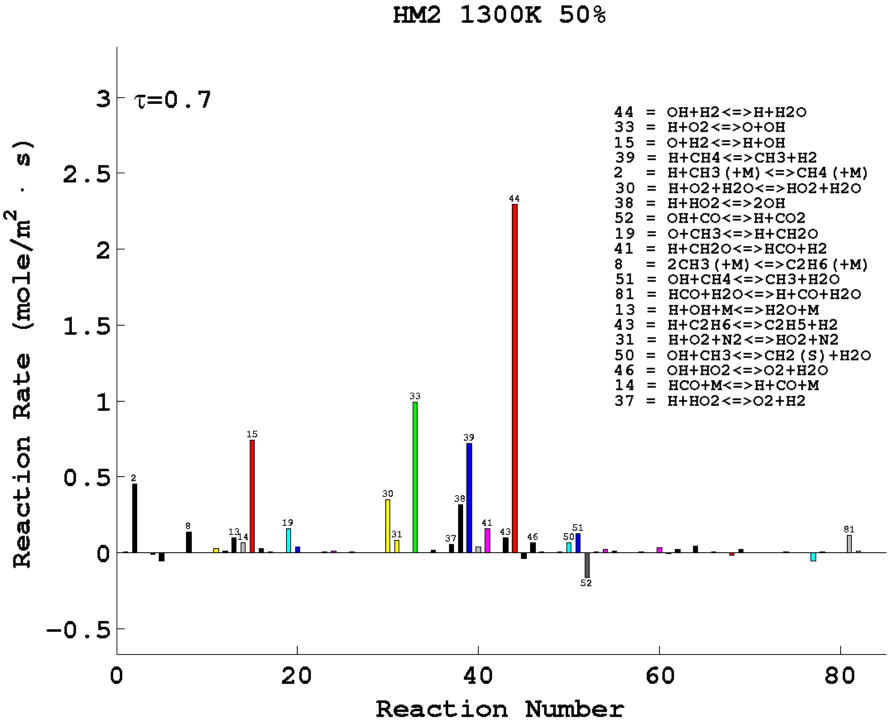

(a) HM2

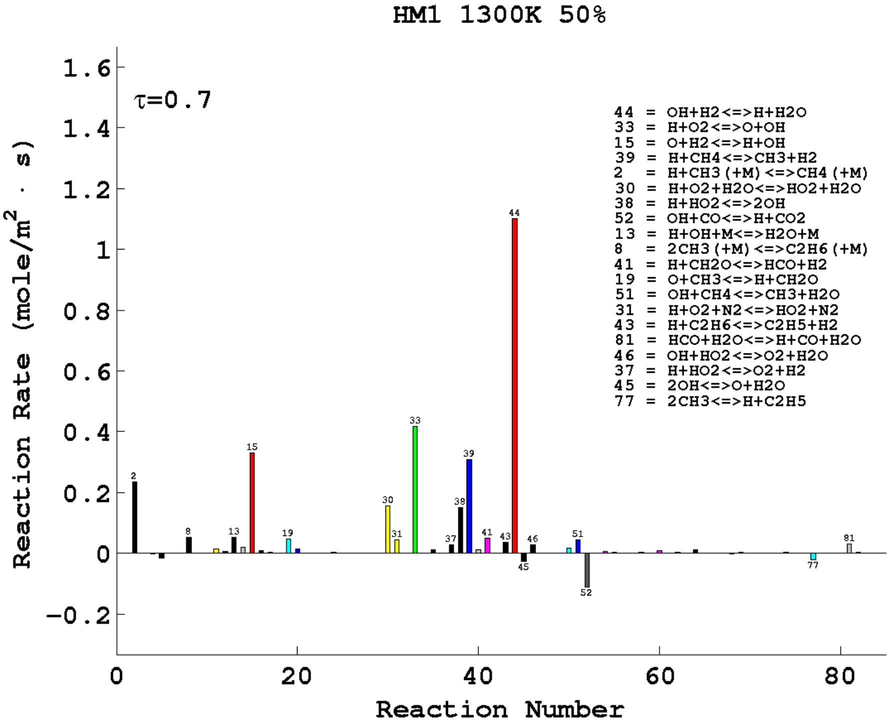

(b) HM1

Figure 5.35: Rates of reaction of the DRM19 mechanism integrated along the cross-stream (y) direction. The reaction rates of the HM2 and HM1 cases are shown. The ordinates are scaled by 1/3 (HM1) and 2/3 (HM2) with respect to the base case, to account for differences due to the oxidiser dilutions.

The comparison between figure 5.37a and 5.37b, carbon pathways for the base case, outlines for τ >0.4 a weakening of the methyl conversion along the middle branch of the $CH_3 -> HCO$ process. In particular, the CH_3 oxidation into CH_2O (R19), which relies on the oxygen presence, is affected in a significant way. In contrast the CH_3 recombination is enhanced, even though the C_2H_6 formation does not contribute to HCO release. As a consequence, the methyl conversion into HCO is reduced, as is $HCO -> CO$ process.

A similar trend is observed for HM2 (Fig. 5.37c and 5.37d) and HM1 (5.37e and 5.37f) cases. The conversion of CH_3 into HCO along the middle branches, present comparable percentage values with respect to the base case. Similar to the base case is also the reduced importance of the $CH_3 -> CH_2O$ process for τ >0.4.

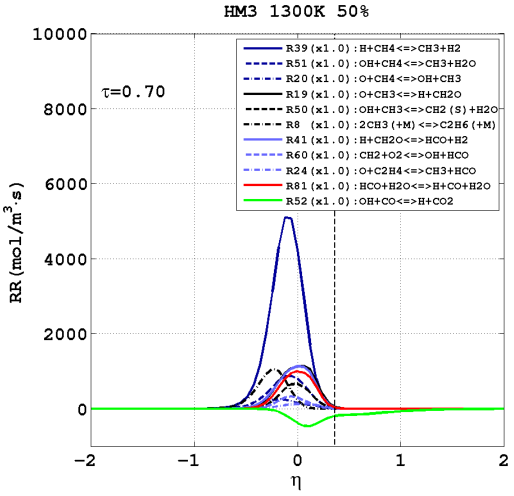

(a) HM3

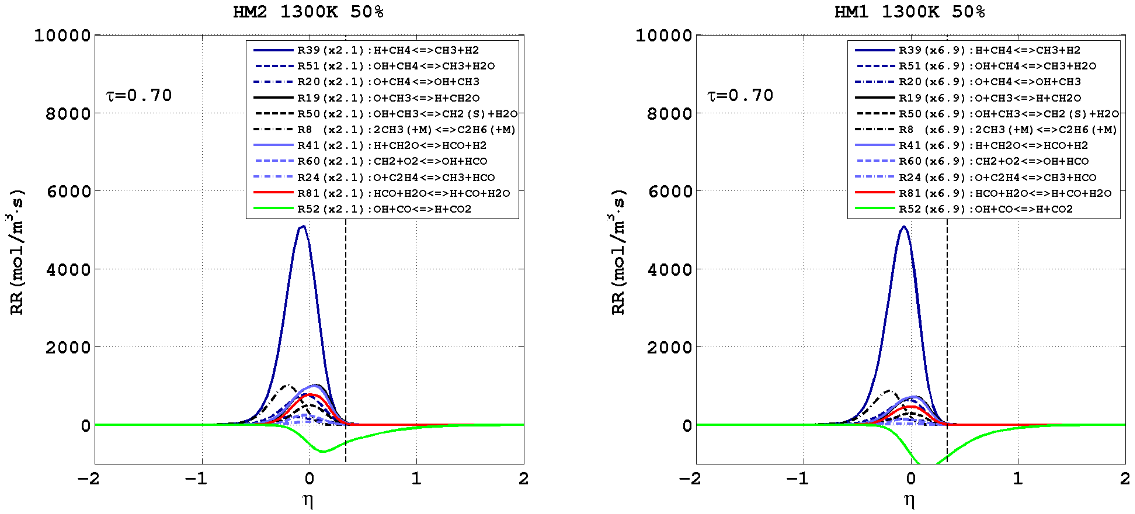

(b) HM2 **(c)** HM2

Figure 5.36: Most important rates of reaction of the methane mechanism plotted at τ=0.7 for HM3 (top), HM2 (bottom-right) and HM1 (bottom-left) case. The vertical dashed line represents the position of the stoichiometric mixture fraction region.

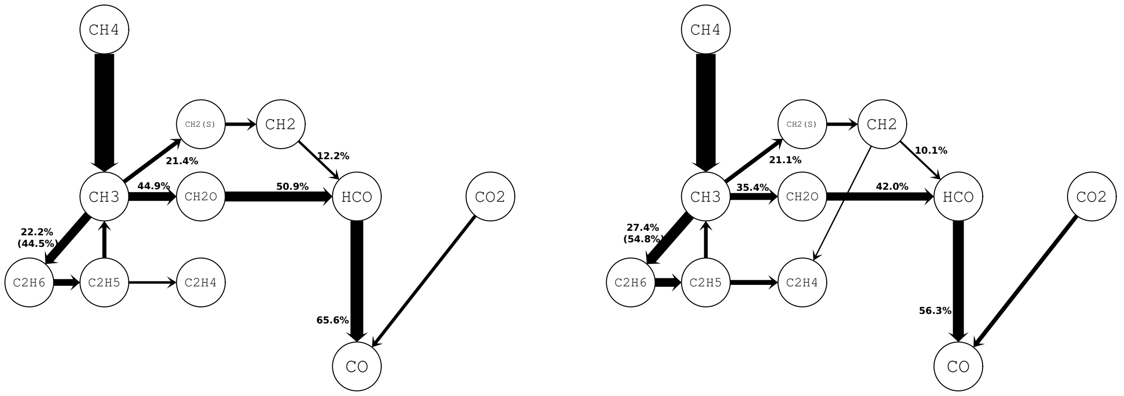

(a) HM3 **(b)** HM3

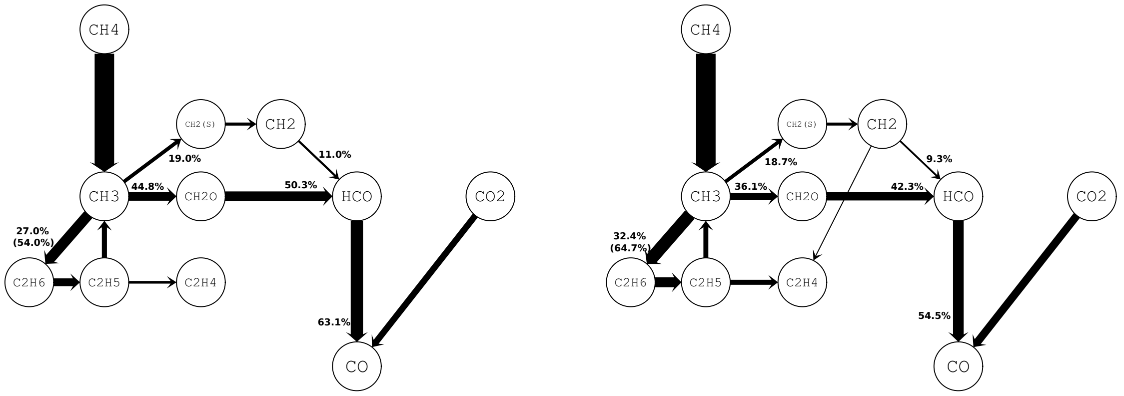

(c) HM2 **(d)** HM2

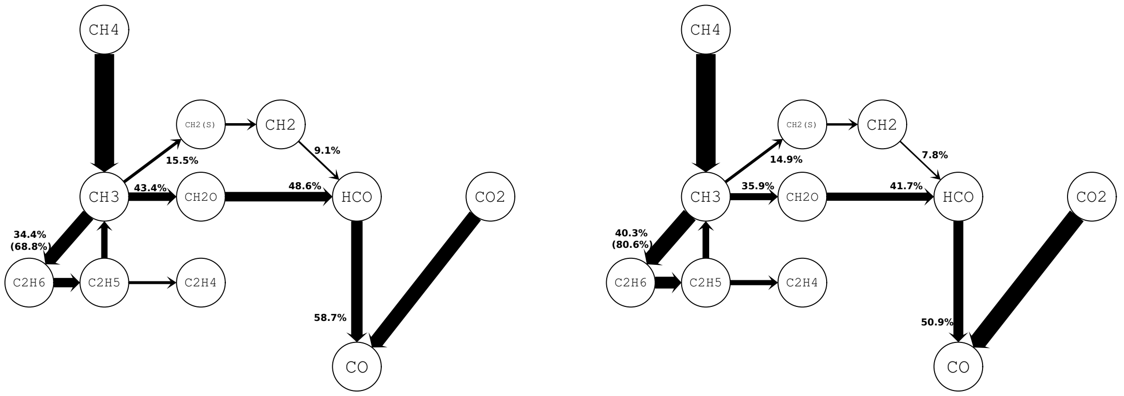

(e) HM1 **(f)** HM1

Figure 5.37: Left column: Carbon atom pathway diagrams for the HM3 (top), HM2 (middle) and HM1 (bottom) case at τ=0.4
Right column: Carbon atom pathway diagrams for the HM3 (top), HM2 (middle) and HM1 (bottom) case at τ=0.7.
Arrows are proportional to the integrated transfer rate of C atoms between species, and normalized with respect to the $CH_4 \rightarrow CH_3$ step. Percentages indicate the fraction of CH_4 destroyed along the various paths. Percentages are rounded to the upper decimal digit (+0.1%). Only arrows at least 5% of the thickest are shown.

Different from the base is the behaviour of the upper and bottom branches describing the methyl conversion. As figure 5.37d and 5.37f shows, with increasing level of dilutions, significant is the reduction of CH_3 conversion through the $CH_3 -> CH_2(s)$ process (R50), which relies, as for $CH_3 -> CH_2O$ process, on the presence of oxygen.

As a consequence of the comparable $CH_3 -> CH_2O$ conversion and a reduced importance of $CH_3 -> CH_2(s)$ process, with increasing dilution levels, a lower percentage of methyl is converted into CO.

It is interesting to note that, even more significant is the CH_3 recombination into C_2 form (R8) with high dilution levels. This is particular true in the HM1 case, where $CH_3 -> CH_2O$ is no longer the preferred methyl conversion process. As for the base case, a significant ethane conversion into HCO is not observed.

As such, the methane chemistry presents in the latest part of the ignition period, for each dilution case, an incomplete conversion of methyl build-up. This is confirmed by contours of CH_3 and HCO on figures 5.8c, 5.8f, 5.8b, 5.8e, 5.8a and 5.8d. Here, while the methyl presence remains significant in the domain for the whole post-ignition period, the HCO level significantly reduces for $\tau >$0.5.

Another interesting trend is represented by greater conversion of CO_2 into CO with increasing dilution level. This is described by bar charts on figure 5.34, 5.35a and 5.35b. With lower amount of oxygen blended in the oxidiser, the role of R52 steps becomes increasingly important.

5.6 Effect of oxygen reduction - Conclusions

The base case analysis focused on the mixing and self-ignition process, of two layers of fuel and oxidiser initially separated. The blends used to set-up the initial fuel and oxidiser made the base case the most reactive among the cases.

In this section the knowledge acquired from the base case is expanded to the HM1 and HM2 cases where the oxygen level in the oxidiser is reduced by 3 and 1.5 times respectively. Two major effects follows the oxygen dilution: the peak temperature decreases and the ignition is delayed. The more diluted is the oxidiser, the lower is the ΔT observed and the higher is the ignition delay.

The investigation of layers self-ignition is performed by analysing the physical and chemical scenarios at selected time points, spanning over the computed ignition period. The temporal normalization of ΔT curves allowed to select five time points in a way consistent with the base case. To account for the different reactants diffusion among cases, each contour plots is presented normalised over time and also space.

The analysis showed differential diffusion playing a major role in each dilution case. A larger amount of H_2 diffuses nearby stoichiometric region, causing hydrogen chemistry to have a major role in the pre-ignition period. The CH_4 presence in the reaction area is instead more limited. Each dilution case outlines two different paths along which methane and hydrogen are mostly being consumed: the hydrogen path lies closer to the oxidiser layer while methane locates below it.

Because of the larger H_2 presence, the kinetic scenario of the reaction zone is dominated by hydrogen chemistry since the earliest part of the ignition period. The H_2/O_2 interaction is observed to control the formation of the radical pool. With higher oxygen dilutions, reduced is H/O/OH excess causing self-ignition to be delayed.

As the flame fronts propagate towards the rich part of the domain, a general increase of reaction rates is observed. After ignition, each dilution case show reaction zones develop mainly below the stoichiometric mixture fraction region, where they remain for the whole ignition period. The O_2 controlling effect becomes evident in the post-ignition period, when oxygen depletion causes a general decrease of reaction rates. Because of their different spatial displacement, the CH_4 and H_2 chemistry are affected differently by the lack of O_2. The investigation of the carbon atom pathways revealed the weakening of the $\mathrm{CH_3}{-}{>}\ \mathrm{CO}$ and the strengthening of the methyl recombination as the O_2 starvation consequences. These two aspects assumed increased importance as more O_2 is diluted in the oxidiser.

As the O_2 level drops, the large H excess in the radical pool enhances steps activated by atomic hydrogen. Particularly, the H excess explains the strong methyl production via R39 step and the unusual CO_2 destruction through the backward R52 reaction.

Chapter 6

1D Study - Effect of hydrogen reduction

In chapter 5, the base case (HM3-50% configuration) was compared to HM2-50% and HM1-50% configurations to gain insights into the effect of oxygen reduction on the self-ignition process. It was observed that the ignition delay, the temperature and the chemical pathway structures, all depend on the O_2 level. Also, the evidence provided showed how the higher H_2 diffusivity controls the methane consumption process and the anomalous CO_2 consumption.

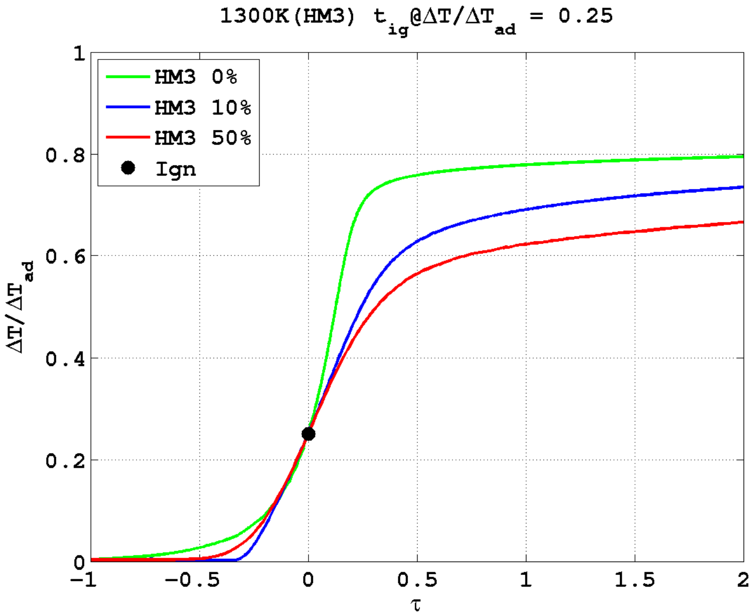

Figure 6.1: Comparison of the temperature rise curves for different level of hydrogen presence in the fuel. The profiles are presented normalised on both axis according to technique described in section 3.3.3.

With the purpose of further investigate the role of H_2 in the self-ignition process, the current chapter provides a comparison between the base case and configurations having a reduced presence of hydrogen in the fuel. More precisely, the HM3-50% case is compared to cases having 10% and 0% (by mole) of H_2 in the fuel. The reduction in hydrogen is balanced by increasing the CH_4 presence. Since the oxygen concentration is fixed at 9% by mass (HM3), the three cases analysed will be often referred as 50%, 10% and 0% or, *fuel blends* or *dilution cases.*

As figures 6.2a, 6.2b and 6.2c demonstrate, the H_2 concentration heavily impacts the self-ignition. Here the temperature increase (ΔT) for each case is plotted against time (t) on a double axis diagram which also show the temperature ($\Delta T/\Delta T_{\mathrm{ad}}$) and time ($\tau$) in normalised form.

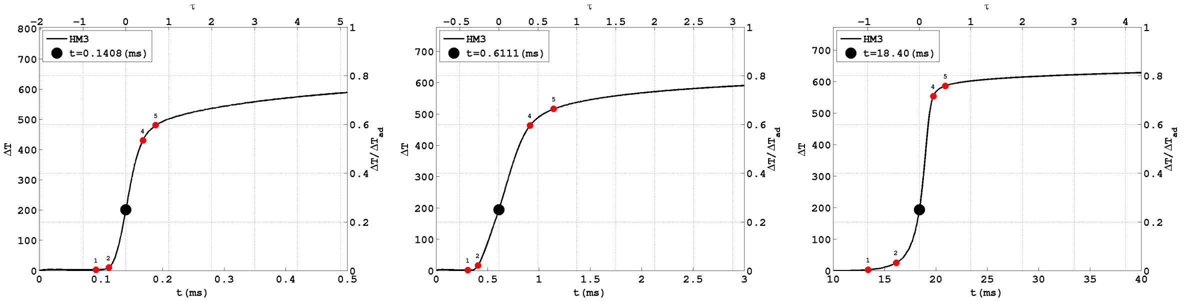

(a) HM3 50% **(b)** HM3 10% **(c)** HM3 0%

Figure 6.2: Temperature rise (ΔT) plotted against time for the 50% (left), 10% (middle) and 0% (right) case. Each graph is presented on a double axis to account for the temperature ($\Delta T/\Delta T_{\mathrm{ad}}$) and time ($\tau$) normalisation. The five circles overlaying each curve represent the points at which the physical and chemical properties of each configuration are investigated.

The pure methane configuration requires approximately 18ms to ignite. The addition of 10% (by mole) of hydrogen to the fuel, ignites the reactants 30 times quicker (t_{ig} ∼0.61ms). An even earlier ignition occurs (t_{ig} ∼0.14ms) by using 50% of H_2 in the fuel blend. In contrast, the H_2 contribution to the temperature rise is small, with all configurations showing a temperature increase of about 600K .

The effects of H_2 concentration are investigated with the help of the temporal normalisation technique described in section 3.3.3. The ignition periods of the three cases, once normalised, are mainly enclosed within the [-0.7,0.7] τ range (Fig. 6.1), the same temporal range used to analyse the base case and the oxygen reduction effects (Chap. 4 and 5) [1]. Therefore, to investigate the hydrogen reduction effect within the ignition period, five points are selected in the [-0.7,0.7] temporal range on each curve, chosen consistently with the set of qualitative rules provided in chapter 4. It should be noted that low hydrogen cases (HM3-10% and HM3-0%) shows different ignition behaviours compared to the base case. In particular the $\Delta T/\Delta T_{\mathrm{ad}}$ profile for the pure methane case (Fig. 6.1) outlines a slow temperature rise in the first part of ignition, and a relatively more steep gradient in the post-ignition period. As a consequence, the same set of investigation points employed to describe the O_2 reduction effects (τ=-0.7, -0.4, 0.0, 0.4 and 0.7) could not be entirely used, since not completely fulfilling the above mentioned criteria.

---

[1] The only exception is represented by the first part of pure methane ignition, which occurs slightly earlier than τ=-0.7

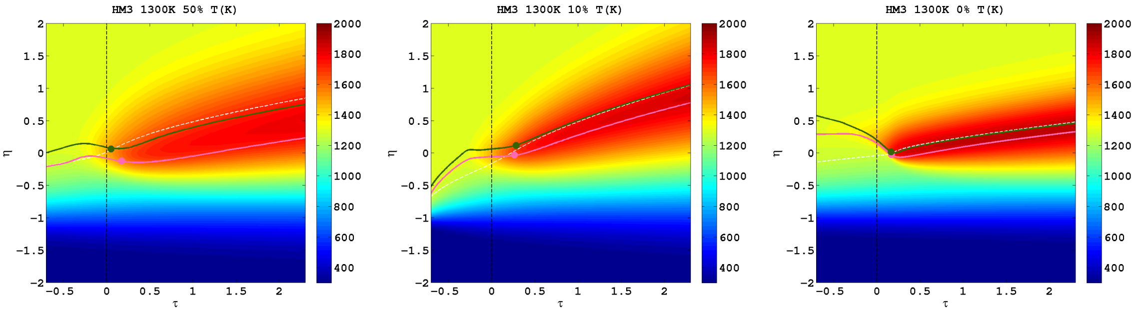

(a) 50% **(b)** 10% **(c)** 0%

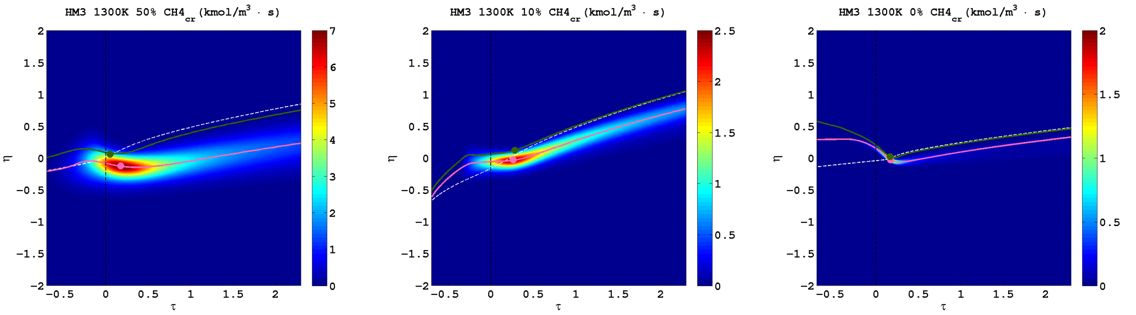

(d) 50% **(e)** 10% **(f)** 0%

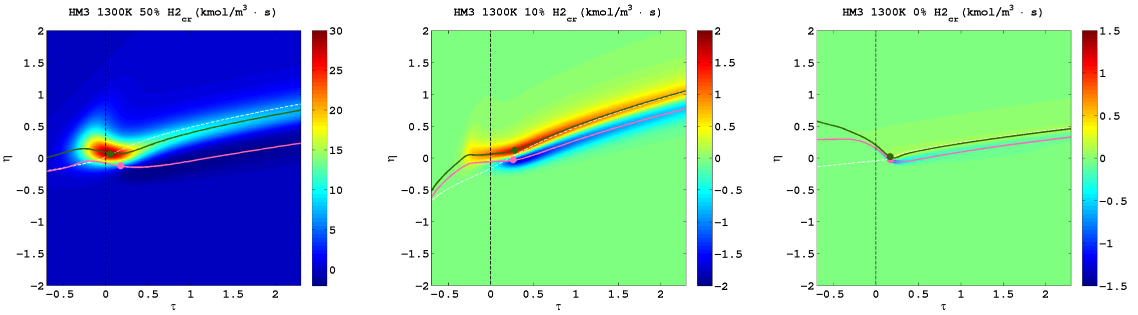

(g) 50% **(h)** 10% **(i)** 0%

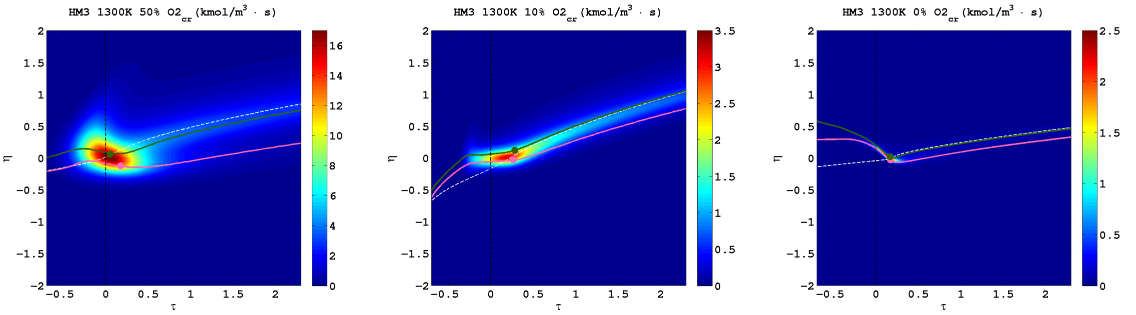

(j) 50% **(k)** 10% **(l)** 0%

Figure 6.3: Comparison of the temperature (first row), methane consumption rate (second row), hydrogen consumption rate (third row) and oxygen consumption rate (fourth row) fields for the 50% (left), 10% (middle) and 0% (right) case. Fields are presented normalised on both axis.

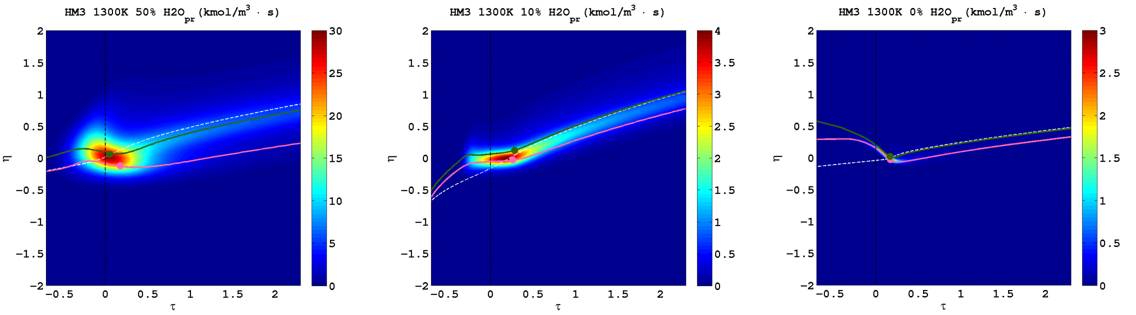

(a) 50% **(b)** 10% **(c)** 0%

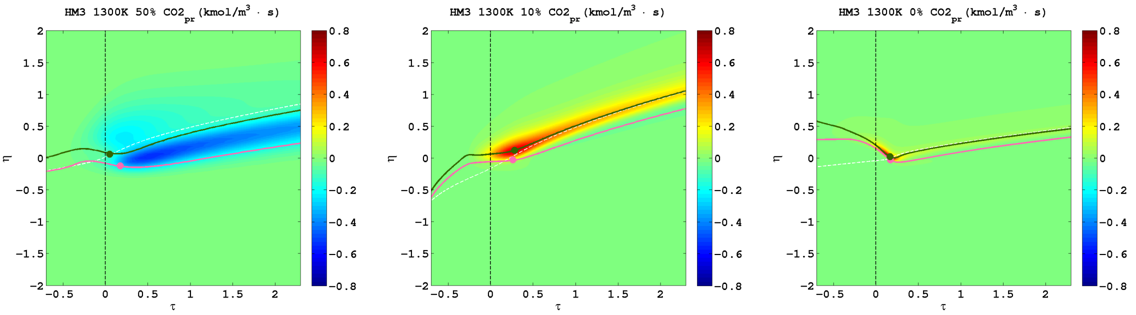

(d) 50% **(e)** 10% **(f)** 0%

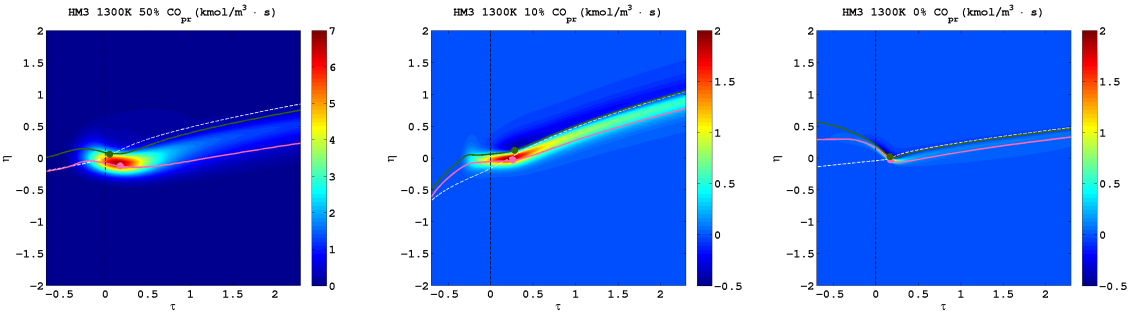

(g) 50% **(h)** 10% **(i)** 0%

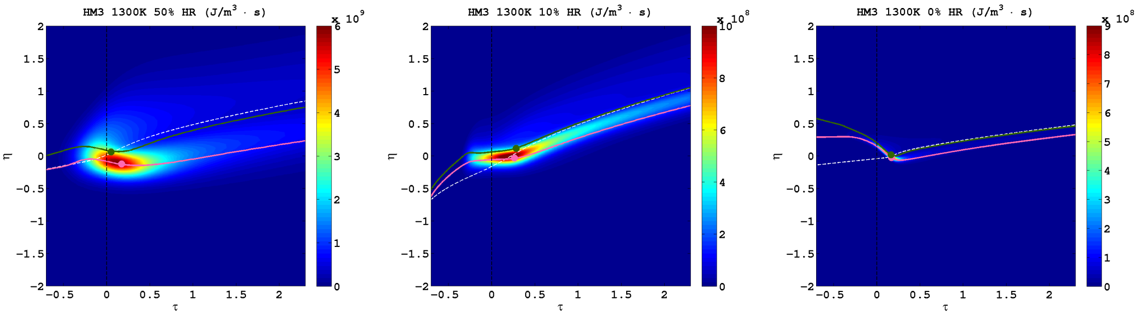

(j) 50% **(k)** 10% **(l)** 0%

Figure 6.4: Comparison of the water production rate (first row), carbon dioxide production rate (second row), carbon monoxide production rate (third row) and heat release (fourth row) fields for the 50% (left), 10% (middle) and 0% (right) case. Fields are presented normalised on both axis.

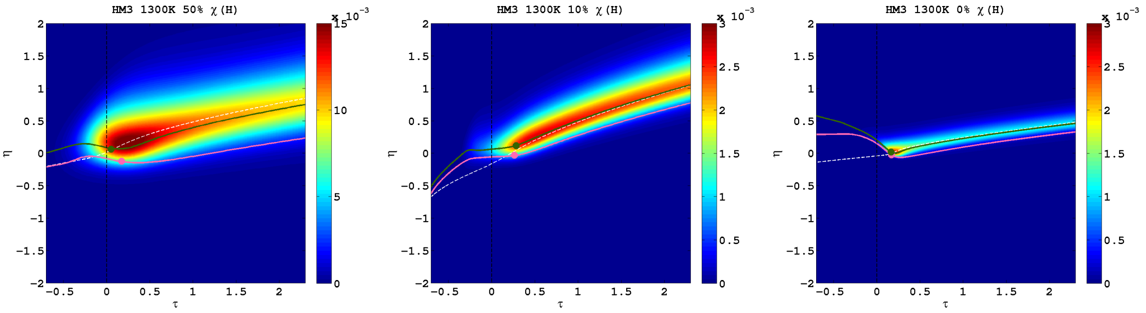

(a) 50% **(b)** 10% **(c)** 0%

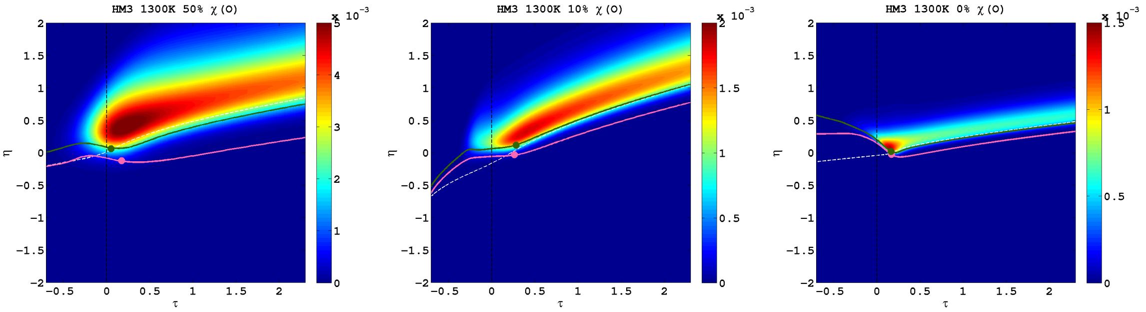

(d) 50% **(e)** 10% **(f)** 0%

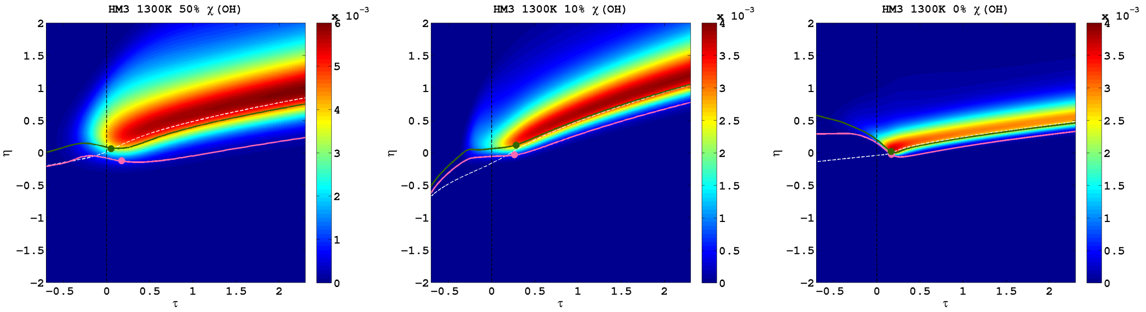

(g) 50% **(h)** 10% **(i)** 0%

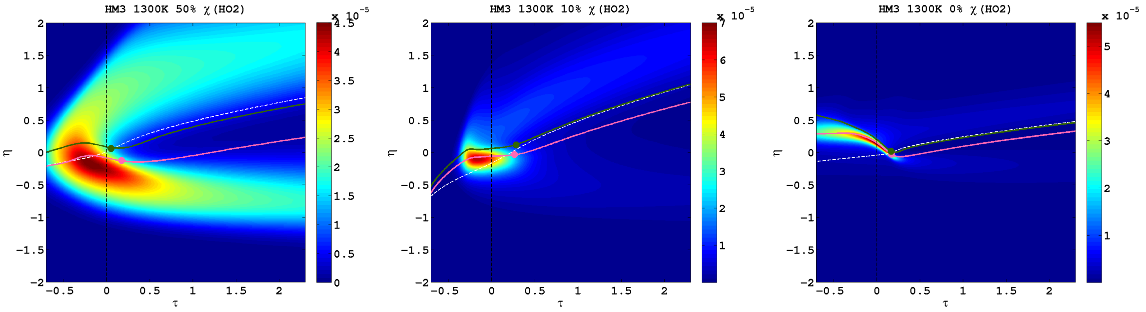

(j) 50% **(k)** 10% **(l)** 0%

Figure 6.5: Comparison of the atomic hydrogen (first row), atomic oxygen (second row), hydroxyl radical (third row) and hydroperoxyl radical (fourth row) mole fraction fields for the 50% (left), 10% (middle) and 0% (right) case. Fields are presented normalised on both axis.

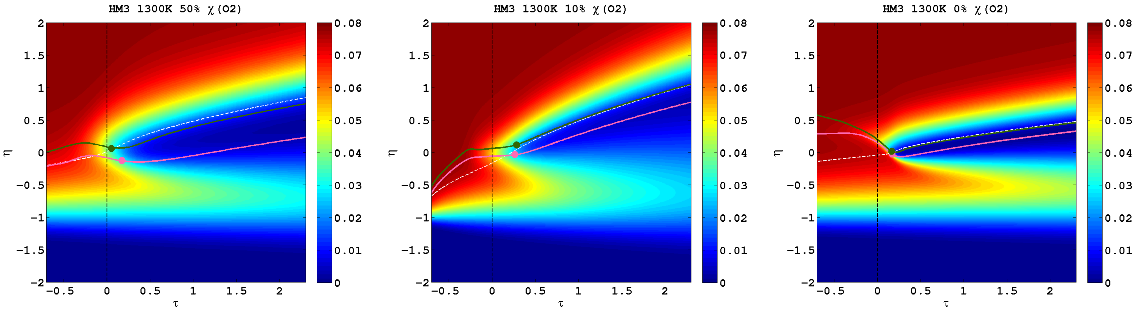

(a) 50% **(b)** 10% **(c)** 0%

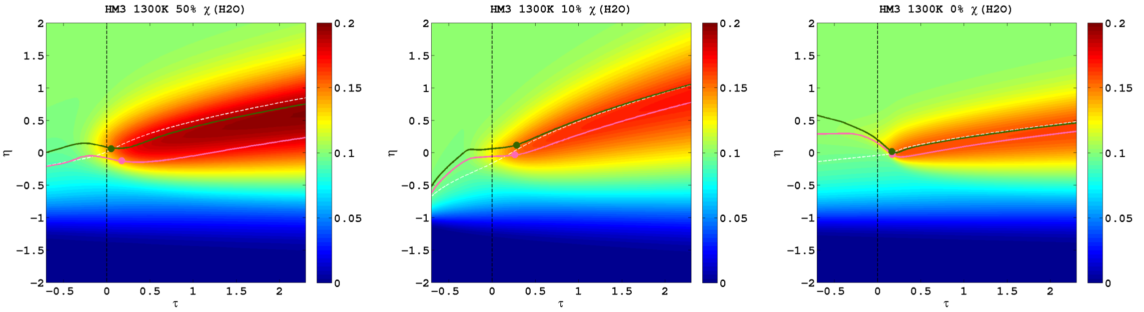

(d) 50% **(e)** 10% **(f)** 0%

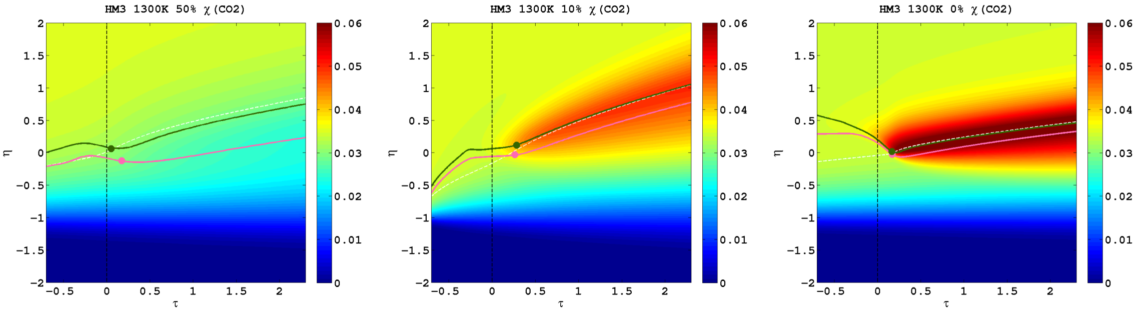

(g) 50% **(h)** 10% **(i)** 0%

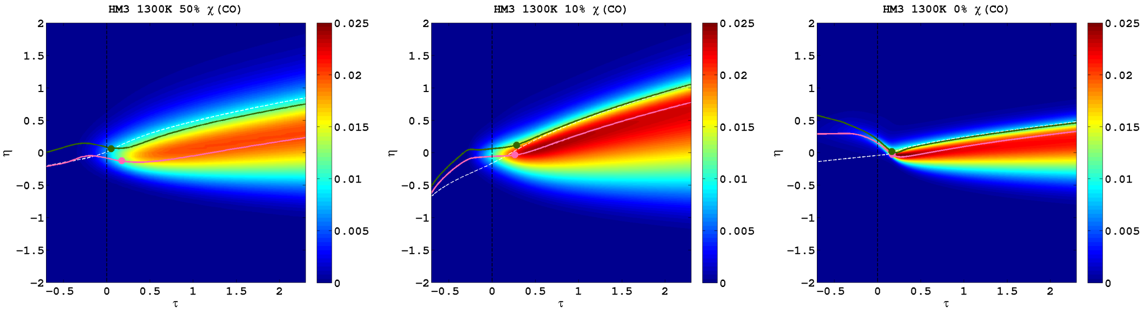

(j) 50% **(k)** 10% **(l)** 0%

Figure 6.6: Comparison of the oxygen (first row), water (second row), carbon dioxide (third row) and carbon monoxide (fourth row) mole fraction fields for the 50% (left), 10% (middle) and 0% (right) case. Fields are presented normalised on both axis.

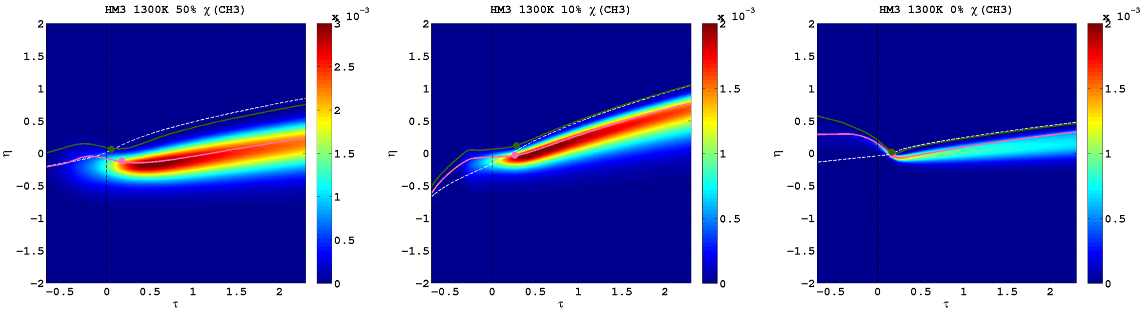

(a) 50% **(b)** 10% **(c)** 0%

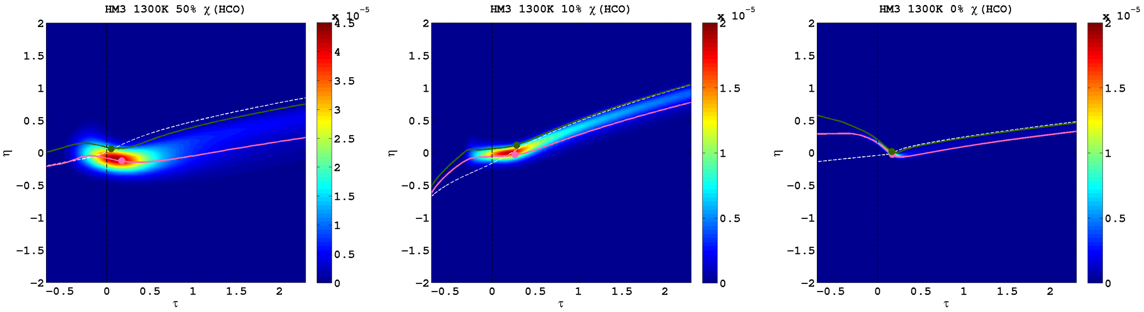

(d) 50% **(e)** 10% **(f)** 0%

Figure 6.7: Comparison of the methyl (first row) and aldehyde (second row) mole fraction fields for the 50% (left), 10% (middle) and 0% (right) case. Fields are presented normalised on both axis.

To this end, points 1 and 2 of 10% case has been chosen at τ=-0.4 and τ=-0.27. Similarly, points 1, 2, 4 and 5 of the 0% case have been selected respectively at τ=-1, -0.45, 0.27 and 0.5. The remaining selection points were chosen consistently to the O_2 reduction effects case study (Fig. 6.2a, 6.2b and 6.2c).

The characterisation of the self-ignition process, across the different time points, for each fuel blend considered, will be often supported by the analysis and comparison of the space-time contour plots. As a consequence of the big impact that H_2 reduction has on the self-ignition time, reactants in 10% and 0% case take significantly longer, with respect to 50% case, to diffuse along cross-stream direction (y) before being consumed, making comparison among contour plots more difficult. In order to account for these diffusion differences, the cross-stream (y) direction has been normalised consistently with equation (5.1) described in chapter 5.

The space normalisation, along with the time normalisation are applied on each contour. The time period of interest ($\tau \in$[-0.7,0.7]) is entirely included within the τ range described by the contours. With the purpose of simplifying the thesis structure, the whole set of fields used (temperature, species consumption/production rate, species mole fraction and intermediates mole fraction) is following shown (Fig. 6.3 - 6.7). During the analysis, these figures will be referred to as required.

6.1 Effect of hydrogen reduction - Point 1

The first investigation point focuses the analysis on the diffusion processes preceding the ignition. As shown on figures 6.2a, 6.2b and 6.2c, at this time the temperature increase is low enough that the role of chemistry can be considered negligible. On the other hand, because of the steep species gradients at the fuel/oxidiser interface, diffusion has a major role in the earliest part of ignition [2].

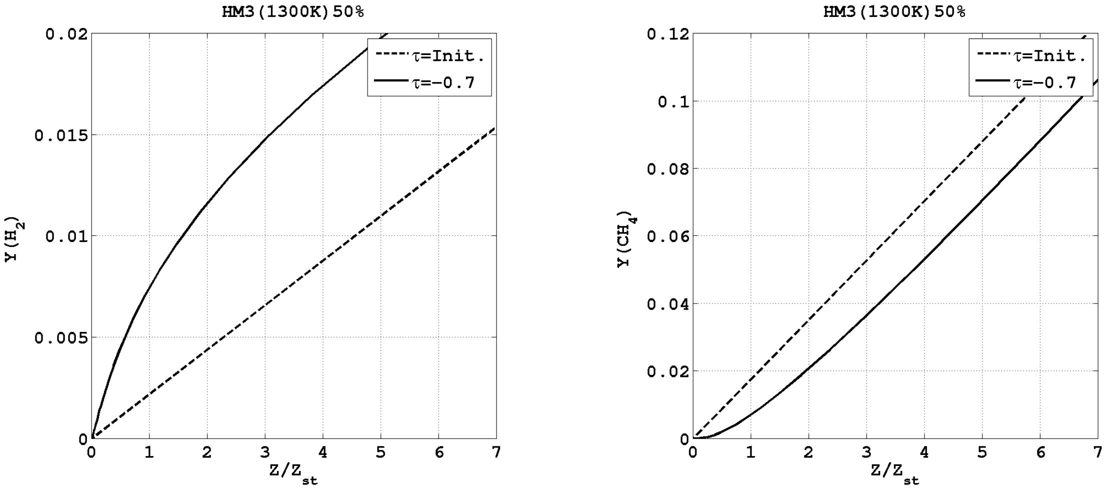

(a) H2 50% **(b)** CH4 50%

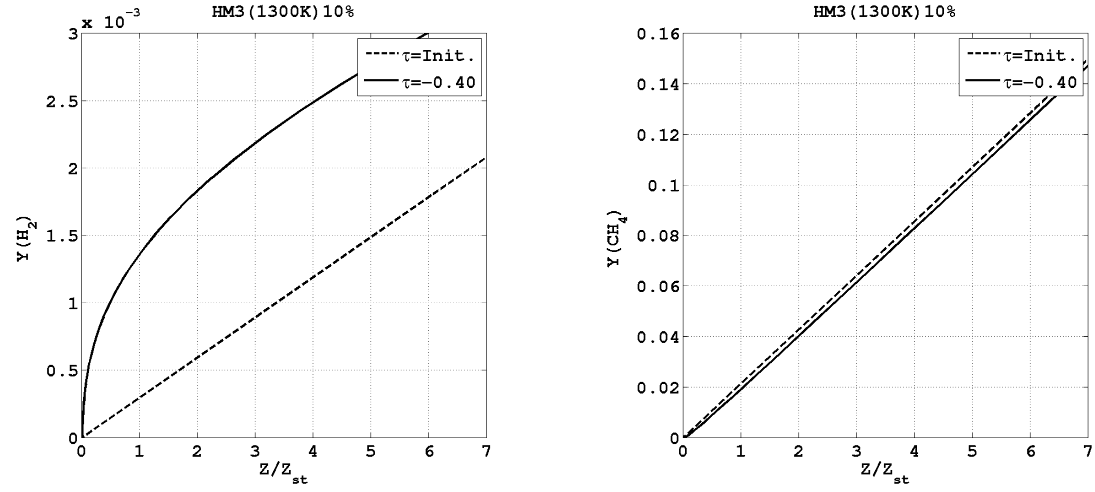

(c) H2 10% **(d)** CH4 10%

Figure 6.8: Mass fraction of H_2 and CH_4 as a function of the scaled mixture fraction (Z/Z_{st}) at τ=-0.7 and τ=-0.4 for 50% (top) and 10% (bottom) fuel blends respectively.

In section 5.1, the important role of differential diffusion was observed in HM1-50%, HM2-50% and HM3-50% cases, with H_2 diffusing more than CH_4 into the oxidiser. In this section, HM3-50%, HM3-10% and HM3-0% cases present different CH_4/H_2 ratios which could potentially

---

[2] The three different dilution cases (HM3-50%, HM3-10% and HM3-0%) have the same geometrical set-up. The fuel and oxidiser layers are initially separated with steep species gradient at the interface.

limit the H_2 diffusion into the oxidiser. As such, the presence of the methane and hydrogen in the mixture fraction space is following investigated. The differential diffusion effect is not studied for the 0% case due to the absence of H_2 in the initial fuel mixture.

The analysis (Fig. 6.8) is focused in the $Z \in [0.1 \cdot Z_{\mathrm{st}}, 7 \cdot Z_{\mathrm{st}}]$ range, where ignition is most likely to occur. This is demonstrated in figure 6.9a and 6.9b, which show the regions where heat is released in time as a consequence of exothermic reactions. Overlaid on each figure there is a set of three dashed lines. The black line indicates the region where reactants are mixed stoichiometrically (Z_{st}). The white iso-lines represent the areas where the fuel/oxidiser ratio equals $0.1 \cdot Z_{\mathrm{st}}$ (top) and $7 \cdot Z_{\mathrm{st}}$ (bottom). As figure shows, the heat released along the ignition process remain enclosed within the white lines.

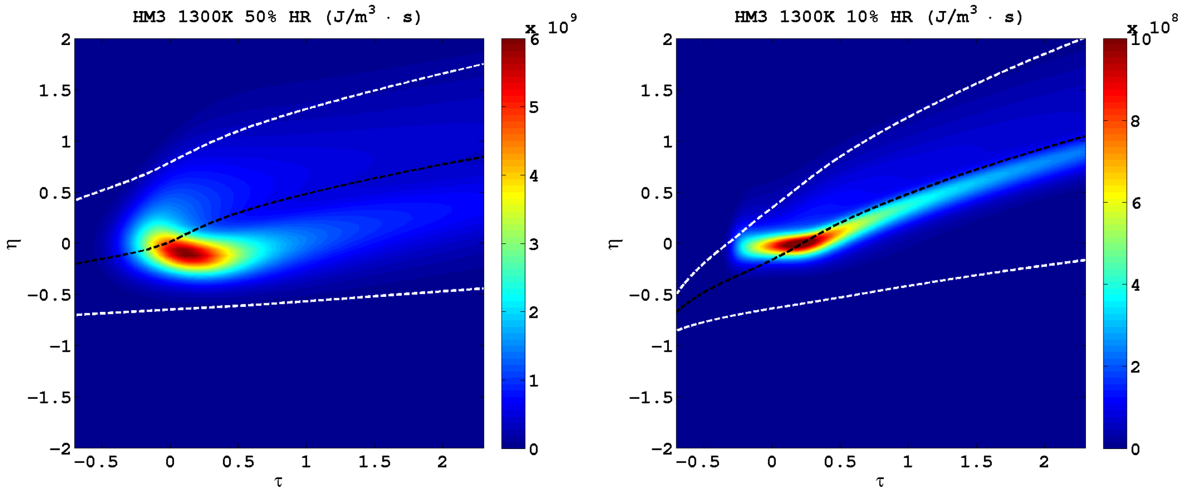

(a) HR 50%

(b) HR 10%

Figure 6.9: Comparison of heat release contours for 50% (left) and 10% (right) cases. Each contour is enclosed between two white dashed lines. The black dashed line indicates the stoichiometric mixture fraction region. The two white dashed lines above and below the black line correspond to 0.1 and 7 times the stoichiometric mixture fraction value respectively.

The mass fraction of H_2 (Fig. 6.8a and 6.8c) and CH_4 (Fig. 6.8b and 6.8d) is plotted against scaled mixture fraction space (Z/Z_{st}) at two different times. The initial separation of the fuel/oxidiser layers is shown for both 50% and 10% cases by the linear trend of the dashed lines at t=0. As the species gradient starts being smoothed by diffusion, the linear trend is no longer observed.

As pointed out in section 4.1, at τ=-0.7 for the base case the differential diffusion of H_2 and CH_4 (Fig. 6.8a and 6.8b) results in an increased hydrogen mass fraction and a decreased methane mass fraction, outlining quicker H_2 diffusion into the region where ignition occurs.

Despite the significant reduction in hydrogen level, at τ=-0.4 the 10% case still present a faster H_2 diffusion in the reaction area. Figures 6.8c and 6.8d show an increased hydrogen and a slight decreased methane mass fraction near the stoichiometric region. As such, a variation of the initial 90/10 CH_4/H_2 molar ratio is observed. However, the presence of H_2 in the stoichiometric region is not as dominant as for the base case. The H_2 mass fraction results is in fact approximately five times lower then the corresponding 50% case at Z/Z_{st}=1 (Fig. 6.8a and 6.8c).

How much the addition of hydrogen affects the structure of the methane pathway in the early part of ignition, and how the addition of hydrogen contributes to the self-ignition process, is investigated by comparing the kinetic pathway of the pure methane case against the 10% and 50% configurations at point 2.

6.2 Effect of hydrogen reduction - Point 2

Point 2 is used to analyse the first chemical differences observed between the 50%, 10% and 0% cases. At this time (τ=-0.4 for the 50% case, τ=-0.27 for the 10% case and τ=-0.45 for the 0% case), chemistry starts being relevant as shown by the initial rise of temperature (Fig. 6.2a, 6.2b and 6.2c). The comparison starts by summarising the major aspects previously observed in the base case. These aspects are then compared with physical and chemical scenarios observed in the pure methane case and in the 10% case.

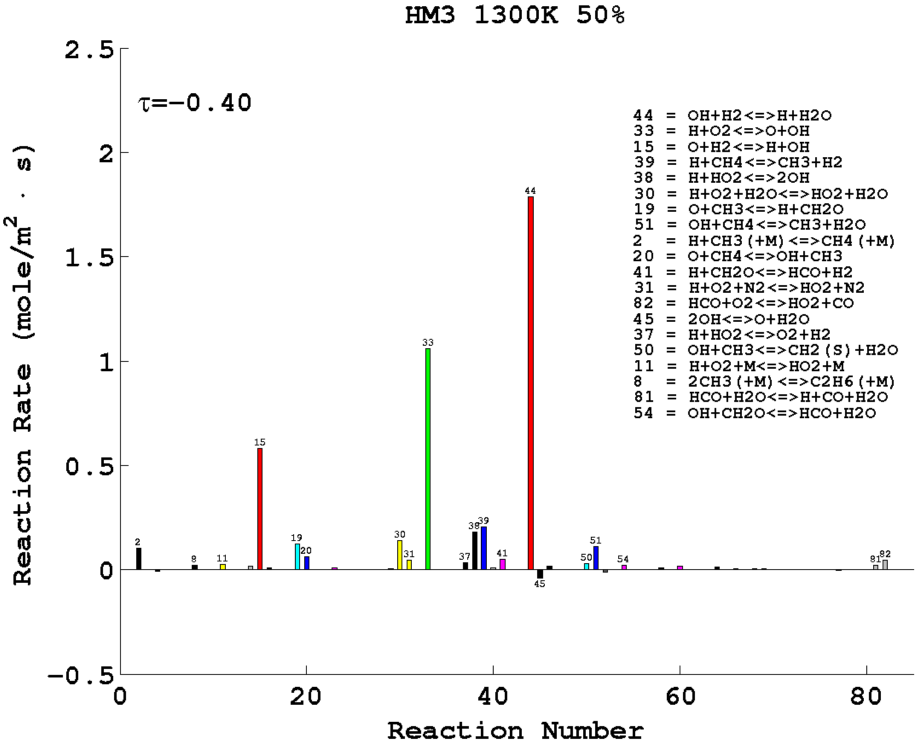

Figure 6.10: Rates of reaction of the DRM19 mechanism integrated along the cross-stream (y) direction. The reaction rates of 50% case are shown.

Because of the large presence of hydrogen in the Z_{st} region, the pre-ignition phase of the base case was characterised by two linked aspects: the dominant role of the hydrogen chemistry (Fig.6.10) and the large excess of H atom in the H/O/OH radical pool (Fig. 6.11). Three processes were observed as having a major role in the radical pool formation and, thereby, in the start of the chain reaction: the hydrogen (R15 and R44) and the oxygen (R33) consuming processes (Fig. 6.10). The R15 (branching) and R44 (propagating) steps were the only significant H_2 consuming processes observed. More processes were observed competing for O_2 (Fig. 6.10), although R33 (branching) playing a major role.

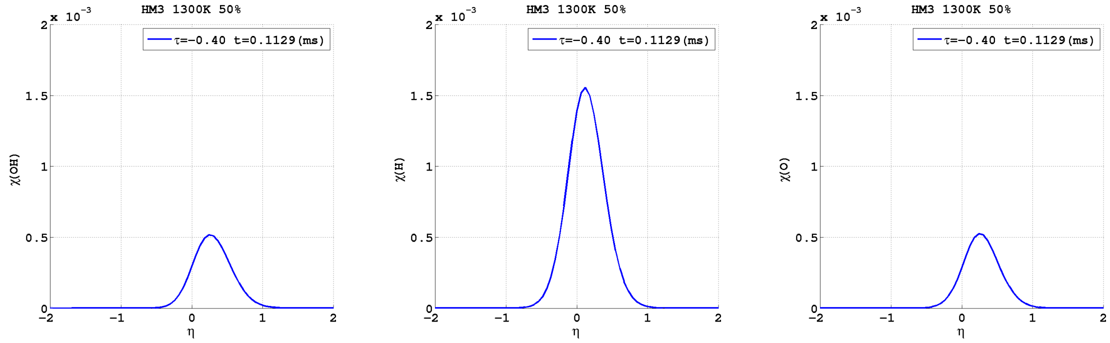

(a) OH **(b)** H **(c)** O

Figure 6.11: Level of OH (left), H (middle) and O radicals in the pre-ignition period. The radical pool of the base case is shown.

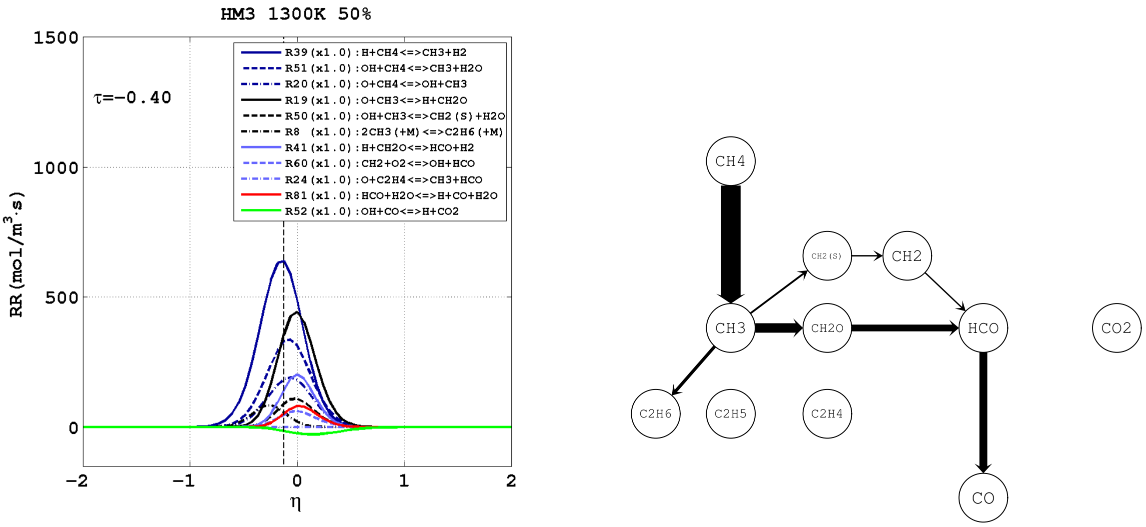

(a) H_2=50% **(b)** H_2=50%

Figure 6.12: Left: Most important rates of reaction for the methane mechanism plotted at τ=-0.4 for the base case. The vertical dashed line represents the position of the stoichiometric mixture fraction.
Right: Carbon atom pathway diagrams for 50% case. Arrows are proportional to the integrated transfer rate of C atoms between species, and normalized with respect to the $CH_4 \rightarrow CH_3$ step. Only arrows at least 5% of the thickest are shown.

Along with branching and propagating, also termination steps (R11, R30 and R31) were caught in the pre-ignition period. Those chain-termination reactions act as sinks for H radicals in the first part of ignition [42, 69]. The HO_2 molecule (hydroperoxyl) which results from R11, R30 and R31, remains stable and is build-up at low temperature while is re-converted into radicals when the temperature rises.

While hydrogen consumption was observed to be mainly advanced by R15 and R44 and terminated by R11, R30 and R31, the CH_4 consumption evidenced a slower but more complex process. The methane abstraction (dehydrogenation of CH_4 molecule) is advanced by R20, R39 and R51 reactions activated respectively by the O, H and OH (Fig.6.10), with R39 presenting the highest rate (Fig. 6.12a). The methyl build-up was observed to be mainly consumed through the path:

$$CH_3 \longrightarrow CH_2O \longrightarrow HCO$$

as shown by the middle branch of the carbon pathway (Fig. 6.12b). The CH_3 molecule is oxidised via R19 to CH_2O, while the following $CH_2O->$ HCO process proceed through two different steps: R41 and R54 (Fig.6.10). Low rate CO producing steps (R81 and R82) were also caught. The final step of the methane chain ($CO-> CO_2$) was not observed in the carbon pathway, although figures 6.10 and 6.12a caught a low CO_2 consumption via R52.

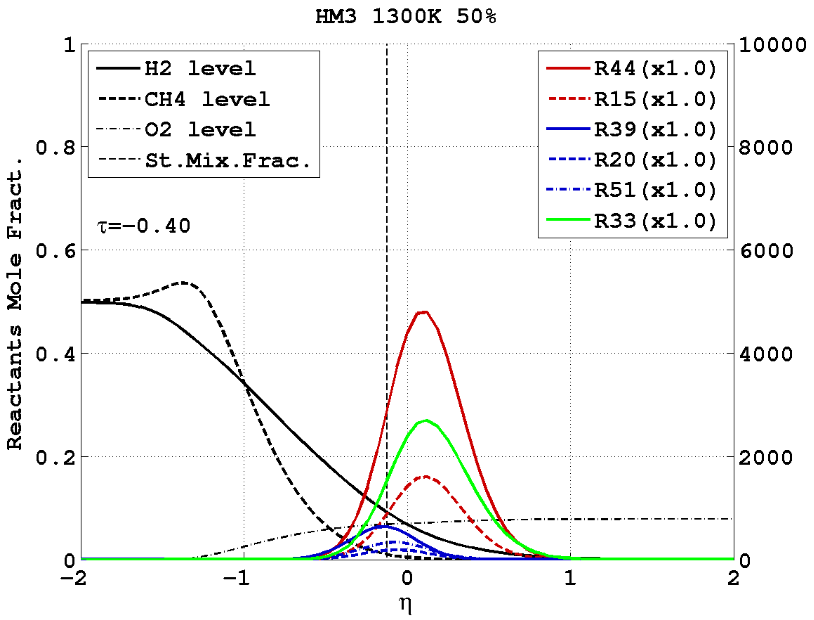

Figure 6.13: Rates of reaction representative of hydrogen (red) and methane (blue) mechanisms plotted with the fuels and oxidiser mole fraction along the cross-stream direction. Figure shows data from HM3-50% case. The right axis expresses the rate of reaction in mol/m^3·s.

Figure 6.13 shows some rates of reaction representative of hydrogen and methane mechanisms within the reaction zone, plotted along with the fuels and oxidiser mole fraction. The figure outlines a region, locating mainly ahead Z_{st}, where H_2 and CH_4 are consumed. Within this area, H_2 and CH_4 are present with different concentrations (solid and dashed black lines). The larger availability of H_2, due to differential diffusion effects, explains the broader extension and the higher rate of hydrogen consuming reactions. Conversely, the reduced availability of CH_4 explains the reduced rate and reduced extension of methane consuming reactions, confined in the lower end of the reaction zone along Z_{st}. The difference in the regions of CH_4 and H_2 consumption is illustrated by the early separation of the fuel consumption paths in figure 6.3d and 6.3g, with the H_2 path locating above the CH_4 one.

The CH_4 consumption scenario in the 0% case is different and more complex. Without any hydrogen in the initial fuel blend, the methane chain reaction initiates in the fuel-lean part of the domain, ahead the Z_{st} line (Fig. 6.4l). Negligible is, as expected, the presence of H_2 consuming steps (R15 and R44) (Fig. 6.14).

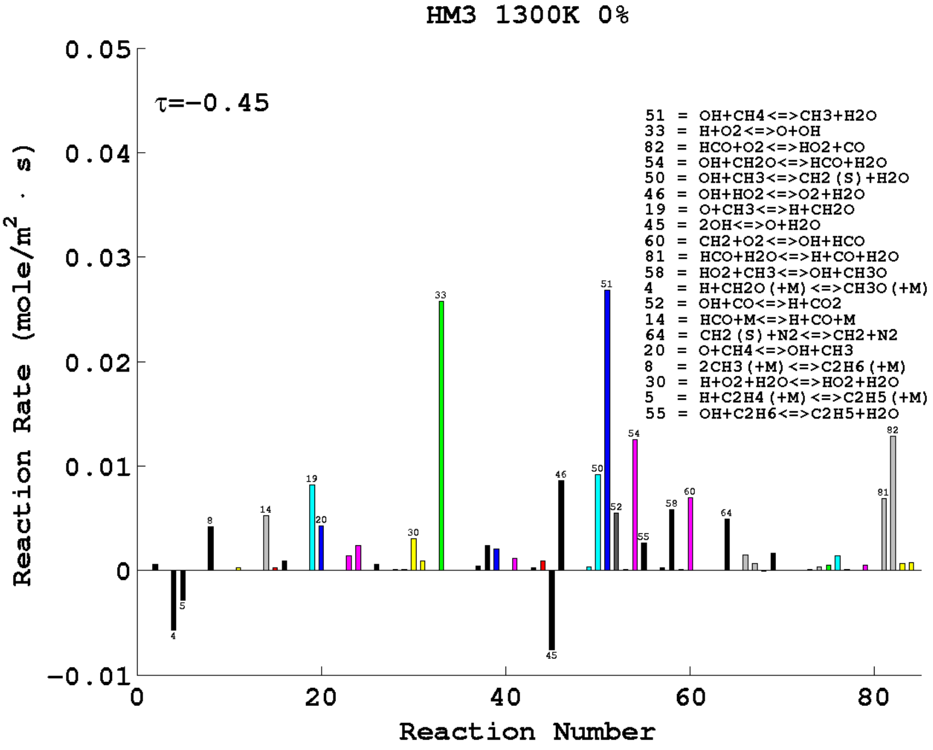

Figure 6.14: Rates of reaction of the DRM19 mechanism integrated along the cross-stream (y) direction. The reaction rates of 0% case are shown.

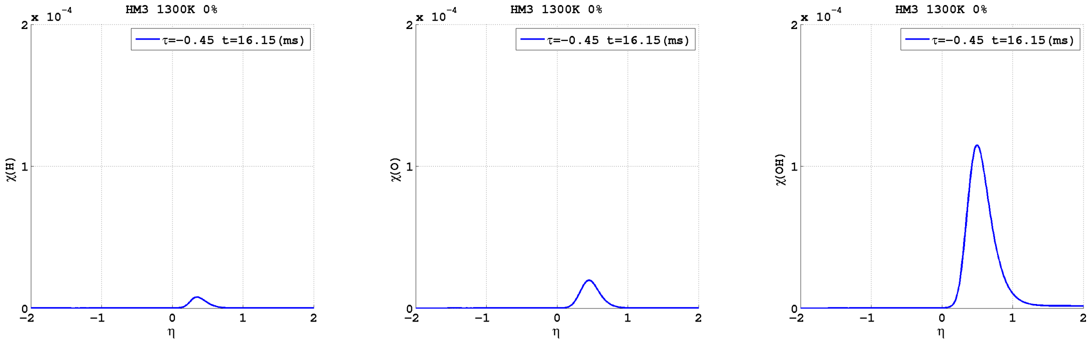

(a) H **(b)** O **(c)** OH

Figure 6.15: Level of OH (left), H (middle) and O radicals in the pre-ignition period. The radical pool of the 0% case is shown.

The reduced H production affects the rate of R33 step (O_2 consumption) and, as a consequence, affects the radical pool. The H, O and OH radicals present a significant reduction of their presence in the reaction zone. Particularly strong is the reduction of H level, which is no longer the dominant intermediate among H, O and OH (Fig. 6.15).

An estimate of the reduced fuel/oxidiser reactivity, which follow the lower radicals presence, can be obtained by analysing the R33 process, representing one of the major chain branching process observed in this study. Figure 6.16 presents reaction rates multiplied by a scaling factor which compares the R33 peak rate for the 0% case with the R33 peak value in the base case. A strong reduction is found in the reactivity of the pure methane case with respect to the base case.

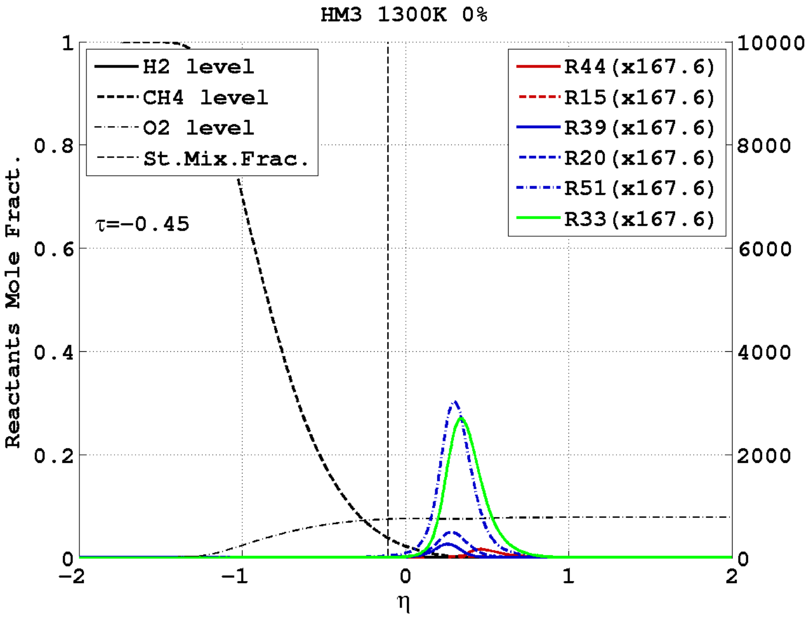

Figure 6.16: Rates of reaction representative of hydrogen (red) and methane (blue) mechanisms plotted with the fuels and oxidiser mole fraction along the cross-stream direction. Figure shows data from HM3-0% case. The right axis expresses the rate of reaction in mol/m^3·s. The scale factor compares the peak rate of the R33 step with the base case.

Together with R33, a number of different elementary reactions now control the radical pool formation. Nonetheless, dominant remains the role of chain branching R33 process, which consumes oxygen providing O and OH chain carriers (fig.6.14). While O atoms are only produced with a significant rate only by R33 [3], more steps provide to the formation of OH, which shows a dominant presence in the earliest part of the ignition process (Fig. 6.15c).

The larger presence of OH causes R51 to control the CH_4 abstraction, while the R20 and R39 show a reduced importance (Fig. and 6.17a). The set of three elementary reaction governing

---

[3] As bar chart in figure 6.14 shows, also R45 describe the O production. Nonetheless, R45 step outline a backward trend (O consumption) in the whole ignition period

the CH_4 abstraction is as follow:

$$O + CH_4 \longleftrightarrow CH_3 + OH \tag{R20}$$
$$H + CH_4 \longleftrightarrow CH_3 + H_2 \tag{R39}$$
$$OH + CH_4 \longleftrightarrow CH_3 + H_2O \tag{R51}$$

The $CH_3 -> HCO$ process, differently to the base case, proceeds through three different branches, as shown on figure 6.17b. The middle branch describes the methyl oxidation into CH_2O via R19 and the subsequent $CH_2O -> HCO$ step through R41 and R54 processes, as follow:

$$CH_3 + O \longleftrightarrow CH_2O + H \tag{R19}$$
$$CH_2O + H \longleftrightarrow HCO + H_2 \tag{R41}$$
$$CH_2O + OH \longleftrightarrow HCO + H_2O \tag{R54}$$

where the role of R41 is shown as minor contribute in the pre-ignition phase (Fig. 6.14).
The upper branch describes three different reactions ($CH_3 \rightarrow CH_2(S) \rightarrow CH_2 \rightarrow HCO$), where CH_2(S) represents the singlet state of methylene. The methyl molecule reacts with OH radical to form CH_2(S) (R50), which is then converted into with CH_2 via R64. The final $CH_2 -> HCO$ process is controlled by R60 which describes the oxidation of CH_2 with molecular oxygen. The set of processes governing the upper branch of $CH_3 -> HCO$ is as follows:

$$OH + CH_3 \longleftrightarrow CH_2(S) + H_2O \tag{R50}$$
$$CH_2(S) + N_2 \longleftrightarrow CH_2 + N_2 \tag{R64}$$
$$CH_2 + O_2 \longleftrightarrow OH + HCO \tag{R60} \cdot$$

The lower branch describes the recombination of two CH_3 radicals to form C_2H_6 via R8. The C_2H_6 molecule proceeds through a series of hydrogen abstractions (C_2H_5 and C_2H_4 via R55 and R5) that lead to the C_2H_4 conversion into HCO via R24. The role of R24 is shown as minor contribute in the pre-ignition phase (Fig. 6.14). As described by R24 expression, part of the C_2H_4 is converted back into CH_3. The set of equations describing the ethane (C_2H_6) formation and destruction is as follows:

$$2\,CH_3 + M \longleftrightarrow C_2H_6 \tag{R8}$$
$$C_2H_6 + OH \longleftrightarrow C_2H_5 + H_2O \tag{R55}$$
$$C_2H_4 + H + M \longleftrightarrow C_2H_5 + M \tag{R5}$$
$$C_2H_4 + O \longleftrightarrow CH_3 + HCO \tag{R24} \cdot$$

It should be noted that the R5 step mainly proceeds backward (Fig. 6.14).

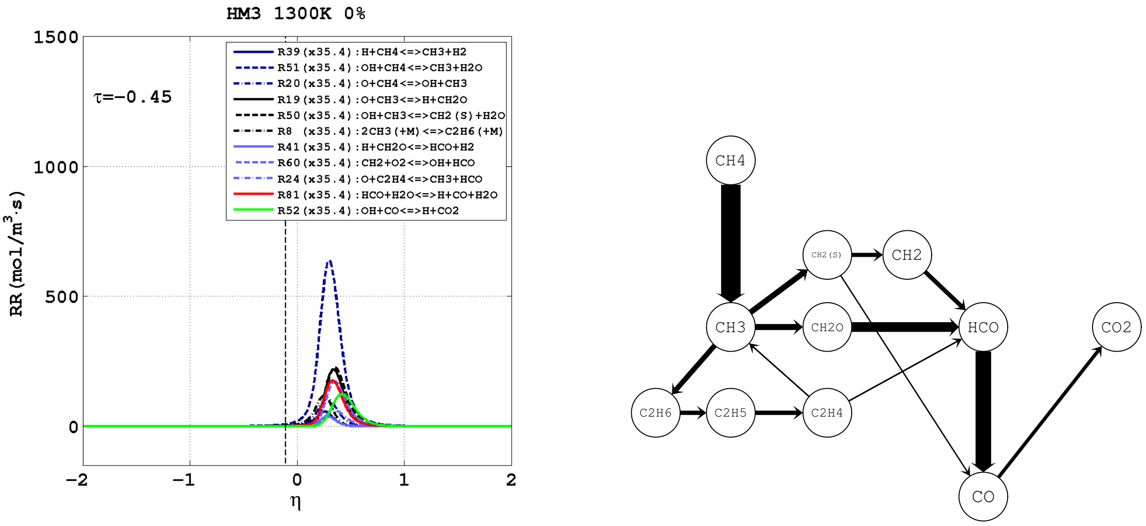

(a) H_2=0% **(b)** H_2=0%

Figure 6.17: Left: Most important rates of reaction for the methane mechanism plotted at τ=-0.45 for the 0% case. The vertical dashed line represents the position of the stoichiometric mixture fraction. The scale factor shown in figure compares the peak rate of the most important $CH_4 \rightarrow CH_3$ step with the base case.
Right: Carbon atom pathway diagrams for 0% case. Arrows are proportional to the integrated transfer rate of C atoms between species, and normalized with respect to the $CH_4 \rightarrow CH_3$ step. Only arrows at least 5% of the thickest are shown.

The $\mathrm{HCO}-> \mathrm{CO_2}$ process (Fig. 6.17b) is described by more reactions which include CO formation (Fig. 6.14). The conversion of HCO into CO occurs because of a molecular splitting (R14) or as a consequence of the HCO reaction with either water (R81) and oxygen (R82). The final $\mathrm{CO}-> \mathrm{CO_2}$ is instead mainly controlled by a single elementary reaction: R52. The set of chemical reactions describing the CO and CO_2 formation is following shown:

$$\mathrm{HCO} + \mathrm{M} \longleftrightarrow \mathrm{H} + \mathrm{CO} + \mathrm{M} \tag{R14}$$

$$\mathrm{HCO} + \mathrm{H_2O} \longleftrightarrow \mathrm{H} + \mathrm{CO} + \mathrm{H_2O} \tag{R81}$$

$$\mathrm{HCO} + \mathrm{O_2} \longleftrightarrow \mathrm{HO_2} + \mathrm{CO} \tag{R82}$$

$$\mathrm{OH} + \mathrm{CO} \longleftrightarrow \mathrm{H} + \mathrm{CO_2} \tag{R52} \cdot$$

Particularly interesting is the behaviour of the R52 process, which, differently from the base case, is now observed to proceed forward (Fig. 6.17a and 6.17b). This behaviour sheds lights on the role of OH and H radicals in controlling carbon dioxide production. In the pure methane case, with a poor presence of H (Fig. 6.15a) and higher level of OH (Fig. 6.15c) where R52 occurs (green line on figure 6.17a), the R52 step proceeds forward producing CO_2. On the contrary with a large amount of hydrogen (50%) blended in the fuel and a strong presence of H radical (Fig. 6.14) where R52 occurs (green line on figure 6.12a), the R52 proceeds backward and the CO_2 molecule results consumed. This suggests that, in agreement with the observation from the base case (Chap. 4), an excess of H_2 in the fuel blend inhibits the last step of methane chain reaction (CO$->$ CO$_2$).

As a final consideration on the methane chain reaction it is interesting to note that, despite the reduced importance of H radicals at this stage, the formation of the HO$_2$ molecule via R30 is still observed (Fig. 6.14). As a consequence, the destruction of hydroperoxyl molecule can be used as tool for identify the ignition stage also for the 0% case.

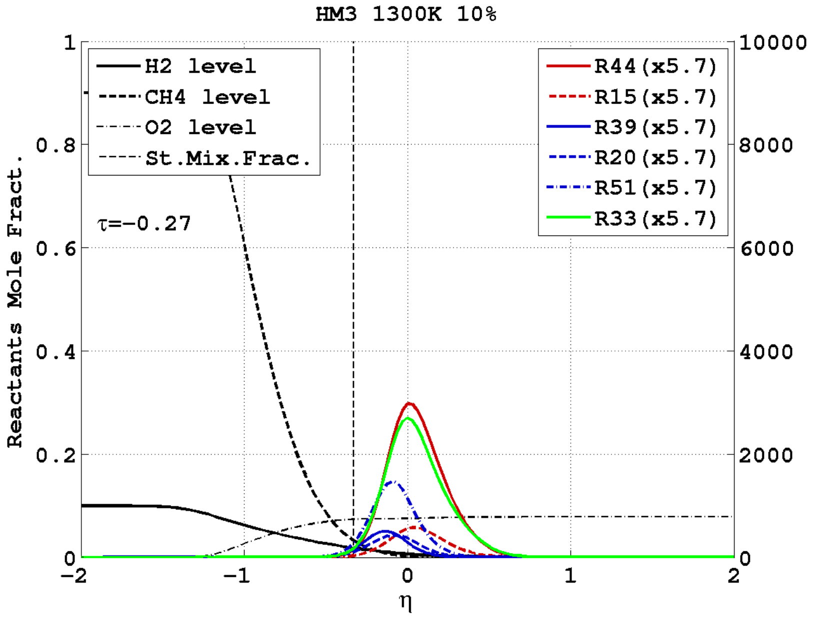

Figure 6.18: Rates of reaction representative of hydrogen (red) and methane (blue) mechanisms plotted with the fuels and oxidiser mole fraction along the cross-stream direction. Figure shows data from HM3-10% case. The right axis expresses the rate of reaction in mol/m^3·s. The scale factor compares the peak rate of the R33 step with the base case.

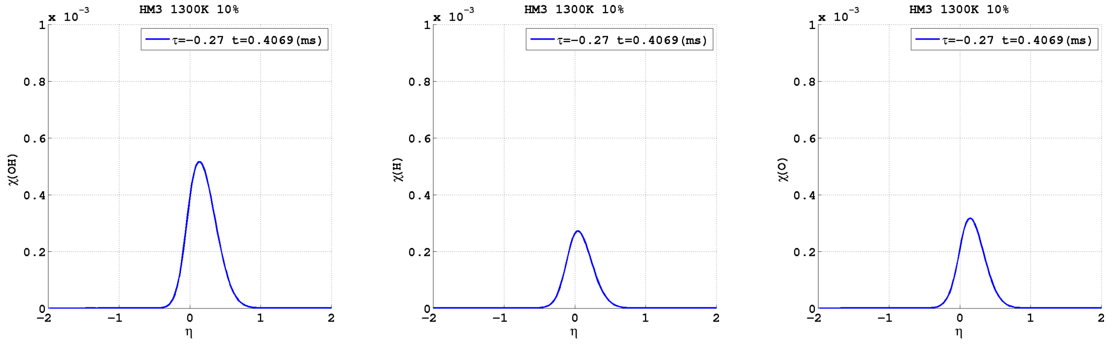

(a) OH **(b)** H **(c)** O

Figure 6.19: Level of OH (left), H (middle) and O radicals in the pre-ignition period. The radical pool of the 10% case is shown.

The chemical scenario of methane consumption change significantly with a low addition of H$_2$ within the fuel (10% of the overall fuel blend volume). As for 50% and 0% cases, the reaction zone is observed developing in the oxidiser area for $Z < Z_{st}$ (Fig. 6.3b). Here, despite the low initial hydrogen concentration limits H_2 diffusion, hydrogen consuming processes (R15 and R44) show significant spatial extension, compared to CH_4 chemistry, and important rates, particularly the R44 step (Fig. 6.18). The H radical production from R15 and R44 is beneficial for the O_2 consuming step (R33), which progresses approximately 30 times faster than the pure methane case (Fig. 6.16). This also favours the build-up of the radical pool, which presents a larger number of H, O and OH intermediates (Fig. 6.19) with respect to the pure methane case (Fig. 6.15).

Even though the hydrogen mechanism becomes prevalent with the addition of H_2, both mechanisms (H_2 and CH_4) are accelerated by the hydrogen concentration in the fuel with respect to the pure methane case, as seen by comparing figures 6.21a and 6.17a.

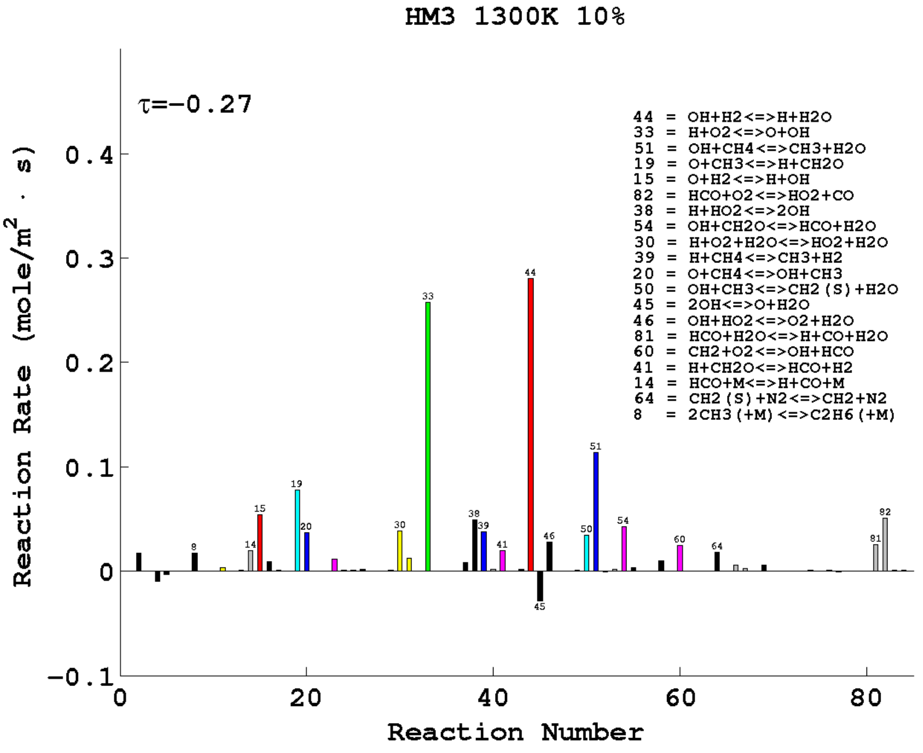

Figure 6.20: Rates of reaction of the DRM19 mechanism integrated along the cross-stream (y) direction. The reaction rates of 10% case are shown.

Figure 6.21a and 6.17a shows the most important rates of reaction for the methane consumption process. A scale factor is applied to each reaction rate profile. This factor compares the peak rate among CH_4−> CH_3 processes (R20, R39 and R51) with the one from the base case. More precisely, for 10% and 0% cases, the peak rate of R51 step in the pre-ignition period is compared with the R39 peak rate for the base case at τ=-0.4. The choice of CH_4−> CH_3 processes to calculate the scale factor is justified since they start the methane consumption process. Despite the qualitative nature of the comparison, it is possible to have a rough estimation of the faster methane consumption with the hydrogen addiction.

The hydrogen presence accelerates the methane chemistry, but it does not alter particularly the methane pathway. Few differences are in fact observed between the 10% and 0% cases. The methyl build up steps are all active (R20, R39 and R51) with R51 still playing the major role (Fig. 6.20). As for the pure methane case, the methyl consumption proceed along three different branches, with the middle one having a stronger importance (Fig. 6.21b). All reactions found responsible for the $CH_3 \rightarrow CH_2O \rightarrow HCO$ process in the pure methane case (R19, R41 and R54), are observed active in the 10% case. In a similar way, reactions R50, R60 and R64 are observed controlling the $CH_3 \rightarrow CH_2(S) \rightarrow CH_2 \rightarrow HCO$ process for both 0% and 10% cases (Fig. 6.20). Differently from the 0% case, the lower branch of the $CH_3 -> HCO$ process is inhibited in the last part ($C_2H_4 -> HCO$), as the R24 process responsible for ethylene (C_2H_4) destruction is not significant (Fig. 6.20). Another difference with the pure methane case is the lack of the $CO -> CO_2$ step (Fig. 6.21b). As already observed in the 50% case, the addition of hydrogen and the consequent increase of H radicals in the O/H/OH pool, affects the R52 step (Fig. 6.20), inhibiting the CO oxidation process.

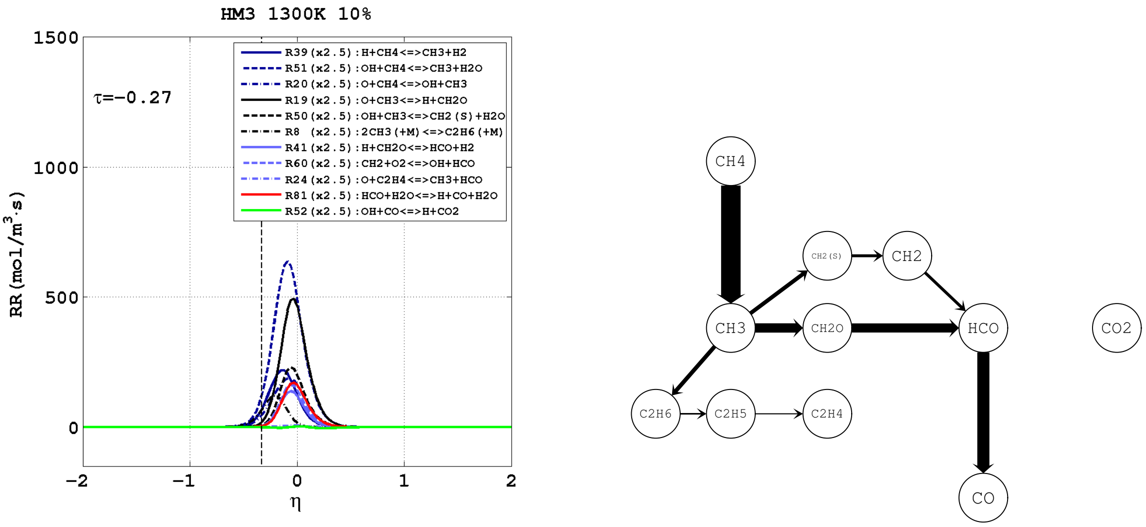

(a) H_2=10% **(b)** H_2=10%

Figure 6.21: Left: Most important rates of reaction for the methane mechanism plotted at τ=-0.27 for the 10% case. The vertical dashed line represents the position of the stoichiometric mixture fraction. The scale factor shown in figure compares the peak rate of the most important $CH_4 \rightarrow CH_3$ step with the base case.
Right: Carbon atom pathway diagrams for 10% case. Arrows are proportional to the integrated transfer rate of C atoms between species, and normalized with respect to the $CH_4 \rightarrow CH_3$ step. Only arrows at least 5% of the thickest are shown.

6.3 Effect of hydrogen reduction - Point 3

The Point 3 is used to investigate the physical and chemical processes observed at ignition (τ=0) for each fuel blend.

The start of chemical reactions observed in the pre-ignition period causes, for each fuel blend, the release of heat (Fig. 6.4j, 6.4k and 6.4l) and, as a consequence, the temperature rise (ΔT).

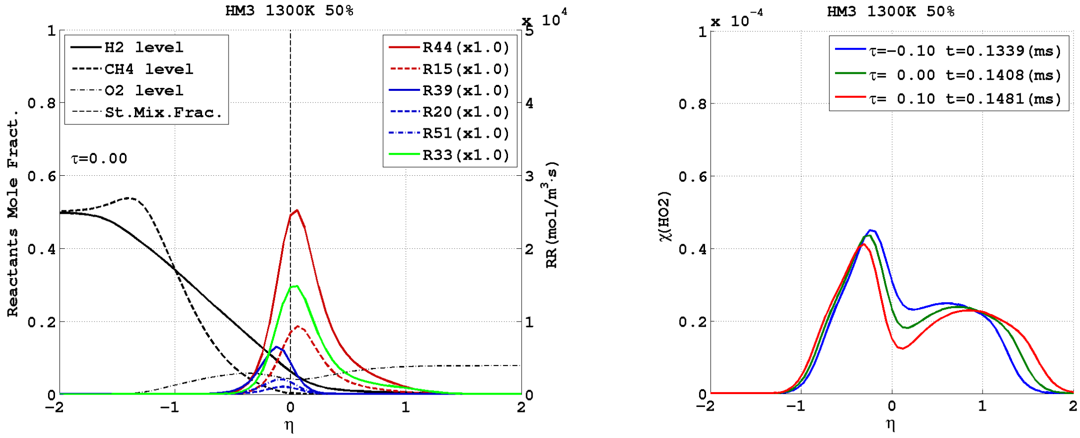

(a) H_2=50% **(b)** H_2=50%

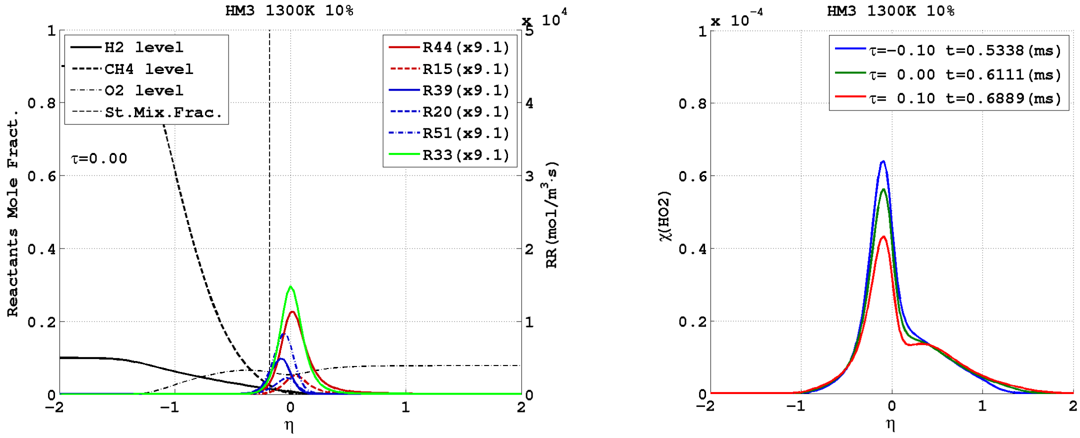

(c) H_2=10% **(d)** H_2=10%

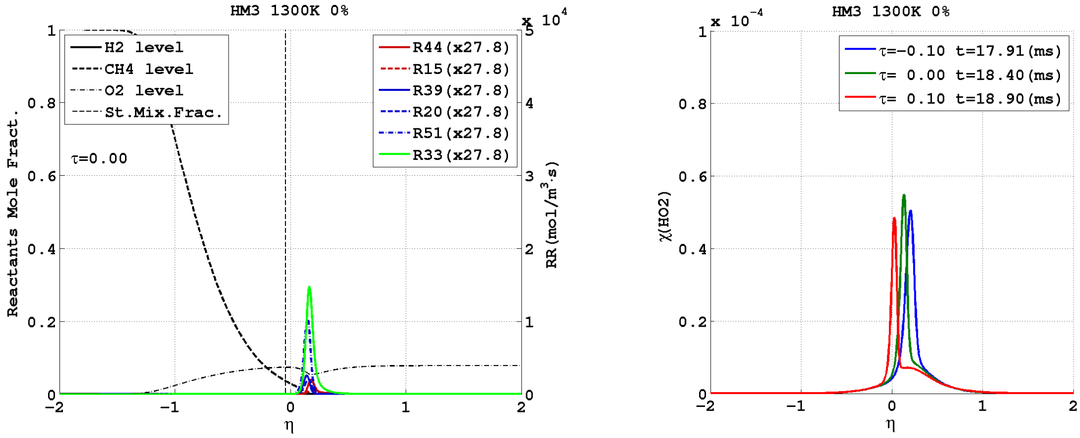

(e) H_2=0% **(f)** H_2=0%

Figure 6.22: Left column: Rates of reaction representative of hydrogen (red) and methane (blue) mechanisms plotted with the fuels and oxidiser mole fraction along the cross-stream direction. The figure shows data from the 50% (top), 10% (middle) and 0% (bottom) cases. The right axis expresses the rate of reaction in mol/m^3·s. The scale factor compares the peak rate of the R33 step with the base case.

Right column: Evolution of the hydroperoxyl radical mole fraction in the ignition period for the 50% (top), 10% (middle) and 0% (bottom) cases.

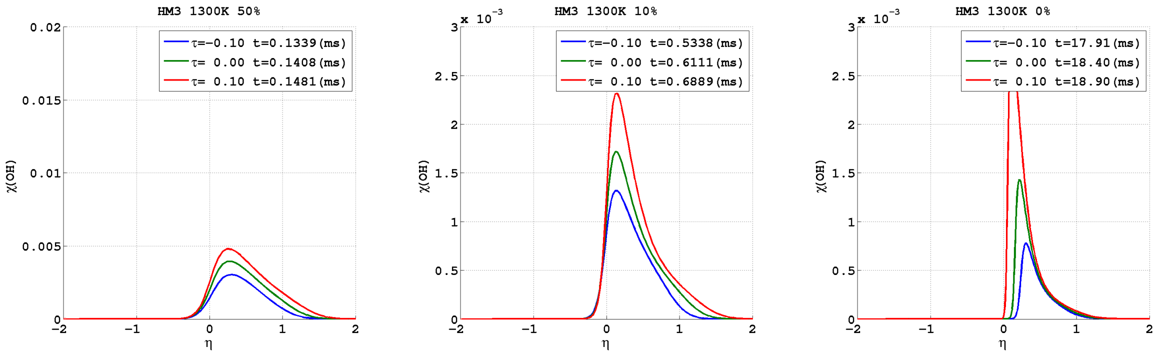

(a) χ(OH) H_2 =50% **(b)** χ(OH) H_2 =10% **(c)** χ(OH) H_2 =0%

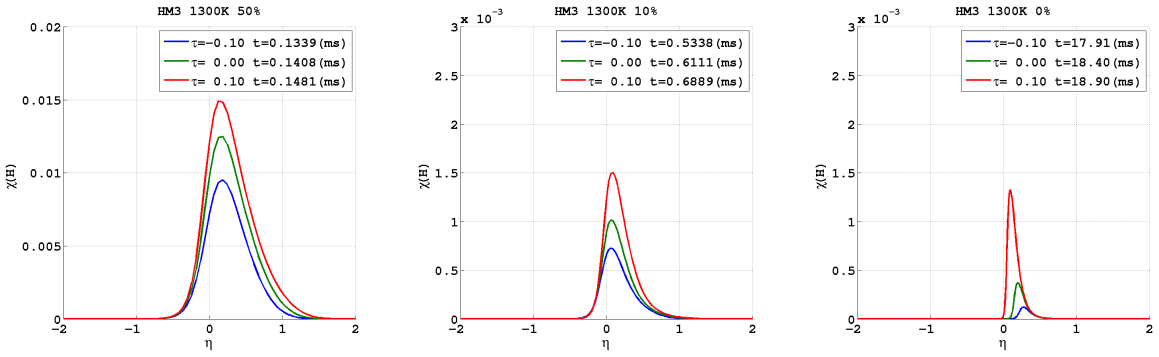

(d) χ(H) H_2 =50% **(e)** χ(H) H_2 =10% **(f)** χ(H) H_2 =0%

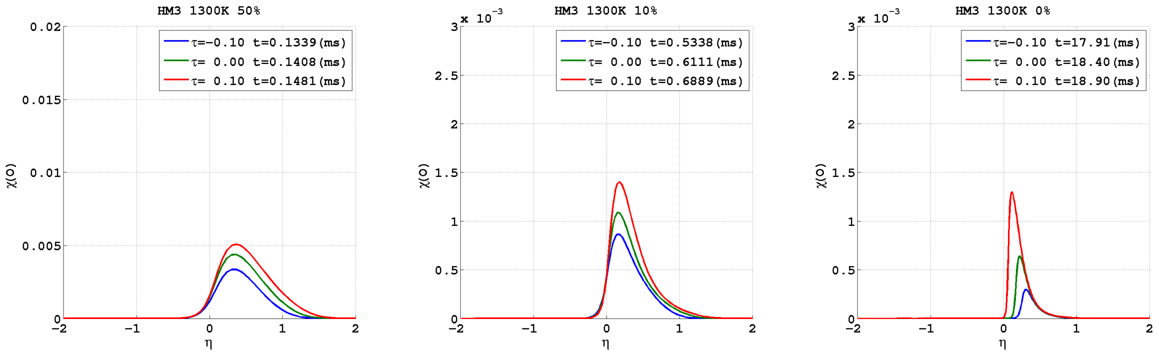

(g) χ(O) H_2 =50% **(h)** χ(O) H_2 =10% **(i)** χ(O) H_2 =0%

Figure 6.23: Mole fraction of OH (top row), H (middle row) and O (bottom row) radicals in the ignition period for the 50% (left), 10% (middle) and 0% (right) case.

As the reactions evolve, larger is the temperature rise. At the ignition time ΔT is approximately 200K for each fuel configuration (Fig. 6.2a, 6.2b and 6.2c).

Because of the temperature dependence of elementary reactions rates, as the temperature rises an overall increase in the reaction rates is observed, as outlined by major CH_4 and H_2 steps on figures 6.22a, 6.22c and 6.22e. The 50% case still presents the most reactive kinetic scenario, while the 0% case the least reactive. This outcome is demonstrable by comparing the rate of the R33 process on figures 6.22a, 6.22c and 6.22e. The rate of the R33 process, in the pure methane case, is approximately 30 times lower than in the base case. More reactive is the 10% case at ignition time, showing a R33 rate approximately 3 times bigger than the 0% case.

The rise in temperature, causes the destruction of the HO_2 radical, which remain stable only in regions of low temperature. This property of hydroperoxyl is exploited to spot the areas where the first important exothermic events occur. To this end, figures 6.22b, 6.22d and 6.22f show the evolution of the HO_2 mole fraction in the ignition period. For each fuel case a local minimum can be observed in the red curves (τ=0.1) for a small positive value of η. The local minimum highlights the regions where the previously formed HO_2 is destroyed into H and OH as a consequence of the temperature rise. Since the stoichiometric mixture fraction region locate at η=0 for the base case and at η <0 for the cases with reduced H_2 content (Fig. 6.22a, 6.22c and 6.22e), the start of ignition events is observed ahead of Z_{st} (fuel lean areas), independently to the fuel blend.

Once ignition is started, each reaction area propagates toward $Z = Z_{\mathrm{st}}$ region, as outlined by the change in slope of H_2 and CH_4 consumption paths (for example green and pink lines on figures 6.3a, 6.3b and 6.3c). As explained with more details on point 4, the propagation occurs with different rates as a consequence of the different reactivity of the fuel blends.

A detailed analysis of kinetic differences observed at ignition time between 50%, 10% and 0% cases is considered below. The analysis has been performed with the help of figure 6.23, which describes the evolution of the O/H/OH radical pool for each fuel mixtures, and figures 6.24, 6.25a and 6.25b which provide an overview of all the integrated rates of reaction of the DRM19 mechanism for each fuel mixtures. In addition, the description of the methane consumption pathway is provided. This is obtained, for each case, by means of carbon atoms pathways on figures 6.26b, 6.27b and 6.27d and by means of the major reaction rate of the CH_4 mechanism on figures 6.26a, 6.27a and 6.27c. With respect to the point 2, the carbon atom pathways also provide informations, in percentage form, about the number of carbon atoms transferred along the various paths [4].

Compared to the pre-ignition period (point 2), the pure methane case shows a similar complex kinetic scenario (Fig. 6.25b) with higher rates of reaction caused by the rise in temperature (Fig. 6.3c) where CH_4 is being consumed (Fig. 6.22e).

As for the point 2, the CH_4 dehydrogenation, remain advanced by R20, R39 and R51 processes with the R51 step playing a major role (Fig. 6.25b and 6.27c). Particularly interesting is the presence, although minor, of the R39 step, not observed in the pre-ignition period. Along with the methyl, this reaction produces H_2, as shown by the dark blue region in figure 6.3i. Being responsible for the H_2 production, the R39 reaction explains the activation of hydrogen chemistry, as confirmed by the presence of R44 step (Fig. 6.25b).

The methyl build up is consumed along the three branches shown in figure 6.27d. The major methyl destruction and HCO production is observed along the middle branch, controlled by R19, R41, R54 steps (Fig. 6.25b). Reactions R50, R64, R60 control the methyl conversion along

---

[4] Percentages refer to the part of methane that takes part to chemical reactions.

the top part of the carbon pathway, while steps R8 R55, R5, R24 describe the CH_3 recombination and the ethane consumption along the bottom one.

All three branches lead to HCO build-up (Fig. 6.27d). Overall, more than the 90% of the methyl produced is converted into HCO. Almost all of the HCO is converted into CO (Fig. 6.27d) via R81 and R82 (Fig. 6.25b). A large part of CO is then further oxidised into CO_2 (Fig. 6.27d) through elementary reaction R52 (Fig. 6.25b).

Few reactions contributes to the oxygen consumption: R33, R82, R30, R60. As with point 2 (Fig. 6.14), the R33 remains the most important O_2 consuming step as well as the only significant O producing process. Differently from the point 2, R33 shows the highest integral rate over the domain (Fig. 6.25b). As the importance of the R33 step rises, the rates of R60 and R82 reactions are relatively reduced, outlining the competing role among these three processes. Different is the case for the R30 step which, even with no H_2 in the initial fuel (R30 is controlled by the presence of O_2 and H, the latter abundant with the addition of H_2), it still performs an important role in the hydroperoxyl production.

The set of most important reactions belonging to the CH_4 mechanism occur within the methyl production area (zone where R20, R39 and R51 steps are observed), with the only exception of reaction R52 (Fig. 6.27c). This step (green line) presents a broader extension towards the oxidiser region. Here a larger presence of OH radical is observed (Fig. 6.23c) which explains the significant conversion of CO into CO_2 (Fig. 6.27d).

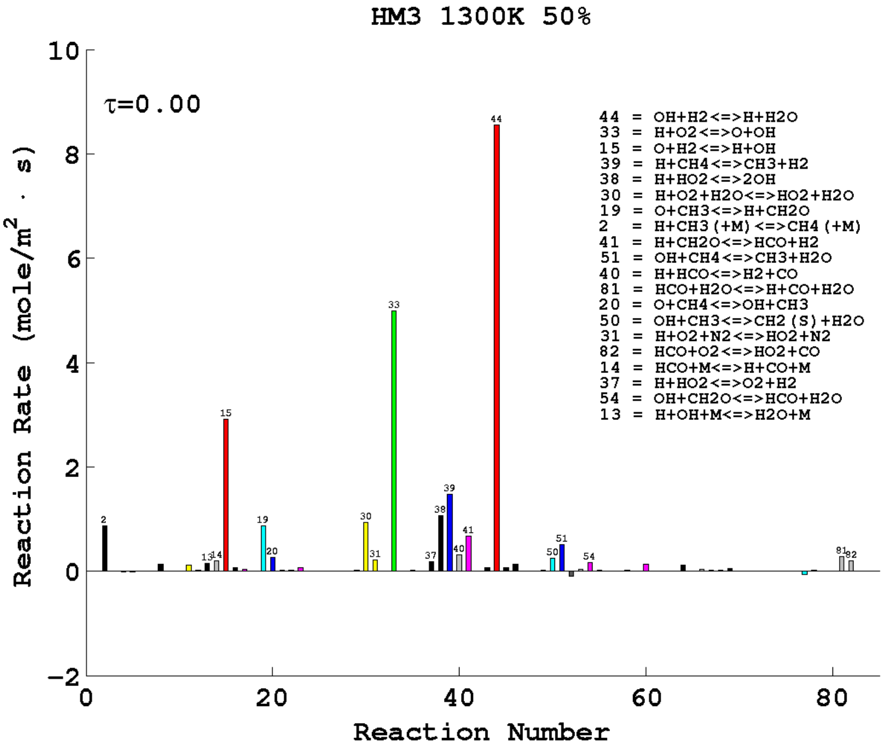

Figure 6.24: Rates of reaction of the DRM19 mechanism integrated along the cross-stream (y) direction. The reaction rates of 50% case are shown.

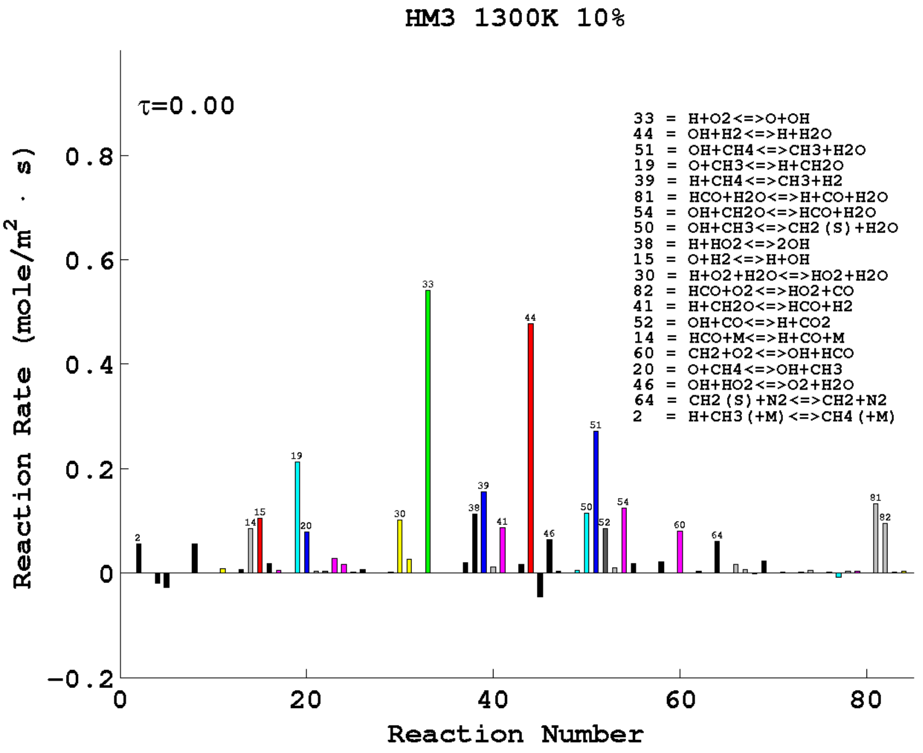

(a) H_2=10%

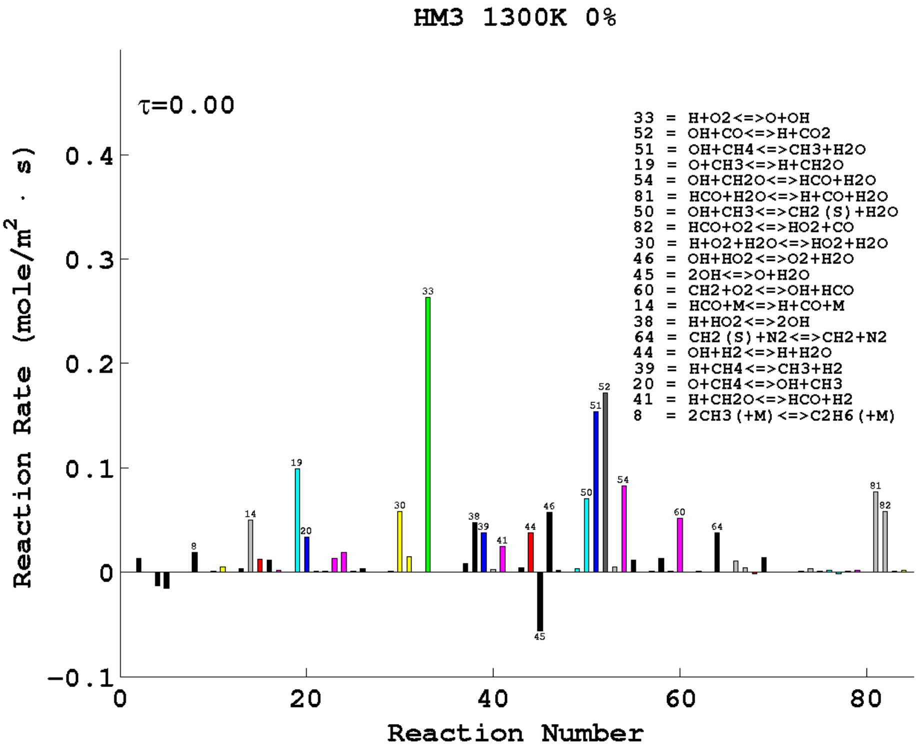

(b) H_2=0%

Figure 6.25: Rates of reaction of the DRM19 mechanism integrated along the cross-stream (y) direction for the 10% (top) and 50% (bottom) cases

The addition of 10% of H_2 in the fuel has a twofold effect: a more important role of hydrogen chemistry (R15 and R44) (Fig. 6.25a) and a larger level of H, O and OH radicals. (Fig. 6.23e, 6.23h, 6.23b).

The stronger radical pool presence is responsible for the higher reactivity of the 10% case, as outlined by the faster oxygen consumption (as shown on figures 6.22e and 6.22c, R33 rate is three times higher than the pure methane case) and an overall increase of the integral rates (Fig. 6.25a). In particular, the methane chemistry proceeds at a faster rate as seen in figure 6.27a. Here, as an example, the major CH_4 consuming steps (R51) present a rate more than doubled with respect to the 0% case (Fig. 6.27c).

The methane pathway, on the other hand, present few differences with respect to the 0% case. The major change observed is the sensitivity of the R52 step to the hydrogen addition. With the 10% of H_2 in the fuel, it is observed a stronger importance of R44 role and a reduced importance of R52 role (Fig. 6.25a). The reduced importance of R52 role is outlined by the weaker $CO -> CO_2$ conversion on figure 6.27b. It is interesting to note that both R44 and R52 reactions requires OH to advance in the forward direction and occur in a similar area (Fig. 6.22c and 6.27a). This evidence suggests a competing action between R52 and R44 steps, with the the latter stronger.

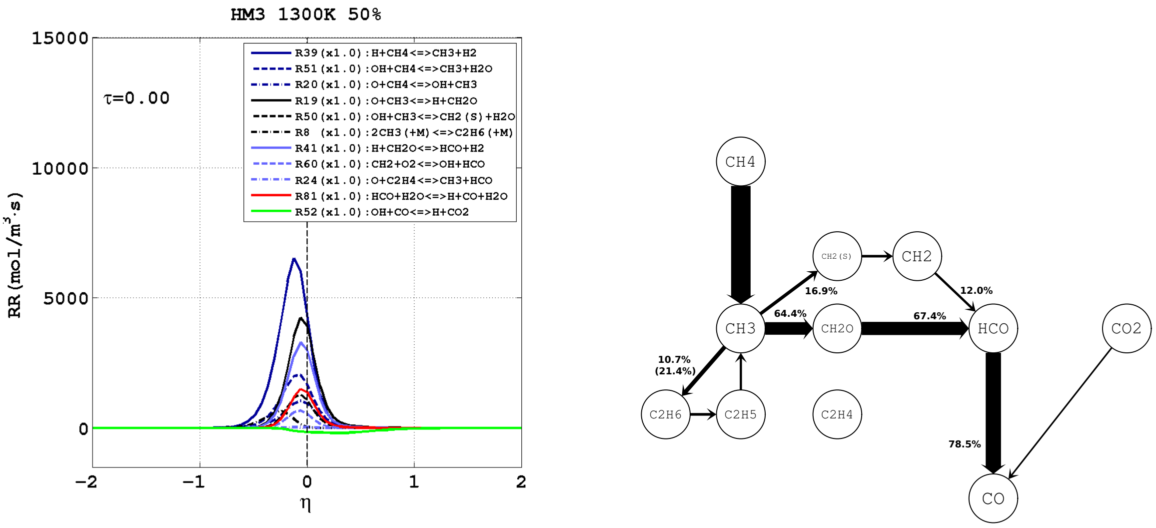

(a) H_2=50% **(b)** H_2=50%

Figure 6.26: Left: Most important rates of reaction for the methane mechanism plotted at τ=0.0 for the 50% case. The vertical dashed line represents the position of the stoichiometric mixture fraction. The scale factor shown in figure compares the peak rate of the most important $CH_4 \rightarrow CH_3$ step with the base case.
Right: Carbon atom pathway diagrams for 50% case. Arrows are proportional to the integrated transfer rate of C atoms between species, and normalized with respect to the $CH_4 \rightarrow CH_3$ step. Percentages indicate the number of carbon atoms transferred along the various paths, relative to the number of CH_4 atoms destroyed. Percentages are rounded to the upper decimal digit (+0.1%). Only arrows at least 5% of the thickest are shown.

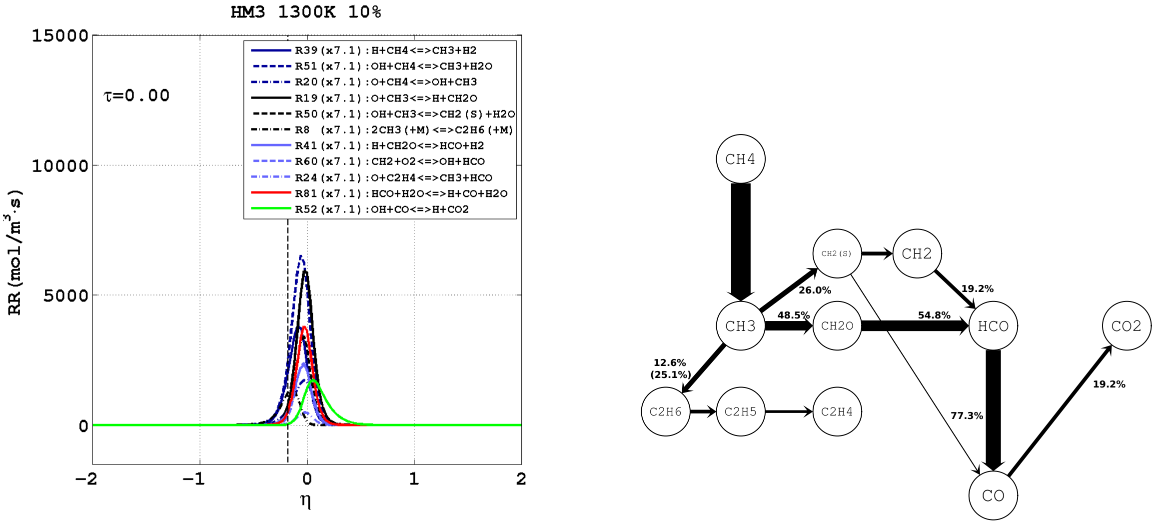

(a) H_2=10% **(b)** H_2=10%

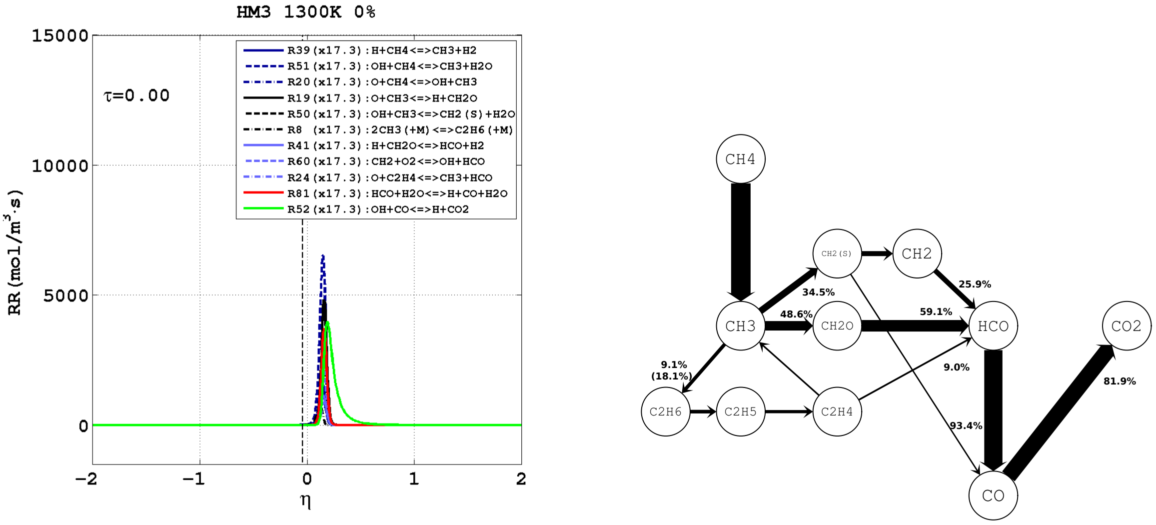

(c) H_2=0% **(d)** H_2=0%

Figure 6.27: Left column: Most important rates of reaction for the methane mechanism plotted at τ=0.0 for the 10% (top) and 0% (bottom) case. The vertical dashed line represents the position of the stoichiometric mixture fraction. The scale factor shown in figure compares the peak rate of the most important $CH_4 \rightarrow CH_3$ step with the base case.
Right column: Carbon atom pathway diagrams for 10% (top) and 0% (bottom) case. Arrows are proportional to the integrated transfer rate of C atoms between species, and normalized with respect to the $CH_4 \rightarrow CH_3$ step. Percentages indicate the number of carbon atoms transferred along the various paths, relative to the number of CH_4 atoms destroyed. Percentages are rounded to the upper decimal digit (+0.1%). Only arrows at least 5% of the thickest are shown.

With the addition of 50% of hydrogen in the fuel blend, the level of methane concentration is further reduced and the role of hydrogen chemistry is more important (Fig. 6.24). As already observed for the second point of analysis, a small number of processes dominate the kinetic scenario and control the O/H/OH pool formation: R15, R33 and R44 (Fig. 6.22a). To higher rates of the mentioned steps correspond a larger O/H/OH presence in the domain (Fig. 6.23d, 6.23g and 6.23a). Particularly large is the excess of H (Fig. 6.23d).

Despite the lower methane presence in the initial fuel, the large excess of radicals results beneficial for the methane chemistry, since an overall increase in the rates of the major CH_4 elementary steps is observed (Fig. 6.26a). Nonetheless, some changes, with respect to the 10% and 0% CH_4 pathways, are observed. They are mostly related to the H excess as follows:

- The R39 step is the preferred methyl production step because of the large H presence (Fig. 6.24),
- The $CH_2O -> CHO$ process is controlled by R41 (CH_2O reacting with H) rather then by R54 (CH_2O reacting with OH) (Fig. 6.24),
- The R52 process (CO reacting with OH) proceeds backward (CO_2 reacting with H) consuming carbon dioxide (Fig. 6.24).

6.4 Effect of hydrogen reduction - Point 4

After ignition a significant drop in the O_2 concentration is observed in all cases. Point 4 is used to investigate if the oxygen depletion influences reactions in the 10% and 0% case, in the same way as observed for the 50% case.

After ignition all cases show a significant O_2 reduction in the reaction zone as clearly shown in figures 6.28a, 6.28b and 6.28c. The areas with low oxygen presence are particularly evident in the contour plots on figures 6.6a, 6.6b and 6.6c, shown as dark blue regions for $\eta > 0$.

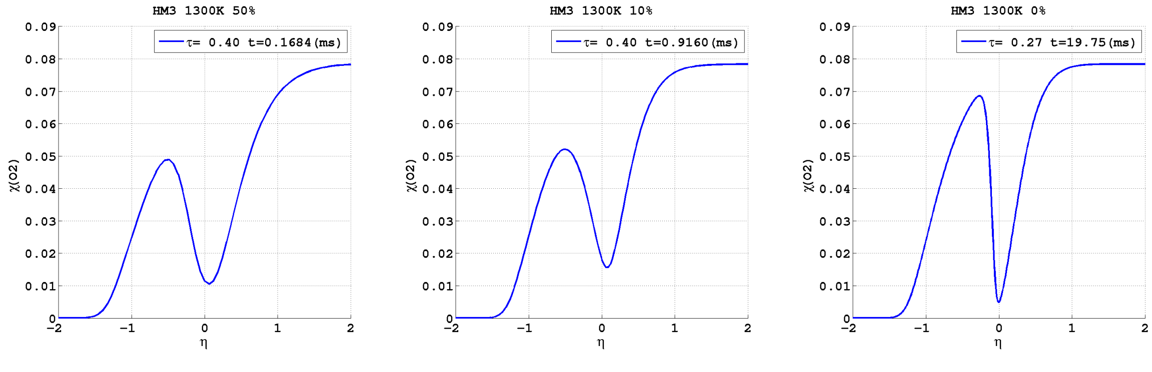

(a) $\chi(O2)$ H_2 =50% **(b)** $\chi(O2)$ H_2 =10% **(c)** $\chi(O2)$ H_2 =0%

Figure 6.28: Oxygen mole fraction in the reaction zone after ignition for the 50% (left), 10% (middle) and 0% (right) dilution case.

In the base case (Chap. 4) it was outlined how the O_2 depletion after ignition was limiting the rates of elementary reactions of both H_2 and CH_4 mechanisms. Because of the low CH_4 diffusivity, particularly limiting was observed for the CH_4 mechanism, starving in a low oxygen area below the main H_2 reaction region (Fig. 6.3g and 6.3d).

The general reduction of reaction rates observed in the base case (Fig. 6.29) is not observed for the 10% and 0% cases, which instead present a further increment of rates of their elementary reactions (Fig. 6.30a and 6.30b). This can be explained by the reduced reactivity in the low H_2 cases, which requires a longer time to reach the optimal mixing conditions. All cases, independently of the level of H_2 addition, present a reaction front propagation from areas above Z_{st} (lean area), where first reactions are observed, down to Z_{st}. The optimal mixing conditions are outlined by the peak in the O_2 consumption rate (Fig. 6.6a, 6.6b and 6.6c) and the highest value of rate of reaction. Once the optimal mixing conditions are achieved, the upwards movement of the reactions zone is observed again. At that time the diffusion-reaction equilibrium among reactants controls the evolution of the flame front.

Independently to the level of H_2 in the fuel, the H_2 mechanism always locates in the upper part of the reaction front close to the Z_{st} line (Fig. 6.3g, 6.3h and 6.3i). The CH_4 mechanism, on the other hand, is always observed developing in the rich part of the flame front ($Z < Z_{\mathrm{st}}$) (Fig. 6.3d, 6.3e and 6.3f). The time required to reach the best mixing, is observed to vary with the hydrogen content. In the 50% case the peak in the O_2 consumption rate is reached approximately at ignition time (Fig. 6.6a) and at the time described by the point 4 (τ=0.4), a drop in the O_2 consumption rate and in the elementary reaction rates is observed (Fig. 6.29). Differently for the 10% and 0% cases the peak of O_2 consumption rate is observed at later time and, as a consequence, at point 4 still high reaction rates are observed (Fig. 6.30a and 6.30b).

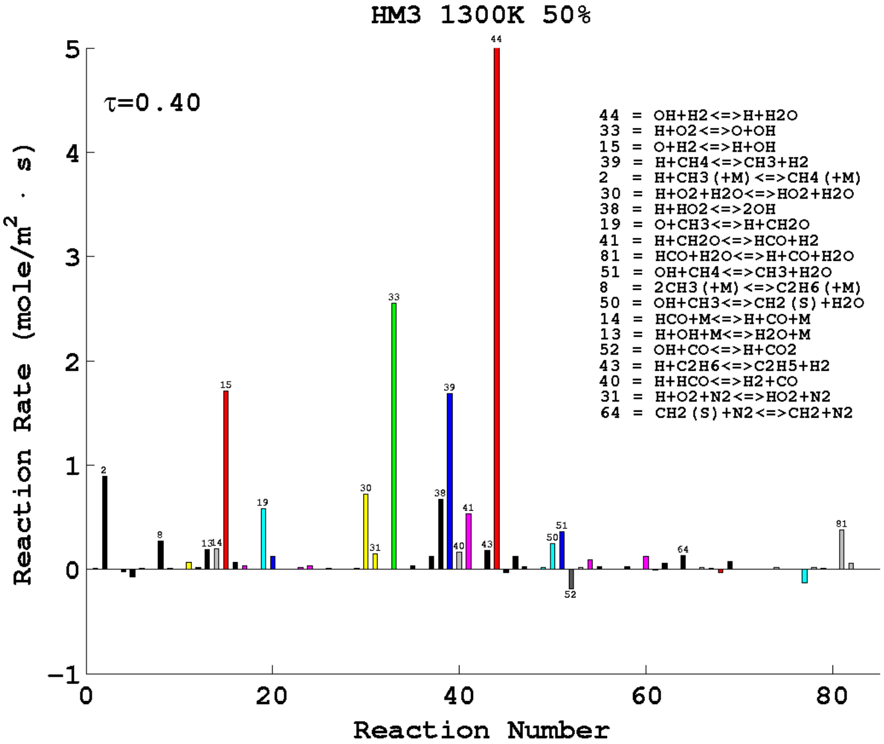

Figure 6.29: Rates of reaction of the DRM19 mechanism integrated along the cross-stream (y) direction. The reaction rates of 50% case are shown.

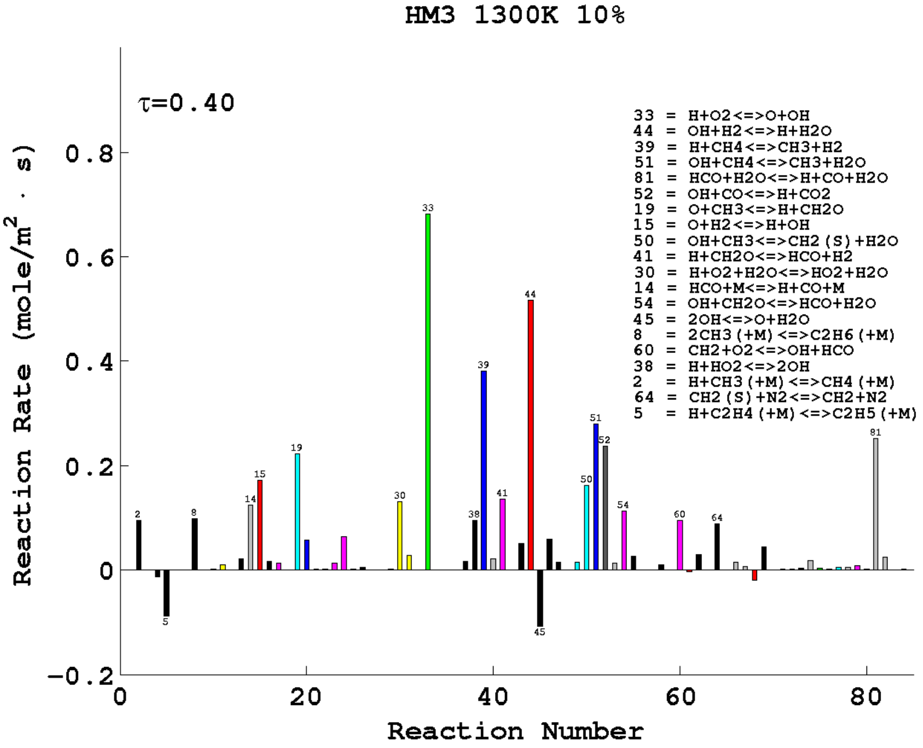

(a) H_2=10%

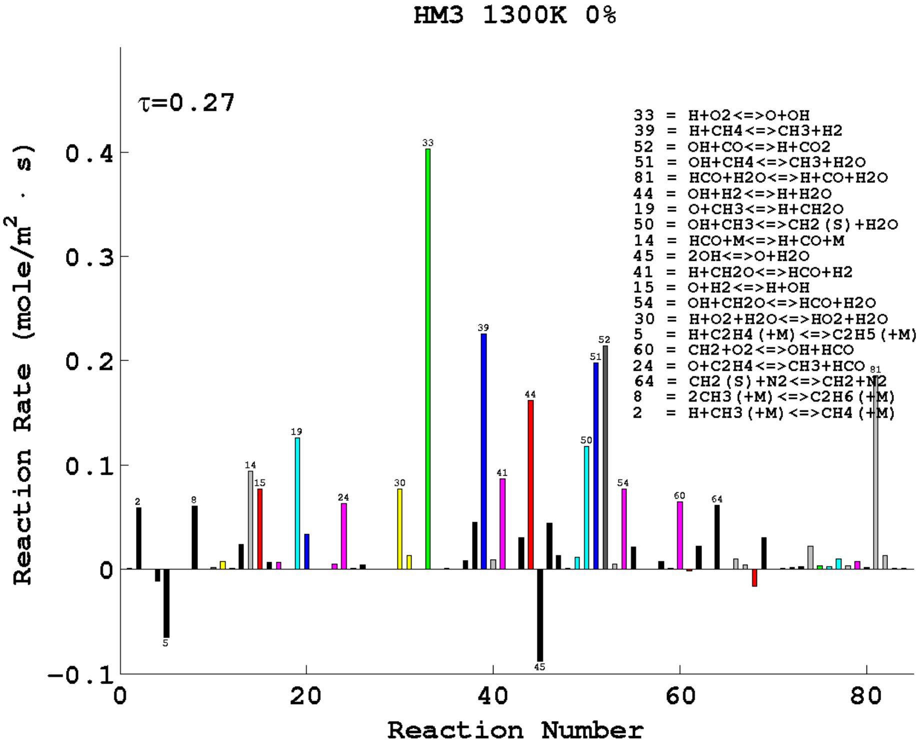

(b) H_2=0%

Figure 6.30: Rates of reaction of the DRM19 mechanism integrated along the cross-stream (y) direction for the 10% (top) and 50% (bottom) case

Following is provided a description of the physical/chemical scenario of each case in the post-ignition period outlining similarities and differences with respect to the previous point. Figure 6.31 shows the O/H/OH radical pool for each fuel case. As already observed in the previous investigation points, the presence of H_2 in the fuel blend enrich the radical pool with a stronger presence of O/H/OH radicals. The Higher the H_2 level, the higher is the presence of those intermediates. Significant is the presence of H in all the cases analysed (Fig. 6.31d, 6.31e and 6.31f).

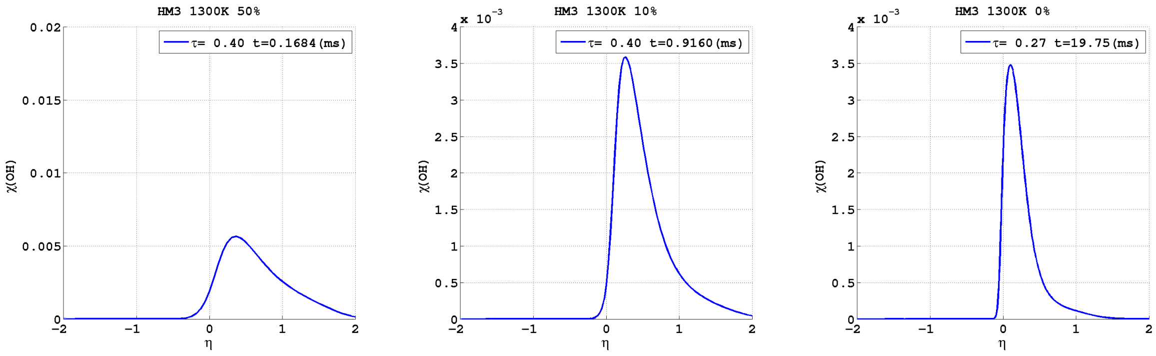

(a) χ(OH) H_2 =50% **(b)** χ(OH) H_2 =10% **(c)** χ(OH) H_2 =0%

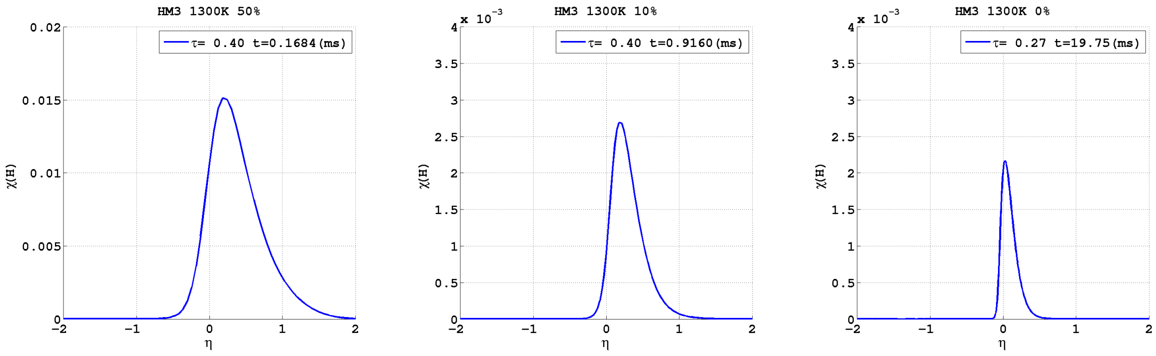

(d) χ(H) H_2 =50% **(e)** χ(H) H_2 =10% **(f)** χ(H) H_2 =0%

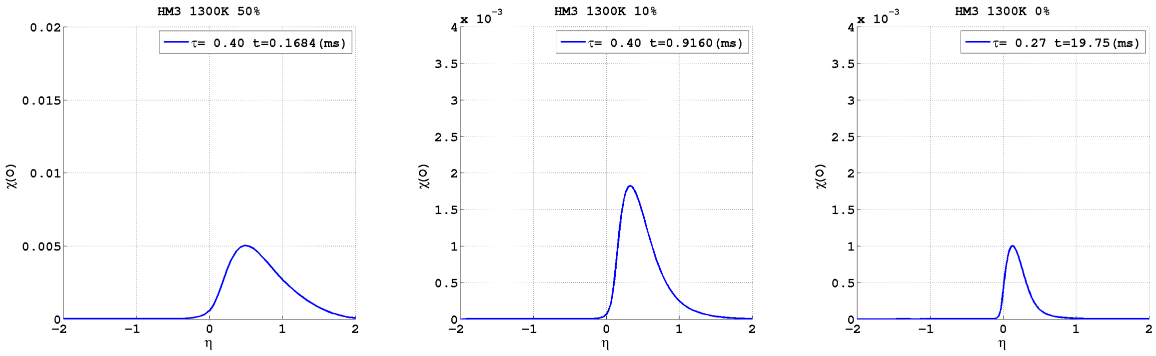

(g) χ(O) H_2 =50% **(h)** χ(O) H_2 =10% **(i)** χ(O) H_2 =0%

Figure 6.31: Mole fraction of OH (top row), H (middle row) and O (bottom row) radicals in the post-ignition period for the 50% (left), 10% (middle) and 0% (right) case.

In the pure methane case in particular, a larger presence of H is observed after ignition because of the H_2 production via R39 and the following activation of hydrogen chemistry (R15 and R44) (Fig. 6.30b).

Related to the higher number of radicals is a higher reactivity of the fuel mixture and, in general, higher rates of reactions (Fig. 6.29, 6.30a and 6.30b). Being the major branching process and the most important O_2 consuming step, the rate of the R33 step has been used for the previous points to evaluate the reactivity of each fuel case. The addition of 10% of H_2 significantly increase (approximately three times) the rate of oxygen consumption with respect of the pure methane configuration (Fig. 6.32b and 6.32c). Even stronger is the rate of oxygen consumption in the 50% case (Fig. 6.32a). At the time considered for the analysis, the R33 rate in the base case is roughly 13 times higher than in the pure methane case. It is possible to observe in figures 6.32a, 6.32b and 6.32c an initial displacement of methane (blue lines) and hydrogen chemistry (red lines). Independently of the level of H_2 addition, the hydrogen chemistry develops close to Z_{st} while methane chemistry occur for $Z < Z_{\mathrm{st}}$. This is due to the important role of differential diffusion. After ignition in fact, it is observed the upward motion of both H_2 (Fig. 6.3g, 6.3h and 6.3i) and CH_4 (Fig. 6.3d, 6.3e and 6.3f) fuels, where more O_2 is available. The faster H_2 diffusion explains the location of hydrogen chemistry, ahead of the methane one.

The different displacements among CH_4 and H_2 chemistry and the different importance of hydrogen chemistry in each fuel case, help to shed lights on differences observed in the methane pathways (Fig. 6.32a, 6.32b and 6.32c). For all the cases under investigation, in the post-ignition period the CH_4 abstraction proceeds mainly because the H/OH radical pool via R39 and R51 (Fig. 6.29, 6.30a and 6.30b). The R39 process is particularly sensitive to the presence of H atom and becomes the methyl production process with the highest rate even in the pure methane case, where the presence of atomic hydrogen becomes significant after ignition (Fig. 6.31f).

All cases show the destruction of the CH_4 proceeding along multiple paths, with differences observed in the percentages of CH_4 destroyed along the various paths (Fig. 6.33b, 6.34b and 6.34d). The path with the highest conversion of CH_3 into HCO remain the middle one (R19 $\rightarrow$ R41/R54) and each fuel case presents a comparable percentage of HCO conversion along this path. Nonetheless, with respect to the ignition time, a reduced HCO formation is observed for each fuel case.

The bottom path, on the contrary, results strengthened for each case, compared to ignition time. As explained by Kee *et al.* [27], this is due to the unusual behaviour of methane consumption pathway which, under fuel-rich conditions ($Z < Z_{\mathrm{st}}$), shows a significant part of the methyl produced recombined to C_2H_6 via R8.

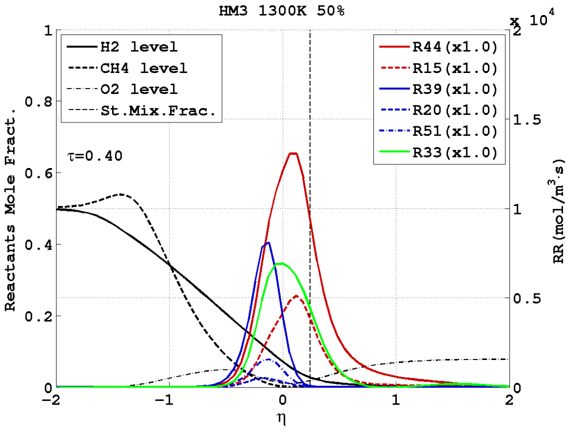

(a) H_2=50%

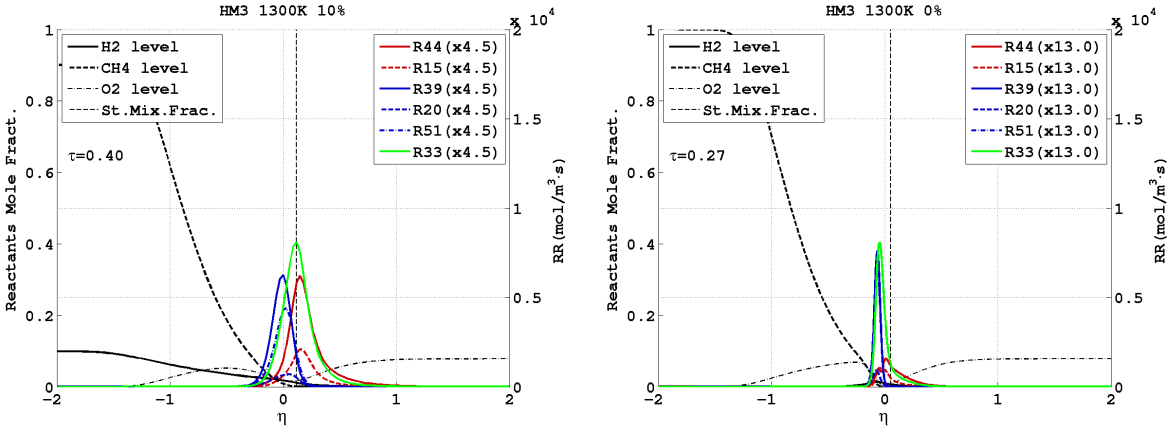

(b) H_2=10%

(c) H_2=0%

Figure 6.32: Rates of reaction representative of hydrogen (red) and methane (blue) mechanisms plotted with the fuels and oxidiser mole fraction along the cross-stream direction. The figure shows data from the 50% (top), 10% (bottom-left) and 0% (bottom-right) cases. The right axis expresses the rate of reaction in $\mathrm{mol/m^3 \cdot s}$. The scale factor compares the peak rate of the R33 step with the base case.

As seen at point 2, the C_2 hydrocarbons formed in the lower branch (C_2H_6, C_2H_5 and C_2H_4) proceed through a series of hydrogen abstractions that could lead to the HCO formation via R24 process (O consuming process). The final $C_2H_4 -> HCO$ conversion step shows reducing percentages with increasing level of H_2. In particular, the $C_2H_4 -> HCO$ process in the 50% case is inhibited. This could be explained by the competing action between the R15 step and the other O consuming processes (R19, R24 and R45). The R15 process, linked to the H_2 chemistry, is particularly sensitive to the H_2 addition, as clearly shown on figures 6.30b, 6.30a and 6.29. Here it can be observed how the difference in the rate between R15 and the other O consuming steps increases strongly with increasing level of H_2 addition. As a consequence, despite a larger C_2H_6 recombination is observed, the final $C_2H_4 -> HCO$ step is less likely to occur.

A similar scenario can be observed in the upper branch of each methane pathways (Fig.

6.33b, 6.34b and 6.34d). With respect to the previous time point (Fig. 6.26b, 6.27b and 6.27d), each branch shows a stronger $CH_3 -> CH_2(S)$ conversion through step R50, and a relatively weaker $CH_2 -> HCO$ step via R60. In addition, the more H_2 is added in the fuel, the weaker is the $CH_2 -> HCO$ step. The competing action between R33 and all the O_2 consuming processes (R30, R60 and R82) explains this observation.

As a consequence of the weaker action of the upper and lower branches of the methane consumption pathway, a reduced CO conversion [5] is observed when more hydrogen is mixed with methane (Fig. 6.33b, 6.34b and 6.34d).

The $HCO -> CO$ step is dominated by the R81 process in all the fuel cases, while the R82 step presents a reduced importance.

Strong differences are observed in the final $CO -> CO_2$ step among cases. As figure 6.34b shows, approximately half of the CO produced is transformed into CO_2 in the 10% case. This is slightly higher in the 0% case: approximately the 60% of CO is oxidised into CO_2 (Fig. 6.34d). In the base case, on the other hand, the CO_2 is consumed rather than produced (Fig. 6.34d).

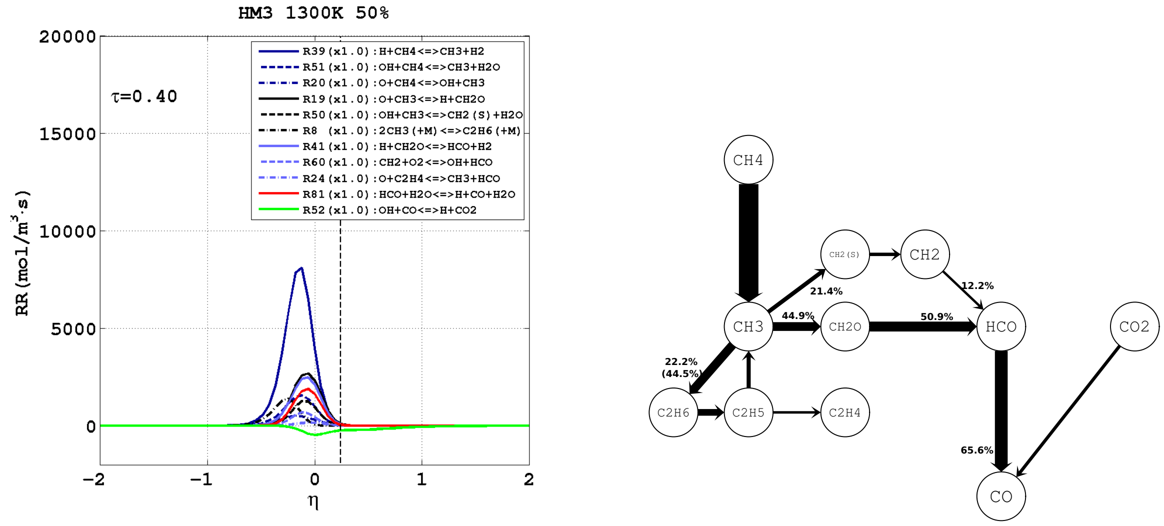

(a) H_2=50% **(b)** H_2=50%

Figure 6.33: Left: Most important rates of reaction for the methane mechanism plotted at τ=0.4 for the 50% case. The vertical dashed line represents the position of the stoichiometric mixture fraction. The scale factor shown in figure compares the peak rate of the most important $CH_4 \rightarrow CH_3$ step with the base case.
Right: Carbon atom pathway diagrams for 50% case. Arrows are proportional to the integrated transfer rate of C atoms between species, and normalized with respect to the $CH_4 \rightarrow CH_3$ step. Percentages indicate the number of carbon atoms transferred along the various paths, relative to the number of CH_4 atoms destroyed. Percentages are rounded to the upper decimal digit (+0.1%). Only arrows at least 5% of the thickest are shown.

---

[5] It should be noted that the conversion is relative to the amount of CH_4 consumed. As a consequence, to a reduced conversion of CH_4 into CO does not necessarily correspond a reduced level of CO in the domain

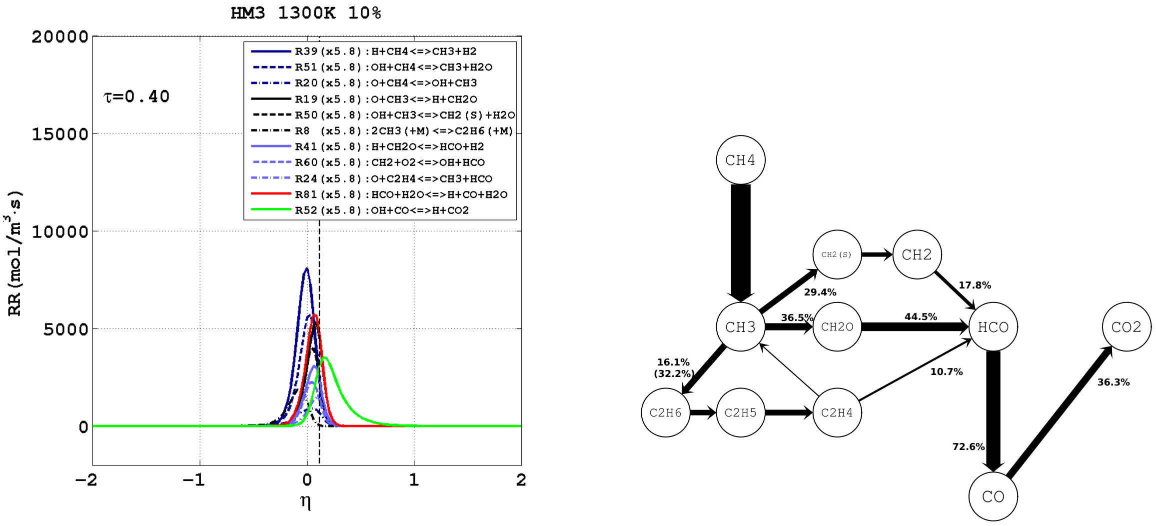

(a) H_2=10% **(b)** H_2=10%

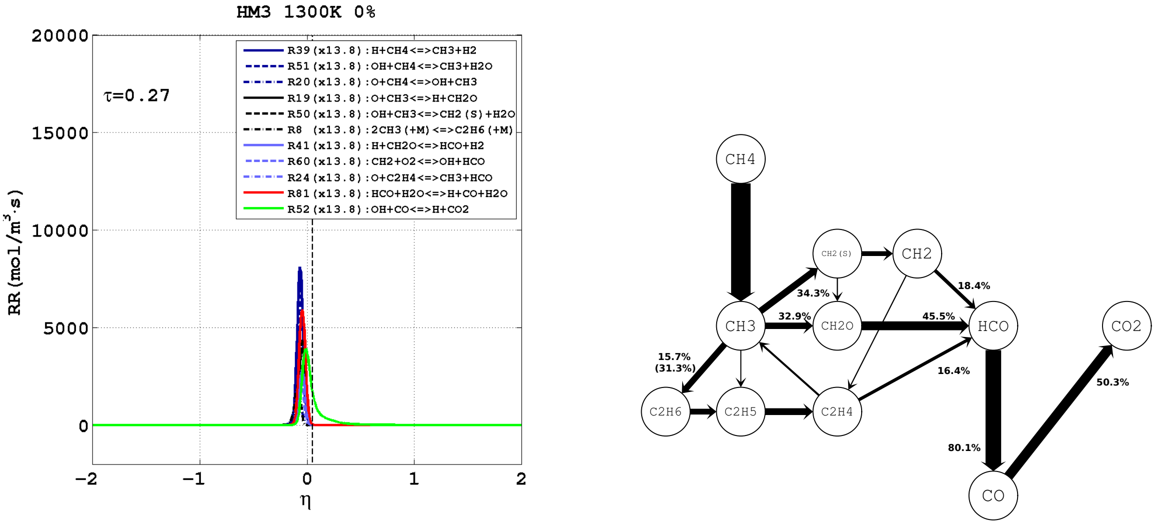

(c) H_2=0% **(d)** H_2=0%

Figure 6.34: Left column: Most important rates of reaction for the methane mechanism plotted at τ=0.4 for the 10% case (top) and at τ=0.27 for the 0% (bottom) case. The vertical dashed line represents the position of the stoichiometric mixture fraction. The scale factor shown in figure compares the peak rate of the most important $CH_4 \rightarrow CH_3$ step with the base case.
Right column: Carbon atom pathway diagrams for 10% (top) and 0% (bottom) case. Arrows are proportional to the integrated transfer rate of C atoms between species, and normalized with respect to the $CH_4 \rightarrow CH_3$ step. Percentages indicate the number of carbon atoms transferred along the various paths, relative to the number of CH_4 atoms destroyed. Percentages are rounded to the upper decimal digit (+0.1%). Only arrows at least 5% of the thickest are shown.

The DRM19 mechanism uses more elementary reactions to predict the CO_2 production: R10, R22, R27, R36, R52, R59, R73 and R74. Among them, only the R52 step presented a significant rate (Fig. 6.30b, 6.30a and 6.29), demonstrating the dominant role of this reaction in the CO_2 production/destruction. The R52 step advances forward (CO_2 production) in the presence of CO and OH, while it proceeds backward (CO_2 consumption) in the presence of CO_2 and H.

In the base case the presence of CO is observed between the H_2 and CH_4 consumption paths (Fig. 6.6j) where the hottest temperatures are reached (Fig. 6.3a). In this area it is possible to observe an excess of H and, to a lesser extent of OH radical, as a consequence of the large H_2 addition in the initial fuel. Furthermore, CO_2 is present in this region (Fig. 6.6g) being used to dilute the initial oxidiser blend. All these factors, led to the conclusion that the combined effect of high temperature and excess of H, pushed the R52 reaction in the backward direction, consuming CO_2 (Fig. 6.4d).

A different scenario is observed in the 10% and 0% cases For both cases the CO presence extends over the area enclosed by H_2 and CH_4 (Fig. 6.6k and 6.6l). In particular, a larger region of CO is observed for $\eta < 0$. Nonetheless the CO_2 production occurs mainly for $\eta > 0$ for both cases (Fig. 6.4e and 6.4f). Here, a temperature similar to the base case is observed (Fig. 6.3b and 6.3c), while there is a difference in the H/O/OH distribution (Fig. 6.31). An excess of OH is in fact observed in the post-ignition period for case with reduced H_2 presence. This explains the forward direction of the R52 process and, as a consequence, the CO_2 production.

6.5 Effect of hydrogen reduction - Point 5

The fifth investigation point focuses on the final part of the selected ignition period (Fig. 6.2a, 6.2a and 6.2a). At this time, the oxygen level is almost zero in the reaction zone and flame front is observed moving upwards, where more oxygen is available.

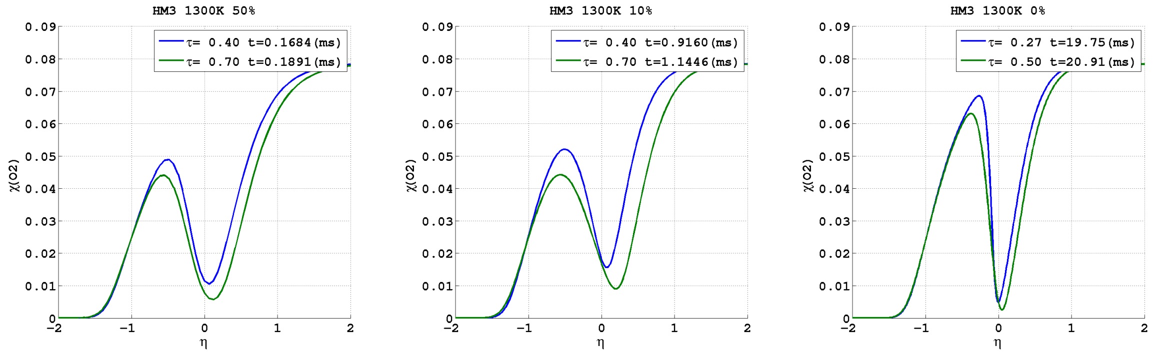

(a) χ(O2) H_2 =50%

(b) χ(O2) H_2 =10%

(c) χ(O2) H_2 =0%

Figure 6.35: Oxygen level evolution in the post-ignition period for the 50% (left), 10% (middle) and 0% (right) case. Graphs show the oxygen depletion regions which moves on the right, indicating the upwards movement of the reaction zones.

Figures 6.35a, 6.35b and 6.35c shows the evolution of the oxygen level in the final part of the ignition period. A significant drop in the oxygen level can be observed in the $\eta \in$[-1,1] range. As seen in figures, oxygen profiles taken at the fifth point of analysis move to the right compared to the curves taken at the forth point of analysis. This represents the upward motion of the reaction zones towards the oxidiser layer. The upward motion of reaction zones flame front is seen in the fuel paths overlaid on contour plots (e.g. Fig. 6.3j, 6.3k and 6.3l).

For all cases considered in this chapter, reaction zones run mainly below Z_{st} (O_2 lean region), with the H_2 chemistry locating in proximity of Z_{st} while the CH_4 consumption occurring below it (Fig. 6.36a, 6.36b and 6.36c). As a consequence, the overall rate reduction observed in the latest point of ignition period (Fig. 6.37, 6.38a and 6.38b) can be ascribed to the oxygen depletion.

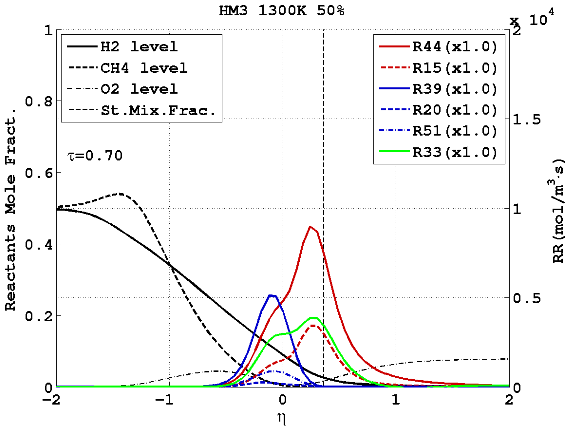

(a) H_2=50%

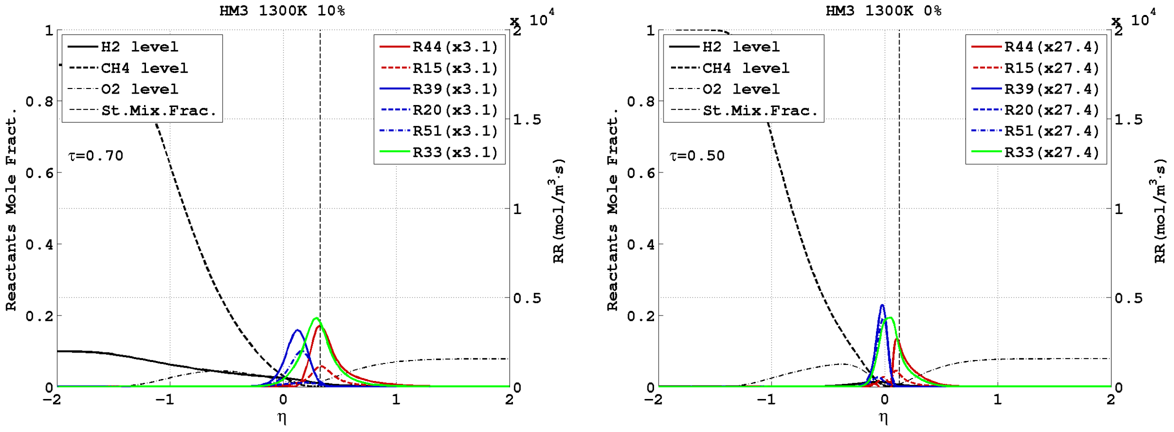

(b) H_2=10%

(c) H_2=0%

Figure 6.36: Rates of reaction representative of hydrogen (red) and methane (blue) mechanisms plotted with the fuels and oxidiser mole fraction along the cross-stream direction. The figure shows data from the 50% (top), 10% (bottom-left) and 0% (bottom-right) cases. The right axis expresses the rate of reaction in $\mathrm{mol/m^3 \cdot s}$. The scale factor compares the peak rate of the R33 step with the base case.

Data following described, reflects the main peculiarities of the physical/chemical scenario observed in the previous investigation point. The major differences are linked to the different level of H_2 in the fuel blend. Differences with the previous point of analysis are thoroughly described, while similarities are briefly mentioned.

As aforementioned, each case considered present a ceH2/CH_4 chemistry displacement, and no exception makes the 0% configuration to this observation. In figure 6.36c, the H_2 consuming processes (solid and dashed red curves) occur in proximity of the stoichiometric region.

The presence of active hydrogen chemistry reactions (R15 and R44) is mostly due to R39 step, controlling the methane dehydrogenation. This step causes the H_2 release in the domain (blue area along methane consumption path in figure 6.3i), which then diffuses ahead CH_4 and is consumed. Thereby for the 0% case, the hydrogen chemistry must be considered as a consequence of the methane consumption, rather than considered as a separate process.

Despite the observed rates reduction (Fig. 6.38b), the methane chemistry keeps a structure similar to the previous investigation point. The CH_4 chemistry occur within the area where methyl is produced (Fig. 6.41c) with the only exception of the $CO -> CO_2$ process. The CH_4 abstraction remains controlled by H/OH pool (Fig.6.38b) and approximately the 75% of the methyl produced is converted by a three way paths into HCO (Fig. 6.41d). The HCO is then completely converted into CO, while approximately the 60% of CO is oxidised into CO_2. With respect to the previous time point, few differences in terms of percentage of CH_4 destroyed along the various paths (Fig. 6.34d and 6.41d) are observed. A weakening of the HCO conversion along the upper and middle branch of the $CH_3 -> HCO$ process is caught, partially balanced by a more important $C_2H_4 -> HCO$ conversion.

The addition of 10% of H_2 (mole basis) to methane both changes the rate of CH_4 chemistry and the way CH_4 consumption pathway evolves in time. As a consequence of the enrichment of the radical pool with a larger H presence (Fig.), the rate limiting step (R33) shows a rate 10 times higher than pure methane case (Fig.6.36b and 6.36c).

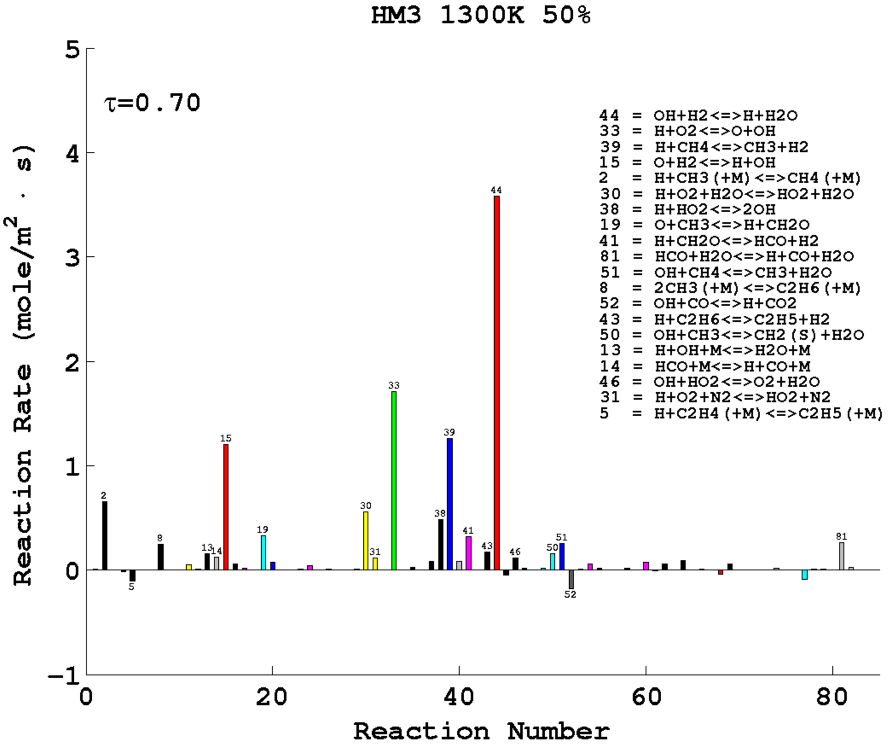

Figure 6.37: Rates of reaction of the DRM19 mechanism integrated along the cross-stream (y) direction. The reaction rates of 50% case are shown.

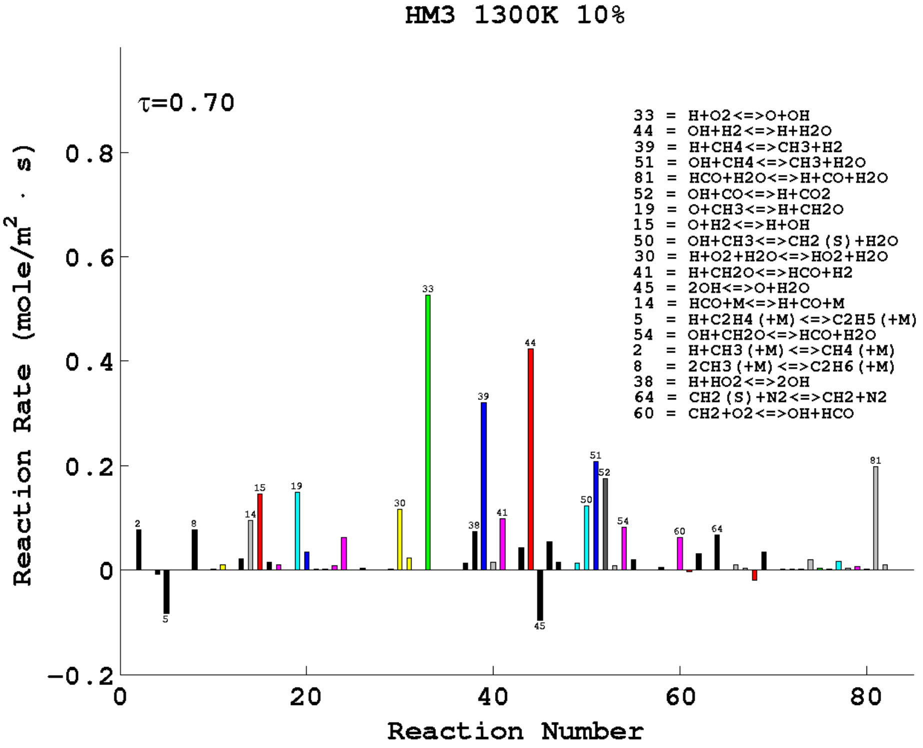

(a) H_2=10%

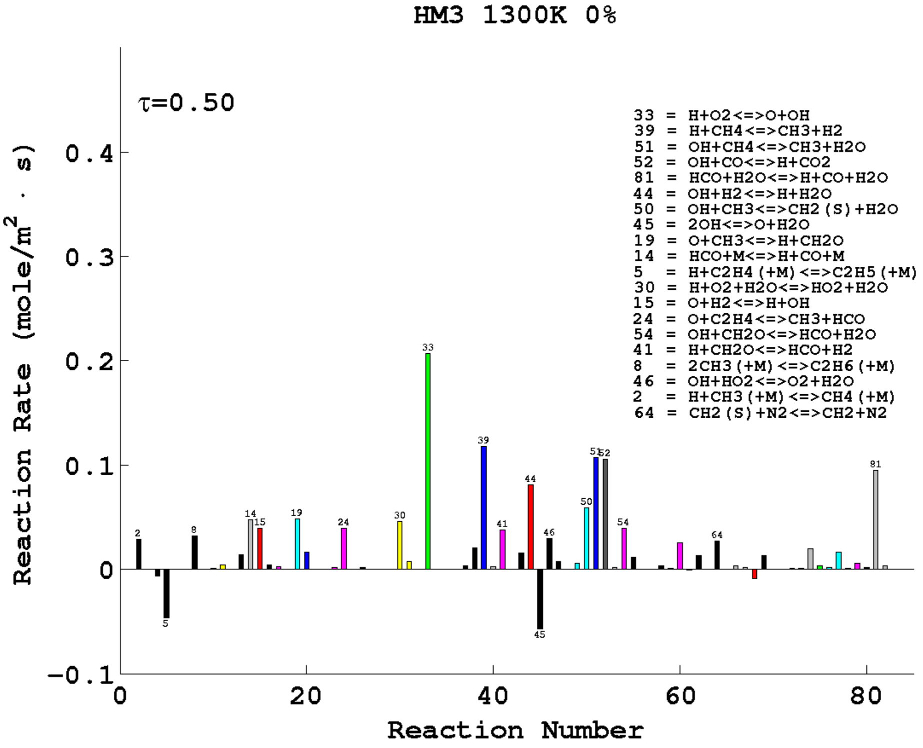

(b) H_2=0%

Figure 6.38: Rates of reaction of the DRM19 mechanism integrated along the cross-stream (y) direction for the 10% (top) and 50% (bottom) case

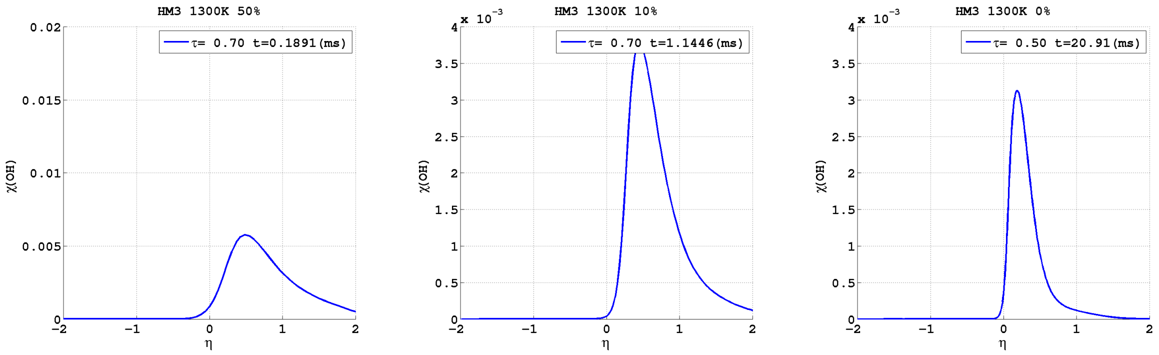

(a) H_2=50% **(b)** H_2=10% **(c)** H_2=0%

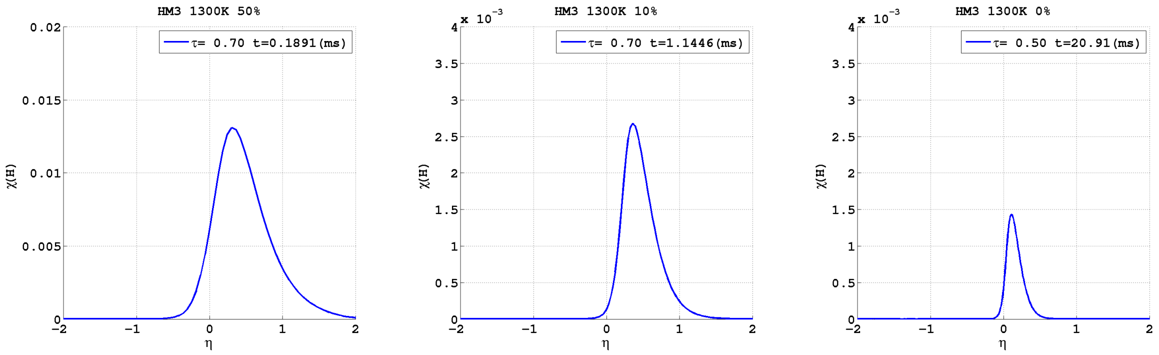

(d) H_2=50% **(e)** H_2=10% **(f)** H_2=0%

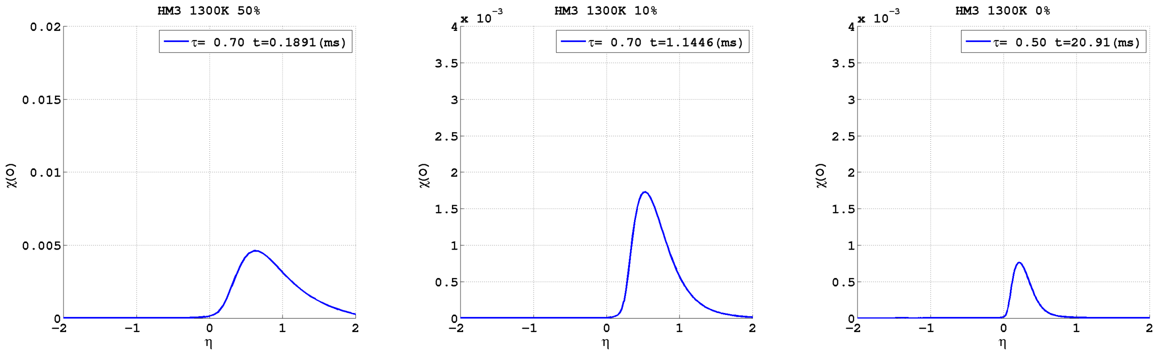

(g) H_2=50% **(h)** H_2=10% **(i)** H_2=0%

Figure 6.39: Mole fraction of OH (top row), H (middle row) and O (bottom row) radicals in the post-ignition period for the 50% (left), 10% (middle) and 0% (right) case.

To the faster rate of R33 process correspondS the larger radicals presence (Fig. 6.39e, 6.39h and 6.39b) and the increased rate of the CH_4 mechanism (Fig. 6.41a). The higher diffusivity of hydrogen causes a displacement between H_2 and CH_4 consumption mechanisms: H_2 diffuses ahead CH_4 and is consumed in proximity of Z_{st}, where the access to O_2 and to the radical pool is favourite.

Despite the faster diffusivity places H_2 chemistry in a privileged position, the hydrogen diffusion is limited in the 10% case, and the methane consumption pathway does not results particularly affected. As in fact figures 6.41b and 6.41d show, methane pathways for 10% and

0% cases present a similar structure and comparable is the conversion of HCO and CO from CH_3. It is important to note that in the 10% case a much higher methyl production rates (R39) is observed (Fig. 6.41a), thereby with a small hydrogen addition is it significantly improved the reactivity of the fuel blend. This is confirmed by stronger CO production rate (R81) observed in the 10% case.

Less beneficial results instead the hydrogen addition for the CO_2 conversion. As shown on figure 6.41b, approximately the 50% of the HCO is transformed in CO_2. This is potentially due to the increased presence of the H radical in the radical pool. As shown on figure 6.41a, the $CO -> CO_2$ conversion (R52) occurs where a strong presence of the H/OH pool is observed (Fig. 6.39e and 6.39h). The H radical in particular, presents an increased level with respect to the pure methane case (Fig. 6.39f) which could affect the $CO -> CO_2$ conversion via R52 step.

As for the 10% and 0% case, in the 50% case H_2 diffuses ahead CH_4 and is consumed in proximity of the stoichiometric mixture fraction (6.36a). Here O_2 is present in larger quantity (Fig. 6.6a). The double peak on the oxygen consumption process (R33) reflect the different availability of O_2 for H_2 and CH_4 chemistry. The highest value of the R33 process is observed at the Z_{st}, where R15 and R44 steps show their peaks. On the other hand, the low peak is observed at a longer distance from Z_{st} where methane diffuses and is consumed.

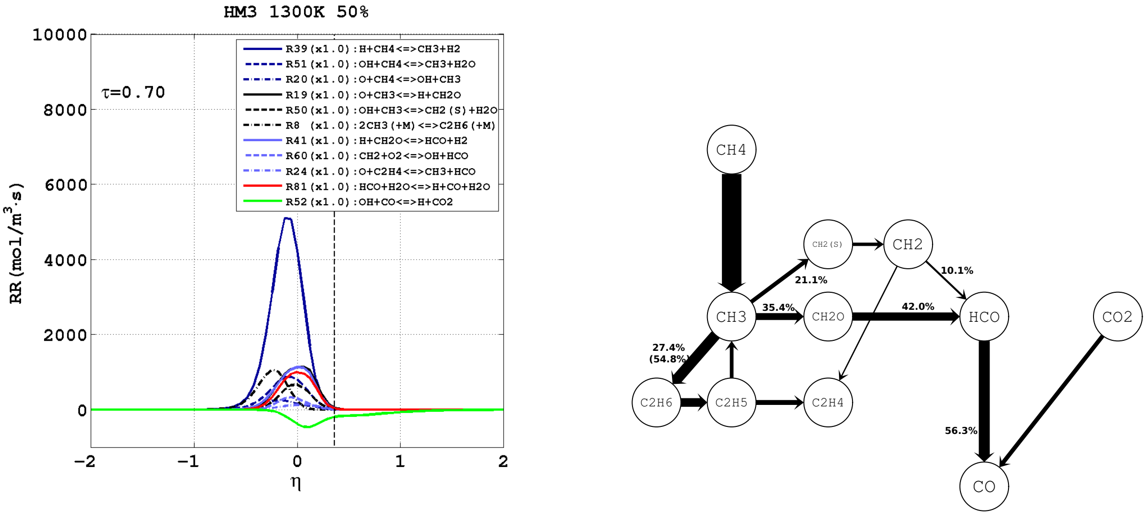

(a) H_2=50%

(b) H_2=50%

Figure 6.40: Left: Most important rates of reaction for the methane mechanism plotted at τ=0.7 for the 50% case. The vertical dashed line represents the position of the stoichiometric mixture fraction. The scale factor shown in figure compares the peak rate of the most important $CH_4 \rightarrow CH_3$ step with the base case.
Right: Carbon atom pathway diagrams for 50% case. Arrows are proportional to the integrated transfer rate of C atoms between species, and normalized with respect to the $CH_4 \rightarrow CH_3$ step. Percentages indicate the number of carbon atoms transferred along the various paths, relative to the number of CH_4 atoms destroyed. Percentages are rounded to the upper decimal digit (+0.1%). Only arrows at least 5% of the thickest are shown.

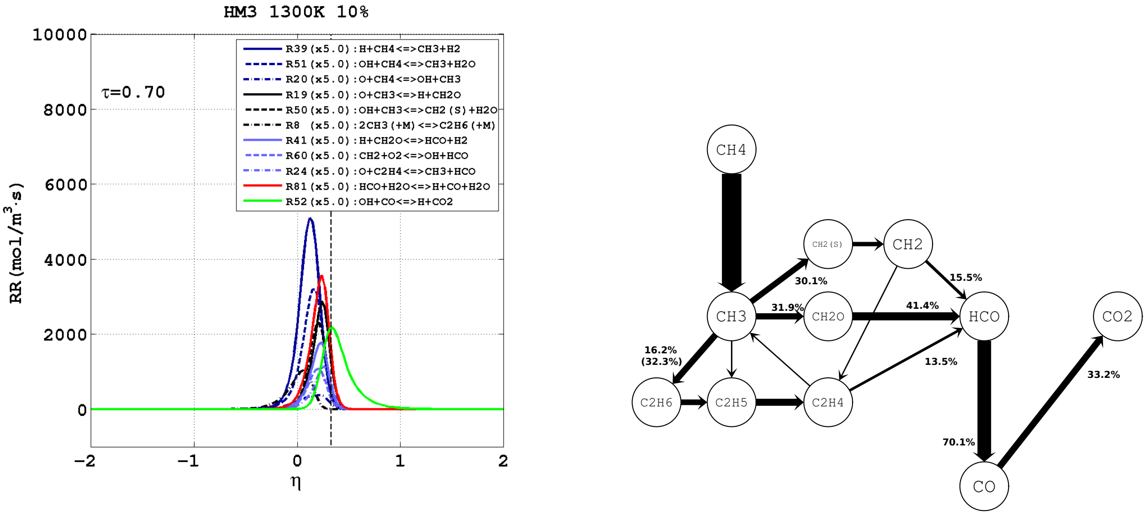

(a) H_2=10%

(b) H_2=10%

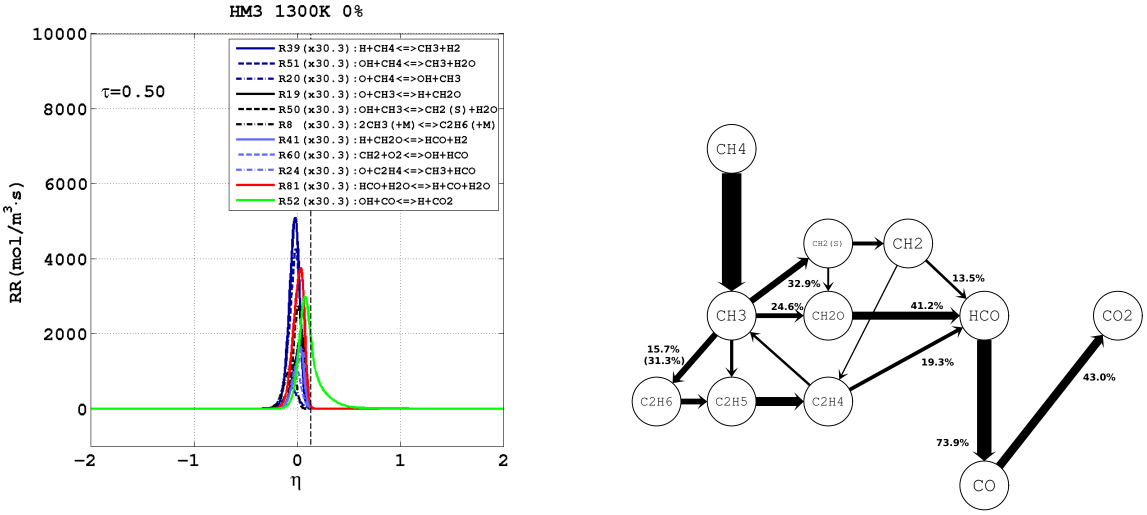

(c) H_2=0%

(d) H_2=0%

Figure 6.41: Left column: Most important rates of reaction for the methane mechanism plotted at τ=0.7 for the 10% case (top) and at τ=0.5 for the 0% (bottom) case. The vertical dashed line represents the position of the stoichiometric mixture fraction. The scale factor shown in figure compares the peak rate of the most important $CH_4 \rightarrow CH_3$ step with the base case.

Right column: Carbon atom pathway diagrams for 10% (top) and 0% (bottom) case. Arrows are proportional to the integrated transfer rate of C atoms between species, and normalized with respect to the $CH_4 \rightarrow CH_3$ step. Percentages indicate the number of carbon atoms transferred along the various paths, relative to the number of CH_4 atoms destroyed. Percentages are rounded to the upper decimal digit (+0.1%). Only arrows at least 5% of the thickest are shown.

The methane starvation process impacts the CH_4 consumption pathway in the latest part of ignition, as can be observed by comparing figures 6.33b and 6.40b. With the lack of O_2, and so O radical, the central path of the methyl consumption process results no longer competitive and a significant part of the methyl produced is recombined to C_2H_6. Nonetheless, because of the difficult access to the O radical, the C_2H_6 conversion into HCO is not observed. This affect the overall $CH_4 -> HCO$ conversion.

Finally, in presence of a large quantity of H_2 in the initial fuel blend, is observed the backward progression of R52 step (Fig. 6.37), which leads to the CO_2 consumption.

6.6 Effect of hydrogen reduction - Conclusion

This chapter investigates the effect of H_2 addition in the fuel blend. Three different cases with different level of H_2 are analysed: the base case (HM3-50%) and two configurations with reduced (HM3-10%) or null (HM3-0%) presence of hydrogen. The H_2 level reduction is balanced with increasing amount of CH_4. The oxidiser composition (HM3) is kept constant for each case.

The H_2 addition acts, with the respect to the pure methane case, as a fuel "enhancer" since it enriches the domain with a larger presence of highly reactive H, O and OH radicals. Self-ignition time results significantly impacted by H_2 addition. The pure methane configuration (HM3-0%) requires approximately 18ms to ignite. The addition of 10% (molar basis) of hydrogen to the fuel, ignites the reactants 30 times quicker ($t_{\mathrm{ig}} \sim$0.6ms). An even earlier ignition occurs ($t_{\mathrm{ig}} \sim$0.14ms) by using as fuel an equi-molar mixture of hydrogen and methane.

Despite the strong time scales differences, the scaling of ΔT curves allowed to analyse physical and chemical characteristics of each case along the entire ignition period.

The effects of hydrogen presence are observed since the earliest part of the ignition period. The pure methane configuration requires to diffuse deep into the oxidiser area to initiate chain reaction. Differently, the early start of methane consumption is observed for the HM3-50% case in proximity of the stoichiometric mixture fraction region, at the fuel/oxidiser interface.

The chemical scenario of low oxygen configurations showed marked differences with respect to HM3-50% case. The dominant role of hydrogen chemistry and the large excess of atomic hydrogen in the radical pool are no longer observed. The reduced H production, sensibly affects the rate of the R33 reaction (O_2 consumption) and the consequent release of radicals. The methane dehydrogenation is mostly advanced by R51 step (rather than R39) in the earliest stages of ignition. The methyl conversion into HCO is now observed to evolve along three different paths. The methyl recombination into the C_2 form particularly, assume reduced importance in the HM3-10% and HM3-0% cases. Nonetheless, the significant ethane conversion into HCO highlight a larger availability of oxygen for the methane chemistry. Moreover, the lower H_2 addition corresponds to enhanced $HCO -> CO$ and $CO -> CO_2$ conversions.

The presence of H_2 in the fuel is particularly beneficial for the HM3-10% case. It accelerates the methane chemistry, but it does not alter particularly the CH_4 consumption pathway.

The R52 reaction controls the carbon dioxide consumption/production independently to the fuel mixture considered. The larger the amount of H_2 in the fuel blend, the more reduced the $CO -> CO_2$ conversion. In the base case particularly, the large hydrogen presence causes the backward direction of R52 which leads to the consumption of carbon dioxide.

Chapter 7

3D Study

As the acronym suggests, MILD regime (Moderate or Intense Low Oxygen Dilution) requires a high degree of combustion products recirculation to achieve the proper oxygen dilution. The large presence of exhaust gases, rises the oxidiser temperature and promotes fuel ignition. For this reason, fuel and oxidiser are commonly kept separated till they reach the combustion chamber, where they interact. In order to guarantee the chemical interaction between reactants, the proper mixing is usually obtained, in both experimental and industrial devices, by means of high speed fuel/oxidiser jets (common geometrical configurations of MILD burners are mentioned in section 1.1). The high velocity of the reactants highlights outlines the intrinsically turbulent nature of the MILD regime.

To reveal the complex interplay between turbulence, diffusion and chemistry, up to the smallest scales of flame structure, a direct numerical simulation (DNS) study of the fuel/oxidiser mixing within the combustion chamber is necessary. Because of the numerical complexities (computational expenses, geometrical set-up, triggering of the turbulent motion, etc), only few studies are present in literature describing the MILD combustion regime simulation by a direct approach [61–63].

Among these, only a single study provides insights into the spontaneous mixing and ignition of reactants as a consequence of the initial fuel and oxidiser separation [63]. In this study, Götkolga *et al.* numerically mimic the experiment of Dally *et al.* [54] by simulating the mixing process of reactants by means of 3D mixing layers. With the purpose of reducing the computational expense, the geometry of the domain is scaled such that the thickness of the fuel layer is 2mm compared to 4.25mm in the experiments. Furthermore, to produce an effective comparison with the 2D case, the rectangular geometry of the 2D fuel jet is simply extended spanwise. Despite this numerical study produces valuable insight into aspects the turbulent regime of MILD combustion, the actual geometry of the JHC experiment is not reproduced and, to the author's knowledge, there are no DNS studies in the literature which directly simulate the 4.25mm circular jet issuing the hot coflow.

In this chapter the spontaneous mixing and ignition of a circular fuel jet issuing a hot oxidiser coflow are investigated. This reproduces numerically the JHC experiment of Dally *et al.* and provide a comparison with the 1D cases previously presented, where the turbulent fluctuations were not considered.

7.1 3D problem description

The three-dimensional DNS study investigates the temporal evolution of a circular fuel jet in a hot diluted oxidiser, during the self-ignition period. The results are compared with results from 1D cases in order to gain insights into the effect of the turbulent fluctuations on the diffusion chemistry interaction.

The three-dimensional domain has dimensions of 10x20x20mm (length x height x width). The circular fuel jet has a diameter of 4.25mm, which is consistent with fuel jet geometry reported in the JHC experiment [54]. It initially flows along the x direction (streamwise) with its axis along the center of the y-z plane. The oxidiser occupies the rest of the domain volume. An overview of the 3D domain is provided on figure 7.1.

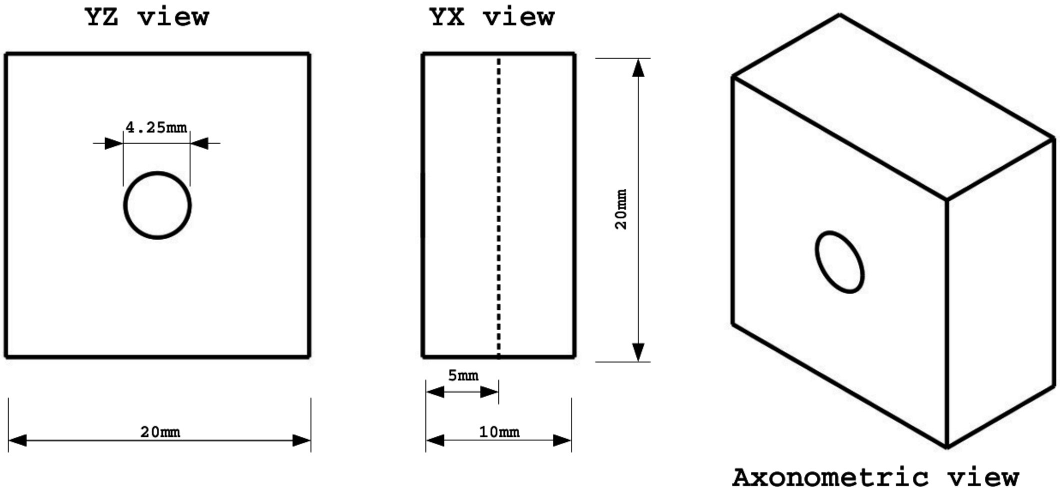

Figure 7.1: Sketch of the three-dimensional domain. The dashed line running along the y direction on the y-x plane indicates the section area from were data are extracted.

The effect of the oxygen dilution and hydrogen addition are both investigated in three dimensions. The effect of hydrogen addition in the fuel blend is studied by modelling the fuel jet with a 50/50 and a 90/10 CH_4/H_2 molar ratio mixture. The effect of the oxygen dilution is accounted by the HM3 and HM1 mixtures, chosen to represent the oxidiser blend. The initial temperature of fuel and oxidiser are kept consistent with the 1D study and the JHC experiment. To reduce the computational costs and the memory storage requirements, the HM2 oxidiser blend and the pure methane fuel have not been considered in this analysis.

Table 7.1 overviews the set of cases investigated and describes the initial physical and chemical characteristics of fuel and oxidiser.

Case	Fuel				Oxidizer					
	u_x(m/s)	T(K)	Y_{CH_4}	Y_{H_2}	u_x(m/s)	T(K)	Y_{O_2}	Y_{N_2}	Y_{H_2O}	Y_{CO_2}
HM1-1300K-50%	35.0	305	0.889	0.111	−35.0	1300	0.03	0.85	0.065	0.055
HM3-1300K-50%	35.0	305	0.889	0.111	−35.0	1300	0.09	0.79	0.065	0.055
HM3-1300K-10%	35.0	305	0.986	0.014	−35.0	1300	0.09	0.79	0.065	0.055

Table 7.1: Set of cases considered for the investigation of the turbulence-diffusion-chemistry interaction under MILD conditions. For each case is shown the initial streamwise velocity, the initial temperature and the chemical composition of fuel and oxidiser.

7.2 3D numerical set-up

One of the drawback of the DNS study of MILD regime in the JHC burner is the complexity of the numerical set-up, which makes difficult to emulate properly the initial conditions used in the experimental burner. Following are provided details of the settings and assumptions used to match conditions observed in the JHC burner as close as possible.

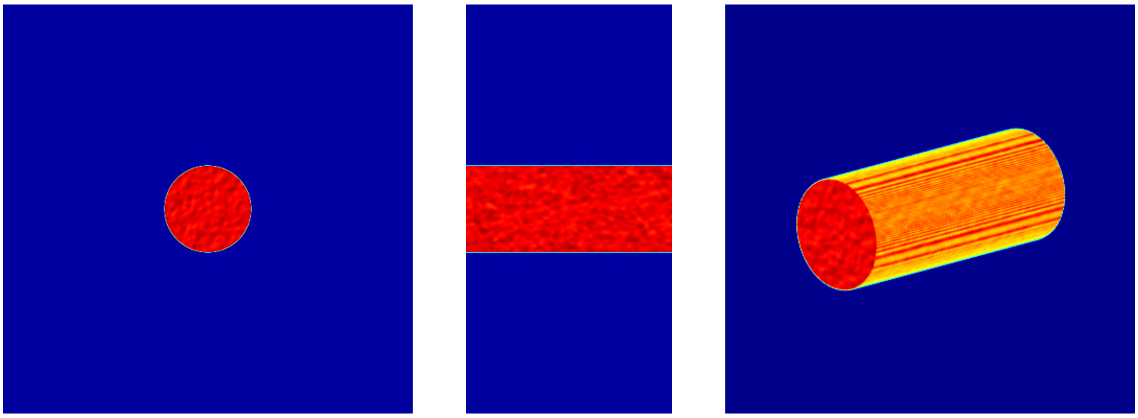
(a) YZ plane **(b)** YX plane **(c)** Jet 3D view

Figure 7.2: Field of the U_x velocity component in the YZ (left) and XY (middle) cross-sectional plane of the computational domain. The XY plane passes through the middle of the jet. The figure (c) shows the U_x velocity component within the fuel jet, plotted in axonometric view. The color scale ranges from -37 (blue) to 42 (red) m/s.

In the experimental setup, the equimolar H_2/CH_4 mixture enters the oxidiser with a Re number of approximately 10000 [54, 55], which outlines the fully turbulent nature of fuel jet. This corresponds, considering $d = 4.25\text{mm}$ and $\nu = 3 \cdot 10^{-5}\text{m}^2/\text{s}$ for the equi-molar fuel mixture, to a relative velocity between fuel and oxidiser of approximately 70m/s [1]. In order to be consistent with the experiment, all the cases analysed have been set up with the same relative velocity. As table 7.1 shows, for each case analysed, fuel and oxidiser have initial velocities equal in modulus but with opposite direction. This has been done to maintain the relative velocity while doubling the value of dt used to advance the governing equations (Equation (3.3)) and so half the time required to complete each simulation.

---

[1] The kinematic viscosity is computed, at 305K, by means of the Sutherland formula [70] and the ideal gas law.

The fully turbulent nature of the fuel jet is modelled by applying an initial homogeneous and isotropic turbulence to the fuel region only. To this end, a series of different numerical procedures were adopted. A field of random numbers was firstly generated in the fuel jet volume and then smoothed 40 times with a 1-2-1 filter in the x, y and z direction. The set of data is then interpreted as a stream function and derivatives taken along the three directions to obtain the velocity component (U_x, U_y and U_z) of the turbulent field [2]. The average value of the velocity components ($\bar{u}_x$, $\bar{u}_y$ and $\bar{u}_z$) are then computed and the oscillating parts (u'_x, u'_y and u'_z) extracted (Sect.2.8). The u'_x, u'_y and u'_z terms allow to compute the rms (root mean square) of the velocity fluctuations, which represents the intensity of the initial turbulent field. The rms has been scaled in order to set the turbulence perturbations in the fuel field equal to 4% of the initial fuel/oxidiser relative velocity. The choice of 4% is from the study of Afarin *et al.* [60] which studied numerically the JHC burner investigating the effect of the different initial turbulence levels in the fuel. Figure 7.2 shows U_x and the generated turbulence at t=0 in two different cross-sectional planes of the domain, as well as in the entire jet volume.

The initial jet perturbation not only mimics the experimental conditions, but also triggers the instabilities and the mixing between fuel and oxidiser. To ensure that turbulent scales that develop were captured correctly, the Kolmogorov length scale was calculated and compared to the grid spacing. The Kolmogorov length scale ($\eta_k = \nu^{3/4}/\epsilon^{1/4}$) was computed considering the kinematic viscosity (ν) of the equimolar fuel mixture at 305K and the turbulent kinetic energy dissipation rate (ϵ) as u'^3/d, where u' is the oscillating part of the fuel velocity which is estimated to be dissipated. Under the assumption of isotropic turbulence ($u'_x = u'_y = u'_z$), the value of the oscillating component of the velocity ($\sim$ 6m/s) is extracted from the turbulent kinetic energy ($k = 3/2u'^2$) measurement of the Götkolga *et al.* study [63], where the relative velocity between fuel and oxidiser is comparable (67m/s).

Under the described assumptions, the Kolmogorov scale was computed as approximately 27μm. In order to be consistent with the 39μm mesh size used for the 1D study, the x, y and z domain directions have been discretised respectively with 256, 512 and 512 uniformly distributed grid points. This implies a mesh size slightly larger than the Kolmogorov scale (39μm). Nonetheless, the used grid spacing is the same order as the Kolmogorov length scale, which guarantees, according to Moin *et al.* study [71], the proper spatial resolution of the smallest turbulent scales. It should be noted that for the 10% case, where the fuel has a CH_4/H_2 molar ratio equal to 90/10, the kinematic viscosity of the fuel is $2 \cdot 10^{-5}$ rather than $3 \cdot 10^{-5}\mathrm{m}^2/\mathrm{s}$. At the defined fuel jet velocity, this implies a higher Re value ($\sim$15000) and a slightly reduced Kolmogorov scale ($\sim$20μm) which, nonetheless, remains in the order of the chosen grid resolution.

The chosen grid resolution is also small enough to resolve the chemical timescales, as indi-

---

[2] Despite the stream function application physically holds true only for 2D cases, this is done with the sole purpose to generate a random field of values, and the divergence-free condition does not need to be satisfied at this stage. Once the random number field is obtained, the projection method (Sect.2.9 ensured the continuity constraint is satisfied.

cated by the 1D study performed by Götkolga *et al.* [63]. Consistently with the 1D study, the DRM19 kinetic mechanism has been used in all the 3D cases. Furthermore, as for the 1D study, the initial steep profile of the chemical source terms at the fuel/oxidiser interface has been smoothed by applying a 1-2-1 filter 10 times. As a consequence, density and temperature also present a smoother profile at the interface (Fig. 7.3). The selected grid resolution has been also validated using the Aspden *et al.* study [72], indicating that the resolution is appropriate for capturing all scales for the 3D turbulent cases.

Along with the spatial and chemical resolution, also the temporal resolution has been checked. It was shown for the 1D study that, the adoption of IS, CM and CFL parameter equal respectively to 0.01, 1.01 and 0.1, was enough to guarantee an accurate ignition time prediction because of the proper temporal resolution in the initial simulations steps.

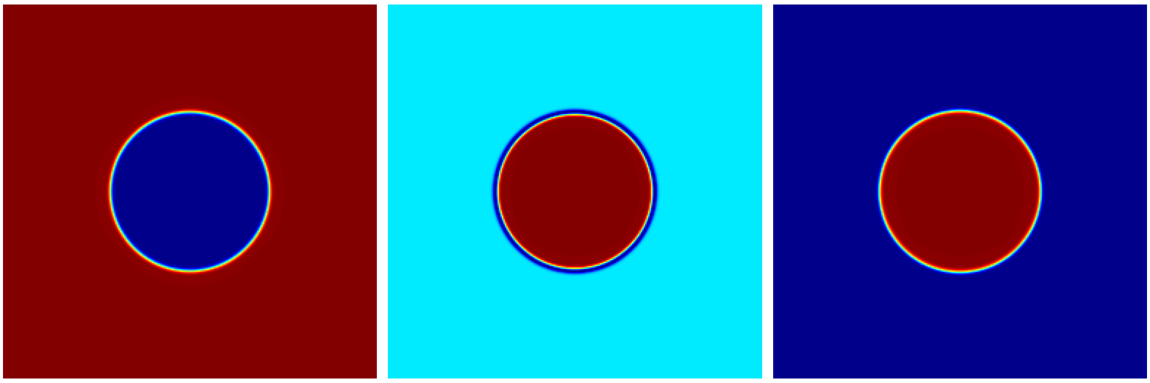

(a) T(K) **(b)** $\rho(\mathrm{kg/m^3})$ **(c)** $\chi(\mathrm{CH_4})$

Figure 7.3: Field of the temperature (left), density (middle) and methane mole fraction (right) at $t = 0$ in the YZ cross-sectional plane of the computational domain. The color scales range (blue to red) from 305 to 1300K for the temperature, from 0.206 to 0.362 $\mathrm{kg/m^3}$ for the density and from 0 to 0.5 for the methane mole fraction.

This gave a dt in the order of $2 \cdot 10^{-8}$s in the earliest timesteps. As explained in section 3.2.2, the value of dt at the initial timestep (dt^i, with i=1) is expressed as a function of IS and dt^0, the latter is much lower in the 3D case as a consequence of the relative velocity between fuel and oxidiser. For this reason, with the purpose of being consistent with the earliest dt values in the 1D simulations and avoiding an excessively low initial dt which increases the simulation expense, the IS parameter has been increased from 1.01 to 1.1. The resulting dt in the initial timesteps are in the order of $1 \cdot 10^{-8}$s.

The boundary conditions are set-up as outflow in all directions except the stream-wise one, where periodic boundary condition are applied.

7.3 Atomic oxygen and ignition time prediction

The methodology used to compute the ignition time for the one-dimensional cases (Sect. 3.3) relies on the temperature calculation in the mixture fraction space. Once estimated the adiabatic flame temperature, the ignition time is defined as the time at which the 25% of T_{ad} is reached. The calculation of the temperature rise conditioned on mixture fraction does not represent an effective method to estimate the ignition timing when the effects of turbulent motion are considered. This is because of the scatter occurring in the temperature field due to convective mixing, well before ignition starts [63].

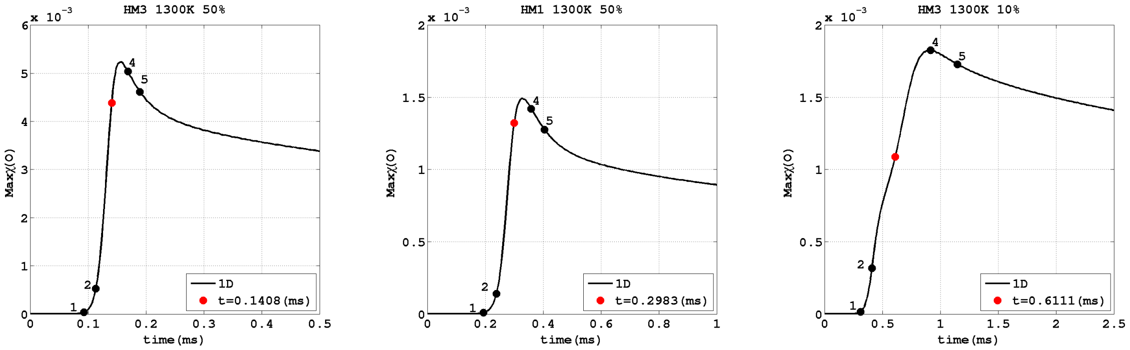

(a) HM3 50% **(b)** HM1 50% **(c)** HM3 10%

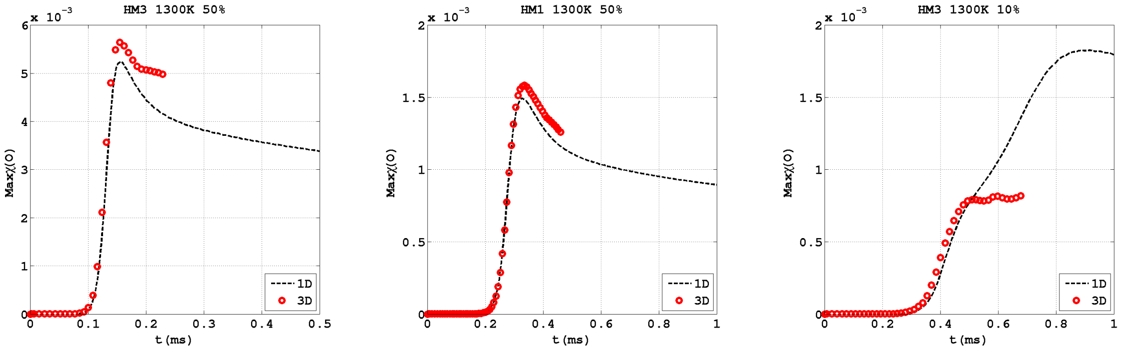

(d) HM3 50% **(e)** HM1 50% **(f)** HM3 10%

Figure 7.4: Top row: Evolution of the maximum atomic oxygen mole fraction for the HM3-50% (left), HM1-50% (middle) and HM3-10% (right) case. Graphs refer to the one-dimensional case studies. The red dot indicates the O maximum mole fraction value at the ignition time (Chap 5 and 6). The black dots outline the O maximum mole fraction value at different evaluation points, from chapters 5 and 6, in the pre-ignition and post-ignition periods. **Bottom row**: Comparison of the O radical evolution between diffusion (dashed line) and turbulent (red circles) configurations. The red circles represent peak $\chi(O)$ values extracted from the whole three-dimensional domain and different times.

As a consequence, tracking the level an intermediate species in time, was considered as a more appropriate method to estimate ignition. Some studies in the literature use the H radical, an intermediate species for both hydrogen and methane combustion, as an indicator of ignition process [63, 69]. In these studies, pure H_2 or an equimolar $H_2{-}CH_4$ fuel blends are considered. Even thought a large excess of H radical is observed in cases where there is a strong H_2

presence in the initial fuel, which makes the use of H radical for computing ignition appropriate, cases with low of null initial H_2 presence showed a poor level of atomic hydrogen in the earliest stages of ignition period. Furthermore, the release of H may corresponds to the early CH_4 abstraction only, rather than the complete start of the methane chemistry.

In this thesis the level of atomic oxygen is proposed as an ignition indicator. The reason relies on the fact that only one elementary reaction, the R33 step of the DRM19 mechanism, is observed producing the O radical at a significant rate. Being the R33 the major O_2 consuming step which controls the rates of the hydrogen and methane mechanisms, by tracking the O radical the fuel/oxidiser interaction is tracked in an unambiguous way.

Figures 7.4b, 7.4a and 7.4c show the evolution of the maximum atomic oxygen mole fraction ($\chi(O)$) for the one-dimensional HM1-50%, HM3-50% and HM3-10% cases. The five points highlighted, represent the level of $\chi(O)$ at the times selected to investigate each case. As the figures show, after an initial period where the atomic oxygen presence is negligible, a rise in the O level is observed till a peak in the build-up is reached. The ignition point is present in the steepest part of the curve, the point 1 and 2 describe the beginning of O build-up, while the points 4 and 5 are located after the peak in the O radical.

A similar analysis is performed for the turbulent cases. For each case considered, HM3-50%, HM1-50% and HM3-10%, the O radical mole fraction ($\chi(O)$) is observed. On figures 7.4d, 7.4e and 7.4f the evolution of peaks $\chi(O)$ (red circles) for turbulent cases are compared with the $\chi(O)$ profiles in the 1D configurations. The peak $\chi(O)$ values are extracted from the whole three-dimensional domain used.

The $\chi(O)$ profile for the turbulent HM3-50% coincides with the 1D profile (Fig. 7.4d) until approximately the $\chi(O)$ peak is reached. After this point, the 3D profile follows a trend similar to the 1D profile, slightly upward shifted. The similarities between the two profiles allow the identification of a *pre-ignition* and a *post-ignition* period in the turbulent case. The pre-ignition period can be identified as time interval ranging from t=0 till the peak of $\chi(O)$ is reached [3]. Conversely, the time at which the peak of $\chi(O)$ is reached and the time at which the simulation ends, represent the limits of the post-ignition period.

Apart from the lower O radical production, the scenario observed for the turbulent HM1-50% case is similar. According to the above mentioned definition, profiles in figure 7.4e can be mainly divided in two parts: the pre-ignition period and the post-ignition period.

Figure 7.4f shows that, in the HM3-10% case the evolution of atomic oxygen build-up strongly differ between the 1D and 3D case studies. The profiles agree until t ~0.5ms, when $\chi(O)$ growth appears arrested.

The similarity of the 1D and 3D $\chi(O)$ profiles in the HM3-50% and HM1-50% cases allows five different investigation points to be selected for the 3D study, comparable in time to the 1D study. Two points are defined in the pre-ignition period, two points in the post-ignition period, one identifies the ignition event. The points selected are shown in figures 7.5d and

---

[3] It should be noted that the peak of $\chi(O)$ is reached in HM3-50% and HM1-50% at slightly later time than ignition

7.5e. Because of the divergence between 1D and 3D $\chi(O)$ profiles in the HM3-10% case (Fig. 7.4f), the resemblance of curves could not be exploited to define the selection points in the low hydrogen case. Investigation points for the HM3-10% case were selected, basing on more qualitative considerations. Two points were selected before the ignition time and two points were taken after ignition (Fig. 7.5f), in such a way as to best match the selection of points for the HM3-50% and HM1-50% cases.

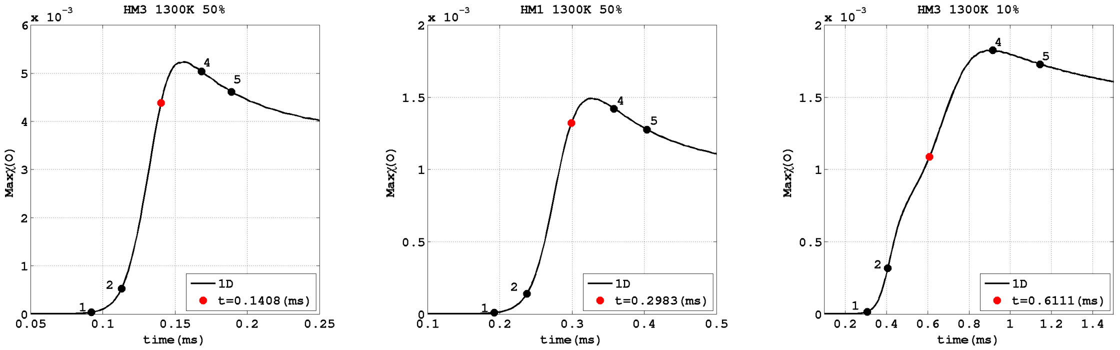

(a) HM3 50% (1D) **(b)** HM1 50% (1D) **(c)** HM3 10% (1D)

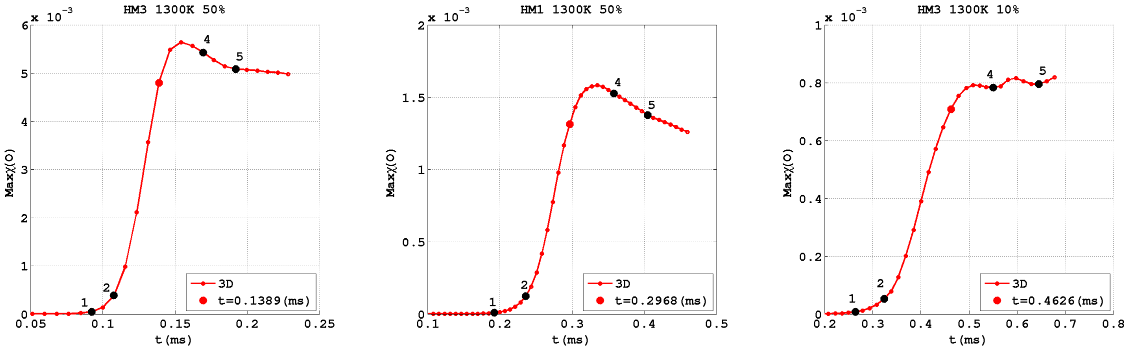

(d) HM3 50% (3D) **(e)** HM1 50% (3D) **(f)** HM3 10% (3D)

Figure 7.5: Top row: Evolution of the maximum atomic oxygen mole fraction for the HM3-50% (left), HM1-50% (middle) and HM3-10% (right) case. Graphs refer to the one-dimensional case studies. The red dot indicates the O maximum mole fraction value at the ignition time (Chap 5 and 6). The black dots outline the O maximum mole fraction value at different evaluation points, from chapters 5 and 6, in the pre-ignition and post-ignition periods.
Bottom row: Evolution of the maximum atomic oxygen mole fraction for the HM3-50% (left), HM3-50% (middle) and HM3-10% (right) case. Graphs refer to the three-dimensional case studies. The large red dots indicate the O radical maximum mole fraction values at the ignition. The black dots indicate the O radical maximum mole fraction values at different evaluation points in the pre-ignition and post-ignition period. The small red dots represent peak $\chi(O)$ values extracted from the whole three-dimensional domain at different times.

Table 7.2 lists the five time points selected for each case in both the 1D and 3D study. Snapshots of important variables (temperature, methane mole fraction and hydrogen mole fraction) will be taken at each of the point selected, in order to describe the evolution of the fuel jet though the ignition period. Point 2, point 3 and point 5 will be used to provide a more detailed description of the turbulence-diffusion-chemistry interplay before and after ignition.

	HM1-50%		HM3-50%		HM3-10%	
	1D time (ms)	3D time (ms)	1D time (ms)	3D time (ms)	1D time (ms)	3D time (ms)
Point 1	0.1924	0.1924	0.0922	0.0925	0.3068	0.2640
Point 2	0.2376	0.2362	0.1129	0.1078	0.4069	0.3236
Point 3	0.2983	0.2968	0.1408	0.1389	0.6111	0.4626
Point 4	0.3583	0.3579	0.1684	0.1695	0.9160	0.5503
Point 5	0.4040	0.4047	0.1891	0.1921	1.1446	0.6454

Table 7.2: Selected investigation points for each case in both 1D and 3D study.

7.4 The base case - 1D-3D comparison

In this section an introductory overview of the effect of turbulence in the base case configuration is provided. To this end, the main aspects observed in the three-dimensional study of the HM3-50% case are compared with insights gained from the diffusion study.

The turbulent conditions under which the fuel jets entrains the hot oxidiser are shown on figure 7.6. Contour plots of temperature, mole fraction of methane and mole fraction of hydrogen along the ignition period are presented. The shear layer between the oxidizer and the fuel jet triggers the instabilities which then grow into vortices. The fuel core spreads and diffuses into the hotter regions of the oxidizer. The similarity of the structure for the hydrogen and methane flow patterns indicate a similar hydrodynamic behaviour throughout the ignition period. The less sharp appearance of the $\chi(H_2)$ snapshots suggests a more significant diffusion for the hydrogen.

Similar conclusions can be drawn from fields in figure 7.7. Here the CH_4 and H_2 mole fraction fields, along with the vorticity magnitude fields, are shown along three different point of the ignition period in axonometric view, highlighting the three-dimensional evolution of the turbulent jet. As aforementioned, figure clearly shows the fuel core spreading as it evolves in time. Particularly, the H_2 3D patterns (Fig. 7.7d, 7.7e and 7.7f) point out the quicker hydrogen diffusion into the oxidiser, since they look smoother than the corresponding CH_4 fields (Fig. 7.7a, 7.7b and 7.7c). Interestingly, the vorticity grows in magnitude at ignition (Fig. 7.7h), as a consequence of vortex stretching associated with a corresponding increase of the component of vorticity in the stretching direction, while keeping a comparable intensity in the post-ignition period (Fig. 7.7i). This suggests an incomplete turbulence development, up to the dissipative scale, in the latest part of ignition period. The influence of turbulence on the reactions kinetic during post-ignition is described in more details later in this chapter.

The ignition event is caught at point 3 (Fig. 7.6m), where an initial temperature rise can be observed. The temperature continue to rise in the post-ignition period as seen for point 4 and point 5 (Fig. 7.6n and 7.6o).

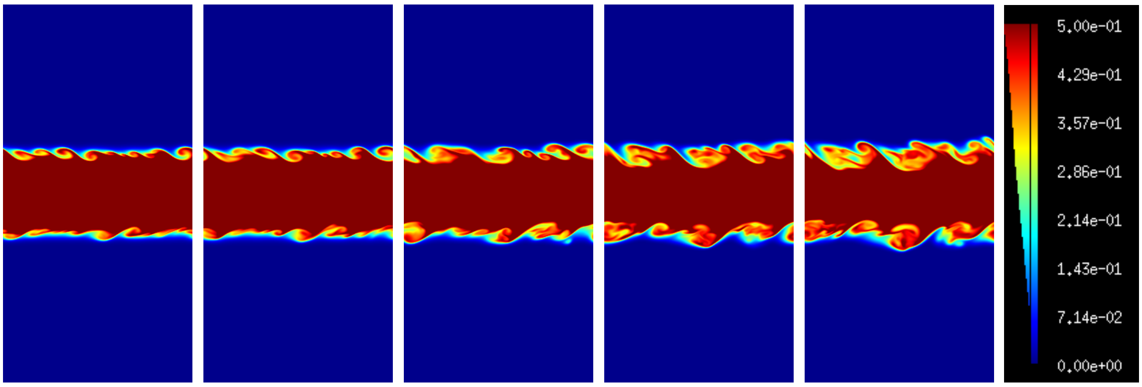

(a) Point 1 **(b)** Point 2 **(c)** Point 3 **(d)** Point 4 **(e)** Point 5 $\chi(\mathrm{CH_4})$

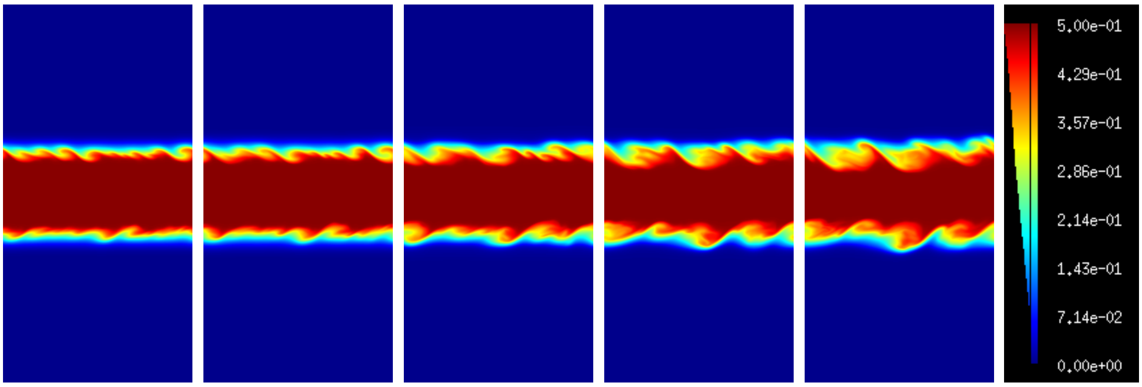

(f) Point 1 **(g)** Point 2 **(h)** Point 3 **(i)** Point 4 **(j)** Point 5 $\chi(\mathrm{H_2})$

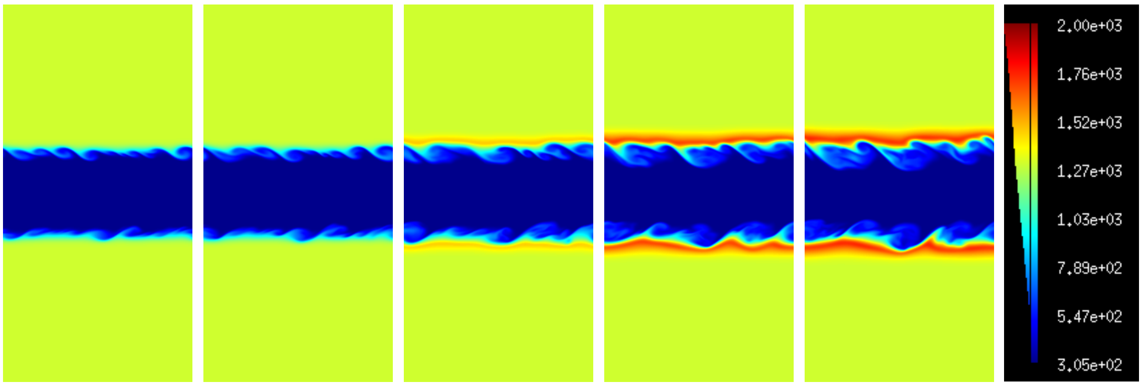

(k) Point 1 **(l)** Point 2 **(m)** Point 3 **(n)** Point 4 **(o)** Point 5 T(K)

Figure 7.6: Methane mole fraction (top row) fields, hydrogen mole fraction (middle row) fields and temperature (bottom row) fields for the base case. Snapshots are taken in the z=0 plane for each of the time investigation points.

Here, the highest temperature can be observed at the fuel/oxidiser interface. The temperature increment shown by snapshots results in the same order of the temperature rise observed in the correspondent 1D case study (Fig. 4.3a).

Similar indication is provided by figure 7.8. Here, the evolution of maximum temperature rise (ΔT) recorded in the 3D domain is compared with the maximum temperature rise observed in the correspondent 1D case study [4]. As the figure shows, the presence of turbulent convection

---

[4] It should be noted that, for both 1D and 3D studies, the ΔT variable represents the difference between the

only slightly influences the chemistry of the base case. The ΔT values from 3D case (red circles) overlay the 1D profile (black dashed line) almost for the entire period of time analysed.

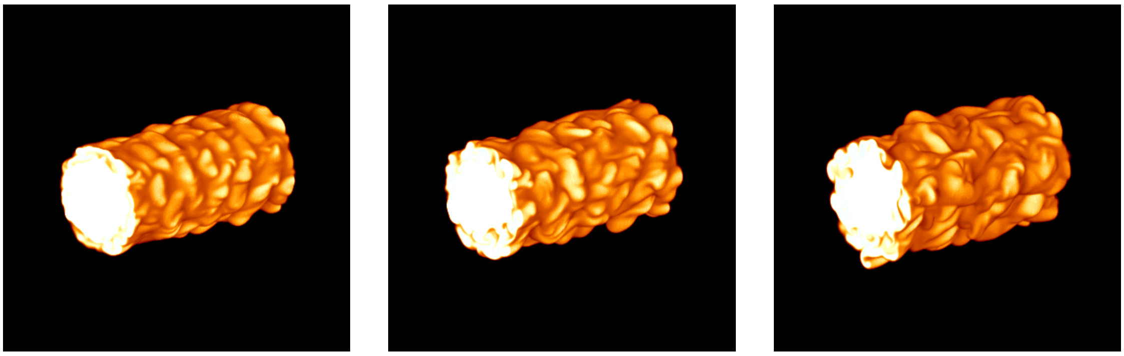

(a) $\chi(\mathrm{CH_4})$-P2 **(b)** $\chi(\mathrm{CH_4})$-P3 **(c)** $\chi(\mathrm{CH_4})$-P5

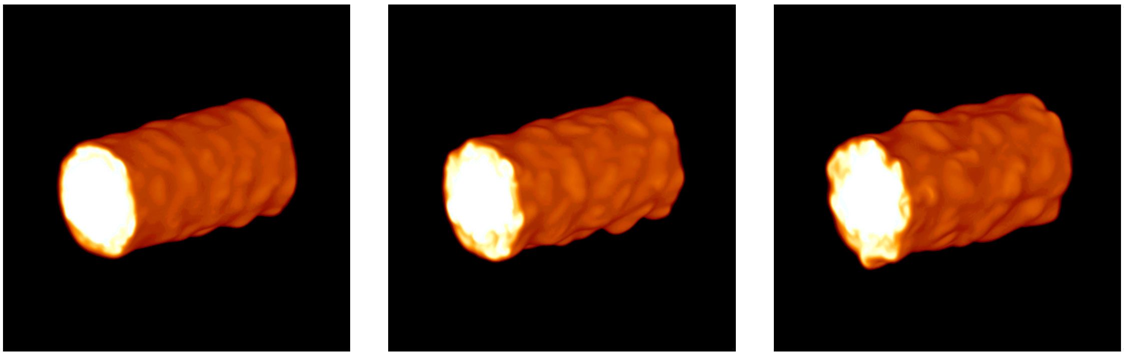

(d) $\chi(\mathrm{H_2})$-P2 **(e)** $\chi(\mathrm{H_2})$-P3 **(f)** $\chi(\mathrm{H_2})$-P5

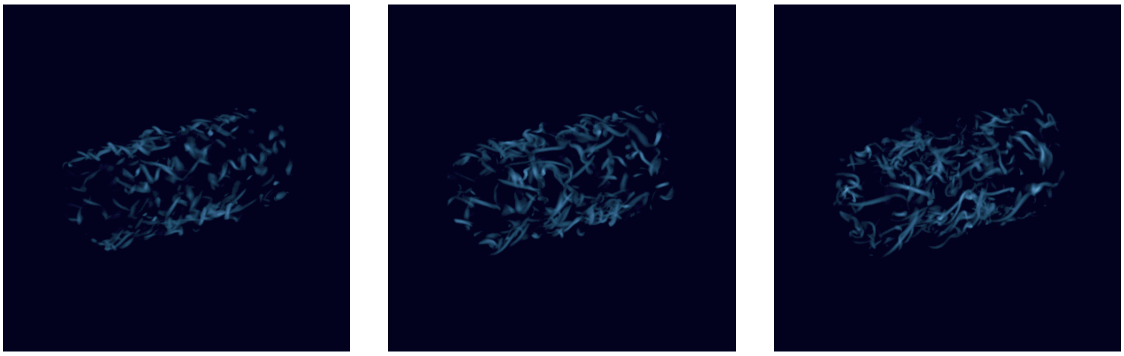

(g) Vorticity-P2 **(h)** Vorticity-P3 **(i)** Vorticity-P5

Figure 7.7: Fields of the methane mole fraction (top row), hydrogen mole fraction (middle row) and vorticity magnitude (bottom row) plotted at three different point of the period observed (pre-ignition, ignition and post-ignition) in axonometric view. The color scales for the methane and hydrogen mole fraction range (orange to white) from 0 to 0.5. The color scales for the vorticity magnitude range (blue to white) from 0 to $1.5e^6$ (1/s).

In order to gain deeper insights into the effect of turbulence to the fuel/oxidiser interaction, is following provided the description of different fields of interests (temperature, heat release, etc) along a specific plane of the numerical domain. It represents a cross-section plane of

---

maximum temperature recorded and the initial oxidiser temperature (1300K). As such it is not to be confused with the ΔT definition given in section 3.3.1, where the temperature increment is conditioned on the mixture fraction space.

the domain at x=5mm, in the middle of the stream-wise direction (Fig. 7.1). On each field a black dashed line is overlaid, which locate the stoichiometric mixture fraction region (Z_{st}). The Z_{st} iso-line will be used as a frame of reference to identify and distinguish the fuel rich area ($Z > Z_{\mathrm{st}}$), enclosed within the line, from the fuel lean region ($Z < Z_{\mathrm{st}}$), in the outer part of the line.

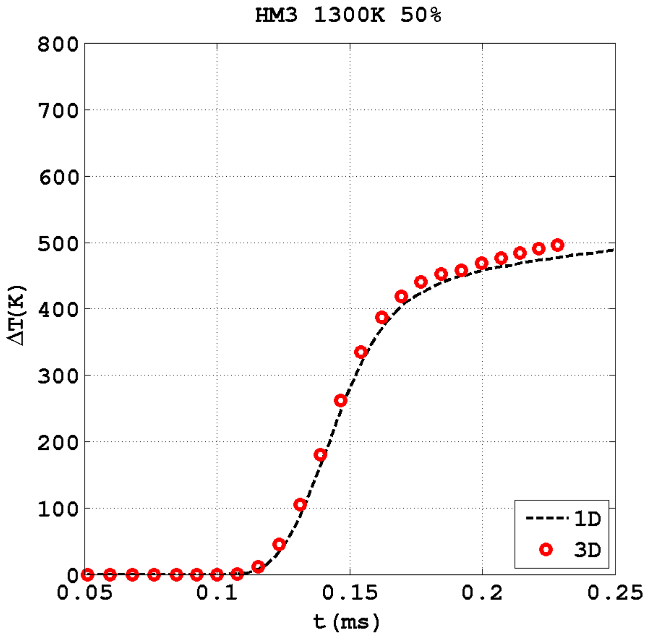

Figure 7.8: Evolution of the maximum temperature recorded in the 3D domain (red circles) plotted against the maximum temperature observed in the correspondent 1D case study. The temperature values from the HM3-50% configuration are here shown. The ΔT variable represents the difference between the maximum temperature recorded and the initial oxidiser temperature (1300K).

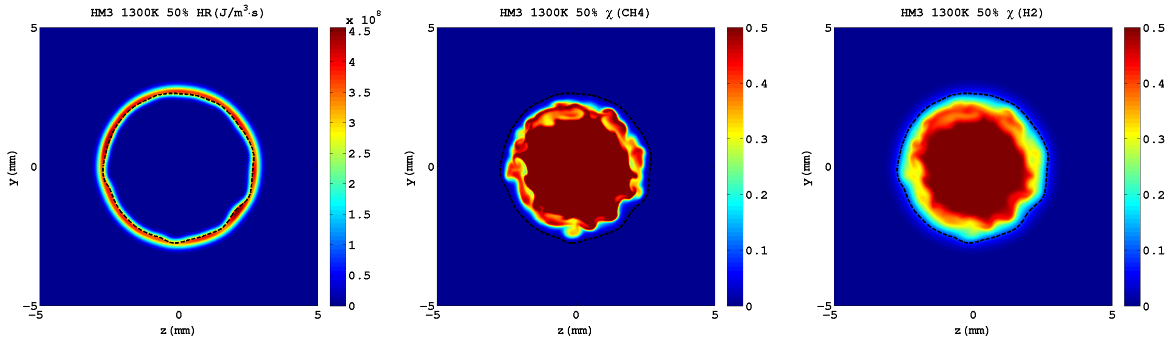

(a) HR-P2 **(b)** $\chi(\mathrm{CH_4})$-P2 **(c)** $\chi(\mathrm{H_2})$-P2

Figure 7.9: Fields of the heat release (left), methane mole fraction (middle) and hydrogen mole fraction (right) taken at the second point of analysis (pre-ignition). The HM3-50% case is considered. Fields are extracted from the cross-sectional plane of domain at x=5mm. The black dashed lines locate the stoichiometric mixture fraction region. Figures are zoomed around the fuel/oxidiser interface.

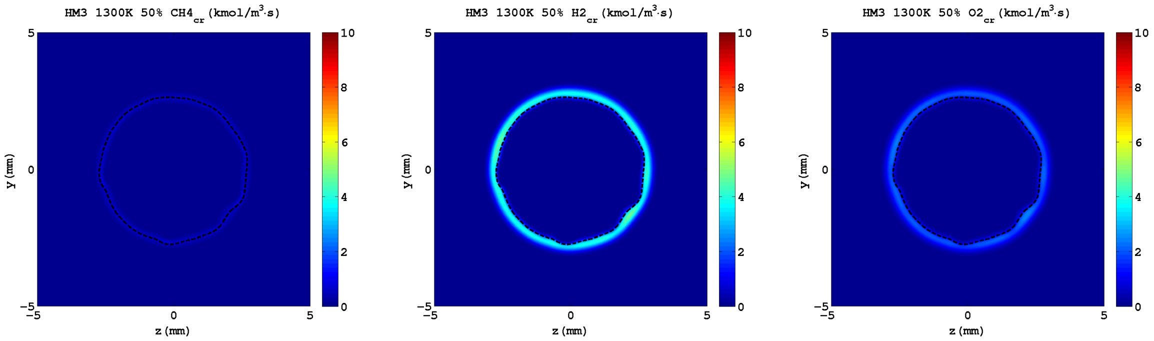

(a) CH_{4cr}-P2 **(b)** H_{2cr}-P2 **(c)** O_{2cr}-P2

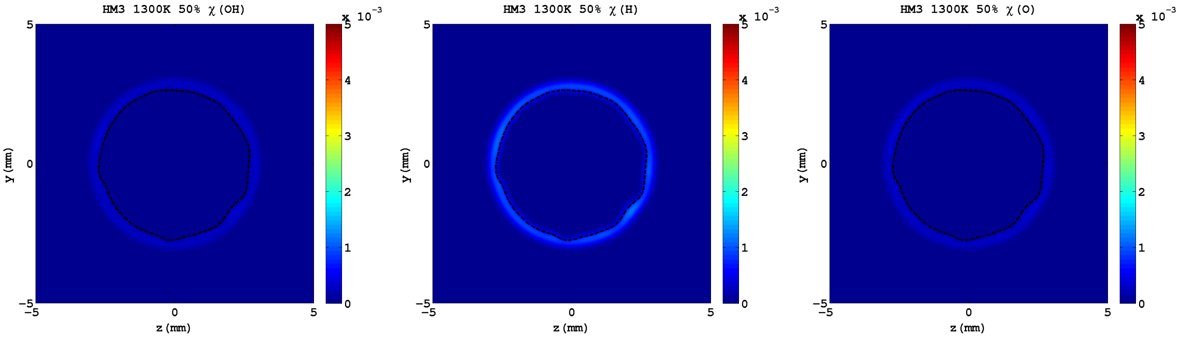

(d) $\chi(OH)$-P2 **(e)** $\chi(H)$-P2 **(f)** $\chi(O)$-P2

Figure 7.10: Top row: Fields of CH_4 (left), H_2 (middle) and O_2 (right) consumption rate taken at the second point of analysis (pre-ignition).
Bottom row: Fields of OH (left), H (middle) and O (right) mole fraction taken at the second point of analysis (pre-ignition).
The HM3-50% case is considered. Fields are extracted from the cross-sectional plane of domain at x=5mm. The black dashed lines locate the stoichiometric mixture fraction region. Figures are zoomed around the fuel/oxidiser interface.

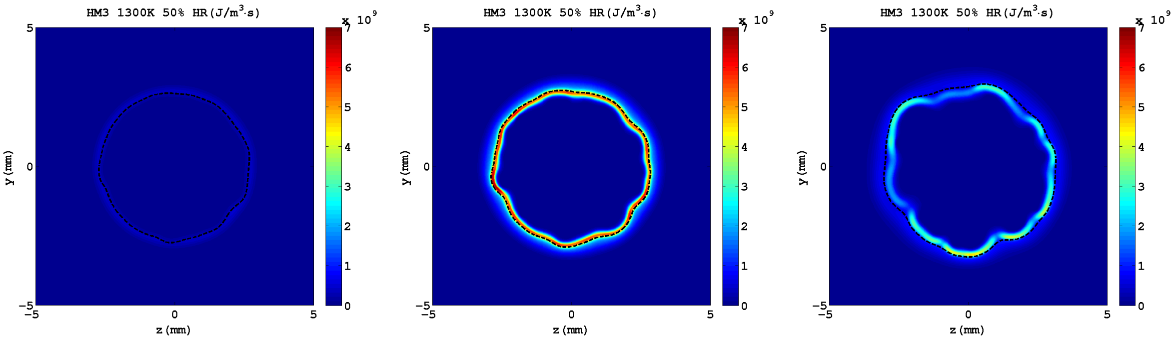

(a) HR-P2 **(b)** HR-P3 **(c)** HR-P5

Figure 7.11: Fields of heat release taken at point 2 - pre-ignition (left), at point 3 - ignition (middle) and at point 5 - post-ignition (right). The HM3-50% case is considered. Fields are extracted from the cross-sectional plane of domain at x=5mm. The black dashed lines locate the stoichiometric mixture fraction region. Figures are zoomed around the fuel/oxidiser interface.

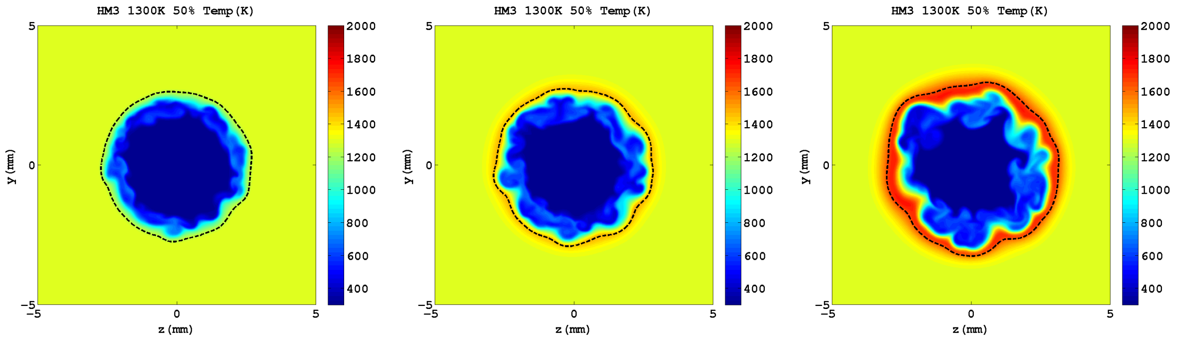

(a) Temp-P2 **(b)** Temp-P3 **(c)** Temp-P5

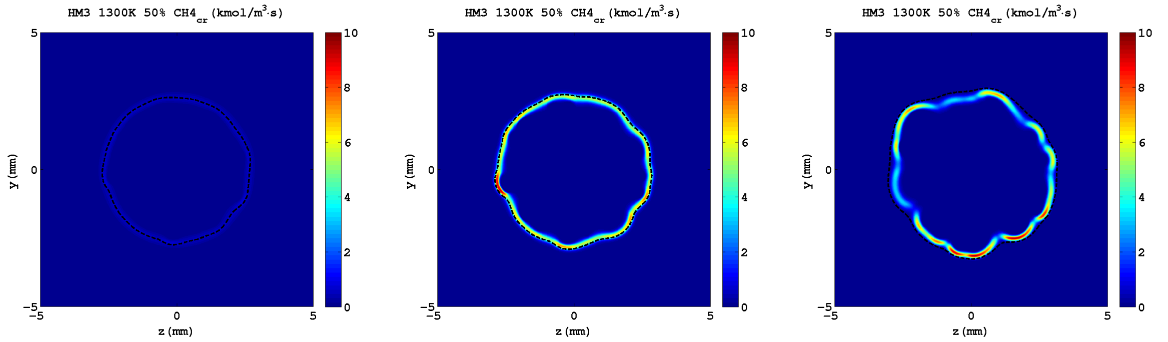

(d) CH_{4cr}-P2 **(e)** CH_{4cr}-P3 **(f)** CH_{4cr}-P5

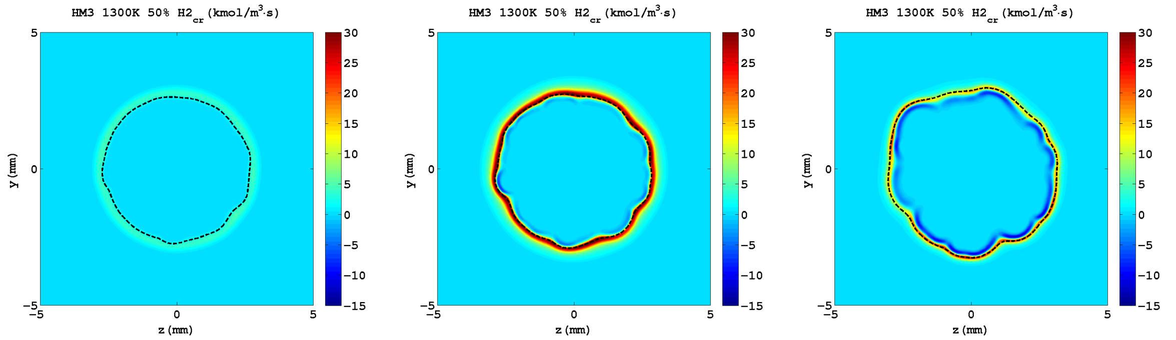

(g) H_{2cr}-P2 **(h)** H_{2cr}-P3 **(i)** H_{2cr}-P5

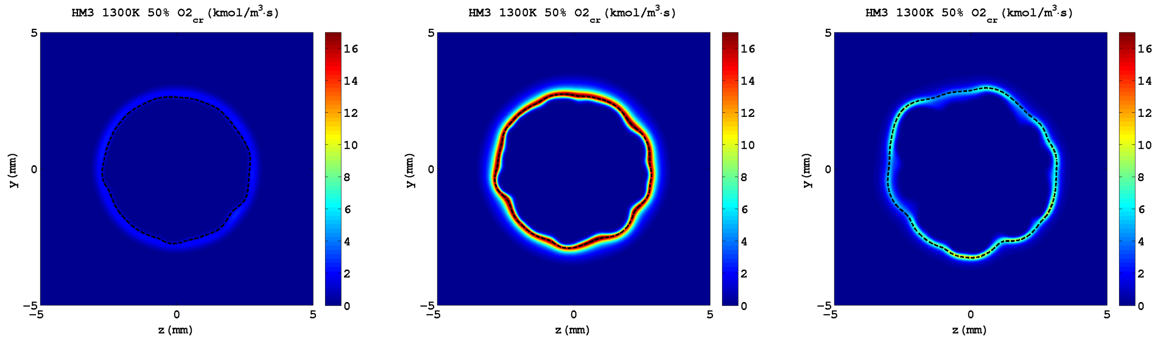

(j) O_{2cr}-P2 **(k)** O_{2cr}-P3 **(l)** O_{2cr}-P5

Figure 7.12: Fields of the temperature (top row), methane consumption rate (second row), hydrogen consumption rate (third row) and oxygen consumption rate (bottom row). Snapshots are taken at point 2 - pre-ignition (left column), at point 3 - ignition (middle column) and at point 5 - post-ignition (right column). The HM3-50% case is considered. Fields are extracted from the cross-sectional plane of domain at x=5mm. The black dashed lines locate the stoichiometric mixture fraction region. Figures are zoomed around the fuel/oxidiser interface.

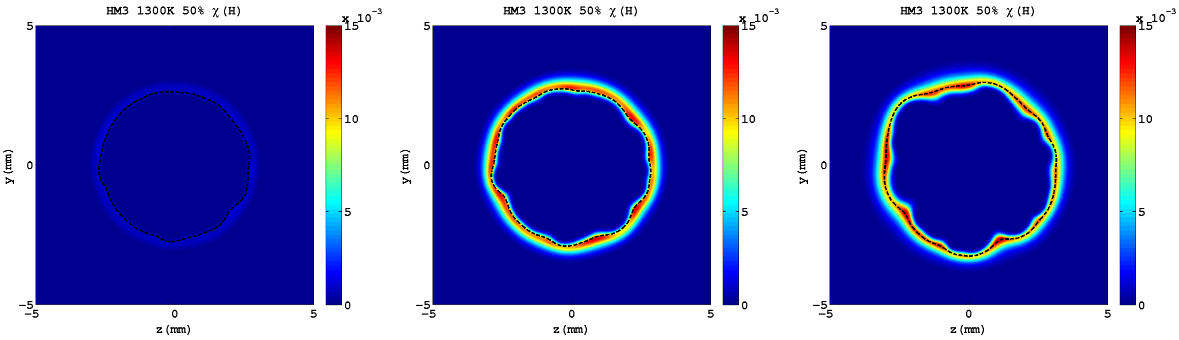

(a) $\chi(H)$-P2 **(b)** $\chi(H)$-P3 **(c)** $\chi(H)$-P5

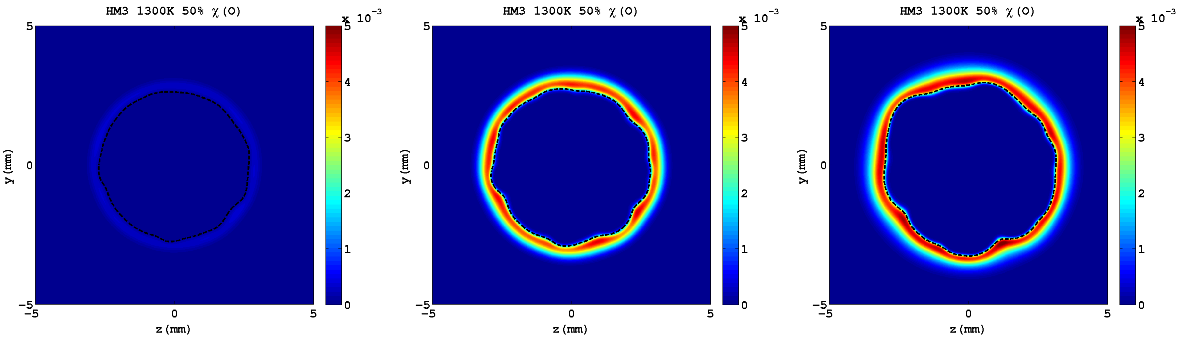

(d) $\chi(O)$-P2 **(e)** $\chi(O)$-P3 **(f)** $\chi(O)$-P5

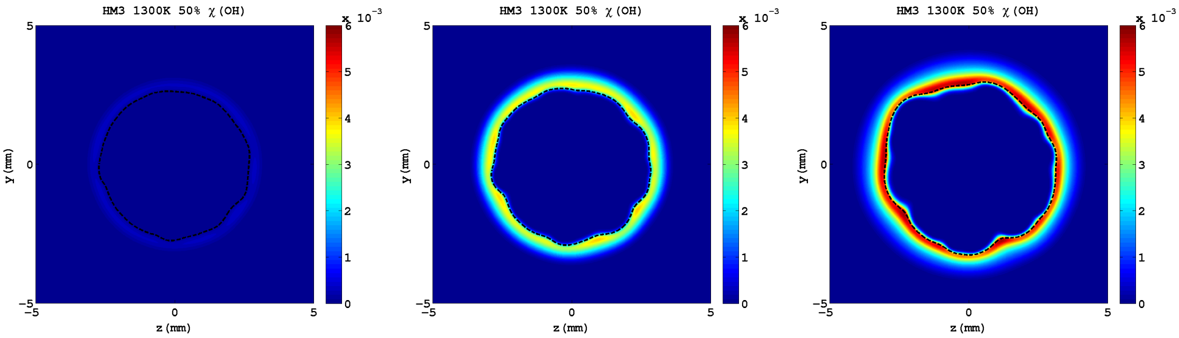

(g) $\chi(OH)$-P2 **(h)** $\chi(OH)$-P3 **(i)** $\chi(OH)$-P5

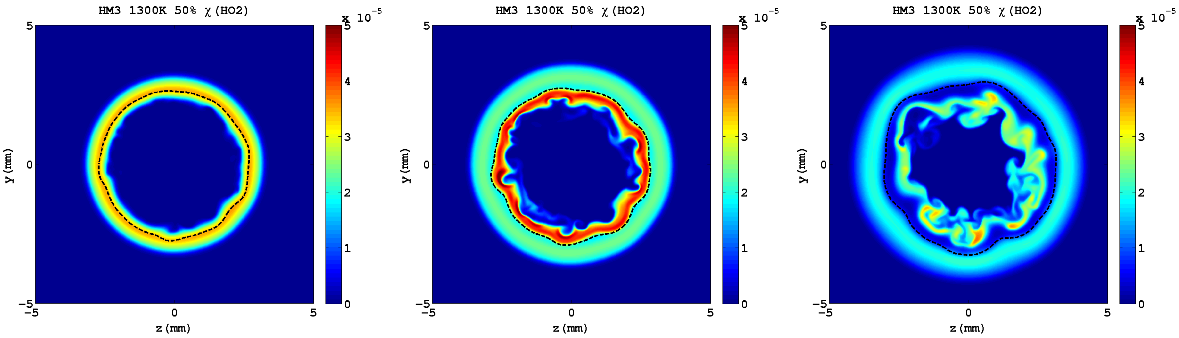

(j) $\chi(\mathrm{HO_2})$-P2 **(k)** $\chi(\mathrm{HO_2})$-P3 **(l)** $\chi(\mathrm{HO_2})$-P5

Figure 7.13: Fields of H mole fraction (top row), O mole fraction (second row), OH mole fraction (third row) and HO_2 mole fraction (bottom row). Snapshots are taken at point 2 - pre-ignition (left column), at point 3 - ignition (middle column) and at point 5 - post-ignition (right column). The HM3-50% case is considered. Fields are extracted from the cross-sectional plane of domain at x=5mm. The black dashed lines locate the stoichiometric mixture fraction region. Figures are zoomed around the fuel/oxidiser interface.

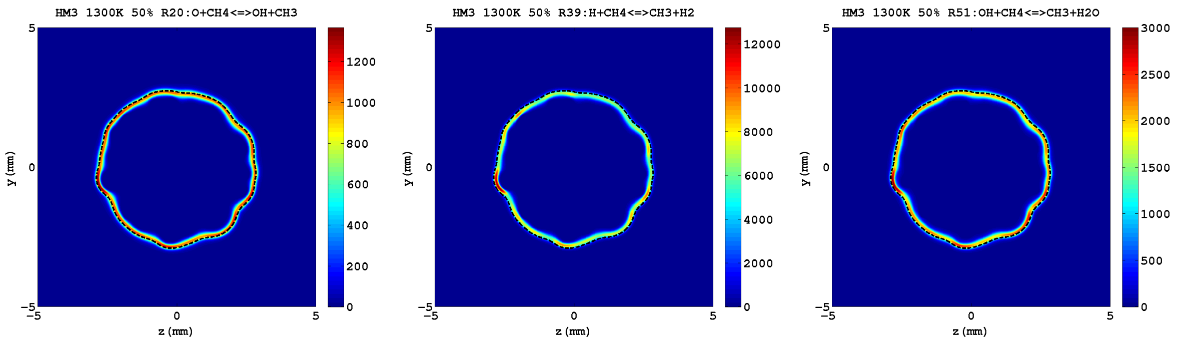

(a) R20-P3 **(b)** R39-P3 **(c)** R51-P3

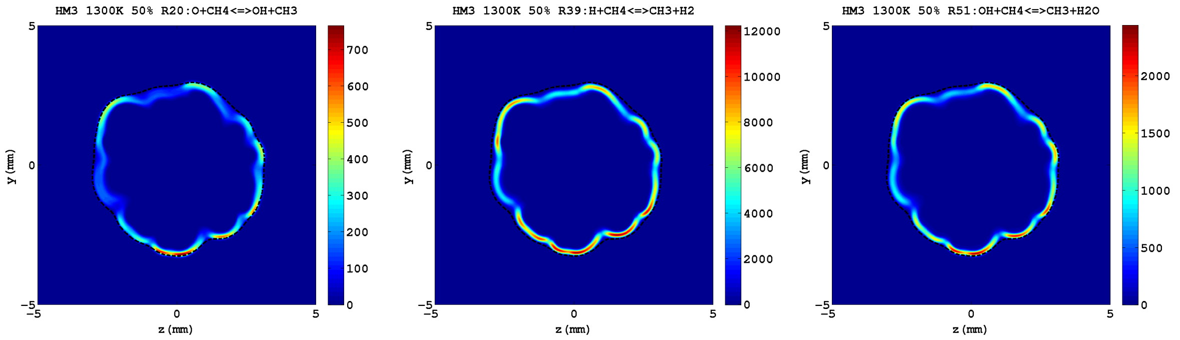

(d) R20-P5 **(e)** R39-P5 **(f)** R51-P5

Figure 7.14: Fields of R20 (left), R39 (middle), and R51 (right) reaction rates taken at point 3 - ignition (top row) and point 5 - post-ignition (bottom row). The HM3-50% case is considered. Reaction rates are expressed in $\mathrm{mole/m^3 \cdot s}$. Fields are extracted from the cross-sectional plane of domain at x=5mm. The black dashed lines locate the stoichiometric mixture fraction region. Figures are zoomed around the fuel/oxidiser interface.

Figure 7.9a shows the heat release field at point 2 of analysis (pre-ignition period). As shown in the figure, the start of the exothermic reaction occurs around the Z_{st}, mainly outside it. The low value of Z_{st} ($\sim$0.02) places the stoichiometric iso-line at the edge of the fuel/oxidiser interface. This is shown in figures 7.9b and 7.9c, where the dashed line encloses the vortical structures. As a result, turbulent eddies appear to play no role in the initiation of fuel/oxidiser chemical interaction. A closer look to figures 7.9b and 7.9c reveals that methane mainly remains confined within Z_{st}, while hydrogen partially diffuses beyond Z_{st}, the hottest part of the domain. This is clearly shown by the more diffuse hydrogen contour, which indicates the important role of differential diffusion even in a turbulent jet.

Because of the faster H_2 diffusion in the hot regions, the fuel/oxidiser interaction in the pre-ignition period resembles the physical/chemical scenario observed in the diffusion case study, where the differential diffusion was found to be the most significant feature in controlling the pre-ignition process.

Figure 7.10a, 7.10b and 7.10c show the fields of CH_4, H_2 and O_2 consumption rate taken at the second point of analysis. In order to make a direct comparison between these three fields, the axis have the same scale ([0,10]). The methane consumption (Fig. 7.10a) occurs in the proximity of Z_{st}. Mainly in the outer part of stoichiometric iso-line occurs the H_2 consumption (Fig. 7.10b), which also shows a broader extension. Figures 7.10a and 7.10b show, in the cross-sectional plane considered, a significantly higher rate at which H_2 is being consumed, which suggests the important role of hydrogen chemistry in the earliest stages of ignition. Also the O_2 consumption is observed mainly occurring in the outer part of stoichiometric iso-line (7.10c), with a rate higher than methane consumption. The similar location of early H_2 and O_2 consumption, coupled with the higher rate at which hydrogen and oxygen are being consumed, outlines a major role of H_2-O_2 interaction in the pre-ignition period.

The early formation of radical pool is described by figures 7.10d, 7.10e and 7.10f, which are presented with the same scale ($[0.5{\cdot}10^{-3}]$) in order to make a direct comparison between them. The H/O/OH build-up can be accounted for mainly the H_2-O_2 interaction. As in fact figures 7.10e, 7.10f and 7.10d show, the presence of these intermediates is observed mostly in the fuel lean region ($Z < Z_{\mathrm{st}}$), where H_2 and O_2 consumption occurs. The presence of H is larger compared with O and OH. As described in the 1D study of the base-case, along with the formation of H/O/OH pool, an early production of hydroperoxyl (HO_2) is observed (Fig. 7.13j), which acts as sinks for H radical in the fist part of ignition.

The evolution in time of major fields of interests is shown in figures 7.11 7.12 and 7.13. Here, each field is shown with a fixed scale in order to appreciate the change in time of the quantity described. At ignition, as the fuel/oxidiser interaction evolves in time, a higher heat release rate (Fig. 7.11b), followed by a significant increase in temperature (Fig. 7.12b), is noticed. As a consequence of the temperature dependence of reaction rates, the rise in temperature, results in higher rates of reactants consumption (Fig. 7.12e, 7.12h and 7.12k).

The rate of H_2 consumption remains higher than for CH_4, as well as occupying a broader area. The hydrogen consumption remains located mainly outside the Z_{st} iso-line, even though a small portion of the region where H_2 chemistry occurs, is visible within Z_{st}. Here ($Z > Z_{\mathrm{st}}$), methane consumption occurs. In the same region, the hydrogen consumption rate contour highlights a small but significant H_2 production (dark blue regions within Z_{st}). This phenomenon was justified in the 1D base case by the role of the R39 step, observed to be dominant, as a consequence of the large excess of H radical, among the three major reactions responsible for the methane dehydrogenation (R20, R39 and R51).

A similar scenario can be observed in the turbulent study. In figure 7.14 are shown the fields of major steps describing the methane dehydrogenation in the DRM19 mechanism: R20, R39 and R51 taken at ignition and in the post-ignition period. As figure suggests, the R39 step represents the reaction controlling the H abstraction from CH_4 molecule. It is also responsible, as explained by R39 kinetic equation (see appendix A), for the observed H_2 production.

As observed in 1D case, at ignition time it is possible to appreciate the temperature dependence of the hydroperoxyl molecule bonds, which tend to cleavage where the temperature rises. Figure 7.13k outlines two regions were the HO_2 presence is observed. Within the Z_{st} iso-line stronger is the hydroperoxyl presence (red region), while reduced is the presence outside Z_{st}

(light green region). In between these two regions, just outside Z_{st}, a small HO_2 consumption is denoted by the light blue area. The HO_2 consumption is particularly evident in the post-ignition period (Fig. 7.13l), denoted by the dark blue area in proximity of Z_{st}. The region where hydroperoxyl initially breaks down (Fig. 7.13k), coincides with the area where a significant H_2 and O_2 consumption are observed (Fig. 7.12h and 7.12k). This suggests a link between H_2-O_2 interaction and the first major exothermic event.

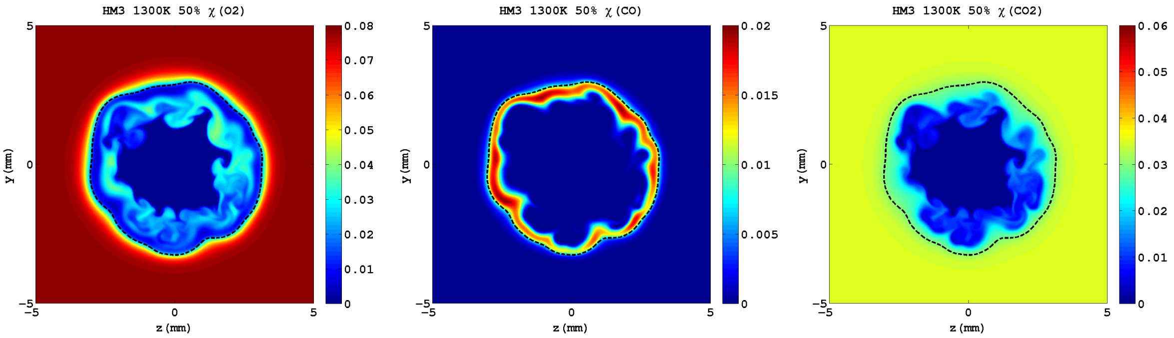

(a) $\chi(O_2)$-P5 **(b)** $\chi(CO)$-P5 **(c)** $\chi(CO_2)$-P5

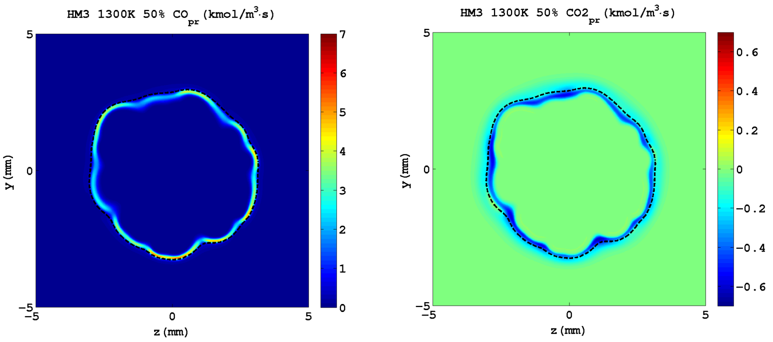

(d) CO_{pr}-P5 **(e)** $CO_{2\mathrm{pr}}$-P5

Figure 7.15: Fields of O_2 mole fraction (top left), CO mole fraction(top middle), CO_2 mole fraction(top right), CO production rate (bottom left) and CO_2 production rate (bottom right) taken at point 5 - post-ignition. Fields are extracted from the cross-sectional plane of domain at x=5mm. The black dashed lines locate the stoichiometric mixture fraction region. Figures are zoomed around the fuel/oxidiser interface.

The post-ignition period was characterised, in the 1D case, by a significant drop of O_2 level in the proximity of the stoichiometric mixture fraction region (Fig. 4.3b). The O_2 depletion exerted a rate limiting role on the majority of reactions examined, followed by a reduction in the rate of heat release and a slowdown of the rate of increase of ΔT over time.

A significant O_2 depletion is also observed in the presence of turbulence. As figure 7.15a shows, a low oxygen presence is observed in both fuel rich and fuel lean areas near Z_{st}. Along the Z_{st} line in particular, oxygen is almost completely consumed. In the area where the oxygen depletion is detected, the rate at which H_2 and O_2 are being consumed (Fig. 7.12i and 7.12l) is also reduced. The consumption of hydrogen is observed, occurring mostly along Z_{st} line. The O_2 concentration is higher in this region relative to the area of CH_4 consumption (Fig.

7.12f). Nonetheless, a rate reduction of methane consumption is not observed. Conversely, the CH_4 consumption outline a rate significantly higher than what observed in the 1D study (Fig. 4.3d).

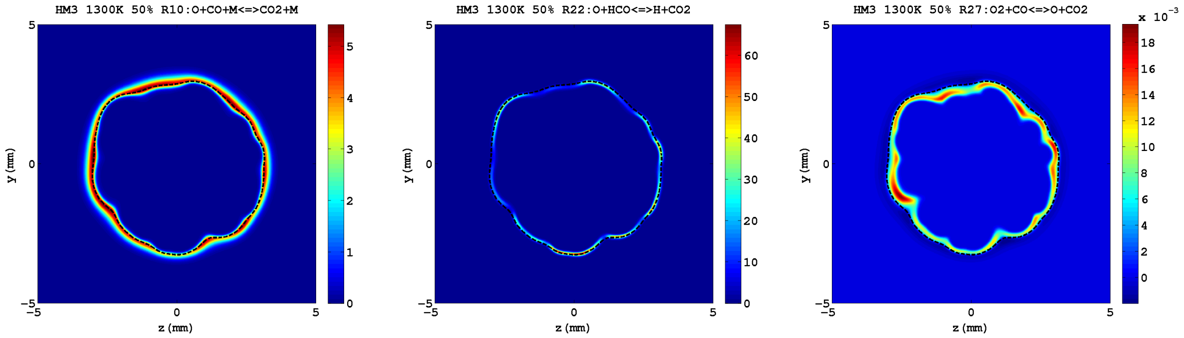

(a) R10-P5 **(b)** R22-P5 **(c)** R27-P5

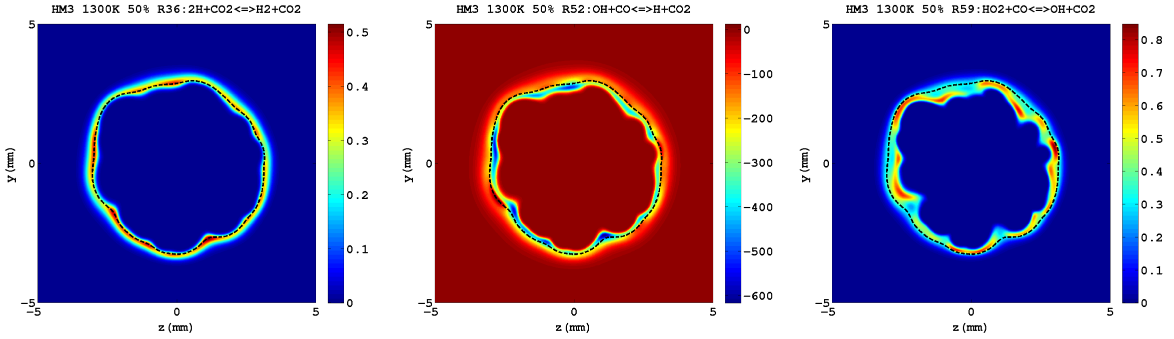

(d) R36-P5 **(e)** R52-P5 **(f)** R59-P5

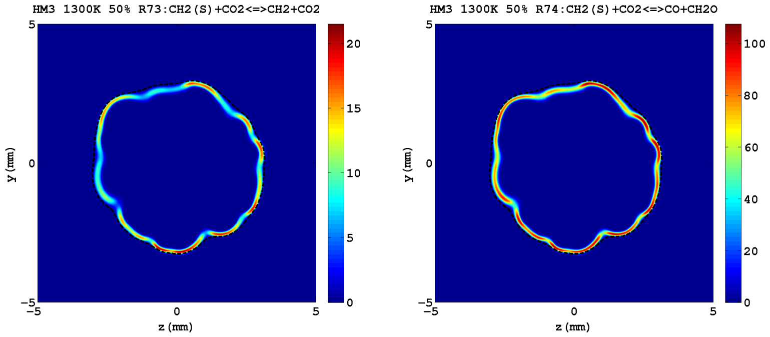

(g) R73-P5 **(h)** R74-P5

Figure 7.16: Reaction rates of all steps (R10, R22, R27, R36, R52, R59, R73 and R74) describing the CO_2 consumption/production in the DRM19 mechanism. Fields are taken at point 5 - post-ignition. Reaction rates are expressed in $\text{mole}/\text{m}^3 \cdot \text{s}$. Fields are extracted from the cross-sectional plane of domain at x=5mm. The black dashed lines locate the stoichiometric mixture fraction region. Figures are zoomed around the fuel/oxidiser interface.

The high rate of CH_4 consumption in the latest stage of ignition was justified in the 1D case with the combined effect of a low O_2 presence and a large excess of atomic hydrogen. In particular it was observed that some of the H activated steps like R2, R39, R30 and R52 were particularly enhanced by the large presence of H, as a consequence of the less competing role of the R33 reaction, also sensitive to the H presence, which followed the oxygen depletion. In a way similar to the 1D case, the R39 step result particularly enhanced in the 3D case by the high level of H in the fuel rich area (Fig. 7.13c), where methane is consumed. As in fact figures 7.14d, 7.14e and 7.14f shown, the R39 rate remains as high as at the previous time point, while R20 and R51 steps show a significant rate reduction.

A potential explanation of the large difference observed in CH_4 consumption between 1D and 3D cases could be the turbulent mixing of methane stream. In the 1D case the methane chemistry resulted particularly affected in the last part of ignition by the lower CH_4 diffusivity as the flame front moved in the upward direction. In the 3D case, the presence of turbulent convention tends to reduce the differential diffusion effect as the turbulence grows and the eddies become smaller.

Consistently with the findings from the 1D case, a reduced rate of heat release (Fig. 7.11c) is also observed where the lack of oxygen is significant.

The large H presence in the final part of the ignition process, also justified, in 1D study, the unusual CO_2 consumption observed in the one-dimensional study of the base case. The analysis of kinetic scenario revealed that the CO presence in the numerical domain was due to two different processes: the $\mathrm{HCO}{-}{>}\ \mathrm{CO}$ and the $\mathrm{CO_2}{-}{>}\ \mathrm{CO}$ conversion. The latter in particular, was analysed in depth. The investigation of all steps describing CO_2 production shown that the backward R52 step played a major role in the carbon dioxide consumption.

Consistently with the one-dimensional study, the turbulent case shows the formation of CO (Fig. 7.15b), while no increase in CO_2 (Fig. 7.15c) is observed. In particular, figure 7.15c highlights a light green region around Z_{st} where the carbon dioxide appears to have been consumed. A similar indication is provided by figure 7.15e, which shows, in the selected sectional plane, only negative values of CO_2 production rate.

A complete picture of all elementary reactions responsible for CO_2 production/destruction included in the DRM19 mechanism is provided in figure 7.16. As figure 7.16e shows, the R52 step presents the highest rate, in the region considered, controlling the CO_2 destruction. All the other steps presented show instead negligible rates. Because of the low rate of steps describing CO_2 production, it is reasonable to consider the carbon dioxide consumption to originates from the oxidiser blend.

More insights into what causes the R52 step to proceed in the backward direction are obtained by analysing the R52 equation:

$$\mathrm{OH} + \mathrm{CO} \longleftarrow \mathrm{H} + \mathrm{CO_2} \qquad \text{(R52)}\cdot$$

The CO_2 consumption occurs in both fuel rich and fuel lean part of the numerical domain. The highest rate of consumption is observed in the rich part of the domain (Fig. 7.16e and 7.15e). Here, a significant presence of CO is observed (Fig. 7.15b). Even more significant is the amount of CO_2 entrained by the turbulent motion (Fig. 7.15c). Furthermore, reduced results here the presence of OH radical (Fig. 7.13i) while higher is the H excess (Fig. 7.13c). As a consequence, the significant presence of H and CO_2 within the region where the highest temperature are observed (7.12c), induces the R52 reaction to proceed towards reactants.

7.5 Effect of oxygen reduction - 1D-3D comparison

In this section an overview of the physical/chemical scenario observed by numerically mimicking the HM1-50% case of the Dally *et al.* experiment [54] is presented. The main aspects observed in the three-dimensional study of the HM1-50% case are compared with insights gained from the diffusion study. The fuel jet presents the same composition (equimolar mixture of hydrogen and methane) as the previous case. The oxidiser mixture is instead changed. The oxygen mass fraction in the oxidiser blend is three times lower than the base case. The reduction in oxygen is balanced by the increased N_2 level in the oxidiser, as described in table 7.1.

One of the key points that arose from the 1D diffusion study was the major impact of O_2 level reduction in limiting rates of reaction. Two major aspects were observed linked to the reaction rates limitation: the lower peak flame temperature and the delayed self-ignition time.

The evolution of the maximum O radical concentration in the domain (Fig. 7.5e) shows that dilution of O_2, delays self-ignition also when turbulence effects are considered. Particularly, as suggested by comparable 1D and 3D profiles in figure 7.4e, turbulent mixing plays a minor role in the self-ignition process.

The turbulent conditions under which the fuel jets entrains the hot oxidiser are shown in figure 7.17. Contour plots of temperature, mole fraction of methane and mole fraction of hydrogen along the ignition period are presented. The shear layer between the oxidizer and the fuel jet triggers the instabilities which then grow into vortices. The fuel core spreads and diffuses into the hotter regions of the oxidizer. Because of the longer time required to achieve ignition, turbulence grows stronger than the previous case presented (Fig. 7.6). The evolution of methane (top row) and hydrogen (middle row) molar fraction highlight similar hydrodynamic behaviour along the ignition period. Nonetheless, the $\chi(\mathrm{CH_4})$ snapshots appears more sharp, pointing out a different diffusion behaviour of hydrogen.

A similar scenario is described by fields in figure 7.18. The CH_4 and H_2 mole fraction fields, along with the vorticity magnitude fields, are shown along three different point of the ignition period in axonometric view, highlighting the three-dimensional evolution of the turbulent jet. The figures clearly show a more important spreading of the fuel jet, with respect to the turbulent base case, following the later ignition. The quicker hydrogen diffusion into the oxidiser is outlined by the H_2 3D patterns (Fig. 7.18d, 7.18e and 7.18f), which appear smoother than the CH_4 ones (Fig. 7.18a, 7.18b and 7.18c). Different from the turbulent base case also results the vorticity evolution along the ignition period. The iso-surface with high vorticity magnitude are observed significantly reduced in number in the latest part of ignition (Fig.

7.18i), indicating the complete development of turbulence up to the dissipative scales.

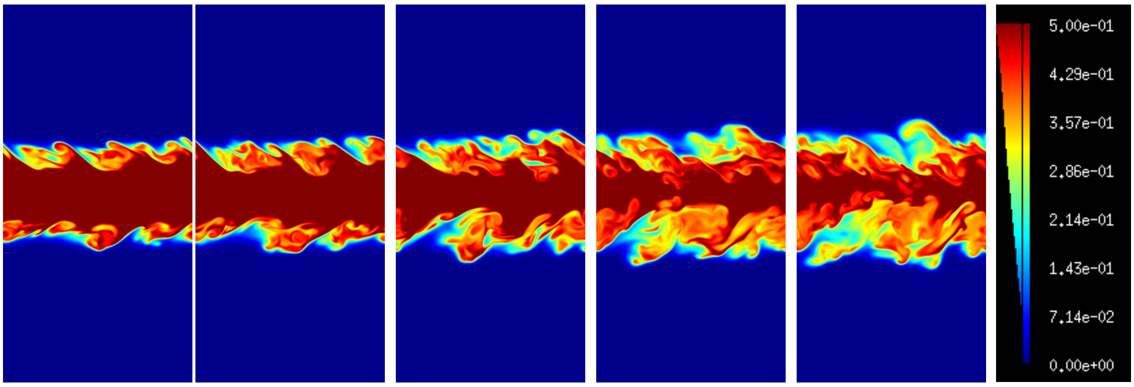

(a) Point 1 **(b)** Point 2 **(c)** Point 3 **(d)** Point 4 **(e)** Point 5 $\chi(\mathrm{CH_4})$

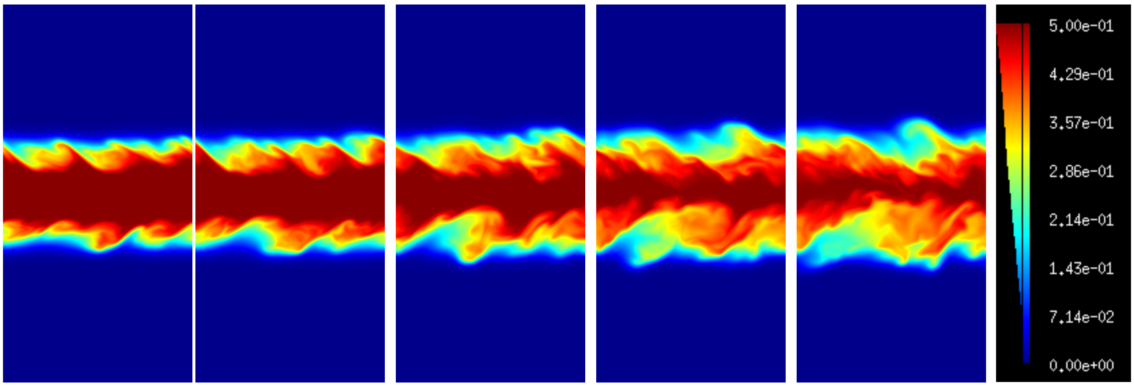

(f) Point 1 **(g)** Point 2 **(h)** Point 3 **(i)** Point 4 **(j)** Point 5 $\chi(\mathrm{H_2})$

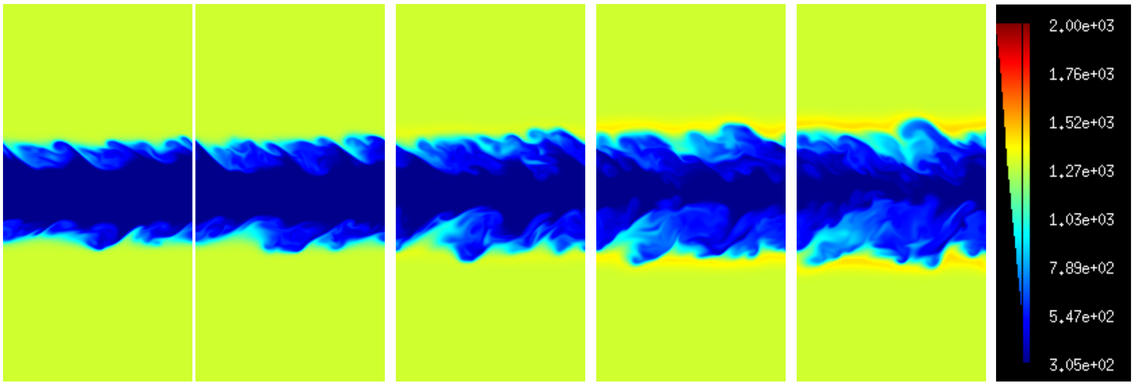

(k) Point 1 **(l)** Point 2 **(m)** Point 3 **(n)** Point 4 **(o)** Point 5 T(K)

Figure 7.17: Methane mole fraction (top row) fields, hydrogen mole fraction (middle row) fields and temperature (bottom row) fields for the HM1-50% case. Snapshots are taken in the z=0 plane for each of the time investigation points.

The temperature increase caused by ignition is hardly noticeable in figure 7.17m. More evident is the rise in temperature in the post-ignition period shown in figures 7.17n and 7.17o. Here snapshots outline the highest temperatures are reached at the fuel/oxidiser interface. As aforementioned for the 1D case study, the oxygen dilution results in a significant temperature reduction with respect to the base case (Fig. 7.6n and 7.6o).

The maximum temperature increase recorded in the turbulent case (~200K), is of the same order of what observed in the diffusion study. This is clearly shown in figure 7.19, where the evolution of maximum temperature rise ($\Delta T = T_{\mathrm{max}} - T_{\mathrm{ox}}$) recorded in the 3D domain (red circles) is compared with the maximum temperature rise in the correspondent 1D case study (black dashed line).

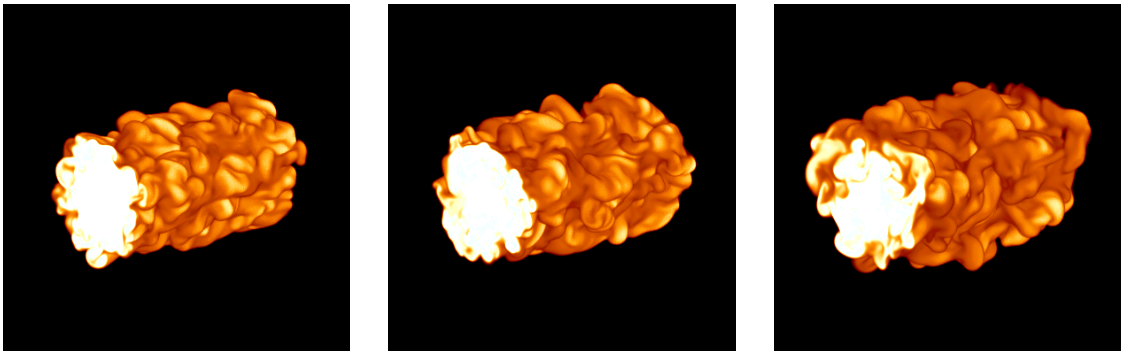

(a) $\chi(\mathrm{CH_4})$-P2 **(b)** $\chi(\mathrm{CH_4})$-P3 **(c)** $\chi(\mathrm{CH_4})$-P5

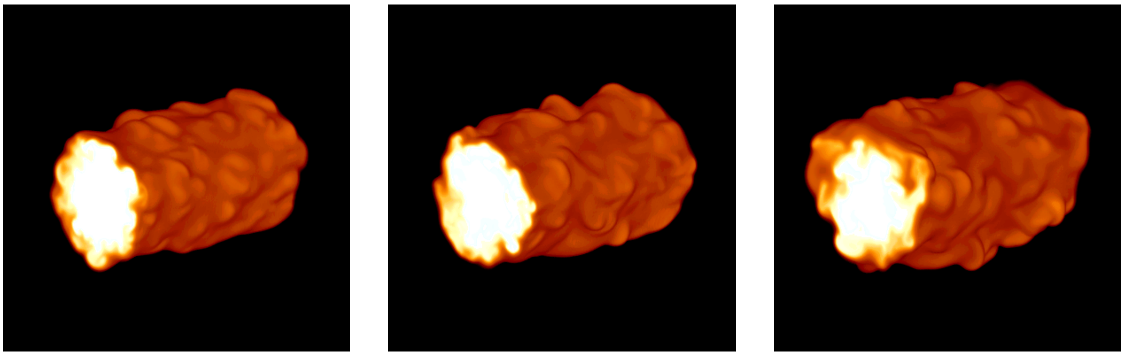

(d) $\chi(\mathrm{H_2})$-P2 **(e)** $\chi(\mathrm{H_2})$-P3 **(f)** $\chi(\mathrm{H_2})$-P5

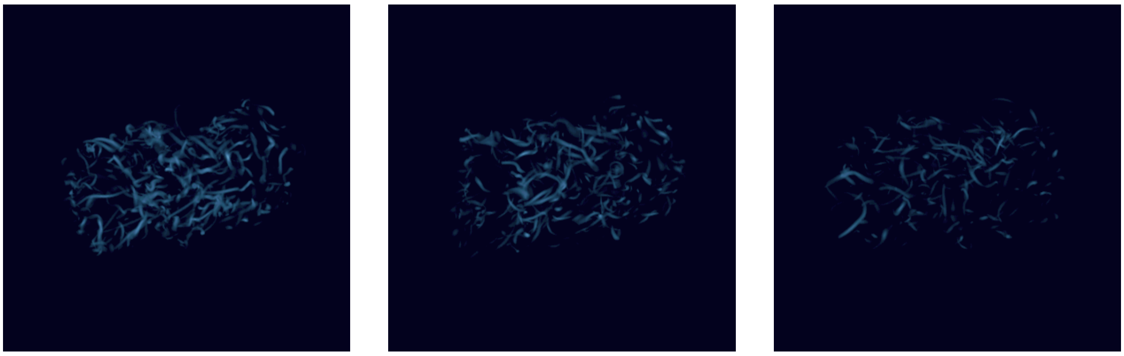

(g) Vorticity-P2 **(h)** Vorticity-P3 **(i)** Vorticity-P5

Figure 7.18: Fields of the methane mole fraction (top row), hydrogen mole fraction (middle row) and vorticity magnitude (bottom row) plotted at three different point of the period observed (pre-ignition, ignition and post-ignition) in axonometric view. The color scales for the methane and hydrogen mole fraction range (orange to white) from 0 to 0.5. The color scales for the vorticity magnitude range (blue to white) from 0 to $1.5e^6$ (1/s).

The figure shows a comparable evolution of temperature profiles up to t=0.4ms. For t >0.4ms (this time corresponds to point 5 in figure 7.5e) on the other hand, a significant divergence between the 1D and 3D curves is noticed. This result is in line with what observed in figure

7.4e. Here, the $\chi(O)$ profile from 3D domain is seen to diverge from the 1D curve in the post-ignition period, suggesting a more important role of turbulent mixing in the latest ignition stages.

More insights into the effect of turbulence on the fuel/oxidiser interaction are provided through the description of different fields of interest (temperature, heat release, etc) taken at different time during the ignition period. As in the previous section, the fields of interest are extracted from a specific cross sectional plane of the domain (plane at x=5mm in the middle of the stream-wise direction).

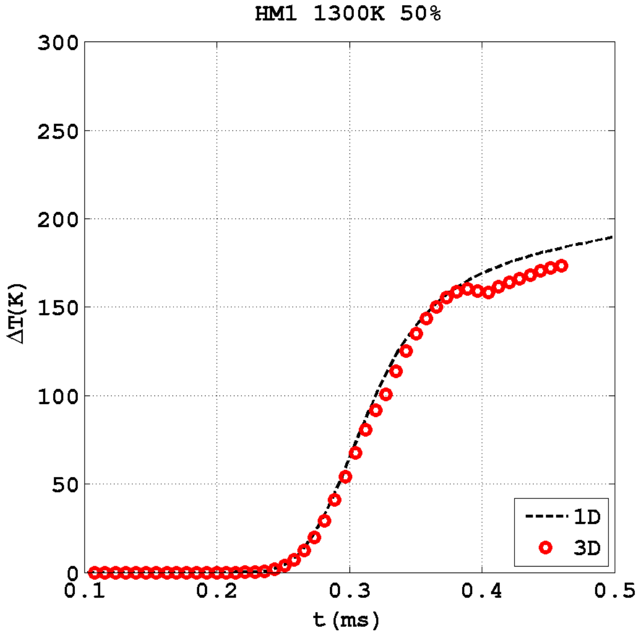

Figure 7.19: Evolution of the maximum temperature recorded in the 3D domain (red circles) plotted against the maximum temperature observed in the correspondent 1D case study. The temperature values from the HM1-50% configuration are here shown. The ΔT variable represents the difference between the maximum temperature recorded and the initial oxidiser temperature (1300K).

The earliest part of the ignition period is investigated by comparing the heat release field with hydrogen and methane mole fraction (Fig. 7.20d, 7.20e and 7.20f). At this time an initial release of heat reveals the starts of exothermic reactions (Fig. 7.20d). As figure shows, the initiation of chemical reaction occurs mostly within $Z > Z_{\mathrm{st}}$, enclosed by the stoichiometric iso-line. This marks a first difference with respect to the turbulent base case, where the start of chemical reaction was observed mostly in the fuel lean part of the domain. This difference can be explained by the lower value of Z_{st} for the HM1 case (Z_{st}=0.0067) with respect to HM3 one (Z_{st}=0.0198), which moves the stoichiometric mixture fraction region deeper into oxidiser. As a consequence, the fuel concentration around Z_{st} is lower. A similar explanation was used in section 5.3 since a similar difference was observed by comparing HM3-50% and HM1-50% diffusion cases. This represents a further confirmation of the minor role of turbulent convection in the pre-ignition period.

A better picture of the strong role of diffusion in the early stages of ignition is provided by comparing figures 7.20e and 7.20f. As the figures show, both CH_4 and H_2 vortical structures result enclosed and detached from stoichiometric iso-line. Particularly evident is the more sharp contour of methane mole fraction, with respect to hydrogen, which is due to the faster H_2 diffusivity in the proximity of the stoichiometric mixture fraction region.

Another interesting difference between the HM1-50% and HM3-50% cases is noticeable by comparing heat release fields in the pre-ignition period. In the base case the heat was found released uniformly along Z_{st} (Fig. 7.20a), while a more localised behaviour is observed in the higher dilution case (Fig. 7.20d). This can be explained by the presence of more developed vortical structures in the HM1-50% case.

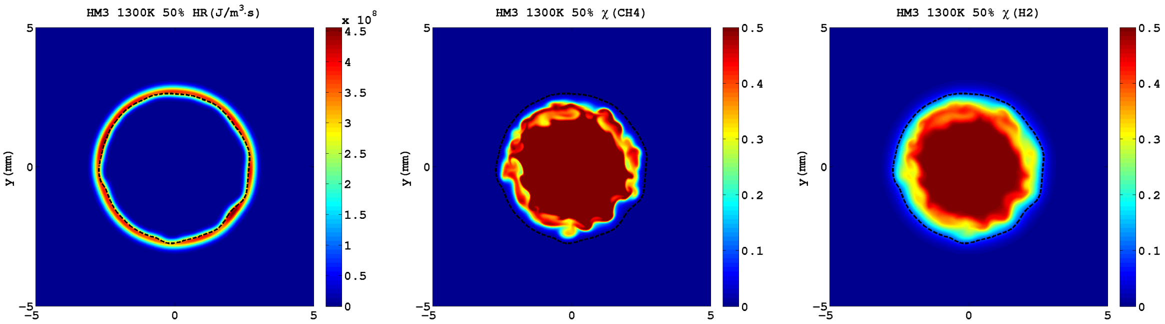

(a) HR-P2 **(b)** $\chi(CH_4)$-P2 **(c)** $\chi(H_2)$-P2

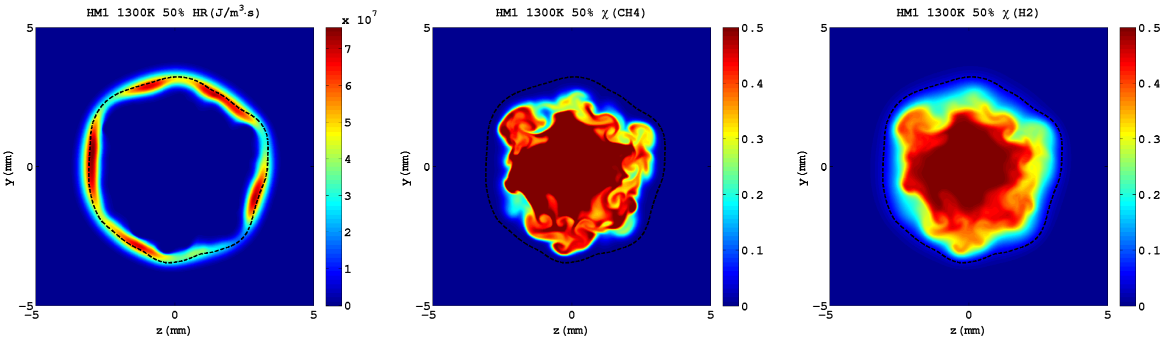

(d) HR-P2 **(e)** $\chi(CH_4)$-P2 **(f)** $\chi(H_2)$-P2

Figure 7.20: **Top row**: Fields of the heat release (left), methane mole fraction (middle) and hydrogen mole fraction (right) taken at the second point of analysis (pre-ignition). The HM3-50% case is considered.

Bottom row: Fields of the heat release (left), methane mole fraction (middle) and hydrogen mole fraction (right) taken at the second point of analysis (pre-ignition). The HM1-50% case is considered.

Fields are extracted from the cross-sectional plane of domain at x=5mm. The black dashed lines locate the stoichiometric mixture fraction region. Figures are zoomed around the fuel/oxidiser interface.

As a consequence of the delayed ignition in fact, the initiation of exothermic reaction is observed in the HM1-50% case at later time with respect to the base case. This allows a stronger development of turbulence and a larger variation of species mole fraction nearby Z_{st} is observed. It follows that in some regions turbulent fluctuations are stronger and dominate over diffusion/reaction phenomena.

Despite the presence of strong species mole fraction fluctuation, the fuel/oxidiser interaction shows, in the pre-ignition period, a scenario comparable with the 1D HM1-50% case. Figure 7.21a, 7.21b and 7.21c show the fields of CH_4, H_2 and O_2 consumption rate taken at the second point of analysis. In order to make a direct comparison between these three fields, the color ranges present the same scale ([0,1]). As figure 7.21a and 7.21b show, a displacement can be observed between areas where hydrogen and methane consumption occur. The methane consumption is all enclosed within the Z_{st} line, in the fuel rich part of the domain. The region where the hydrogen consumption is observed, presents a broader radial extension on both sides of the stoichiometric iso-line. Similar to H_2 is the physical extension and location of the O_2 consumption area (Fig. 7.21c).

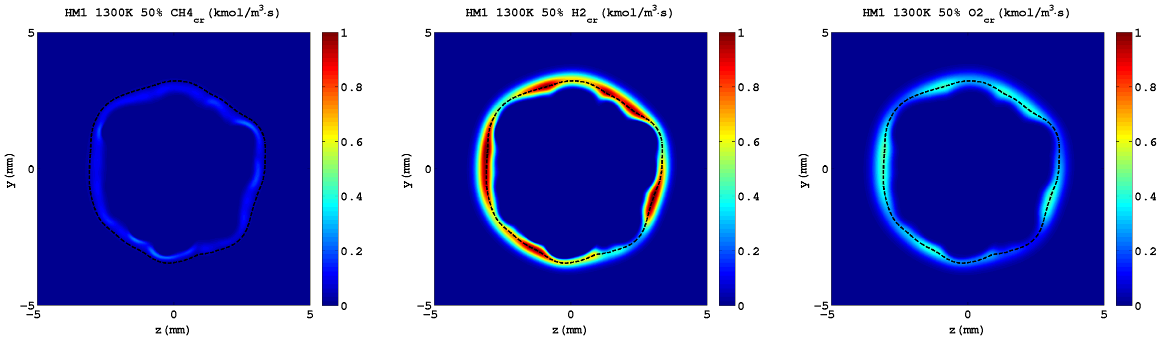

(a) $CH_{4\mathrm{cr}}$-P2 **(b)** $H_{2\mathrm{cr}}$-P2 **(c)** $O_{2\mathrm{cr}}$-P2

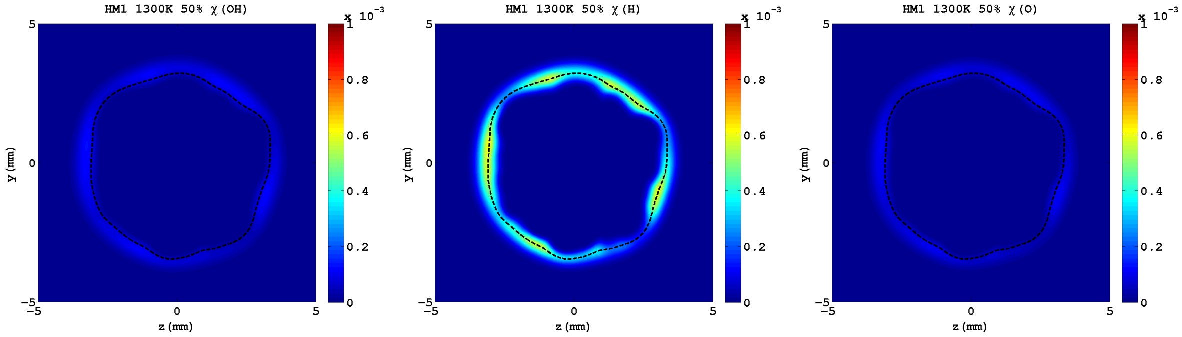

(d) $\chi(OH)$-P2 **(e)** $\chi(H)$-P2 **(f)** $\chi(O)$-P2

Figure 7.21: Top row: Fields of CH_4 (left), H_2 (middle) and O_2 (right) consumption rate taken at the second point of analysis (pre-ignition).
Bottom row: Fields of OH (left), H (middle) and O (right) mole fraction taken at the second point of analysis (pre-ignition).
The HM1-50% case is considered. Fields are extracted from the cross-sectional plane of domain at x=5mm. The black dashed lines locate the stoichiometric mixture fraction region. Figures are zoomed around the fuel/oxidiser interface.

As already pointed out in the previous section, there is also a difference in terms of rate of consumption of the reactants. The hydrogen contour (Fig. 7.21b) shows the highest rate of consumption, while methane contour (Fig. 7.21a) the lowest. It is interesting to note that the variability of the field of oxygen consumption rate (Fig. 7.21c) resemble the heat release as well as the hydrogen consumption rate. This outlines the major role of H_2-O_2 interaction in the pre-ignition period.

The early formation of radical pool is described by figures 7.21d, 7.21e and 7.21f, which are presented with the same scale ($[0,1\cdot 10^{-3}]$) to make a direct comparison between them. The H_2-O_2 chemical interaction plays a major role in the earliest part of ignition and the H/O/OH build-up can be mostly ascribed to the hydrogen oxidation process. This is confirmed by the correspondence, in terms of spatial location and extension, between the H/O/OH mole fraction fields and the H_2/O_2 consumption rate contour. As observed in the one-dimensional study, the H/O/OH pool shows a dominant presence of atomic hydrogen. Together with H, O and OH radicals, also the formation of hydroperoxyl (Fig. 7.24j) is noticed in the first part of ignition.

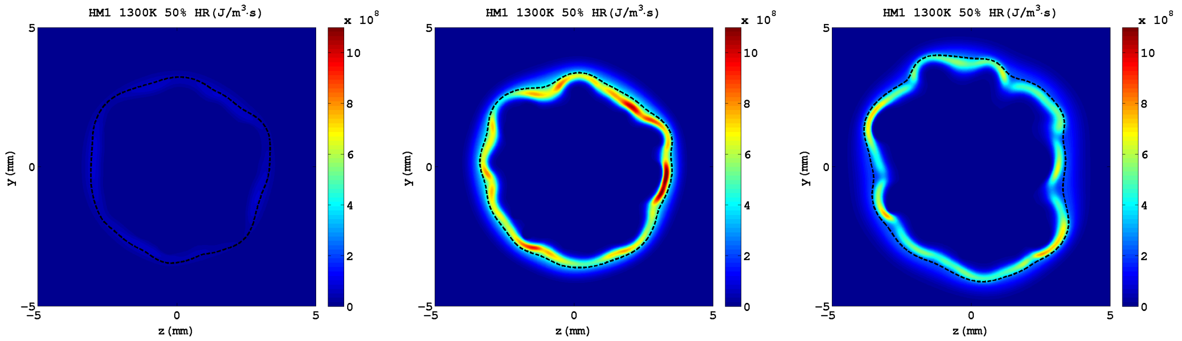

(a) HR-P2 **(b)** HR-P3 **(c)** HR-P5

Figure 7.22: Fields of heat release taken at point 2 - pre-ignition (left), at point 3 - ignition (middle) and at point 5 - post-ignition (right). The HM1-50% case is considered. Fields are extracted from the cross-sectional plane of domain at x=5mm. The black dashed lines locate the stoichiometric mixture fraction region. Figures are zoomed around the fuel/oxidiser interface.

The evolution in time of major fields of interests is shown in figures 7.22, 7.23 and 7.24. Here, each field is shown with a fixed scale in order to appreciate the change in time of the quantity described. As the chemical reactions evolve in time, more heat is released (Fig. 7.22b) and temperature becomes higher. With respect to the base case, the ignition time (point 3) is identified by a mild rise in temperature along the stoichiometric iso-line (Fig. 7.23b).

With the rise in temperature, an increased rate of reactant consumption is observed (Fig. 7.23e, 7.23h and 7.23k). The consumption behaviour of both oxygen and hydrogen is similar to the previous time point (the highest rates of O_2 consumption are observed where the peaks of H_2 consumption rates are shown), confirming the major role of H_2-O_2 interaction also at the ignition time. The hydrogen consumption region remains in the same location observed at pre-ignition, remaining positioned along the stoichiometric mixture fraction line. Along the Z_{st} line, areas where there is a trough of the hydroperoxyl molecule are identified by a light blue colour (Fig. 7.24k).

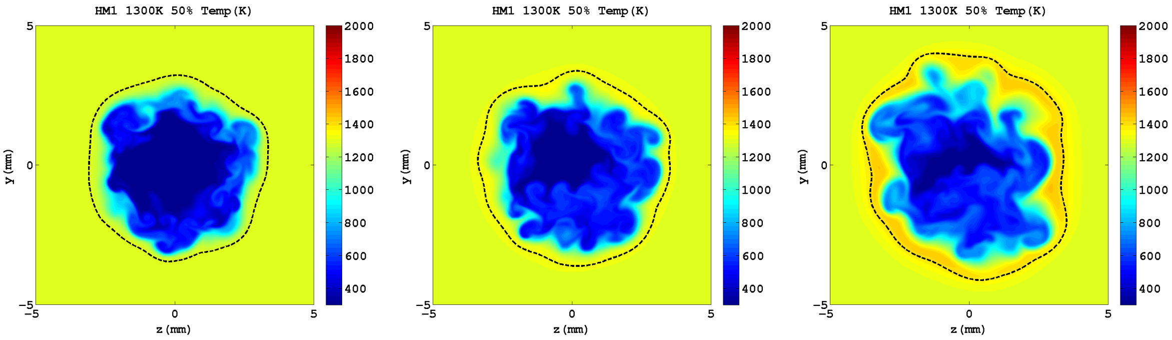

(a) Temp-P2 **(b)** Temp-P3 **(c)** Temp-P5

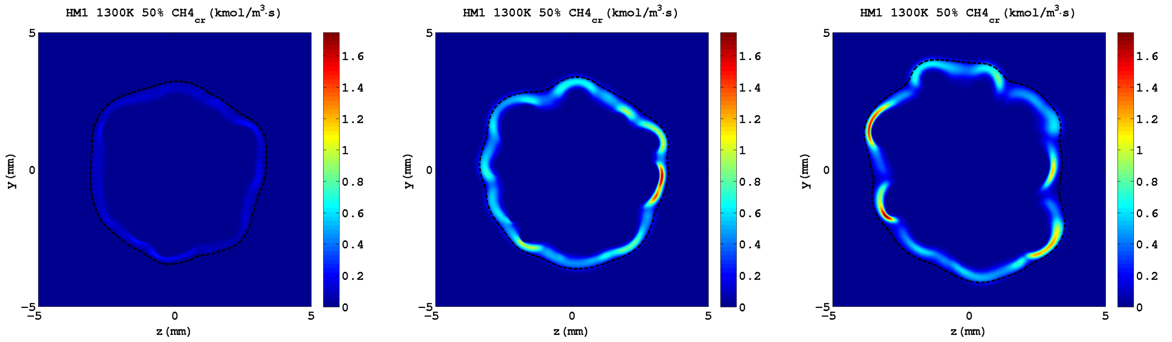

(d) CH_{4cr}-P2 **(e)** CH_{4cr}-P3 **(f)** CH_{4cr}-P5

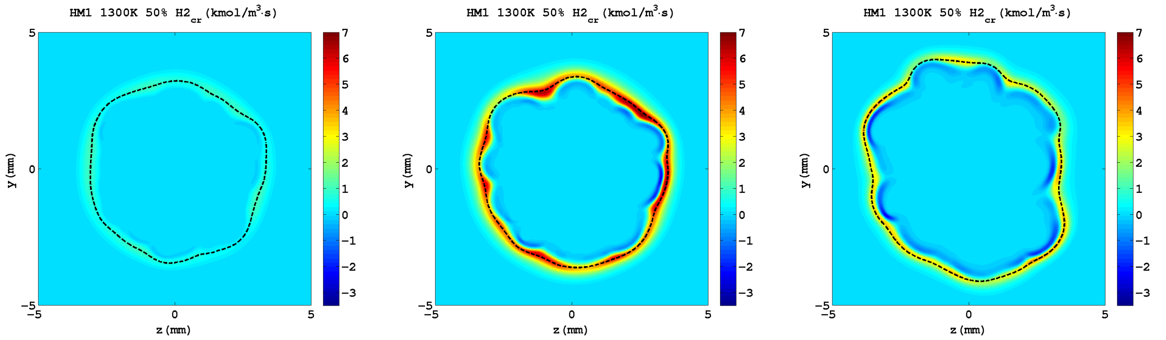

(g) H_{2cr}-P2 **(h)** H_{2cr}-P3 **(i)** H_{2cr}-P5

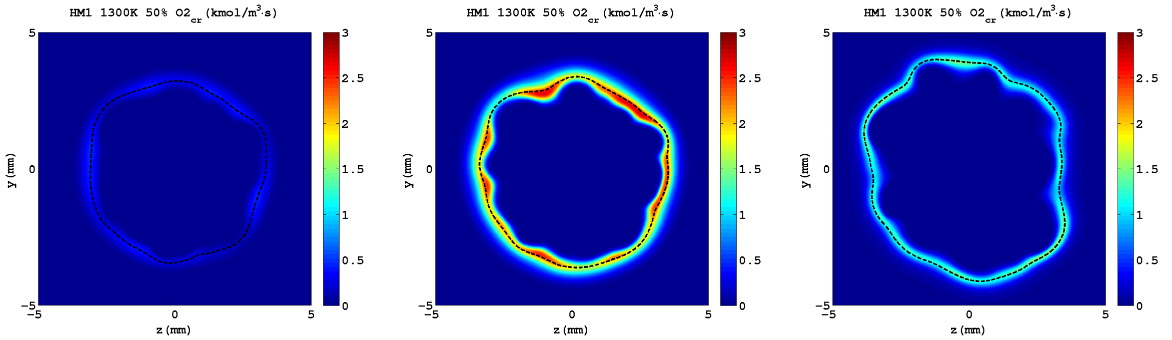

(j) O_{2cr}-P2 **(k)** O_{2cr}-P3 **(l)** O_{2cr}-P5

Figure 7.23: Fields of the temperature (top row), methane consumption rate (second row), hydrogen consumption rate (third row) and oxygen consumption rate (bottom row). The HM1-50% case is considered. Snapshots are taken at point 2 - pre-ignition (left column), at point 3 - ignition (middle column) and at point 5 - post-ignition (right column). Fields are extracted from the cross-sectional plane of domain at x=5mm. The black dashed lines locate the stoichiometric mixture fraction region. Figures are zoomed around the fuel/oxidiser interface.

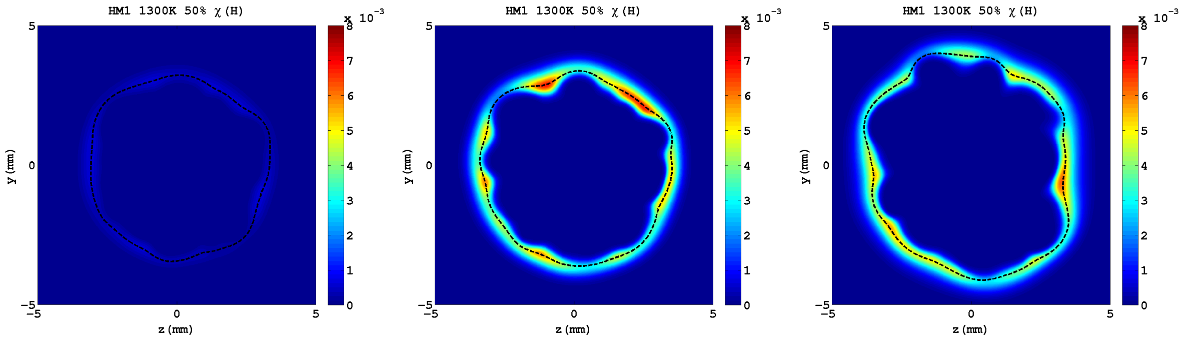

(a) $\chi(H)$-P2 **(b)** $\chi(H)$-P3 **(c)** $\chi(H)$-P5

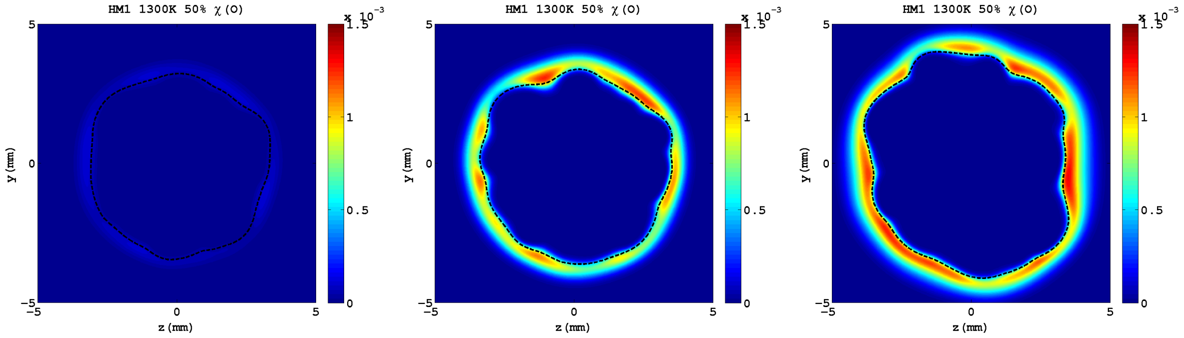

(d) $\chi(O)$-P2 **(e)** $\chi(O)$-P3 **(f)** $\chi(O)$-P5

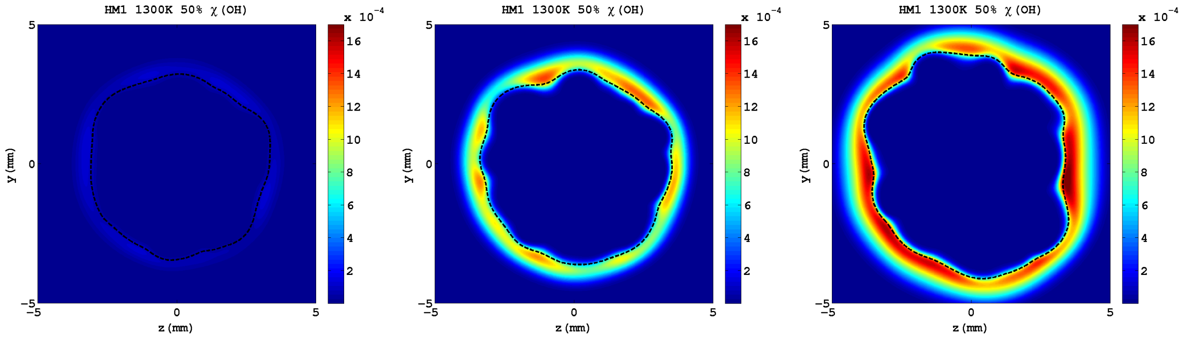

(g) $\chi(OH)$-P2 **(h)** $\chi(OH)$-P3 **(i)** $\chi(OH)$-P5

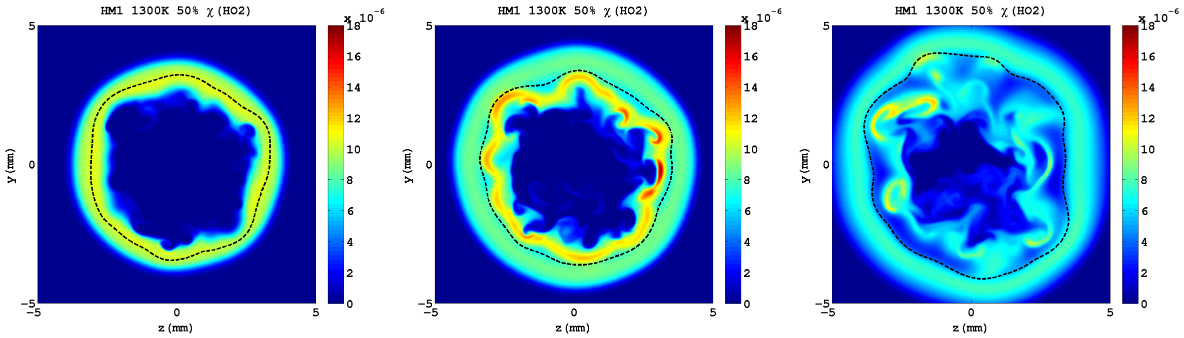

(j) $\chi(\mathrm{HO_2})$-P2 **(k)** $\chi(\mathrm{HO_2})$-P3 **(l)** $\chi(\mathrm{HO_2})$-P5

Figure 7.24: Fields of H mole fraction (top row), O mole fraction (second row), OH mole fraction (third row) and HO_2 mole fraction (bottom row). The HM1-50% case is considered. Snapshots are taken at point 2 - pre-ignition (left column), at point 3 - ignition (middle column) and at point 5 - post-ignition (right column). Fields are extracted from the cross-sectional plane of domain at x=5mm. The black dashed lines locate the stoichiometric mixture fraction region. Figures are zoomed around the fuel/oxidiser interface.

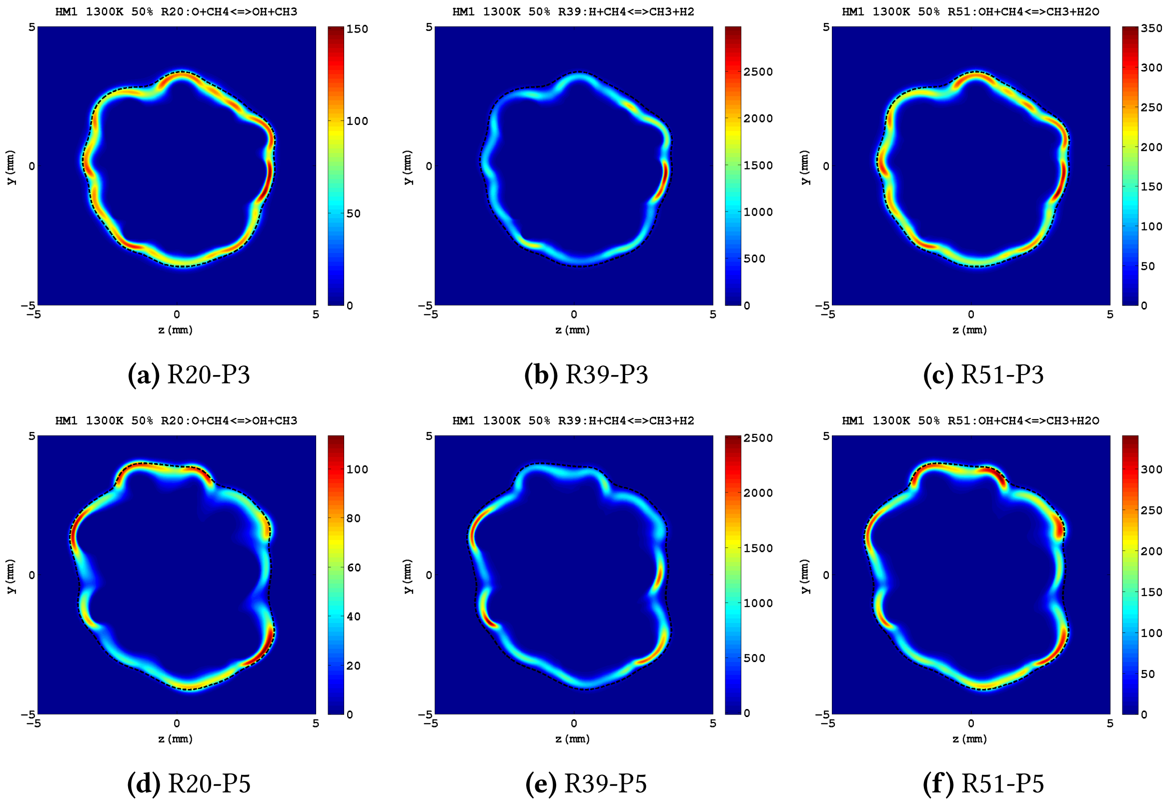

(a) R20-P3 **(b)** R39-P3 **(c)** R51-P3

(d) R20-P5 **(e)** R39-P5 **(f)** R51-P5

Figure 7.25: Fields of R20 (left), R39 (middle), and R51 (right) reaction rates taken at point 3 - ignition (top row) and at point 5 - post-ignition (bottom row). Reaction rates are expressed in $\mathrm{mole/m^3 \cdot s}$. The HM1-50% case is considered. Fields are extracted from the cross-sectional plane of domain at x=5mm. The black dashed lines locate the stoichiometric mixture fraction region. Figures are zoomed around the fuel/oxidiser interface.

These areas coincide with regions where the H_2-O_2 interaction is observed, suggesting that, as already pointed out in the turbulent base case, the early major exothermic events can be ascribed, to the hydrogen oxidation process.

It is possible to observe a reduced portion of the hydrogen consumption field, laying within the Z_{st} line, where the H_2 results produced rather than consumed (dark blue region of the contour). This subregion of the hydrogen consumption field (Fig. 7.23h) has strong geometrical similarities with the methane consumption behaviour (Fig. 7.23e). Figure 7.23e shows that, the areas where the highest rate of methane consumption are observed, coincide with the areas where the highest rate of hydrogen production are shown (Fig. 7.23h). This phenomenon, already observed in the turbulent base case, has been explained by the major role of the R39 step among the three reactions responsible for the methane dehydrogenation (R20, R39 and R51). The R39 elementary reaction explains both the methane molecule destruction and the production of hydrogen. In figure 7.25a, 7.25b and 7.25c are shown the fields of major steps describing the methane dehydrogenation in the DRM19 mechanism: R20, R39 and R51 taken at ignition. As figures suggest, also for the turbulent HM1-50% case, the R39 step plays a major role in the abstraction of CH_4 molecule. Methane consumption trough the R39 step is by the combined presence of H and CH_4. As figures 7.24h, 7.24b and 7.24e demonstrate, the dominant presence of atomic hydrogen where methane is being consumed (Fig. 7.23e), justifies the major role of R39 reaction.

It is interesting to note that the field describing the methane consumption (Fig. 7.23e) shows areas where the CH_4 consumption rate is significantly higher than what observed in the diffusion cases at ignition (Fig. 5.4d). Conversely, hydrogen and oxygen rates of consumption (Fig. 7.23h and 7.23k), show values comparable with the diffusion study (Fig. 5.4g and 5.4j). The R39 reaction field at ignition (Fig. 7.25b) confirms this finding, as it shows a rate higher than what observed in the diffusion case (Fig. 5.17c). Because the level of atomic hydrogen is comparable in 3D and 1D studies (Fig. 7.24b and 5.20f), it is likely that the observed increased rate of CH_4 dehydrogenation is due to turbulent mixing which enhances the methane transport into regions where high level of H is present.

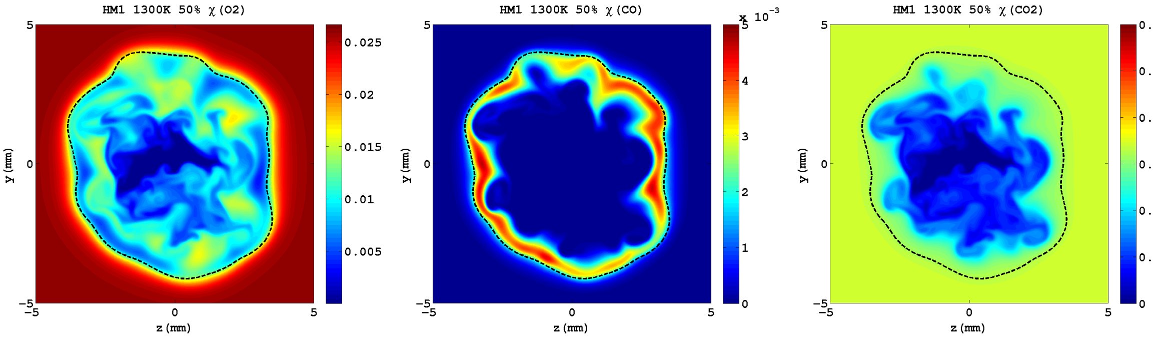

(a) $\chi(O_2)$-P5 **(b)** $\chi(CO)$-P5 **(c)** $\chi(CO_2)$-P5

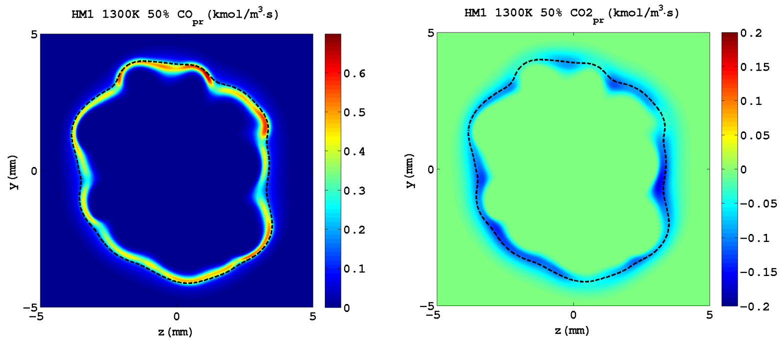

(d) CO_{pr}-P5 **(e)** CO_{2pr}-P5

Figure 7.26: Fields of O_2 mole fraction (top left), CO mole fraction(top middle), CO_2 mole fraction(top right), CO production rate (bottom left) and CO_2 production rate (bottom right) taken at point 5 - post-ignition. The HM1-50% case is considered. Fields are extracted from the cross-sectional plane of domain at x=5mm. The black dashed lines locate the stoichiometric mixture fraction region. Figures are zoomed around the fuel/oxidiser interface.

The post-ignition period is characterised by the drop in the oxygen level at the fuel/oxidiser interface. This can be observed in figure 7.26a, which shows regions nearby $Z_{\rm st}$, where O_2 is almost completely consumed. The drop in O_2 level, is followed by a significant rate reduction at which oxygen and hydrogen are being consumed (Fig. 7.23i and 7.23l) and a reduced rate of heat release (Fig. 7.22c). Furthermore, the rate limiting role of the oxygen depletion is also identified by the lowered slope of the maximum temperature increase (Fig. 7.19) in the final part of ignition (t ~0.4ms).

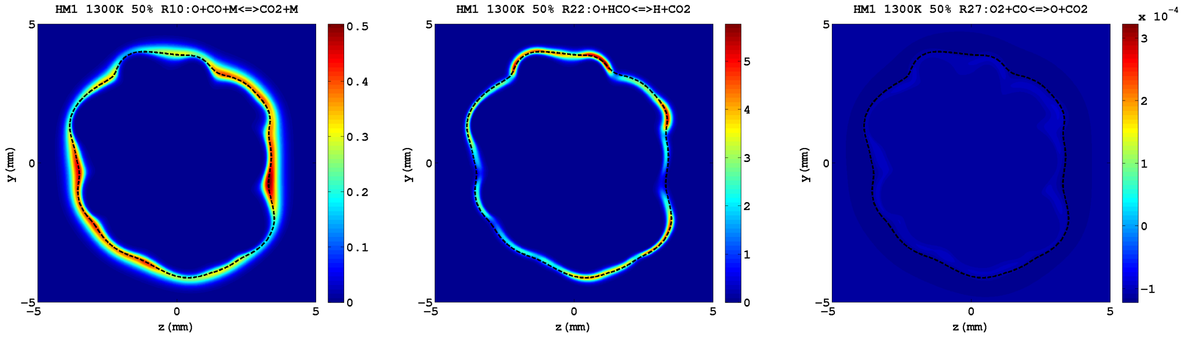

(a) R10-P5 **(b)** R22-P5 **(c)** R27-P5

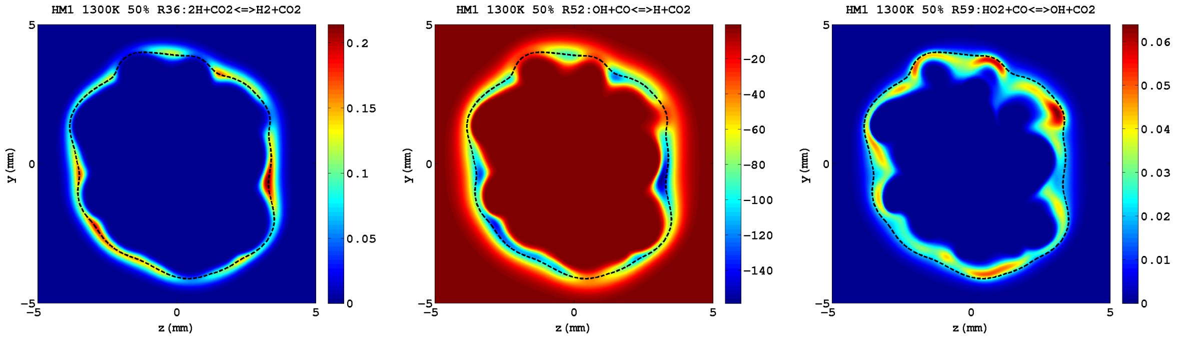

(d) R36-P5 **(e)** R52-P5 **(f)** R59-P5

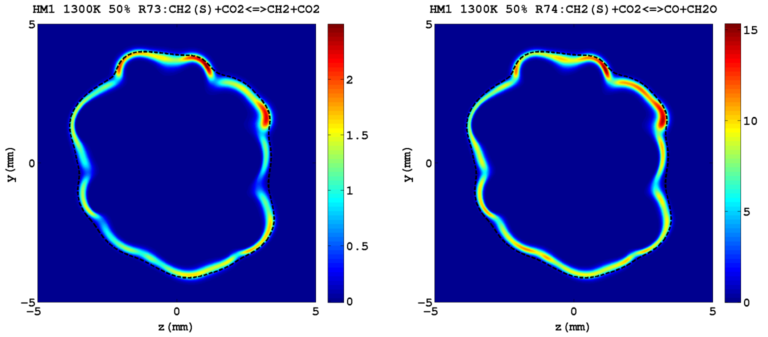

(g) R73-P5 **(h)** R74-P5

Figure 7.27: Reaction rates of all steps (R10, R22, R27, R36, R52, R59, R73 and R74) describing in the DRM19 mechanism the CO_2 consumption/production. Fields are taken at point 5 - post-ignition. Reaction rates are expressed in $\mathrm{mole}/\mathrm{m}^3 \cdot \mathrm{s}$. The HM1-50% case is considered. Fields are extracted from the cross-sectional plane of domain at x=5mm. The black dashed lines locate the stoichiometric mixture fraction region. Figures are zoomed around the fuel/oxidiser interface.

Differently from H_2 and O_2, the rate at which methane is being consumed (Fig. 7.23f) remain as high as at ignition time (Fig. 7.23e). As the similarity between figures 7.23f and 7.25e suggests, the R39 step, because of the large excess of H where methane is consumed (Fig. 7.24c), still exerts a controlling action on CH_4 destruction. This represents an important difference with respect to the diffusion case, where all reactants showed in the last part of ignition a reduction of their rate of consumption. The explanation of the large difference observed in CH_4 consumption between 1D and 3D cases could be due, as observed in the previous section, on the turbulent mixing of the methane stream. While in the 1D case the methane consumption is affected in the last part of ignition by the low CH_4 diffusivity, in the 3D case the turbulent mixing helps to reduce the differential diffusion effect as turbulence grows.

While a presence of CO is observed in the numerical domain (Fig. 7.26b), the level of CO_2 does not result increased with respect to initial level 7.26c. This result is in line with findings from the HM1-50% diffusion case, where the CO presence in the domain resulted from the combined effect of $HCO->$ CO and $CO_2->$ CO conversions. Consistently with the one dimensional case, the turbulent case shows production of CO (Fig. 7.26d) and destruction of CO_2 (Fig. 7.26e). The rates at which CO is being produced and CO_2 is being consumed are similar to the one dimensional case (Fig. 5.5g and 5.5d). This suggests that the turbulent mixing enhances significantly only the first part (dehydrogenation) of the methane chain reaction [5].

Figure 7.27 shows all steps linked, within the DRM19 mechanism, with the CO_2 production/consumption. The rate of the backward R52 reaction is by far the highest among the steps presented. Consistently with the diffusion case, this demonstrate the major role of the R52 step in the carbon dioxide consumption process.

Because of the negligible rates of all the steps describing the CO2 production (Fig. 7.27), it is reasonable to consider that the carbon dioxide consumed has originating from the initial oxidiser blend. As explained in detail in the turbulent base case analysis, the R52 kinetic equation (see appendix A) provides a clear picture of what causes this step to proceed backward. The significant presence of H (Fig. 7.24c) and CO_2 (Fig 7.26c) within the region where the highest temperature are observed (Fig. 7.23c) induces the R52 reaction to proceed towards reactants. This is confirmed by the resemblance between figures 7.24c and 7.26e. As figures show, a negative CO_2 production is detected where there is high presence of atomic hydrogen.

7.6 Effect of hydrogen reduction. 1D-3D comparison.

This section provides an initial description of the physical/chemical scenario observed by numerically mimicking the HM3-10% case in three dimensions. As the name would suggests, the HM3-50% configuration proposed in the Dally *et al.* experiment [54] has been modified to investigate the effects of a reduced presence of hydrogen in the fuel blend. The fuel mixture is set-up as a 90/10 molar mixture of methane and hydrogen. The oxidiser has the same composition of the base case (Tab. 7.1).

This particular configuration has already been investigated by means of a one-dimensional

---

[5] The analysis is here based on the comparison of contour plots from 1D and 3D case studies. In order to obtain more insights into the effect of turbulence on methane kinetics, a more detailed investigation of the pathway followed by CH_4 consumption is necessary.

study in chapter 6. The major aspects found in the three-dimensional study will be compared with insights gained from the diffusion study. One of the major aspects outlined by the 1D study was the significant impact of the reduced presence of hydrogen on the ignition time. While the self-ignition time was computed at t ~0.14ms in the base case, the time required to ignite reactants was approximately 4 times larger (t ~0.60ms) in the HM3-10% configuration.

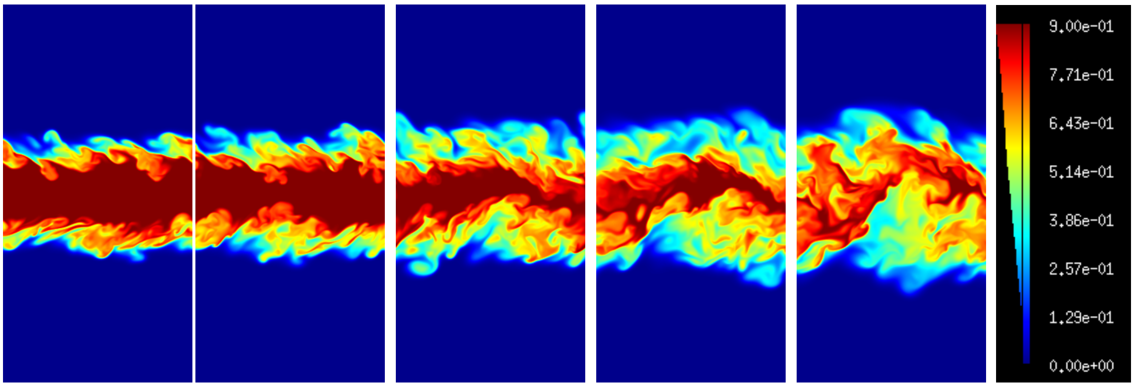

(a) Point 1 **(b)** Point 2 **(c)** Point 3 **(d)** Point 4 **(e)** Point 5 $\chi(\mathrm{CH_4})$

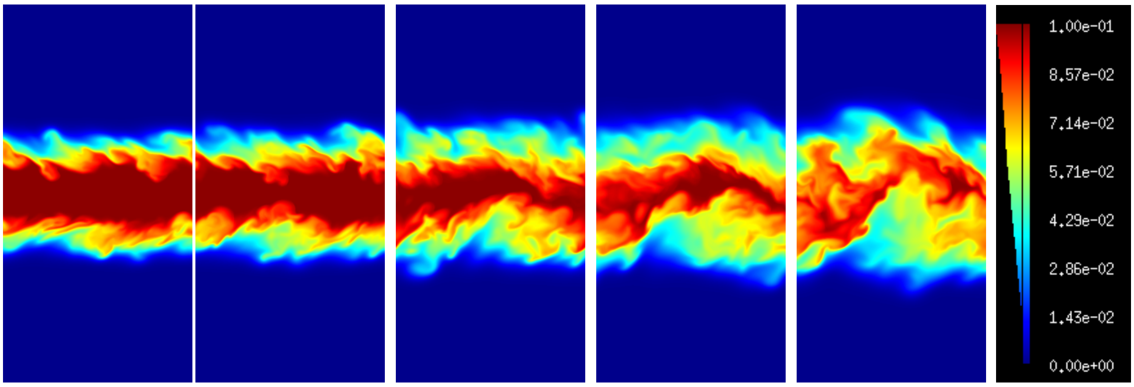

(f) Point 1 **(g)** Point 2 **(h)** Point 3 **(i)** Point 4 **(j)** Point 5 $\chi(\mathrm{H_2})$

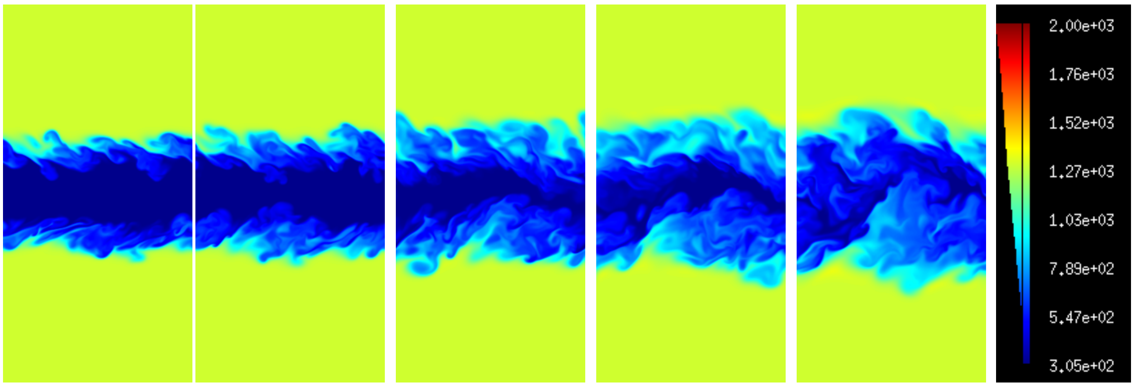

(k) Point 1 **(l)** Point 2 **(m)** Point 3 **(n)** Point 4 **(o)** Point 5 T(K)

Figure 7.28: Methane mole fraction (top row) fields, hydrogen mole fraction (middle row) fields and temperature (bottom row) fields for the HM3-10% case. Snapshots are taken in the z=0 plane for each of the time investigation points.

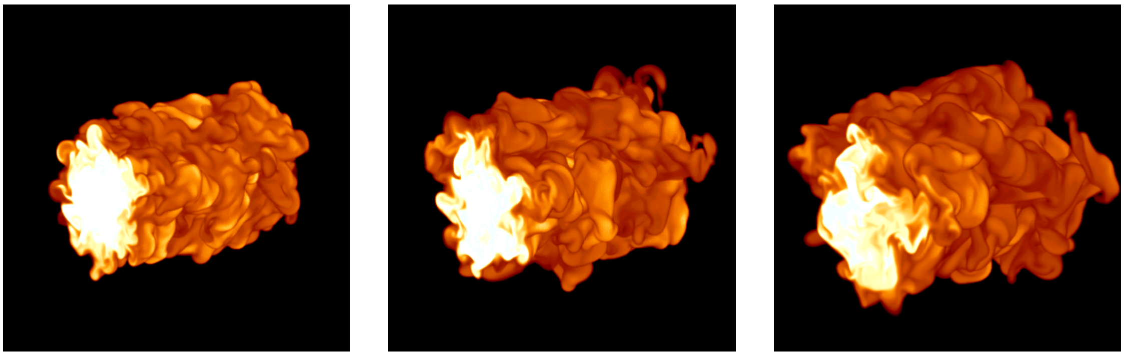

(a) $\chi(\mathrm{CH_4})$-P2 **(b)** $\chi(\mathrm{CH_4})$-P3 **(c)** $\chi(\mathrm{CH_4})$-P5

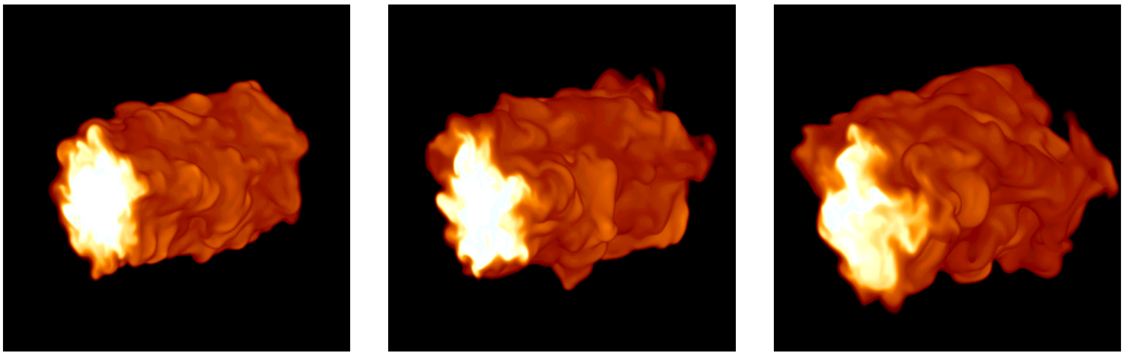

(d) $\chi(\mathrm{H_2})$-P2 **(e)** $\chi(\mathrm{H_2})$-P3 **(f)** $\chi(\mathrm{H_2})$-P5

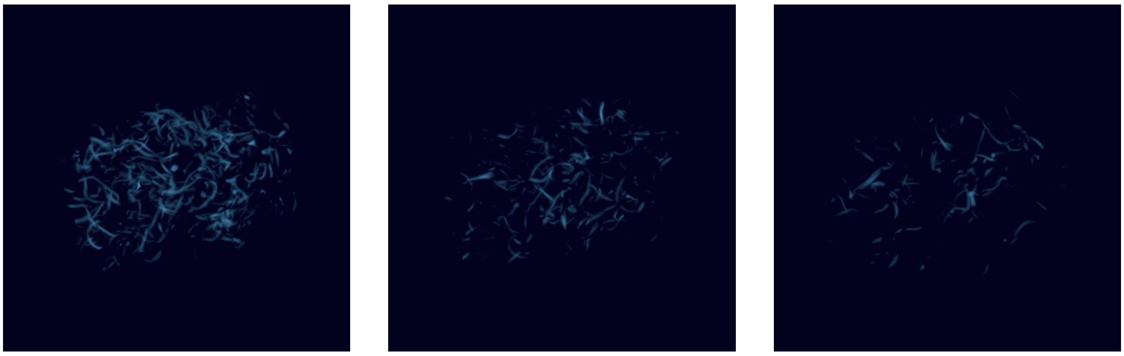

(g) Vorticity-P2 **(h)** Vorticity-P3 **(i)** Vorticity-P5

Figure 7.29: Fields of the methane mole fraction (top row), hydrogen mole fraction (middle row) and vorticity magnitude (bottom row) plotted at three different point of the period observed (pre-ignition, ignition and post-ignition) in axonometric view. The color scales for the methane and hydrogen mole fraction range (orange to white) from 0 to 0.9 and from 0 to 0.1 respectively. The color scales for the vorticity magnitude range (blue to white) from 0 to $1.5e^6$ (1/s).

Comparison between 1D and 3D profiles in figure 7.4f outlines a comparable growth of the O radicals in the first part of ignition. Drastically changed results instead the ignition scenario in the remaining part of temporal range investigated. For t >0.5ms the rapid growth of $\chi(O)$ is reduced and a large divergence is observed between the 1D and 3D profiles.

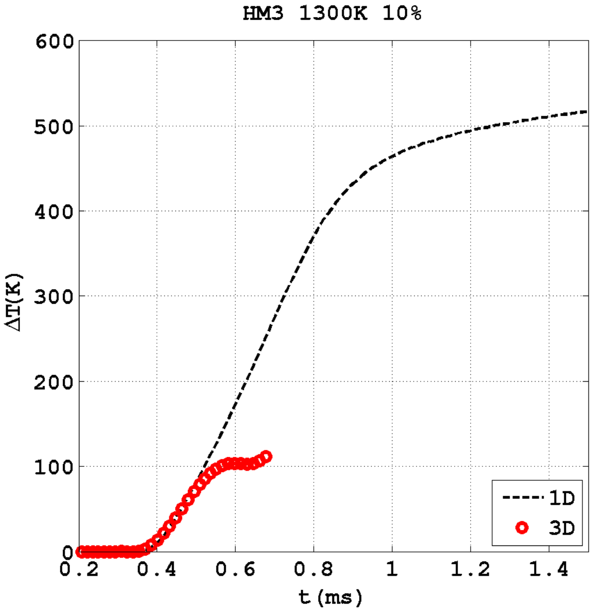

Figure 7.30: Evolution of the maximum temperature recorded in the 3D domain (red circles) plotted against the maximum temperature observed in the correspondent 1D case study. The temperature values from the HM3-10% configuration are here shown. The ΔT variable represents the difference between the maximum temperature recorded and the initial oxidiser temperature (1300K).

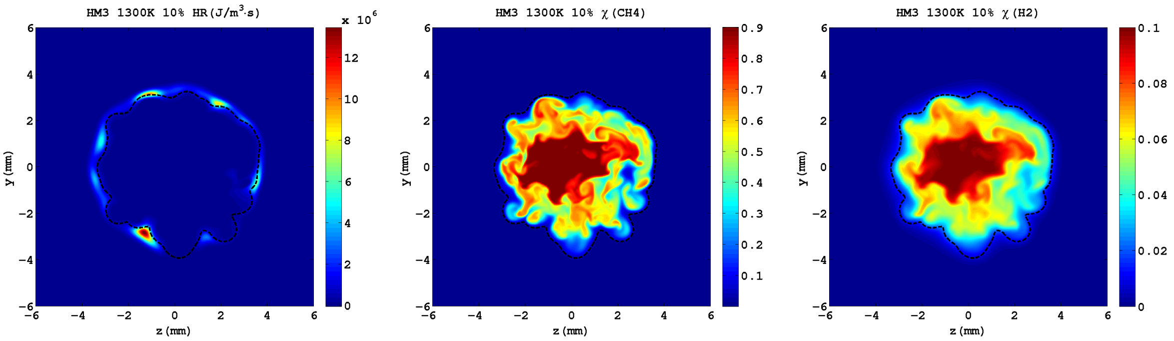

(a) HR-Point 2 **(b)** $\chi(\mathrm{CH}_4)$-Point 2 **(c)** $\chi(\mathrm{H}_2)$-Point 2

Figure 7.31: Fields of the heat release (left), methane mole fraction (middle) and hydrogen mole fraction (right) taken at the second point of analysis (pre-ignition). The HM1-50% case is considered. Fields are extracted from the cross-sectional plane of domain at x=5mm. The black dashed lines locate the stoichiometric mixture fraction region. Figures are zoomed around the fuel/oxidiser interface.

Similar behaviour is observed for the maximum temperature increase in figure 7.30. For t >0.5ms the increase in temperature is substantially arrested in the 3D case (ΔT ~100K), while ΔT continues to grow in the 1D case, reaching a peak value of about 500K at later times. Because of the longer time required by HM3-10% configuration to self-ignite, a stronger development of turbulence (higher number of vortical structures) is observed (Fig. 7.28) with respect to previously described HM3-50% and HM1-50% cases (Fig. 7.6 and 7.17) [6].

Contour plots of temperature, mole fraction of methane and mole fraction of hydrogen along the ignition period are presented in figure 7.28. As observed in the previous cases, the evolution of methane (top row) and hydrogen (middle row) molar fraction show similar hydrodynamic behaviour along the ignition period, despite the fact that they are present in the fuel blend with different molar proportion. The $\chi(\mathrm{CH_4})$ contours remain more sharp than hydrogen counterpart, pointing out different diffusion behaviours between H_2 and CH_4. Because of the reduced ΔT observed ($\sim$100K) in the 3D case (Fig. 7.30), the temperature increase in hardly noticeable on all the T snapshots shown (bottom row). Later in this section the temperature rise will be shown by using contour plots scaled by a narrower T range.

Similar conclusions suggest the 3D fields in figure 7.29. The figures highlight a significantly broader jet spreading, with respect to HM3-50% and HM1-50% turbulent cases, as a consequence of the late ignition. Consistently with the CH_4 and H_2 contours in figure 7.28, the three-dimensional methane pattern (Fig. 7.29a, 7.29b and 7.29c) appears sharper than the hydrogen counterpart (Fig. 7.29d, 7.29e and 7.29f), confirming the different diffusion behaviours between H_2 and CH_4 flows. Particularly interesting is the vorticity evolution along the ignition period (Fig. 7.29g, 7.29h and 7.29i). The number of iso-surface, especially in the post-ignition period, with high vorticity magnitude is remarkably lower with respect to the cases with high H_2 content. This confirms the strong turbulence development within the time period selected.

More insights into the effect of turbulence to the fuel/oxidiser interaction are provided through the description of different fields of interest (temperature, heat release, etc) taken at different time points of the ignition period. The fields of interest are extracted from a specific cross sectional plane of the domain (plane at x=5mm in the middle of the stream-wise direction). As for the previous cases studies, the analysis of fuel/oxidiser interaction along the ignition period starts at point 2, observing the region where the initiation of exothermic reactions occurs.

The low Z_{st} value (0.0217) places the stoichiometric iso-line at the edge of the fuel/oxidiser interface, as shown in figure 7.31b and 7.31c, where the black dashed line encloses entirely the fuel jet. As shown by heat release field (Fig. 7.31a), the early start of exothermic reaction occurs, consistently with 1D case (Fig. 6.4j), in the fuel lean region ($Z < Z_{\mathrm{st}}$) of the domain, where the hottest temperature are present (Fig. 7.34a).

The heat release field outlines a particularly discontinuous behaviour. Few parts of the contour show a release of heat significantly higher than other. This is consistent with the observed stronger turbulence development, which results in a wider range of velocity scales and larger variation of species distribution. As such, in some regions vortical structures dominate over molecular diffusion, while in some other diffusion plays a major role. This is observed as the

---

[6] It should be noted that the stronger development of turbulence is also due to the higher Re of the case under investigation. This because of the different kinematic viscosity of the 90/10 CH_4/H_2 molar mixture with respect to the 50/50 molar mixture of the HM3-50% and HM1-50% cases.

initiation of reactions at different location and with different timing.

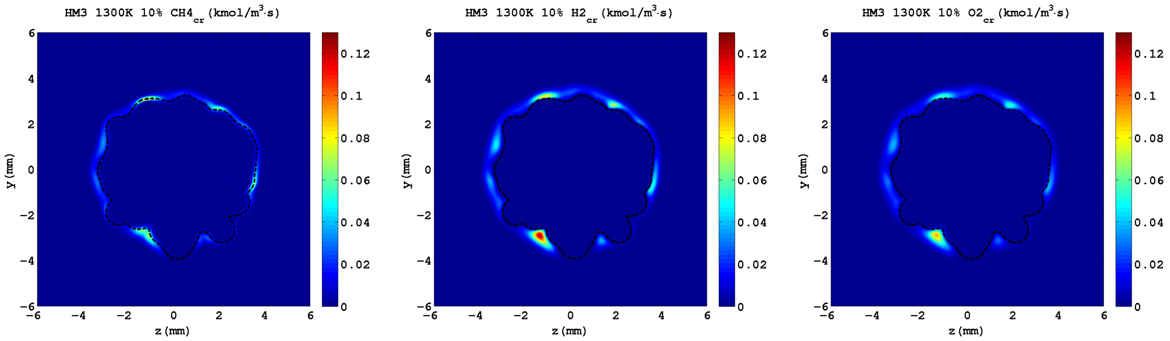

(a) CH_{4cr}-P2 **(b)** H_{2cr}-P2 **(c)** O_{2cr}-P2

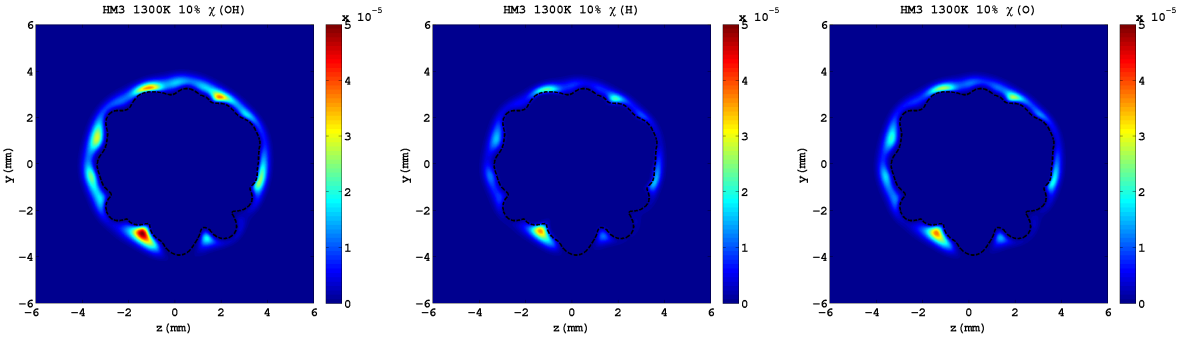

(d) $\chi(OH)$-P2 **(e)** $\chi(H)$-P2 **(f)** $\chi(O)$-P2

Figure 7.32: Top row: Fields of CH_4 (left), H_2 (middle) and O_2 (right) consumption rate taken at the second point of analysis (pre-ignition).
Bottom row: Fields of OH (left), H (middle) and O (right) mole fraction taken at the second point of analysis (pre-ignition).
The HM3-10% case is considered. Fields are extracted from the cross-sectional plane of domain at x=5mm. The black dashed lines locate the stoichiometric mixture fraction region. Figures are zoomed around the fuel/oxidiser interface.

Figures 7.32a, 7.32b and 7.32c show the fields of CH_4, H_2 and O_2 consumption rate taken at the second point of analysis. In order to make a direct comparison between these three fields, the color ranges present the same scale ([0,0.13]). Despite the dominant presence of CH_4 in the fuel and despite the additional contribution of turbulence, which should help CH_4 to mix with the hot co-flow and dissociate, the diffuse $\chi(H_2)$ contour suggests still an important presence of hydrogen along Z_{st}. The field of H_2 consumption rate (Fig. 7.32b) confirms this, as it shows slightly higher rates of consumption than CH_4 (Fig. 7.32a). It is important to note that a similar scenario was observed in the 1D case, where the hydrogen chemistry played an important role in the pre-ignition period. This suggests that the presence of turbulence convection does not cancel the effects of differential diffusion in the earliest part of the ignition process.

The early formation of OH/H/O radical pool is described by figures 7.32d, 7.32e and 7.32f, which are presented with the same scale ([0,5·10^{-5}]) to make a direct comparison between them. As pointed out in the 1D case study, the reduced level of H_2 in the fuel is strongly linked with the reduced importance of atomic hydrogen among H, O and OH intermediates. Figures

7.32d, 7.32e and 7.32f demonstrates this, as atomic hydrogen no longer shows a dominant presence in the radical pool.

The third point of analysis (t ~0.46ms) is characterised, by a modest (ΔT=50K) temperature increment (Fig. 7.30). The temperature increase along the ignition period can be appreciated in figures 7.33d, 7.33e and 7.33f, where the color scale has been narrowed to [1300,1400] range.

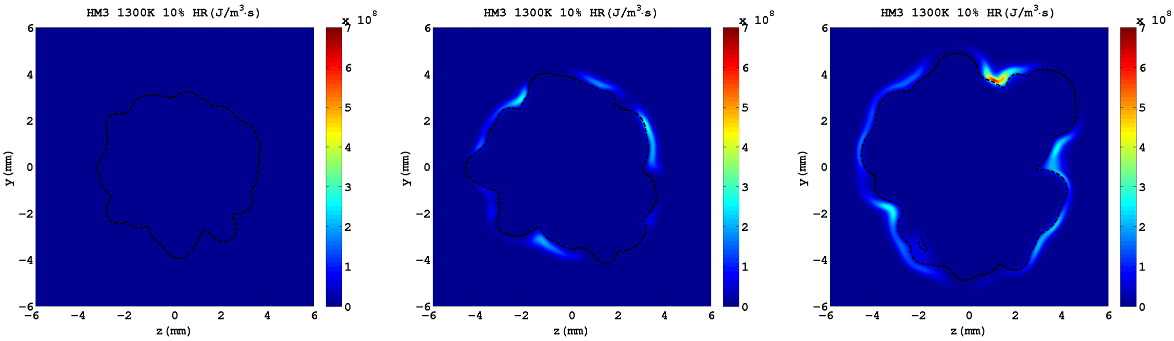

(a) HR-P2 **(b)** HR-P3 **(c)** HR-P5

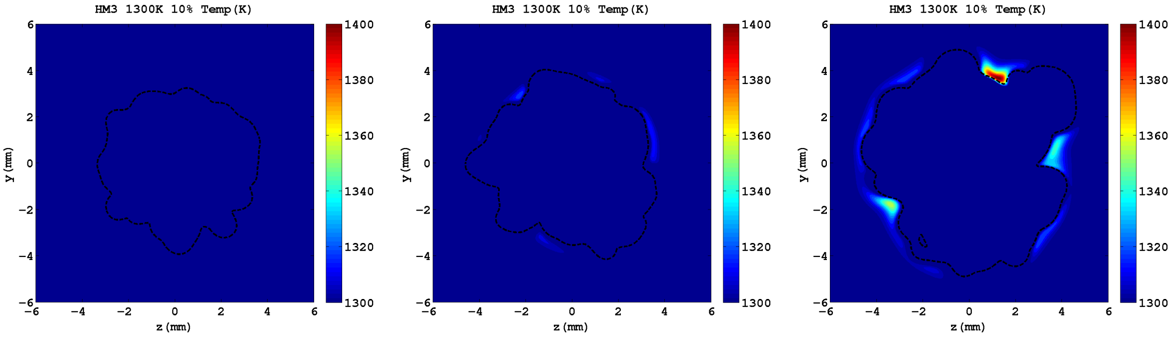

(d) Temp-P2 **(e)** Temp-P3 **(f)** Temp-P5

Figure 7.33: Fields of heat release (top row) and temperature (bottom row) taken at point 2 - pre-ignition (left column), at point 3 - ignition (middle column) and at point 5 - post-ignition (right column). The HM3-10% case is considered. Fields are extracted from the cross-sectional plane of domain at x=5mm. The black dashed lines locate the stoichiometric mixture fraction region. Figures are zoomed around the fuel/oxidiser interface.

More significant is the rise in the rate of reactant consumption (Fig. 7.34e, 7.34h and 7.34k). The areas where fuels and oxygen are being consumed remain located outside Z_{st} line. Because of the reduced presence of H_2 in the fuel jet, the hydrogen consumption does not show rates significantly higher than methane. For the same reason, the large excess of H radical in the radical pool is no longer observed (Fig. 7.35a, 7.35d and 7.35a).

In the one-dimensional case was observed that, because of dominant presence of OH in the H/O/OH pool, the R51 step was controlling the methane dehydrogenation while R20 and R39 reactions showed reduced importance (Fig. 6.20). Those findings are observed also in the turbulent case where the step R51 shows the highest rate among reaction describing methane abstraction (Fig. 7.36c).

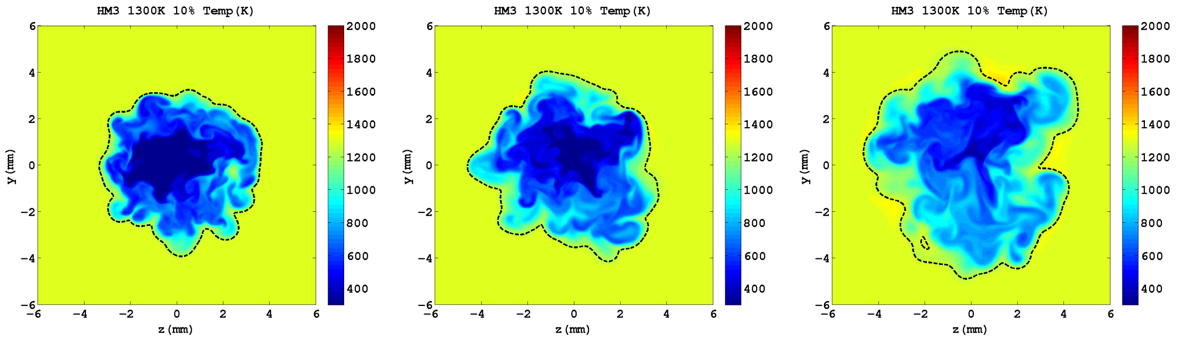

(a) Temp-P2 **(b)** Temp-P3 **(c)** Temp-P5

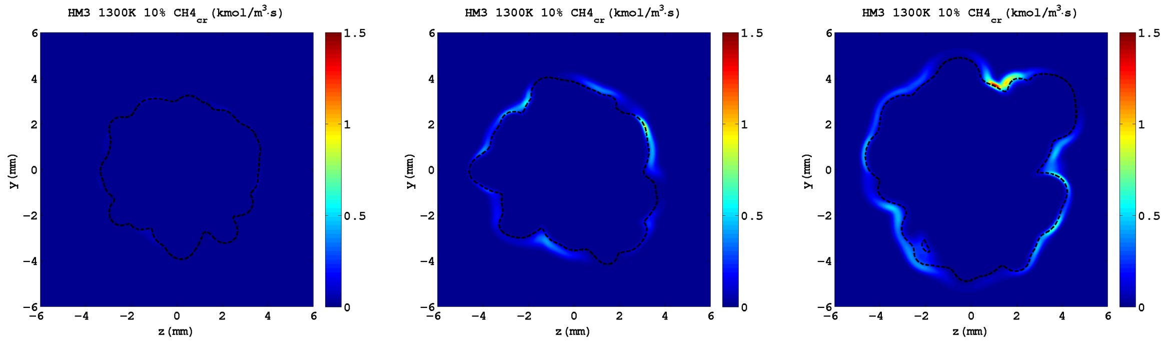

(d) CH_{4cr}-P2 **(e)** CH_{4cr}-P3 **(f)** CH_{4cr}-P5

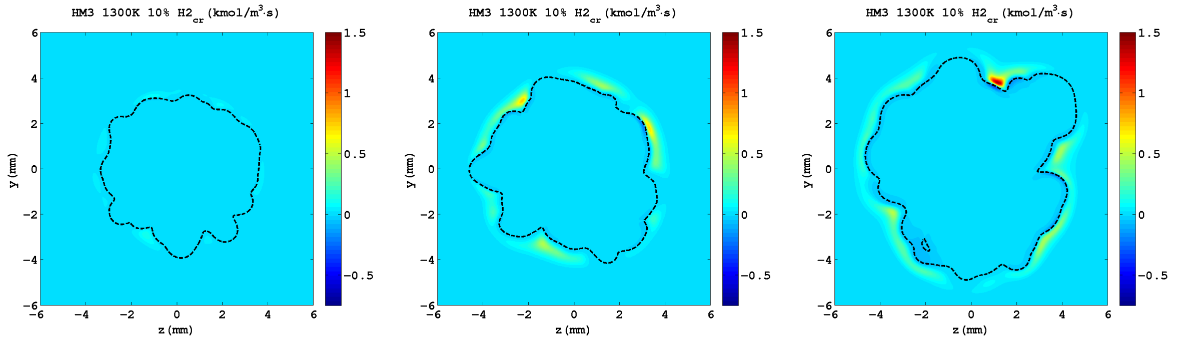

(g) H_{2cr}-P2 **(h)** H_{2cr}-P3 **(i)** H_{2cr}-P5

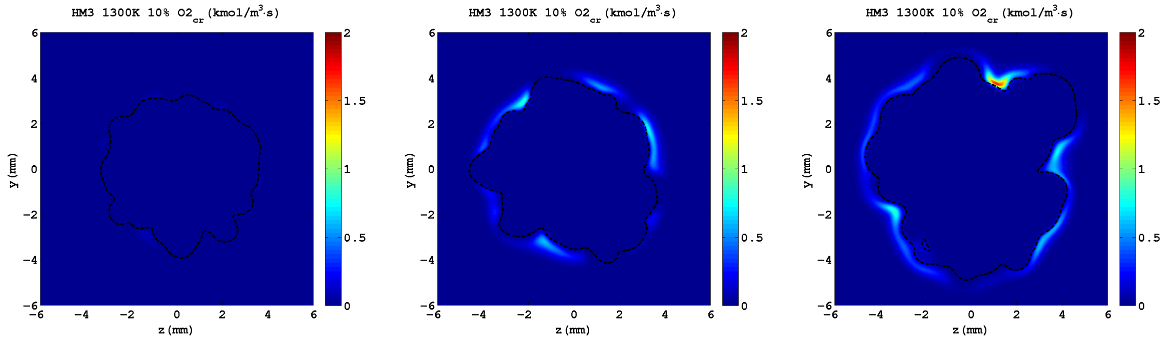

(j) O_{2cr}-P2 **(k)** O_{2cr}-P3 **(l)** O_{2cr}-P5

Figure 7.34: Fields of the temperature (top row), methane consumption rate (second row), hydrogen consumption rate (third row) and oxygen consumption rate (bottom row). The HM3-10% case is considered. Snapshots are taken at point 2 - pre-ignition (left column), at point 3 - ignition (middle column) and at point 5 - post-ignition (right column). Fields are extracted from the cross-sectional plane of domain at x=5mm. The black dashed lines locate the stoichiometric mixture fraction region. Figures are zoomed around the fuel/oxidiser interface.

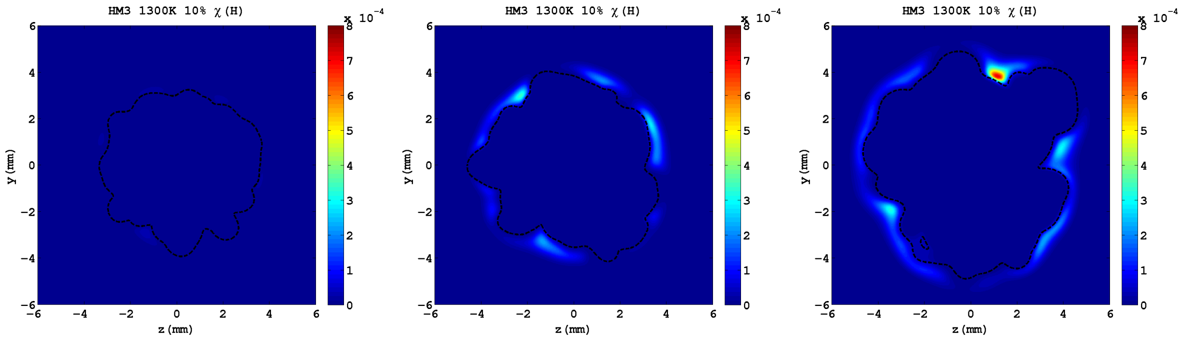

(a) $\chi(H)$-P2 **(b)** $\chi(H)$-P3 **(c)** $\chi(H)$-P5

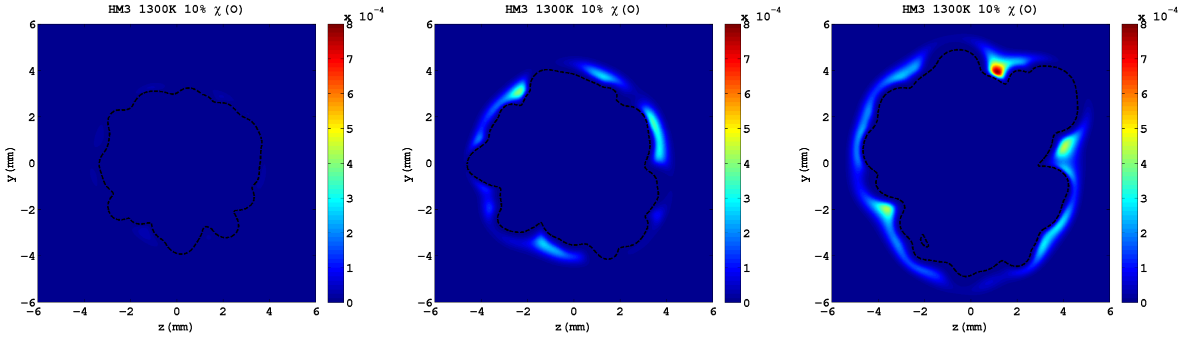

(d) $\chi(O)$-P2 **(e)** $\chi(O)$-P3 **(f)** $\chi(O)$-P5

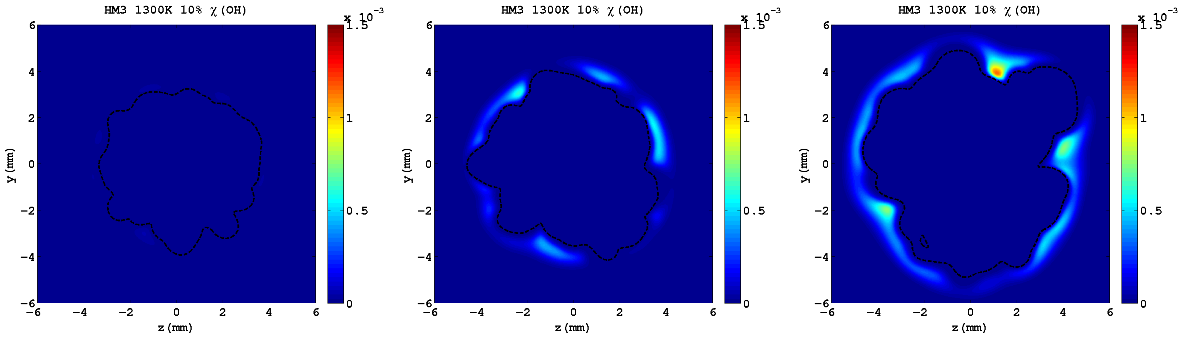

(g) $\chi(OH)$-P2 **(h)** $\chi(OH)$-P3 **(i)** $\chi(OH)$-P5

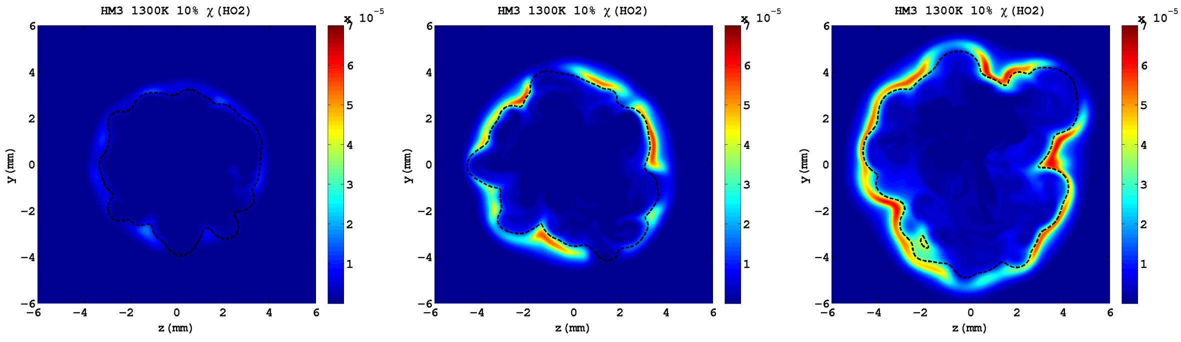

(j) $\chi(\mathrm{HO_2})$-P2 **(k)** $\chi(\mathrm{HO_2})$-P3 **(l)** $\chi(\mathrm{HO_2})$-P5

Figure 7.35: Fields of H mole fraction (top row), O mole fraction (second row), OH mole fraction (third row) and HO_2 mole fraction (bottom row). The HM3-10% case is considered. Snapshots are taken at point 2 - pre-ignition (left column), at point 3 - ignition (middle column) and at point 5 - post-ignition (right column). Fields are extracted from the cross-sectional plane of domain at x=5mm. The black dashed lines locate the stoichiometric mixture fraction region. Figures are zoomed around the fuel/oxidiser interface.

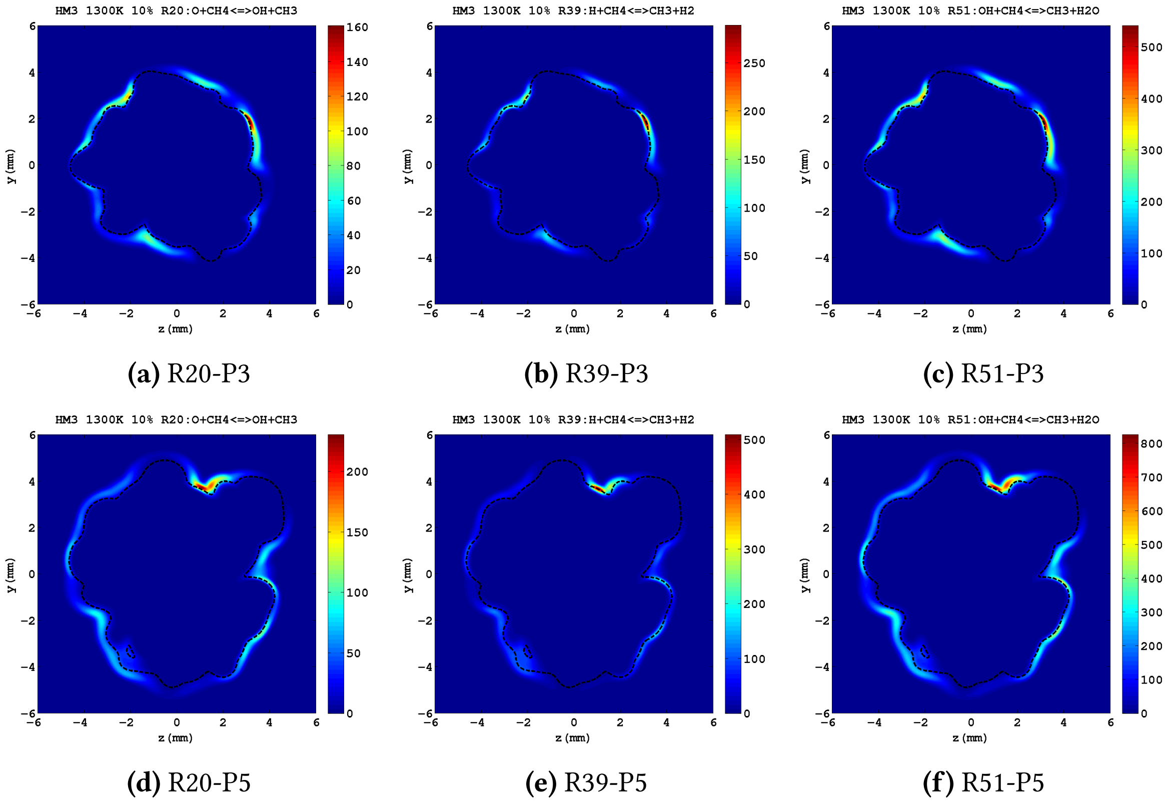

(a) R20-P3 **(b)** R39-P3 **(c)** R51-P3

(d) R20-P5 **(e)** R39-P5 **(f)** R51-P5

Figure 7.36: Fields of R20 (left), R39 (middle), and R51 (right) reaction rates taken at point 3 - ignition (top row) and at point 5 - post-ignition (bottom row). The HM3-10% case is considered. Reaction rates are expressed in $\mathrm{mole/m^3} \cdot \mathrm{s}$. Fields are extracted from the cross-sectional plane of domain at x=5mm. The black dashed lines locate the stoichiometric mixture fraction region. Figures are zoomed around the fuel/oxidiser interface.

The last point of analysis (point 5), is used to investigate the final part of the ignition process. As shown in the previous cases, this period of ignition process is identified by a series of different linked phenomena. The significant oxygen depletion in proximity of Z_{st} (Fig. 7.15a and 7.26a), is accompanied by a drastic reduction of rate of H_2-O2 interaction (Fig. 7.12i, 7.12l, 7.23i and 7.23l), a significant reduction of heat release rate (Fig. 7.11c and 7.22c) and the slowdown of the temperature rise over time (Fig. 7.8 and 7.19).

Figure 7.37a shows the field of oxygen mole fraction in the last part of the ignition process for the HM3-10% case. The snapshot presents a significant entrainment of oxygen within the fuel jet, particularly along the stoichiometric iso-line. However, significant oxygen consumption consumption is not observed in the Z_{st} region. Furthermore, differently from HM3-50% and HM1-50% cases, the reactant consumption contours do not reveal any particular rate reduction. This support the hypothesis that the arrest of the temperature increase (Fig. 7.30), as well as the arrest of the $\chi(O)$ growth (Fig. 7.4f) observed in the post-ignition period, is not due to lack of oxygen, but rather to convective mixing. More precisely, it can be argued that in the last period of ignition, turbulent time scales dominate over the diffusive ones, hampering parts of the chemical processes.

Another interesting aspect sheds light on the chemical scenario change in presence of turbulent motion. In the 1D study, it was observed that the reaction zone propagates over the ignition period, moving from the fuel lean to the fuel rich region of the domain. Both H_2 and CH_4 consumption paths were first observed above the stoichiometric mixture fraction region and then, after ignition, relocating along Z_{st} (H_2 consumption path) or below it (CH_4 consumption path). In particular, it was observed that the chemistry of methane occurs in the $Z > Z_{\mathrm{st}}$ area after ignition (Fig. 6.41a). This is not observed in the 3D study, where the methane consumption remains outside Z_{st} iso-line (Fig. 7.34f).

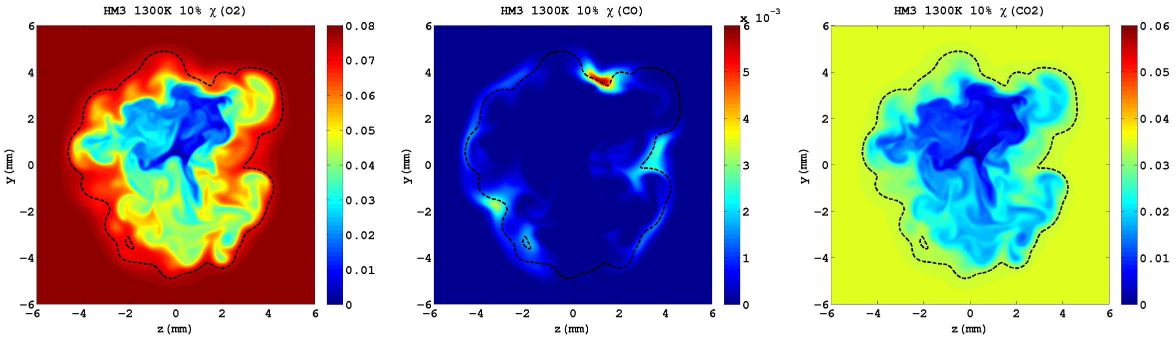

(a) $\chi(O_2)$-P5 **(b)** $\chi(CO)$-P5 **(c)** $\chi(CO_2)$-P5

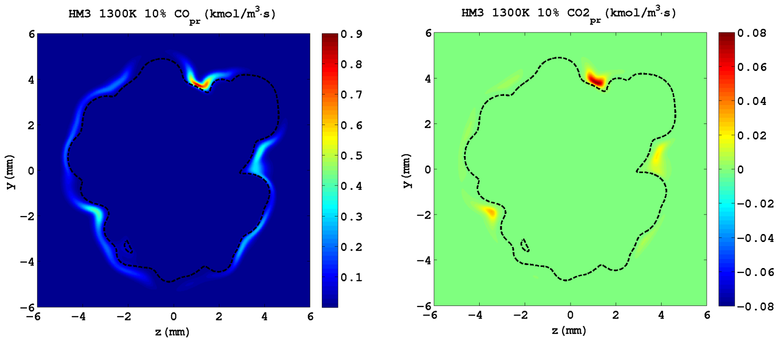

(d) CO_{pr}-P5 **(e)** $CO_{2\mathrm{pr}}$-P5

Figure 7.37: Fields of O_2 mole fraction (top left), CO mole fraction(top middle), CO_2 mole fraction(top right), CO production rate (bottom left) and CO_2 production rate (bottom right) taken at point 5 - post-ignition. The HM3-10% case is considered. Fields are extracted from the cross-sectional plane of domain at x=5mm. The black dashed lines locate the stoichiometric mixture fraction region. Figures are zoomed around the fuel/oxidiser interface.

The fifth point of analysis also gives a picture of the CO/CO_2 release in the domain. Differently from the HM3-50% and HM1-50% cases, a positive production of both CO and CO_2 is observed (Fig. 7.37d and 7.37e). This was noticed already in the 1D case, where it was pointed out that the reduced presence of atomic hydrogen, following the reduced presence of H_2 in the fuel blend, was no longer controlling the $CO_2 -> CO$ process.

The contours (Fig. 7.37d and 7.37e) identify localised areas where CO and CO_2 are being produced. In particular it is noticed that in the areas where the CO production has the highest rate, a more intense CO_2 production is observed. Significantly lower is the rate at which CO_2 is produced with respect to CO, suggesting a partial CO conversion into CO_2 in the post-ignition period.

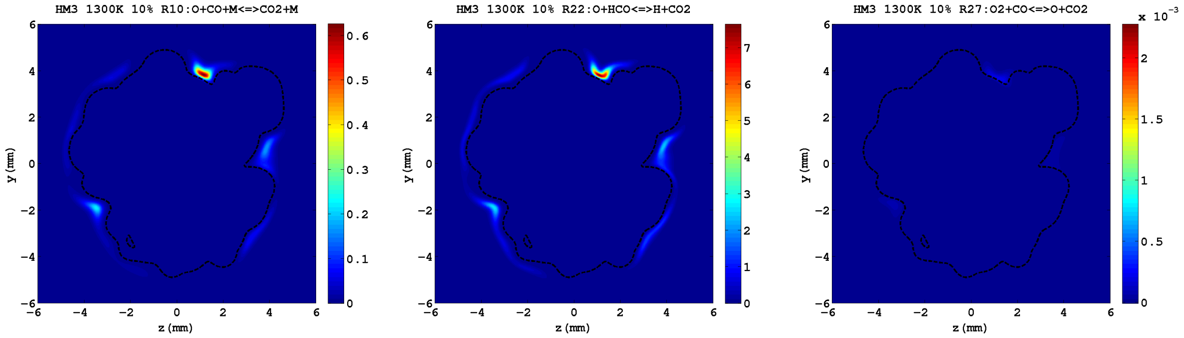

(a) R10-P5 **(b)** R22-P5 **(c)** R27-P5

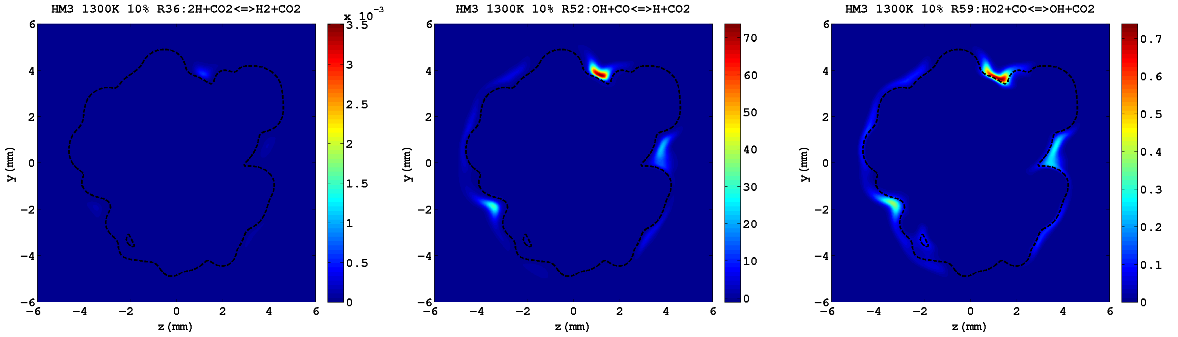

(d) R36-P5 **(e)** R52-P5 **(f)** R59-P5

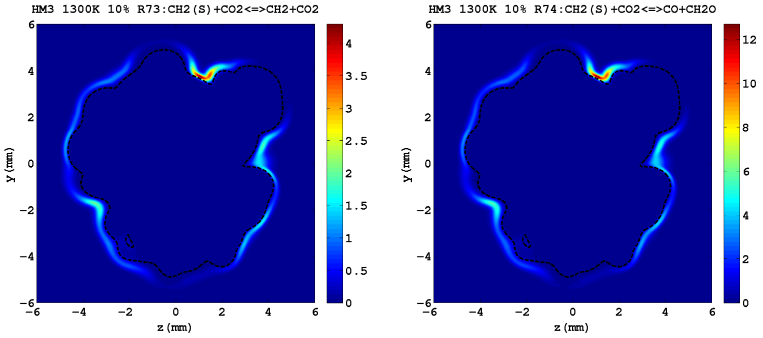

(g) R73-P5 **(h)** R74-P5

Figure 7.38: Reaction rates of all steps (R10, R22, R27, R36, R52, R59, R73 and R74) describing in the DRM19 mechanism the CO_2 consumption/production. Fields are taken at point 5 - post-ignition. The HM3-10% case is considered. Reaction rates are expressed in $\mathrm{mole/m^3 \cdot s}$. Fields are extracted from the cross-sectional plane of domain at x=5mm. The black dashed lines locate the stoichiometric mixture fraction region. Figures are zoomed around the fuel/oxidiser interface.

All steps linked, within the DRM19 mechanism, with the CO_2 production/consumption are shown in figure 7.38. Among the different elementary reactions shown, the R52 step presents the highest rate, demonstrating its major role in controlling the CO_2 release. The R52 step now proceeds towards products, outlining a CO_2 production rather than consumption. As pointed out in the diffusion case, this is due to reduced level of atomic hydrogen (Fig. 7.35c) and the higher level of OH (Fig. 7.35i) in the H/O/OH pool. The higher level of OH (Fig. 7.35i) induces the R52 reaction towards the products (see equation R52 on appendix A) in the regions where high temperatures (Fig. 7.33f) and the presence of CO (Fig. 7.37b) is observed.

7.7 3D Study - Conclusion

In this chapter, the mixing and the spontaneous ignition of a circular fuel jet within a hot diluted oxidiser is overviewed. The study reproduce numerically the JHC experiment of Dally *et al.* [54] and provide a comparison with the 1D cases previously presented, where the turbulent fluctuations were not considered.

Three different cases were presented. The first two cases mimic respectively the HM3 and HM1 configurations from Dally experiment [54], where an equimolar mixture of methane and hydrogen is used as fuel jet. In the third case the fuel jet has a reduced amount of hydrogen as the CH_4/H_2 molar proportion is changed to 90/10.

The first case analysed, the base case, revealed a minor role played by turbulence along the ignition period. Both methane and hydrogen vortical structures were enclosed within the stoichiometric mixture fraction region during the earliest part of ignition, while the higher hydrogen diffusivity in the hottest part of the domain is responsible for initiating the reactions. Methane and hydrogen chemistry evolve along different spatial location and extension: the hydrogen consumption, showing a broader extension, occurs in proximity of the stoichiometric region, while the consumption of methane mostly takes place in the fuel rich area. The H_2-O_2 interaction is dominant in the pre-ignition, as well as in the rest of ignition period, controlling the radical pool formation. The H/O/OH pool shows, as in the corresponding 1D case, a large excess of atomic hydrogen during all stages of ignition.

The latest stages of ignition are characterised by a strong oxygen consumption in proximity of Z_{st}, which limits the rate of H_2-O_2 interaction. Conversely, a significant rate reduction of the methane consumption rate is not observed. The large H presence where CH_4 is consumed, suggests that the convective transport of methane, in regions where significant is the atomic hydrogen build-up, reduces the effect of differential diffusion and enhances CH_4 dehydrogenation.

The presence of H is equally important for the CO formation in the domain. The investigation of major reactions describing the production/consumption of carbon dioxide revealed CO partially formed by the $\mathrm{CO_2} -> \mathrm{CO}$ process through R52 step.

The next case analysed (HM1-50%) showed, because of the longer self-ignition time, a stronger development of turbulence. As a consequence, self-ignition occurs along Z_{st} with a more discontinuous fashion. The earliest part of ignition remains controlled by differential diffusion which explains the major role of the H_2-O_2 interaction and the strong presence of atomic hydrogen in the H/O/OH radical pool.

Apart from the lower temperature observed, the physical/chemical scenario observed in the ignition and post-ignition period is similar to the base case. At ignition time an increase of reactants consumption rates accompanied by the temperature rise is observed. In the post-ignition period a rate reduction of oxygen and hydrogen consumption is observed, while methane consumption rates are as high as at ignition. The highest values of methane consumption rate are observed where high levels of atomic hydrogen are present. In the same regions, the high levels of atomic hydrogen induces R52 step to move backward, consuming carbon dioxide.

The turbulence convection presents major effects in the HM3-10% case. The strong turbulence development results in reactions initiations at different location and with different timing. Despite the dominant CH_4 presence in the fuel, turbulence convection does not cancel the effects of differential diffusion, as H_2 keeps diffusing along Z_{st} in the earliest part of ignition. The reduced level of H_2 in the fuel mixture is linked with the reduced importance of atomic hydrogen in the H/O/OH radical pool along the whole ignition period. The greater presence of OH changes, with respect to HM3-50% and HM1-50% cases, the chemistry of CH_4 abstraction as the R51 step results controlling the methane dehydrogenation. Moreover, the dominant presence of OH in the radical pool induces the R52 reaction towards products, promoting the $\mathrm{CO}->\mathrm{CO}_2$ process.

The strongest differences with respect to the corresponding 1D case are observed in the last part of the ignition process. The post-ignition period is characterised, in the presence of turbulent mixing, by the temperature increment being limited to around 100K, a value significantly lower that the increase in temperature observed in the diffusion case (1D). Moreover, the drop of oxygen level followed by the drastic reduction of the heat release rate is not observed at this time. It is argued that, despite the large presence of oxygen along the stoichiometric iso-line, the turbulent time scales dominate over the diffusive ones, hampering part of the chemical processes.

Chapter 8

Conclusions and future works

This dissertation presents a numerical investigation of the MILD combustion regime. MILD combustion has caught the attention of the scientific and industrial communities because of its capability to enhance thermal efficiency and reduce emissions. Following the high potential offered by this combustion regime, a broad range of numerical and experimental studies is present in the literature, investigating the complex interaction among turbulence, diffusion and chemistry in a MILD flame.

Despite the large number of studies in the literature, the broad transition to this combustion regime in the industrial field is hampered by the lack of MILD specific numerical models able to test full-scale burners and by the production of reliable set of predictions. Development of reliable numerical models requires high quality sets of data against which the models can be validated. The ability of Direct Numerical Simulations (DNS) to provide detailed descriptions of the complex interplay between turbulence, diffusion and chemistry within a flame is well known in the literature. Also known is that the high quality dataset from a DNS study comes at a numerical cost, which often force researchers to use some level of simplifications in order to reduce the numerical expenses and the complexity of initial conditions modelling.

To the author's knowledge, only few studies in the literature present an investigation of MILD combustion regime by means of direct numerical simulation [8, 61–63].

Both Van Oijen and Göktolga *et al.* studies [8, 63] rely on the experimental setup proposed by Dally *et al.* [54]. The Van Oijen study mimics numerically the HM1/HM2 and HM3 configurations of the JHC burner (see Sect. 2.10 for more details) by means of 1D and 2D simulations. The Göktolga *et al.* study presents a comparison between 1D, 2D and 3D simulations of the HM1 case. Both studies shed lights on the self-ignition behaviour of MILD flames, capturing the main characteristics of flame structure over the ignition period. Less attention is given to the evolution of the kinetic scenario along ignition.

A detailed description of reaction zones in the MILD flame was provided in the works Minamoto *et al.* [61, 62], where a particular emphasis was given to the morphological aspects of reaction zones. These studies were based on premixed initial conditions and, as such, insights into spontaneous mixing and reaction among fuel and oxidiser were not provided.

The present work broadens the knowledge of MILD combustion by adding new case studies and more insights into the literature. The set of simulations presented here are based on the JHC (Jet in Hot Coflow) burner experiment of Dally *et al.* [54], which represents an important milestone in the literature, being able to reproduce the common set-up of an industrial scale MILD burner by means of a simpler experimental configuration. The description of different one-dimensional and three-dimensional numerical studies is provided.

The numerical tool used to advance the governing equations, is the Low Mach Combustion (LMC) code developed at the Centre for Computational Sciences and Engineering (CCSE) of Lawrence Berkeley National Laboratory, California. The parallel computing feature of the code has been used to run the 3D simulations on multiple processors. The DRM19 is the kinetic mechanism used to follow, in time, the rates of each elementary reaction involved.

Since a major milestone in the complete understanding of the MILD combustion regime is knowledge of the fuel/oxidiser mixing process that leads to self-ignition, emphasis is given, in 1D diffusion cases, to the temporal evolution of the kinetic scenarios describing the fuel/oxidiser interaction.

The diffusion-chemistry interplay during self-ignition under MILD firing mode is extensively investigated in chapter 4, 5 and 6. These chapter presents the description of five different cases: each of them presents different fuel and/or oxidiser blend.

A normalisation technique has been developed aimed at facilitate the comparison between cases presenting significant differences in spacial and time scales, as a consequence of the broad set of fuel/oxidiser blends used. In chapter 3 a time normalisation technique is proposed. In chapter 5 and 6, this technique is coupled with a space normalisation. Both account for the changes in the ignition time, for the different configurations, and the associated variations in diffusion.

Initially the base case is considered. The oxidiser layer is set up as a $O_2/N_2/H_2O/CO_2$ mixture at 1300K, with the oxygen accounting for the 9% of the total mass. The fuel layer is set up as an equimolar mixture of CH_4 and H_2 at 305K.

The analysis showed differential diffusion playing a major role in the pre-ignition period. As a consequence of its higher diffusion rate, a larger H_2 presence is observed close to the stoichiometric region. Here, earliest reactions are observed and the flame front starts developing. Along the whole ignition period, the flame front outlines two different paths along which methane and hydrogen are being predominantly consumed: the hydrogen path is closer to the oxidiser layer while methane is located below it. Since the earliest part of the ignition period, the H_2 chemistry is dominant, representing the major cause of oxygen consumption and controlling the formation of the H/O/OH radical pool. The large excess of atomic hydrogen compared to O and OH is linked with the methane dehydrogenation via the R39 step and the unusual CO_2 consumption. The investigation of all reactions responsible for CO_2 production/destruction included in the DRM19 mechanism revealed two major aspects: the

CO_2 consumed originates from the $O_2/N_2/H_2O/CO_2$ oxidiser blend and the backward R52 step controls the $CO_2 -> CO$ process. The oxygen depletion observed after the ignition time has a rate limiting function over the vast majority of reactions. Because of their different spatial displacement, the CH_4 and H_2 mechanisms are affected differently by the lack of O_2. The methane chemistry in particular starves in a low oxygen area, limiting the methyl oxidation and promoting the methyl recombination into the C_2 form (ethane).

The knowledge acquired from the base case (HM3-50%) is then expanded, in chapter 5, with the investigation of the HM2-50% and HM1-50% cases where the oxygen level in the oxidiser is reduced by 1.5 and 3 times respectively. The reduction in oxygen is balanced by increasing the N_2 presence. Two major effects follow a higher oxygen dilution: the peak temperature decreases and the ignition is delayed. The latter effect is strongly linked with the reduced H/O/OH excess in the reaction zone. The self-ignition process continues to be controlled in the high dilution cases by the differential diffusion effect. A larger amount of H_2 diffuses near to the stoichiometric region, while the CH_4 presence in the reaction area is limited. As more diluted is O_2 in the oxidiser, the weakening of the $CH_3 -> CO$ process and the strengthening of the methyl recombination assume increased importance. In a way similar, in the HM2-50% and HM1-50% case the CO_2 destruction through the R52 reaction assume greater importance compared to the HM3-50%.

With the purpose of investigate the role of H_2 in the fuel blend, chapter 6 presents a comparison between the base case (HM3-50%) and configurations with reduced and zero hydrogen (HM3-10% and HM3-0%). The H_2 addition acts, with the respect to the pure methane case, as a fuel “enhancer” since it enriches the domain with a larger presence of highly reactive H, O and OH radicals. Self-ignition time is significantly impacted. The pure methane configuration (HM3-0%) requires approximately 18ms to ignite. The addition of 10% (molar basis) of hydrogen to the fuel, ignites the reactants 30 times quicker (t_{ig} $\sim$0.6ms). An even earlier ignition occurs (t_{ig} $\sim$0.14ms) by using an equi-molar mixture of hydrogen and methane as the fuel. The chemical scenario of low hydrogen configurations showed marked differences with respect to the HM3-50% case. The reduced H production, affects the rate of the R33 reaction (O_2 consumption) and the consequent release of radicals. The methane dehydrogenation is mostly advanced by the R51 step (rather than R39) in the earliest stages of ignition. The methyl conversion into HCO is now observed to evolve along three different paths. The methyl recombination into the C_2 form particularly, assume reduced importance in the HM3-10% and HM3-0% cases. Nonetheless, the significant ethane conversion into HCO highlight a larger availability of oxygen for the methane chemistry. Moreover, the lower H_2 addition corresponds to enhanced $HCO -> CO$ and $CO -> CO_2$ conversions. The presence of H_2 in the fuel is particularly beneficial for the HM3-10% case. It accelerates the methane chemistry, but it does not particularly alter the CH_4 consumption pathway. The R52 reaction controls the carbon dioxide consumption/production independently of the fuel mixture considered. The larger the amount of H_2 in the fuel blend, the more reduced the $CO -> CO_2$ conversion.

In chapter 7 the interplay between turbulence, diffusion and chemistry is investigated by means of three different 3D studies. The JHC experiment of Dally *et al.* [54] is numerically studied by means of a circular fuel jet mixing with a hot oxidiser co-flow. The effect of the oxygen dilution and hydrogen addition are both investigated in three dimensions. The effect of hydrogen addition is studied by modelling the fuel jet with a 50/50 and a 90/10 CH_4/H_2 molar mixtures. The effect of the oxygen dilution is accounted for by considering the HM3 and HM1 oxidiser configurations. The initial temperature of fuel and oxidiser are kept consistent with the 1D study and the JHC experiment.

For each of the HM3-50%, HM1-50% and HM3-10% cases, an introductory overview of the effect of turbulence on diffusion chemistry interplay is presented. Insights into each case follow through the investigation of the ignition period at three different time points: one point selected in the pre-ignition period, one at ignition time and one in the post-ignition period. The methodology used to define the ignition period and compute the ignition time no longer relies on the temperature calculation conditioned on the mixture fraction space, but rather on the tracking the level of an intermediate species. In this thesis the level of atomic oxygen is proposed as an ignition indicator. At each selected time point the description of different fields of interests (temperature, heat release, etc) along a specific plane of the numerical domain is provided.

The first case analysed, the base case, revealed a minor role played by turbulence during the ignition period. Both methane and hydrogen vortical structures were found enclosed within the stoichiometric mixture fraction region during the earliest part of ignition, while the hydrogen diffusivity in the hottest part of the domain explained the reactions initiation. Methane and hydrogen chemistry evolve along different spatial location and extension consistently with the 1D analysis. The H_2-O_2 interaction was observed dominant in the entire ignition period, controlling the radical pool formation. The H/O/OH pool showed, as in the corresponding 1D case, a large excess of atomic hydrogen, which controls the methane dehydrogenation (R39) and the CO_2 consumption (R52). As the turbulence effect grows stronger, the effect of differential diffusion is reduced and the methane abstraction is enhanced, with respect to the 1D case.

As a consequence of the longer self-ignition time, the HM1-50% case showed a stronger development of turbulence and a “spotty” self-ignition behaviour along Z_{st} was observed. Nonetheless, the earliest part of ignition remains controlled by differential diffusion, which explains the major role of the H_2-O_2 interaction and the strong presence of atomic hydrogen in the H/O/OH radical pool. The physical/chemical scenario observed in the ignition and post-ignition period is comparable to the base case. At ignition time an increase in reactants consumption rates is observed, followed by a rise in temperature. In the post-ignition period, the oxygen depletion in the proximity of Z_{st} explains the rate reduction of hydrogen consumption. Conversely, a rate reduction of CH_4 consumption is not observed. The highest value of methane consumption rate are observed where high levels of atomic hydrogen are present. In the same regions, the high levels of atomic hydrogen induces the R52 step to move backward, consuming carbon dioxide.

The turbulent mixing presents major effects in the HM3-10% case, where self-ignition is delayed with respect to HM3-50% and HM1-50% configurations. The strong turbulence development causes initiation of reactions at different locations and with different timing. Despite the dominant CH_4 presence in the fuel, turbulence convection does not cancel the effects of differential diffusion, as H_2 keeps an important role in the earliest part of ignition, diffusing along Z_{st}. The reduced level of H_2 in the fuel mixture is linked with the reduced importance of atomic hydrogen within H/O/OH pool. The larger presence of OH controls CH_4 abstraction through the R51 step and promotes promoting the $\mathrm{CO}->\mathrm{CO}_2$ process. The strongest differences with respect to the corresponding 1D case are observed in the last part of the ignition process. The post-ignition period is characterised by the arrest of the temperature increment at around 100K, a value significantly lower than the temperature rise in the diffusion case. The significant oxygen depletion which characterised the HM3-50% and HM1-50% case along Z_{st}, is not observed for the HM3-10% configuration. It is argued that, despite the large presence of oxygen along the stoichiometric iso-line, turbulent scales dominate over the diffusive ones, hampering part of the chemical processes.

Future works

The study provides different insights into the fuel/oxidiser interaction under MILD conditions. With the insights, several questions arose, requiring further numerical modelling, in both 1D and 3D spaces, to be answered.

The methodology used to scale the different ignition periods, was found particularly useful for the selection of time points used to investigate physical and chemical properties of reaction zones. While no particular difficulties were observed in applying this methodology to different oxidiser dilutions (Chap. 5), some adjustments in points selection were necessary to compare cases with different fuel blends (Chap. 6). This highlights the possibility of future improvements of the technique, with the purpose to apply the scaling to a broader range of cases. The method used in the 3D study to define the ignition time, encourages the development of a scaling technique based on tracking of intermediate species rather than temperature increment.

Deeper insights into the physical evolution of the reaction zone may come from the quantification of the CH_4/H_2 path distance as a function of the fuel and oxidiser blends. This knowledge could shed light on the effect of different fuel and oxidiser dilutions on the flame thickness.

Equally interesting would be an investigation of different diluents in the oxidiser mixture. Particularly, interesting would be tracking the different polluting species (e.g. NOx, CO and CO_2) with the help of more detailed chemical mechanism (e.g. GRI-Mech 3.0).

The 3D study provides an overview of the turbulence diffusion chemistry interplay, which re-

quires a follow-up analysis. Central to the future investigations is the study of the kinetic scenario in the presence of turbulent mixing. In particular, how the methane chemistry changes when the differential diffusion effect is reduced.
A related issue which requires satisfactory explanation is the knowledge of turbulent/chemistry scales relation which hampers the chemical processes in the HM3-10%. To this end, 3D numerical studies with different Re values are necessary.

Appendix A

DRM19 Mechanism

		Forward Rate Coefficient[1]		
N.	Reaction	A_f	β_f	E_f
1	$\mathrm{H + CH_2 + M \longleftrightarrow CH_3 + M}$	3.200E+27	-3.140	1230.00
2	$\mathrm{H + CH_3 + M \longleftrightarrow CH_4 + M}$	2.477E+33	-4.760	2440.00
3	$\mathrm{H + HCO + M \longleftrightarrow CH_2O + M}$	1.350E+24	-2.570	1425.00
4	$\mathrm{H + CH_2O + M \longleftrightarrow CH_3O + M}$	2.200E+30	-4.800	5560.00
5	$\mathrm{H + C_2H_4 + M \longleftrightarrow C_2H_5 + M}$	1.200E+42	-7.620	6970.00
6	$\mathrm{H + C_2H_5 + M \longleftrightarrow C_2H_6 + M}$	1.990E+41	-7.080	6685.00
7	$\mathrm{H_2 + CO + M \longleftrightarrow CH_2O + M}$	5.070E+27	-3.420	84350.00
8	$\mathrm{2\,CH_3 + M \longleftrightarrow C_2H_6 + M}$	1.770E+50	-9.670	6220.00
9	$\mathrm{O + H + M \longleftrightarrow OH + M}$	5.000E+17	-1.000	0.00
10	$\mathrm{O + CO + M \longleftrightarrow CO_2 + M}$	6.020E+14	0.000	3000.00
11	$\mathrm{H + O_2 + M \longleftrightarrow HO_2 + M}$	2.800E+18	-0.860	0.00
12	$\mathrm{2\,H + M \longleftrightarrow H_2 + M}$	1.000E+18	-1.000	0.00
13	$\mathrm{H + OH + M \longleftrightarrow H_2O + M}$	2.200E+22	-2.000	0.00
14	$\mathrm{HCO + M \longleftrightarrow H + CO + M}$	1.870E+17	-1.000	17000.00
15	$\mathrm{O + H_2 \longleftrightarrow H + OH}$	5.000E+04	2.670	6290.00
16	$\mathrm{O + HO_2 \longleftrightarrow OH + O_2}$	2.000E+13	0.000	0.00
17	$\mathrm{O + CH_2 \longleftrightarrow H + HCO}$	8.000E+13	0.000	0.00
18	$\mathrm{O + CH_2(S) \longleftrightarrow H + HCO}$	1.500E+13	0.000	0.00
19	$\mathrm{O + CH_3 \longleftrightarrow H + CH_2O}$	8.430E+13	0.000	0.00
20	$\mathrm{O + CH_4 \longleftrightarrow OH + CH_3}$	1.020E+09	1.500	8600.00
21	$\mathrm{O + HCO \longleftrightarrow OH + CO}$	3.000E+13	0.000	0.00
22	$\mathrm{O + HCO \longleftrightarrow H + CO_2}$	3.000E+13	0.000	0.00
23	$\mathrm{O + CH_2O \longleftrightarrow OH + HCO}$	3.900E+13	0.000	3540.00
24	$\mathrm{O + C_2H_4 \longleftrightarrow CH_3 + HCO}$	1.920E+07	1.830	220.00
25	$\mathrm{O + C_2H_5 \longleftrightarrow CH_3 + CH_2O}$	1.320E+14	0.000	0.00

		Forward Rate Coefficient[1]		
N.	Reaction	A_f	β_f	E_f
26	$O + C_2H_6 \longleftrightarrow OH + C_2H_5$	8.980E+07	1.920	5690.00
27	$O_2 + CO \longleftrightarrow O + CO_2$	2.500E+12	0.000	47800.00
28	$O_2 + CH_2O \longleftrightarrow HO_2 + HCO$	1.000E+14	0.000	40000.00
29	$H + 2\,O_2 \longleftrightarrow HO_2 + O_2$	3.000E+20	-1.720	0.00
30	$H + O_2 + H_2O \longleftrightarrow HO_2 + H_2O$	9.380E+18	-0.760	0.00
31	$H + O_2 + N_2 \longleftrightarrow HO_2 + N_2$	3.750E+20	-1.720	0.00
32	$H + O_2 + AR \longleftrightarrow HO_2 + AR$	7.000E+17	-0.800	0.00
33	$H + O_2 \longleftrightarrow O + OH$	8.300E+13	0.000	14413.00
34	$2\,H + H_2 \longleftrightarrow 2\,H_2$	9.000E+16	-0.600	0.00
35	$2\,H + H_2O \longleftrightarrow H_2 + H_2O$	6.000E+19	-1.250	0.00
36	$2\,H + CO_2 \longleftrightarrow H_2 + CO_2$	5.500E+20	-2.000	0.00
37	$H + HO_2 \longleftrightarrow O_2 + H_2$	2.800E+13	0.000	1068.00
38	$H + HO_2 \longleftrightarrow 2\,OH$	1.340E+14	0.000	635.00
39	$H + CH_4 \longleftrightarrow CH_3 + H_2$	6.600E+08	1.620	10840.00
40	$H + HCO \longleftrightarrow H_2 + CO$	7.340E+13	0.000	0.00
41	$H + CH_2O \longleftrightarrow HCO + H_2$	2.300E+10	1.050	3275.00
42	$H + CH_3O \longleftrightarrow OH + CH_3$	3.200E+13	0.000	0.00
43	$H + C_2H_6 \longleftrightarrow C_2H_5 + H_2$	1.150E+08	1.900	7530.00
44	$OH + H_2 \longleftrightarrow H + H_2O$	2.160E+08	1.510	3430.00
45	$2\,OH \longleftrightarrow O + H_2O$	3.570E+04	2.400	-2110.00
46	$OH + HO_2 \longleftrightarrow O_2 + H_2O$	2.900E+13	0.000	-500.00
47	$OH + CH_2 \longleftrightarrow H + CH_2O$	2.000E+13	0.000	0.00
48	$OH + CH_2(S) \longleftrightarrow H + CH_2O$	3.000E+13	0.000	0.00
49	$OH + CH_3 \longleftrightarrow CH_2 + H_2O$	5.600E+07	1.600	5420.00
50	$OH + CH_3 \longleftrightarrow CH_2(S) + H_2O$	2.501E+13	0.000	0.00
51	$OH + CH_4 \longleftrightarrow CH_3 + H_2O$	1.000E+08	1.600	3120.00
52	$OH + CO \longleftrightarrow H + CO_2$	4.760E+07	1.228	70.00
53	$OH + HCO \longleftrightarrow H_2O + CO$	5.000E+13	0.000	0.00
54	$OH + CH_2O \longleftrightarrow HCO + H_2O$	3.430E+09	1.180	-447.00
55	$OH + C_2H_6 \longleftrightarrow C_2H_5 + H_2O$	3.540E+06	2.120	870.00
56	$HO_2 + CH_2 \longleftrightarrow OH + CH_2O$	2.000E+13	0.000	0.00
57	$HO_2 + CH_3 \longleftrightarrow O_2 + CH_4$	1.000E+12	0.000	0.00
58	$HO_2 + CH_3 \longleftrightarrow OH + CH_3O$	2.000E+13	0.000	0.00
59	$HO_2 + CO \longleftrightarrow OH + CO_2$	1.500E+14	0.000	23600.00
60	$CH_2 + O_2 \longleftrightarrow OH + HCO$	1.320E+13	0.000	1500.00
61	$CH_2 + H_2 \longleftrightarrow H + CH_3$	1.320E+13	0.000	1500.00
62	$CH_2 + CH_3 \longleftrightarrow H + C_2H_4$	4.000E+13	0.000	0.00

		Forward Rate Coefficient[1]		
N.	Reaction	A_f	β_f	E_f
63	$CH_2 + CH_4 \longleftrightarrow 2\,CH_3$	2.460E+06	2.000	8270.00
64	$CH_2(S) + N_2 \longleftrightarrow CH_2 + N_2$	1.500E+13	0.000	600.00
65	$CH_2(S) + AR \longleftrightarrow CH_2 + AR$	9.000E+12	0.000	600.00
66	$CH_2(S) + O_2 \longleftrightarrow H + OH + CO$	2.800E+13	0.000	0.00
67	$CH_2(S) + O_2 \longleftrightarrow CO + H_2O$	1.200E+13	0.000	0.00
68	$CH_2(S) + H_2 \longleftrightarrow CH_3 + H$	7.000E+13	0.000	0.00
69	$CH_2(S) + H_2O \longleftrightarrow CH_2 + H_2O$	3.000E+13	0.000	0.00
70	$CH_2(S) + CH_3 \longleftrightarrow H + C_2H_4$	1.200E+13	0.000	-570.00
71	$CH_2(S) + CH_4 \longleftrightarrow 2\,CH_3$	1.600E+13	0.000	-570.00
72	$CH_2(S) + CO \longleftrightarrow CH_2 + CO$	9.000E+12	0.000	0.00
73	$CH_2(S) + CO_2 \longleftrightarrow CH_2 + CO_2$	7.000E+12	0.000	0.00
74	$CH_2(S) + CO_2 \longleftrightarrow CO + CH_2O$	1.400E+13	0.000	0.00
75	$CH_3 + O_2 \longleftrightarrow O + CH_3O$	2.675E+13	0.000	28800.00
76	$CH_3 + O_2 \longleftrightarrow OH + CH_2O$	3.600E+10	0.000	8940.00
77	$2\,CH_3 \longleftrightarrow H + C_2H_5$	4.990E+12	0.100	10600.00
78	$CH_3 + HCO \longleftrightarrow CH_4 + CO$	2.648E+13	0.000	0.00
79	$CH_3 + CH_2O \longleftrightarrow HCO + CH_4$	3.320E+03	2.810	5860.00
80	$CH_3 + C_2H_6 \longleftrightarrow C_2H_5 + CH_4$	6.140E+06	1.740	10450.00
81	$HCO + H_2O \longleftrightarrow H + CO + H_2O$	2.244E+18	-1.000	17000.00
82	$HCO + O_2 \longleftrightarrow HO_2 + CO$	7.600E+12	0.000	400.00
83	$CH_3O + O_2 \longleftrightarrow HO_2 + CH_2O$	4.280E-13	7.600	-3530.00
84	$C_2H_5 + O_2 \longleftrightarrow HO_2 + C_2H_4$	8.400E+11	0.000	3875.00

Table A.1: DRM19 reduced set of elementary reactions from GRI-MECH methane mechanism [66,73].

---

[1] The *Forward Rate Coefficient* (K_f) is expressed following the relationship $K_\mathrm{f}(T) = A_\mathrm{f} T^{\beta_\mathrm{f}} \exp(-E_\mathrm{f}/RT)$, where A_f is the frequency factor, T is the temperature, E_f is the activation energy and R is the universal gas constant. The algebraic power dependence T^{β_f} is referred as pre-exponential temperature dependence as it modifies the exponential term. The subscript f refers to the forward direction of elementary reaction. With concentration of species expressed in mol/cm^3, the units of A_f are $1/s$, $cm^3/mol \cdot s$, $cm^6/mol^2 \cdot s$ for first, second, and third order reactions, respectively. The activation energy E_f is expressed in cal/mol.

References

[1] Climate change 2014. Technical report, Intergovernmental Panel on Climate Change, 2014.

[2] World energy outlook report. Technical report, International Energy Agency, 2015.

[3] The global status of ccs. Technical report, Global CCS Institute, 2015.

[4] J. Hansen and P. Kharecha. Assessing ”Dangerous Climate Change”: Required Reduction of Carbon Emissions to Protect Young People , Future Generations and Nature. *PLOS ONE*, 8(12), dec 2013.

[5] M. Meinshausen, N. Meinshausen, W. Hare, S.C.B. Raper, K. Frieler, R. Knutti, D.J. Frame, and M.R. Allen. Greenhouse-gas emission targets for limiting global warming to 2 degrees c. *Nature*, 458(7242):1158–1162, 2009.

[6] P.F. Li, J.C. Mi, B.B. Dally, et al. Progress and recent trend in MILD combustion. *Science China Technological Sciences*, 54(2):255–269, 2011.

[7] E Abtahizadeh. *Numerical study of Mild combustion.* PhD thesis, Eindhoven University of Technology, 2014.

[8] J.A. van Oijen. Direct numerical simulation of autoigniting mixing layers in mild combustion. *Proceedings of the Combustion Institute*, 34(1):1163–1171, 2013.

[9] A. Milani. Ifrf combustion handbook. `http://www.handbook.ifrf.net/handbook/`, 2002.

[10] E. Abtahizadeh, J. van Oijen, and P. de Goey. Numerical study of Mild combustion with entrainment of burned gas into oxidizer and/or fuel streams. *Combustion and Flame*, 159(6):2155–2165, 2012.

[11] J.A. Wünning and J.G Wünning. Flameless oxidation to reduce thermal NO-formation. *Progress in energy and combustion science*, 23:81–94, 1997.

[12] A. Milani and A. Saponaro. Diluted combustion technlogies. *IFRF Combustion Journal*, pages 1–32, 2001.

[13] H. Tsuji, K. Gupta, T. Hasegawa, M. Katsuki, K Kishimoto, and M. Morita. *High Temperature Air Combustion*. CRC Press, 2003.

[14] M. Katsuki and T. Hasegawa. The science and technology of combustion in highly preheated air. In *Symposium (International) on Combustion*, volume 27, pages 3135–3146, 1998.

[15] A.K. Gupta. Flame characteristic and challenges with high temperature air combustion. In *Proceedings of Second International Seminar on High Temperature Combustion in Industrial Furnaces, Jernkontoret-KTH, Stockholm, Sweden*, volume 1, 2000.

[16] N. Peters. Principles and potential of hicot combustion. In *Proceedings of the Forum on High-Temperature Air Combustion Technology*, page 109, 2001.

[17] A. Cavaliere and M. De Joannon. Mild combustion. *Progress in Energy and Combustion Science*, 30(4):329–366, 2004.

[18] T. Poinsot and D. Veynante. *Theoretical and numerical combustion*. CNRS, 3rd edition, 2012.

[19] N. Peters. Fifteen lectures on laminar and turbulent combustion, 1995.

[20] CFD Online Wiki. Navier-stokes equations. `http://www.cfd-online.com/Wiki/Navier-Stokes_equations`.

[21] K.K Kuo. *Priciples of Combustion*. Wiley, 1st edition, 1986.

[22] M.S. Day and J.B. Bell. Numerical simulation of laminar reacting flows with complex chemistry. *Combustion Theory and Modelling*, 4:535–556, 2000.

[23] R. Verzicco. Lezioni del corso di fluidodinamica, 2002.

[24] A. Nonaka, J.B. Bell, M.S. Day, C. Gilet, A.S. Almgren, and M.L. Minion. A deferred correction coupling strategy for low Mach number flow with complex chemistry. *Combustion Theory and Modelling*, 16(December):1–36, 2012.

[25] J.F. Grcar. An explicit runge-kutta iteration for diffusion in the low mach number code. *Lawrence Berkley National Laboratory report LBNL-63375*, pages 1–17, 2007.

[26] Y. Xin, W. Liang, W. Liu, T. Lu, and C.K. Law. A reduced multicomponent diffusion model. *Combustion and Flame*, 162(1):68–74, 2015.

[27] R.J. Kee, M.E. Coltrin, and P. Glarborg. *Chemically Reacting Flow - Theory and Practice.* Wiley-Interscience, 1st edition, 2003.

[28] J.F. Grcar, J.B. Bell, and M.S. Day. The soret effect in naturally propagating, premixed, lean, hydrogenfi?!air flames. *Proceedings of the Combustion Institute*, 32(1):1173–1180, dec 2009.

[29] R.W. Bilger, S.H. Stårner, and R.J. Kee. On reduced mechanisms for methaneair combustion in nonpremixed flames. *Combustion and Flame*, 80(2):135–149, 1990.

[30] S.R. Turns. *An Introduction to Combustion: Concepts and Applications.* McGraw-Hill Education, 3rd edition, 2011.

[31] J.F. Grcar, M.S. Day, and J.B. Bell. A taxonomy of integral reaction path analysis. *Combustion Theory and Modelling*, 10(4):559–579, 2006.

[32] R. Verzicco. Appunti di turbolenza, 2007.

[33] A.N Kolmogorov. Dissipation of Energy in the Locally Isotropic Turbulence. *Dokl. Akad. Nauk SSSR*, 30(30):301–305, 1941.

[34] A.N Kolmogorov. The local structure of turbulence in an incompressible fluid for very large Reynolds numbers. *Dokl. Akad. Nauk SSSR*, 31(31):538–540, 1941.

[35] T Echekki and E Mastrorakos. *Turbulent Combustion Modelling.* Springer, 2011.

[36] H. Pitsch. Large-Eddy Simulation of Turbulent Combustion. *Annual Review of Fluid Mechanics*, 38(1):453–482, jan 2006.

[37] M. Germano, U. Piomelli, P. Moin, and W.H. Cabot. A dynamic subgrid-scale eddy viscosity model. *Physics of Fluids A*, 3:1760–1765, 1991.

[38] B. Rogg and N. Peters. The asymptotic structure of weakly strained stoichiometric methane-air flames. *Combustion and Flame*, 79(3-4):402–420, 1990.

[39] H. Pitsch. Improved pollutant predictions in large-eddy simulations of turbulent nonpremixed combustion by considering scalar dissipation rate fluctuations. *Proceedings of the Combustion Institute*, 29(2):1971–1978, jan 2002.

[40] J. Bell. AMR for low Mach number reacting flow. In *Proceedings of the Chicago Workshop on Adaptive Mesh Refinement Methods, Sept. 3fi5, 2003*, pages 203–221, 2003.

[41] J.H. Chen, A. Choudhary, B.D. Supinski, M. DeVries, E.R. Hawkes, S. Klasky, W.K. Liao, K.L. Ma, J. Mellor-Crummey, N. Podhorszki, R. Sankaran, S. Shende, and C.S. Yoo. Terascale direct numerical simulations of turbulent combustion using S3D. *Computational Science and Discovery*, 1:1–32, 2009.

[42] T.F. Lu, C.S. Yoo, J.H. Chen, et al. Three-dimensional direct numerical simulation of a turbulent lifted hydrogen jet flame in heated coflow: a chemical explosive mode analysis. *Journal of Fluid Mechanics*, 652:45–64, 2010.

[43] A.J. Aspden, M.S. Day, and J.B. Bell. Three-dimensional direct numerical simulation of turbulent lean premixed methane combustion with detailed kinetics. *Combustion and Flame*, 2016.

[44] J. Bell. *AMR for low Mach number reacting flow.* Springer Berlin Heidelberg, 2005.

[45] A.J. Chorin. Numerical solution of the Navier-Stokes equations. *Mathematics of Computation*, 22:745–762, 1968.

[46] R. Weber, J.P. Smart, and W. Kamp. On the (MILD) combustion of gaseous, liquid, and solid fuels in high temperature preheated air. *Proceedings of the Combustion Institute*, 30 II(2):2623–2629, 2005.

[47] H. Stadler, D. Ristic, M. Förster, A. Schuster, R. Kneer, and G. Scheffknecht. NOx-emissions from flameless coal combustion in air, Ar/O 2 and CO2/O2. *Proceedings of the Combustion Institute*, 32 II(x):3131–3138, 2009.

[48] T. Plessing, N. Peters, and J.G. Wünning. Laseroptical investigation of highly preheated combustion with strong exhaust gas recirculation. *Symposium (International) on Combustion*, 27(2):3197–3204, jan 1998.

[49] A. Cavigiolo, M.A. Galbiati, A. Effuggi, D. Gelosa, and R. Rota. Mild combustion in a laboratory-scale apparatus. *Combustion Science and Technology*, 175(8):1347–1367, 2003.

[50] M. Derudi, A. Villani, and R. Rota. Sustainability of mild combustion of hydrogen-containing hybrid fuels. *Proceedings of the Combustion Institute*, 31 II:3393–3400, 2007.

[51] Alessandro Effuggi, Davino Gelosa, Marco Derudi, and Renato Rota. Mild Combustion of Methane-Derived Fuel Mixtures: Natural Gas and Biogas. *Combustion Science and Technology*, 180(3):481–493, 2008.

[52] Marco Derudi and Renato Rota. Experimental study of the mild combustion of liquid hydrocarbons. *Proceedings of the Combustion Institute*, 33(2):3325–3332, 2011.

[53] P. Sabia, M. de Joannon, S. Fierro, A. Tregrossi, and A. Cavaliere. Hydrogen-enriched methane Mild Combustion in a well stirred reactor. *Experimental Thermal and Fluid Science*, 31:469–475, 2007.

[54] B.B. Dally, A.N. Karpetis, and R.S. Barlow. Structure of turbulent non-premixed jet flames in a diluted hot coflow. *Proceedings of the Combustion Institute*, 29(x):1147–1154, 2002.

[55] F.C. Christo and B.B. Dally. Modeling turbulent reacting jets issuing into a hot and diluted coflow. *Combustion and Flame*, 142(1-2):117–129, jul 2005.

[56] Seung Hyun Kim, Kang Y. Huh, and Bassam Dally. Conditional moment closure modeling of turbulent nonpremixed combustion in diluted hot coflow. *Proceedings of the Combustion Institute*, 30(1):751–757, jan 2005.

[57] A. Frassoldati, P. Sharma, A. Cuoci, T. Faravelli, and E. Ranzi. Kinetic and fluid dynamics modeling of methane/hydrogen jet flames in diluted coflow. *Applied Thermal Engineering*, 30(4):376–383, mar 2010.

[58] Amir Mardani, Sadegh Tabejamaat, and Mohsen Ghamari. Numerical study of influence of molecular diffusion in the Mild combustion regime. *Combustion Theory and Modelling*, 14(5):747–774, 2010.

[59] M. Ihme, J. Zhang, G. He, and B. Dally. Large-eddy simulation of a jet-in-hot-coflow burner operating in the oxygen-diluted combustion regime. *Flow, Turbulence and Combustion*, 89(3):449–464, 2012.

[60] Y. Afarin and S. Tabejamaat. Effect of hydrogen on H2/CH4 flame structure of MILD combustion using the les method. *International Journal of Hydrogen Energy*, 38(8):3447–3458, 2013.

[61] Y. Minamoto, T.D. Dunstan, N. Swaminathan, and R.S. Cant. DNS of EGR-type turbulent flame in MILD condition. *Proceedings of the Combustion Institute*, 34(2):3231–3238, jan 2013.

[62] Y. Minamoto, N. Swaminathan, S.R. Cant, and T. Leung. Morphological and statistical features of reaction zones in MILD and premixed combustion. *Combustion and Flame*, 161(11):2801–2814, 2014.

[63] M. Ugur Göktolga, Jeroen A. van Oijen, and L. Philip H. de Goey. 3D DNS of MILD combustion: A detailed analysis of heat loss effects, preferential diffusion, and flame formation mechanisms. *Fuel*, 159:784–795, 2015.

[64] P. Li, F. Wang, J. Mi, B.B. Dally, Z. Mei, J. Zhang, and A. Parente. Mechanisms of NO formation in MILD combustion of CH4/H2 fuel blends. *International Journal of Hydrogen Energy*, 39(33):19187–19203, 2014.

[65] Z. Chen, V.M. Reddy, S. Ruan, N.A.K. Doan, W.L. Roberts, and N. Swaminathan. Simulation of MILD combustion using Perfectly Stirred Reactor model. *Proceedings of the Combustion Institute*, 000:1–8, 2016.

[66] Smith G.P., Golden D.M., Frenklach M., Moriarty N.W., Eiteneer B., Goldenberg M., Bowman C.T., Hanson R.K., Song S., Gardiner W.C., Lissianski V.V., and Qin Z. Gri-mech 3.0. `http://www.me.berkeley.edu/gri_mech/`, 1999.

[67] M. De Joannon, A. Saponaro, and A. Cavaliere. Zero-Dimensional analysis of diluted oxidation of methane in rich conditions. *Proceedings of the Combustion Institute*, 28:1639–1646, 2000.

[68] J. Aminian, C. Galletti, S. Shahhosseini, and L. Tognotti. Numerical investigation of a MILD combustion burner: Analysis of mixing field, chemical kinetics and turbulence-chemistry interaction. *Flow, Turbulence and Combustion*, 88(4):597–623, 2012.

[69] T. Echekki and J.H. Chen. Direct numerical simulation of autoignition in non-homogeneous hydrogen-air mixtures. *Combustion and Flame*, 134(3):169–191, 2003.

[70] S. Chapman and T.G Cowling. *The Mathematical Theory of Non-uniform Gases*. Cambridge Mathematical Library, 3rd edition, 1991.

[71] P. Moin and K. Mahesh. DIRECT NUMERICAL SIMULATION: A Tool in Turbulence Research. *Annual Review of Fluid Mechanics*, 30(1):539–578, 1998.

[72] A.J. Aspden, N. Nikiforakis, S. Dalziel, and J.B. Bell. Communications in Applied Mathematics and Computational Science. *Analysis of implicit LES methods*, 3(1):103–126, 2008.

[73] Kazakov A. and Frenklach M. Drm19. `http://combustion.berkeley.edu/drm/`, 1994.

Certificate of Ethics Review

Project Title:	A NUMERICAL STUDY OF TURBULENCE-FLAME INTERACTION IN MILD COMBUSTION
User ID:	675521
Name:	Vincenzo Panebianco
Application Date:	18/12/2016 20:13:44

You must download your certificate, print a copy and keep it as a record of this review.

It is your responsibility to adhere to the University Ethics Policy and any Department/School or professional guidelines in the conduct of your study including relevant guidelines regarding health and safety of researchers and University Health and Safety Policy.

It is also your responsibility to follow University guidance on Data Protection Policy:

- General guidance for all data protection issues
- University Data Protection Policy

You are reminded that as a University of Portsmouth Researcher you are bound by the UKRIO Code of Practice for Research; any breach of this code could lead to action being taken following the University's Procedure for the Investigation of Allegations of Misconduct in Research.

Any changes in the answers to the questions reflecting the design, management or conduct of the research over the course of the project must be notified to the Faculty Ethics Committee. Any changes that affect the answers given in the questionnaire, not reported to the Faculty Ethics Committee, will invalidate this certificate.

This ethical review should not be used to infer any comment on the academic merits or methodology of the project. If you have not already done so, you are advised to develop a clear protocol/proposal and ensure that it is independently reviewed by peers or others of appropriate standing. A favourable ethical opinion should not be perceived as permission to proceed with the research; there might be other matters of governance which require further consideration including the agreement of any organisation hosting the research.

GovernanceChecklist
A1-BriefDescriptionOfProject: Numerical study of turbulent combustion by means of a fluid dynamic code.
A2-Faculty: Technology
A3-VoluntarilyReferToFEC: No
A5-AlreadyExternallyReviewed: No
B1-HumanParticipants: No
HumanParticipantsDefinition
B2-HumanParticipantsConfirmation: Yes

C6-SafetyRisksBeyondAssessment: No
D2-PhysicalEcologicalDamage: No
D4-HistoricalOrCulturalDamage: No
E1-ContentiousOrIllegal: No
E2-SociallySensitiveIssues: No
F1-InvolvesAnimals: No
F2-HarmfulToThirdParties: No
G1-ConfirmReadEthicsPolicy: Confirmed
G2-ConfirmReadUKRIOCodeOfPractice: Confirmed
G3-ConfirmReadConcordatToSupportResearchIntegrity: Confirmed
G4-ConfirmedCorrectInformation: Confirmed

FORM UPR16

Research Ethics Review Checklist

Please include this completed form as an appendix to your thesis (see the Postgraduate Research Student Handbook for more information

Postgraduate Research Student (PGRS) Information		**Student ID:**	675521
PGRS Name:	Vincenzo Panebianco		
Department:	Engineering	**First Supervisor:**	Dr. James Buick
Start Date: (or progression date for Prof Doc students)	October 2012		

Study Mode and Route:	Part-time ☐	Full-time ☒	MPhil ☐	PhD ☒	MD ☐	Professional Doctorate ☐

Title of Thesis:	A Numerical Study of Turbulence-Flame Interaction in MILD Combustion
Thesis Word Count: (excluding ancillary data)	Approximately 72000

If you are unsure about any of the following, please contact the local representative on your Faculty Ethics Committee for advice. Please note that it is your responsibility to follow the University's Ethics Policy and any relevant University, academic or professional guidelines in the conduct of your study

Although the Ethics Committee may have given your study a favourable opinion, the final responsibility for the ethical conduct of this work lies with the researcher(s).

UKRIO Finished Research Checklist:

(If you would like to know more about the checklist, please see your Faculty or Departmental Ethics Committee rep or see the online version of the full checklist at: http://www.ukrio.org/what-we-do/code-of-practice-for-research/)

a) Have all of your research and findings been reported accurately, honestly and within a reasonable time frame?	YES ☒ NO ☐
b) Have all contributions to knowledge been acknowledged?	YES ☒ NO ☐
c) Have you complied with all agreements relating to intellectual property, publication and authorship?	YES ☒ NO ☐
d) Has your research data been retained in a secure and accessible form and will it remain so for the required duration?	YES ☒ NO ☐
e) Does your research comply with all legal, ethical, and contractual requirements?	YES ☒ NO ☐

Candidate Statement:

I have considered the ethical dimensions of the above named research project, and have successfully obtained the necessary ethical approval(s)

Ethical review number(s) from Faculty Ethics Committee (or from NRES/SCREC):	N/A

If you have *not* submitted your work for ethical review, and/or you have answered 'No' to one or more of questions a) to e), please explain below why this is so:

The study described within the submitted dissertation consists of numerical simulations, which are not related to any ethical aspect.

Signed *(PGRS)*:	Vincenzo Panebianco	**Date:** 03/08/2017